UNIVERSITY OF SOUTHAMPTON

FACULTY OF NATURAL AND ENVIRONMENTAL SCIENCES

School of Ocean And Earth Science

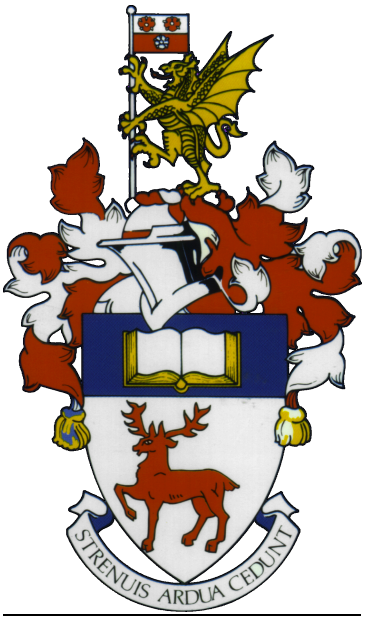

Orbital-scale atmospheric CO_2 and barium cycle reconstruction during the late Pleistocene using boron and barium isotopes in planktonic foraminifera

by

Elwyn de la Vega

Thesis for the degree of Doctor of Philosophy

April 2019

UNIVERSITY OF SOUTHAMPTON

ABSTRACT

FACULTY OF NATURAL AND ENVIRONMENTAL SCIENCES
School of Ocean and Earth Science
Geochemistry and Palaeoceanography
Thesis for the degree of Doctor of Philosophy

Orbital-scale atmospheric CO_2 and barium cycle reconstruction during the late Pleistocene using boron and barium isotopes in planktonic foraminifera

By Elwyn de la Vega

In the context of increasing atmospheric carbon dioxide (CO_2) caused by anthropogenic activity, knowledge of the impacts of CO_2 on the climate system, ecosystems, and sea-level is of primary importance. Palaeoclimate archives offer the unique possibility to study periods where climate was different and to investigate causal links between natural processes, atmospheric CO_2 and the climate response. One major driver of natural variations in atmospheric CO_2 is the biological pump in the oceans which strongly influences atmospheric CO_2 by sequestering carbon out of the atmosphere into the deep ocean. Hence for a comprehensive understanding of natural climate, reconstructing both CO_2 and palaeoproductivity is a powerful combination. Boron isotopes in planktonic foraminifera are a promising proxy to reconstruct pH and therefore atmospheric CO_2 beyond the ice core record (0-800 thousand years before present). Yet it has only been tested in few locations and at relatively low resolution, obscuring our ability to robustly quantify its accuracy, and spatial variability. Furthermore, the standard approach requires complex and time-consuming analytical procedures, limiting the generation of a large number of data sets due to the specialist training required. Here we present three aims: (1) Testing the boron-isotope-CO_2 proxy against the ice-core-CO_2 record at several locations and at high temporal resolution in order to build the confidence in the application of the proxy deeper geological time and to investigate the relationship between ice core CO_2 forcing and $\delta^{11}B$-derived relative pH change. We find that the broad pattern of $\delta^{11}B$-CO_2 reconstructions closely follow the ancient atmosphere record in the Pacific, and sub-Atlantic Oceans, although there are details within each record which both expand and caution the utility of the proxy. (2) Present the method development of automating the boron purification using the prepFAST-MC from carbonate matrix in order to remove the analytical bottleneck and increase the throughput of samples. We show that this method is capable of accurate and complete matrix separation of B from carbonate matrices in a variety of materials. (3) Explore the potential of barium

isotopes in planktonic foraminifera over the last deglaciation to track biological productivity in the palaeorecord as a new proxy of productivity. We show that interspecies differences are important hindering the use of $\delta^{138}Ba$ in bulk foraminifera and that non-spinose foraminifera may record marine particle microenvironment making spinose foraminifera better suited to explore ocean barium cycling in the paleorecord.

Table of Contents

Table of Tables

Table of Figures

List of Accompanying Materials

Appendix A. Supplementary data showing automation of boron purification for foraminifera samples.

Appendix B. Supplementary information for Chapter 3

Appendix C. The particular case of MIS 13. Supplementary data to Chapter 3 presenting boron-derived CO_2 data during MIS 13 and discussion.

Appendix D. Supplementary information for Chapter 4.

Academic Thesis: Declaration Of Authorship

I, Elwyn de la Vega, declare that this thesis and the work presented in it are my own and has been generated by me as the result of my own original research.

"Orbital-scale atmospheric CO_2 and barium cycle reconstruction during the late Pleistocene using boron and barium isotopes in planktonic foraminifera"
I confirm that:

1. This work was done wholly or mainly while in candidature for a research degree at this University;
2. Where any part of this thesis has previously been submitted for a degree or any other qualification at this University or any other institution, this has been clearly stated;
3. Where I have consulted the published work of others, this is always clearly attributed;
4. Where I have quoted from the work of others, the source is always given. With the exception of such quotations, this thesis is entirely my own work;
5. I have acknowledged all main sources of help;
6. Where the thesis is based on work done by myself jointly with others, I have made clear exactly what was done by others and what I have contributed myself;
7. None of this work has been published before submission

Signed: .....

Date: .....

Acknowledgements

A variety of people are to be thanked for the last 4 years spent at NOCS working with many different people.

I'll of course start thanking my primary supervisor Gavin Foster for his steady supervision throughout the thesis, encouragement, advice and good discussion on many aspects of science and lab work. Thank you for giving me the chance to conduct this job and for hiring me in the first place to work on my master thesis in the Foster lab. Thank you to Tristan Horner for welcoming me for 3 months in WHOI and introducing me to the world of barium isotope and for all the useful discussions we had on the data. Thank you to Paul Wilson my second supervisor, for following my work during the last 4 years and for feedbacks on the manuscript.

I'd also like to thank Laura Robinson and Philip Goodwin my viva examiners for the interesting discussion and comments on the manuscripts.

Next, I would like to acknowledge a few members of the B-team, that is the best support one could ever have when working long hours in the lab. Thank you to Miguel Martinez-Boti my Masters' supervisor who thoroughly taught me all the procedures in the lab from the prepFAST, the column chemistry to the wizardries of the Neptune. I owe most of my practical lab skills to you! Thank you to Eleni Anagnostou for being always around for support either on work or on personal level. Always good chatting to you!

Of course, comes Tom Chalk, who luckily managed to come back closer to me after his post-doc abroad. You give a constant support on all aspects of this PhD, including help in R, lab work and discussions of all kind, so big thank you for everything! Rachel, thanks for the company in the office and the long hours in the lab. Chris and Tali, great to have had you on board over the last year and make the B-team the friendly group it is. Thank you to Andy Milton, for the support for these so many sessions running boron isotopes or elements, we are lucky to have you running the plasma lab with so much passion! Thanks to Hannah and Sara for their company, to Megan Spencer for running C and O isotopes and running the paleo prep lab, and to Agnes Michalik and Matt Cooper for their back-ground work indispensable to keep the clean-lab running.

I don't forget Michael, Joe and Rosana, former B-teamers who have left NOCS earlier on. It's great to have boron colleagues around and have meet ups at conferences around the world.

I would also like to thank a few other people for informal discussions that have been always helpful. Thank you to Mathis Hain for your expertise and helpful discussion on the data and climate forcing, as well as support in Matlab, to Aly Lough for friendly discussions on geochemistry and lab work, to Ross Whiteford for discussions on modelling, to Miros Charidemou for insights on the Agulhas system and discussion on the data, and to Nayiu Zhang for advices on marine snow.

This PhD gave me the opportunity to stay in other great institutes, at WHOI and Bristol! I would like to thank Maureen Auro for teaching me procedures in the lab in Woods Hole and to Stephanie Bates and Kate Hendry for discussion and hosting me in the Bristol labs, as well as Serginio for providing me with a roof.

On a more social level, too many are to thank in this brilliant PhD community at NOCS. Thank you to my office mates: Lina for company in the office sometimes until late, Ed, Nayiu, Stu, Joel and Anas for their good company; to Melanie for being my writing buddy until the very end, and to Amaya, David, Cobain, Matthias, Oli, Manon, Adeline, Jan, Giuseppe, Luca, Barbara, Bhargav, Sahoo for the good times and support over the last years.
Last but not least, thoughts go to my family in France and New Caledonia, that I don't get to see often, thank you for the interest you had in my work. I hope you find this thesis interesting and see why paleoclimatology can be useful!

Definitions and Abbreviations

yrs – years

kyr – thousands of years

Myr – millions of years

ya – years ago

ka – thousands of years ago

Ma – millions of years ago

AA – Antarctic

AABW – Antarctic bottom water

AAIW – Antarctic intermediate water

ALK – total alkalinity

CDW–Circumpolar Deep Waters

DIC – Dissolved inorganic carbon

EEP – East equatorial Pacific

EUC – Equatorial Undercurrent Current

G-IG – Glacial-interglacial

GNAIW – Glacial North Atlantic intermediate water

MC-ICPMS – Multicollector Inductively coupled plasma mass spectrometer

JCp-1 – Japanese coralline standard Porites

LGM – Last glacial maximum

LR04 – Lisiecki and Raymo 2004, benthic oxygen isotope stack

MBE – Mid Brunhes Event

MBDI – Mid Brunhes Dissolution Interval

MIS – marine isotope stage

NADW – North Atlantic Deep Water

NEC – North Equatorial Current

S – Salinity

SEC – South Equatorial Current

SO – Southern Ocean

SST – Sea surface temperature

T – temperature

WEP – Western Equatorial Pacific

Chapter 1: Thesis introduction

1.1 Overview and key questions: Why study CO_2 and biological productivity in the past ?

Atmospheric CO_2 is a gas that is known to play a significant role in regulating the climate of the Earth due to its greenhouse properties capturing heat from solar radiation. Atmospheric CO_2 today is rapidly increasing due to the release of carbon caused by the burning of fossil fuels for energy, which has so far increased CO_2 concentrations from 280 ppm during the pre-industrial era to >400 ppm today (+ 30 % increase relatively to normal interglacial concentrations) (IPCC report AR5). Such levels of CO_2 were last observed during the Pliocene (2.6-5.2 Ma) and, in particular, during the Pliocene warm period where boron isotope data show concentrations of CO_2 of 300-400 ppm (Seki et al., 2010, Bartoli et al 2011, Martinez-Boti et al., 2013). Although the modern CO_2 rise is a transient response and the system is yet to reach full equilibrium, it remains beneficial to reconstruct CO_2 in warm periods of the past to determine the full equilibrated response of temperature, ice sheet and sea level to high levels of CO_2. For instance, recent reconstructions of CO_2 in the Pliocene (Martinez-Boti et al., 2015) have shown a similar relative range of CO_2 over glacial interglacial (G-IG) cycles compared to the Pleistocene (~100ppm), and yet each time period has a distinct response between temperature and ice volume (determined by oxygen stable isotopes of benthic foraminifera. e.g. Lisiecki and Raymo, 2004, Figure 1.1). This highlights that the response of global temperature to radiative forcing (also known as climate sensitivity) is likely different between the background climate states due to variations in the strength of feedbacks operating in the climate system at any given time (Lunt et al., 2010; PALEOSENS Project Members, 2012).

The levels of atmospheric CO_2 are well known for the past 800 thousand years from measurements of CO_2 in ancient air bubbles trapped in ice cores (Bereiter et al. 2015; Figure 1.2). These records are characterised by low levels during glacials (~180 ppm) and high levels in interglacials (~280ppm), and are a composite of ice cores from the Vostock East Antarctic station (0-420 ky, Petit et al., 1999); and the EPICA dome Concordia (Siegenthaler et al., 2005; Luthi et al., 2008; Bereiter et al., 2015; Figure 1.2).

The atmospheric concentration of CO_2 also varies on million year timescales (Figure 1.3) due to solid Earth processes such as silicate weathering, volcanism or tectonics (e.g. Pearson and Palmer, 2000 and references therein) although a complete understanding the causes of these long term changes remains uncertain. Similarly, despite many decades of study, the exact causes of the orbital variations in CO_2 superimposed on the long-term trends remain elusive, although changes in water mass structure, nutrient contents of surface waters and associated intensity of the biological pump (e.g. Sigman and Boyle, 2010; Hain et al., 2010) are thought to be key mechanisms, with a particularly strong focus on the Southern Ocean (e.g. Jaccard et al., 2013).

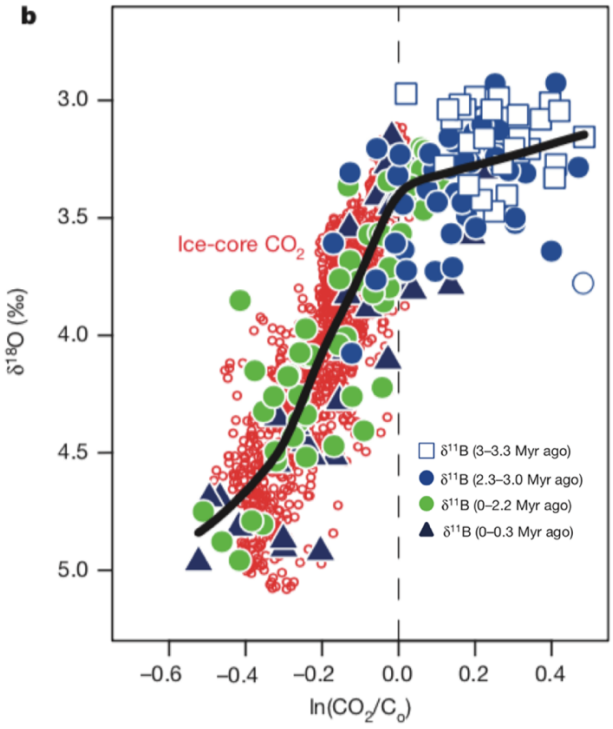

Figure 1.1 Relationship between benthic stack $\delta^{18}O$ (Lisiecki and Raymo, 2004) and CO_2 forcing showing a different response of $\delta^{18}O$ for different concentrations of CO_2 through time, here expressed in terms of CO_2 forcing. Figure modified from Martinez-Boti et al. (2015).

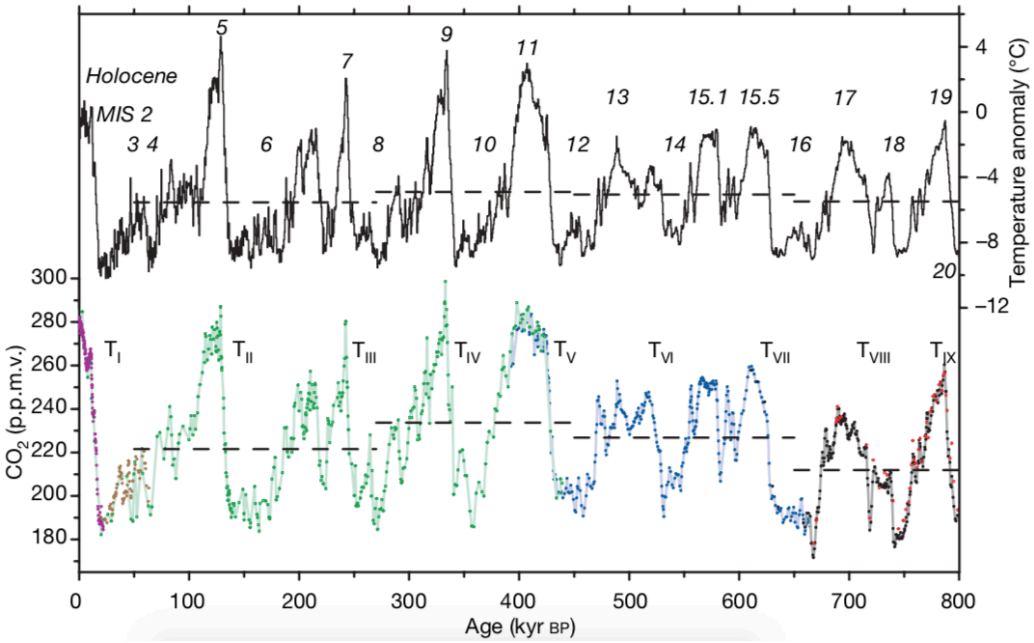

Figure 1.2 Compilation of atmospheric CO_2 over the last 800 ky from Antarctic ice (EPICA Dome C) and Antarctic temperature (derived from deuterium data) anomaly relatively to last millennium (Luthi et al., 2008).

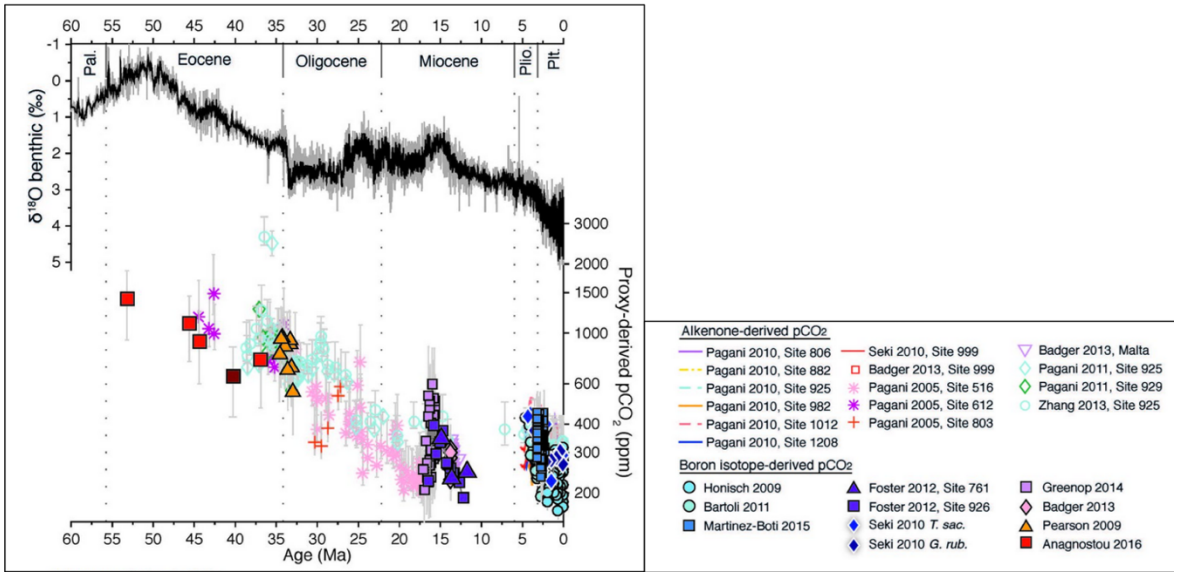

Figure 1.3 Compilation of CO_2 (www.pCO2.org) over the Cenozoic from boron isotopes and alkenones proxy. Top black line shows a compilation of benthic oxygen isotopes (LR04, Lisiecki and Raymo, 2004).

Hence proxies of CO_2 in the past (beyond 800 ky) coupled with proxies of paleoproductivity are essential to understand not only the causes of climate evolution but also the causes of CO_2 change. Many proxies of CO_2 and paleoproductivity exist (section 1.3 and 1.4), each associated with its own set of assumptions, limitations and caveats. Studies using the boron isotopic composition of planktonic foraminifera are one of the most promising methods for reconstructing pH and CO_2, yet they remain relatively scarce due to the complexity of the specialist chemical treatments needed to produce accurate values (e.g. Foster et al., 2013). Likewise, a number of proxies exist for tracing palaeoproductivity in the past (e.g. Ragueneau et al., 2000; Schoepfer et al., 2015) but different proxies applied to the same regions often paint contrasting pictures of the evolution of productivity through time (e.g. Diester-Haass and Faul, 2019). The barium isotopic composition of seawater has recently been determined at several locations and has been shown to be sensitive to barite precipitation in the ocean surface, a process intimately associated with the remineralisation of organic matter (e.g. Horner et al., 2015; Hsieh and Henderson, 2018). The potential of the isotopic composition of Ba as a proxy for paleoproductivity however remains untested.

The overall aim of this study is to provide a significant advance in the utility and applicability of the boron isotope proxy and investigate a potential new proxy for tracing variations in past biological productivity via the barium isotopic composition of foraminifera. The principal aims are:

1- Improve the methods of boron purification via ion exchange chromatography in order to increase the throughput of samples processing (Chapter 2).

2- Validate the boron isotope proxy over the last 800 thousand years, the interval covered by the ice core records, and investigate the relation between surface pH and climate CO_2 forcing (Chapter 4).

3- Explore the barium isotopic composition of ancient deep-sea sediments and foraminifera as a potential new proxy for past biological productivity (Chapter 4).

In the following sections an outline of oceanic carbonate chemistry is first presented as this forms an essential basis to the boron isotope pH proxy but also as a means to understand the variations in the carbon cycle. Then current hypotheses proposed to explain variations in atmospheric CO_2 on glacial (G) interglacial (IG) time scales and existing proxies of past CO_2 and biological productivity are compared and summarised.

1.2 Causes of CO_2 variations over glacial-interglacial cycles

1.2.1 The oceanic carbonate system

The oceanic carbonate system is composed of six variables and is of primary importance in understanding the global carbon cycle in modern times and in the past due to the close link between: (i) atmospheric CO_2, (ii) the biological pump, (iii) the abundance of marine calcifying organisms, and (iv) response of carbonate sediments at depth. The six variables are CO_2, the bicarbonate ion (HCO_3^-), the carbonate ion (CO_3^{2-}), dissolved organic carbon (DIC), total alkalinity (ALK) and pH (-log10 [H+]). When atmospheric CO_2 dissolves in the seawater it is transformed into aqueous CO_2 (and in a very minor proportion into carbonic acid H_2CO_3) such that:

$$CO_2\ (g) \overset{K_0}{\Leftrightarrow} CO_2\ (aq)\ (Eq\ 1.1.a)$$

CO_2 (aq) is then equilibrated with the other carbonate species CO_3^{2-}, and HCO_3^-, as follows:

$$CO_2\ (aq) + H_2O \overset{K_1}{\Leftrightarrow} HCO_3^- + H^+\ \ (Eq\ 1.1.b)$$

$$HCO_3^- \overset{K_2}{\Leftrightarrow} CO_3^{2-} + H^+\ \ (Eq\ 1.1.c)$$

The equilibrium constants of these three equations are K_0, K_1 and K_2 respectively and K_1 and K_2 are often referred as the first and second dissociation constants of carbonic acid and are defined as:

$$K_1 = \frac{[HCO_3^-]*[H^+]}{[CO_2]_{aq}} \text{ (Eq. 1.2.a)}$$

$$K_2 = \frac{[CO_3^{2-}]*[H^+]}{[HCO_3^-]} \text{ (Eq. 1.2.b)}$$

where the bracketed terms refer to the concentration of the species.

The sum of the three carbonate species is called dissolved inorganic carbon (DIC) and is defined as:

$$DIC = [CO_2] + [HCO_3^-] + [CO_3^{2-}] \text{ (Eq. 1.3)}$$

pH is defined as:

$$pH = -log[H^+] \text{ (Eq. 1.4)}$$

and is intrinsically controlled by the proportions of the three carbonate species such that at low pH, DIC is predominantly in the form of CO_2 and at high pH predominantly in the form of CO_3^{2-}. This is illustrated by the Bjerrum plot shown in Figure 1.4.

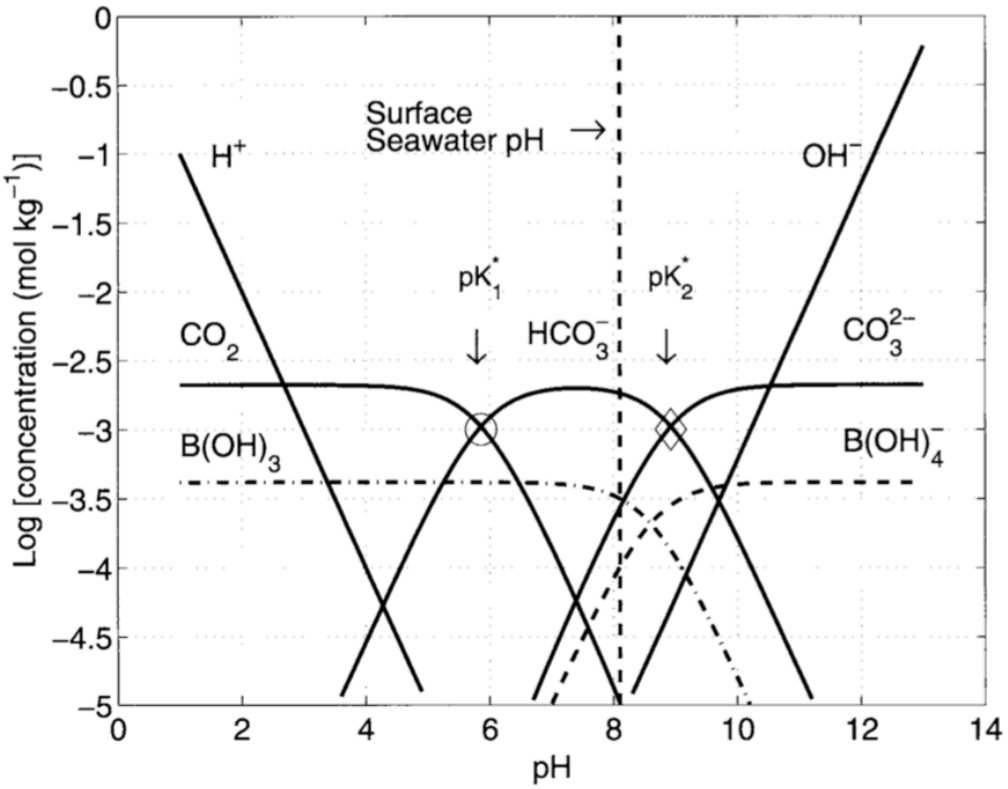

Figure 1.4 Bjerrum plot showing the concentration of carbonate (CO_2, HCO_3^-, CO_3^{2-}), and boron species (boric acid $B(OH)_3$ and borate ion $B(OH)_4^-$) H^+ and OH^- ion as a function of pH. Figure modified from Zeebe and Wolf-Gladrow (2001).

The last carbonate parameter, total alkalinity ALK is defined as:

$$ALK = [HCO_3^-] + 2[CO_3^{2-}] + [B(OH)_4^-] + [OH^-] - [H^+] + minor\ compounds$$

(Eq.1.5a)

This definition expresses the excess of proton (H^+) acceptors over proton donors.
Another way of defining alkalinity is the charge imbalance of conservative ions. In seawater conservative cations are present in a slight excess relative to the conservative anions and this imbalance defines total alkalinity such as:

$$ALK = [Na^+] + 2[Mg^{2+}] + 2[Ca^{2+}] + [K^+] - [Cl^-] - 2[SO_4^{2-}] - [NO_3^-] - [HCO_3^-] - 2[CO_3^{2-}] - [B(OH)_4^-] - [OH^-]\ + minor\ compounds$$ (Eq.1.5b)

This definition has a number of consequences and useful implications. Firstly, ALK is a conservative property such that it is not affected by change in temperature and pressure. Second, any transfer of CO_2 between seawater and the atmosphere does not change the concentration of conservative ions and hence ALK (i.e. even though the absolute concentrations of the carbon species in equations 1.3 and 1.5 change, ALK does not). Thirdly, precipitation or dissolution of $CaCO_3$, expressed by the equations 6a or 6b, impacts alkalinity due to the involvement of the charged species (Ca^{2+}, CO_3^{2-}, HCO_3^-).

$$Ca^{2+} + CO_3^{2-} \Leftrightarrow CaCO_3$$ (Eq.1.6a)

$$Ca^{2+} + 2HCO_3^- \Leftrightarrow CaCO_3 + CO_2\ + H_2O$$ (Eq. 1.6b)

Precipitation (dissolution) of 1 mol of $CaCO_3$ will increase (decrease) ALK and DIC in a 2:1 ratio. The production (respiration) of 1 mol of organic carbon will decrease (increase) DIC by 1 mol and, due to the uptake of NO_3^- (Eq 1.5b) by phytoplankton, will cause TA to decrease (increase) by 16/106 of a mol (based on the redfield ratio C:N:P=106:16:1).

All these chemical processes can be illustrated in ALK-DIC space (Figure 1.5) showing the influence of photosynthesis, respiration and $CaCO_3$ dissolution or precipitation. These processes are key in setting the state of the oceanic carbonate system.

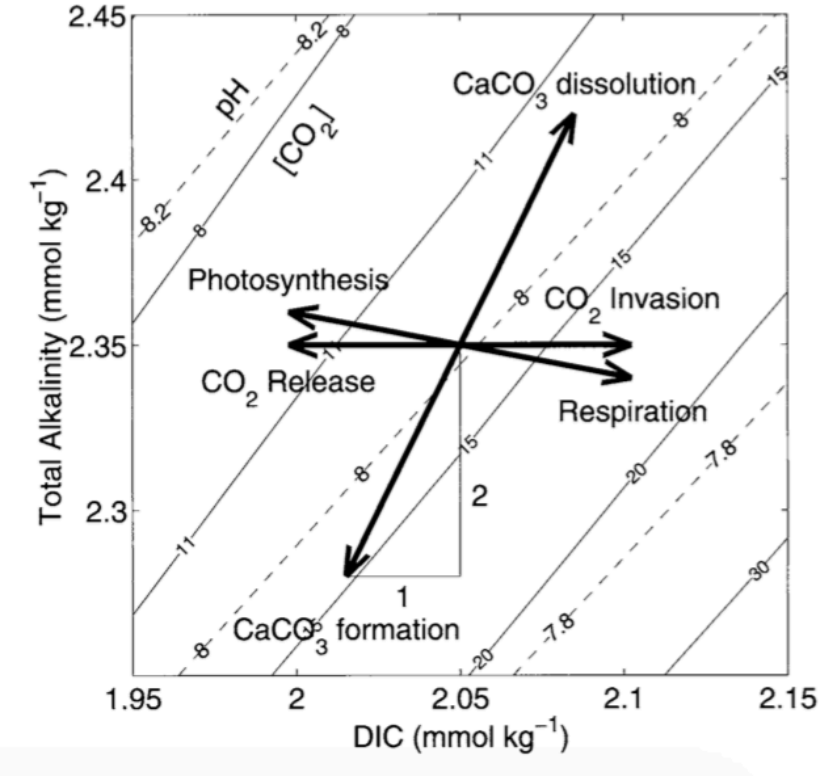

Figure 1.5 Effect of main biogeochemical processes on total alkalinity (ALK), dissolve inorganic carbon (DIC), CO_2 and pH.

The six variables of the carbonate system are linked by four equations (the expression of K_1, K_2, ALK and DIC). Consequently, the determination of only two variables enables the reconstruction of the other four.

Equation 1.a illustrates the communication between the ocean and atmosphere, CO_2 in the surface ocean is either degassed or pumped to/out from the atmosphere as shown by the map of air-sea CO_2 disequilibrium in Figure 1.6. This is mainly caused by temperature (see thermal pump section 1.2.2), variations in vertical water masses and the efficiency of biological productivity (section 1.2.2). The majority of the carbon stored in the exosphere (the ocean, atmosphere and biosphere) is in the deep ocean with 37,100 PgC, whereas the atmosphere contains 589 PgC (IPCC AR5) hence making the ocean and its carbonate system main players in regulating atmospheric CO_2 through variation in upwelling and biological pump.

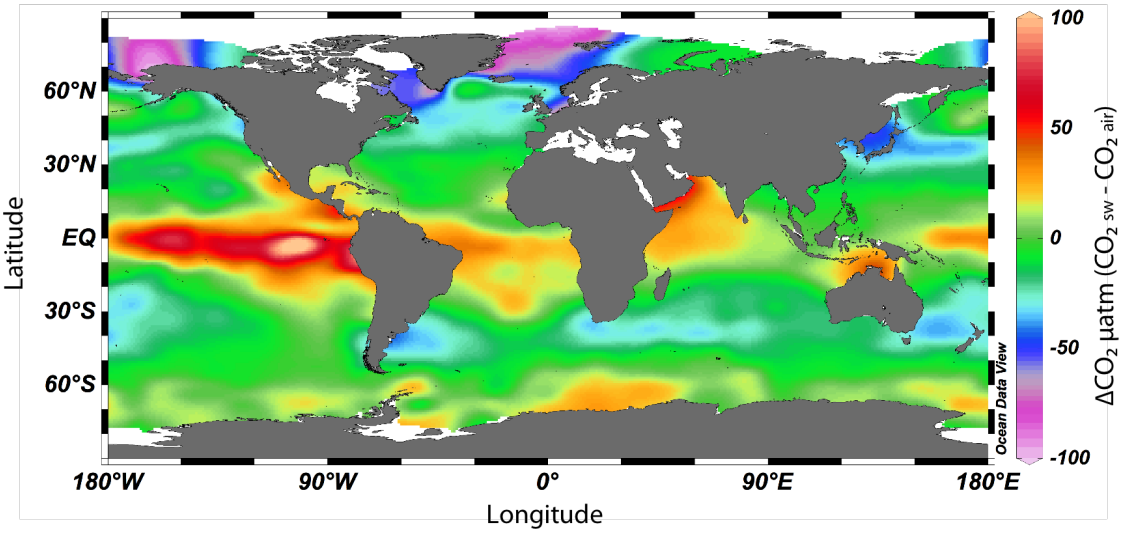

Figure 1.6 Map of Air-sea CO_2 disequilibrium ($\Delta CO_2 = pCO_{2\text{-sw}} - pCO_{2\text{-air}}$) for the global ocean (Takahashi et al., 2009) highlighting areas of source of CO_2 (upwelling areas, warm colours) and areas of CO_2 sink (downwelling of waters in Northern high latitudes, cold waters).

1.2.2 The three CO_2 pumps: the solubility, soft tissue and carbonate pump

There are three "pumps" that operate in the ocean to influence the concentration of CO_2 within surface and deep water. They are called pumps because their net effect is often (but not always) to transfer carbon from the surface to the deep ocean. Together these pumps are key in setting the depth profiles of pH and other parts of the carbonate system.

The thermal or solubility pump describes the temperature effect on the solubility of CO_2 in seawater. At low temperature, CO_2 preferentially dissolves in seawater whilst at higher temperature it degasses to the atmosphere. Because this pump changes CO_2 it influences DIC but has no effect on ALK.

The soft tissue pump describes the uptake of CO_2 from net photosynthesis of marine organisms in the surface ocean (e.g. diatoms, coccolithophores, dinoflagellates). It decreases surface DIC of seawater and slightly increases ALK (by a 1 to 16/106 ~ 0.15 ratio). significant part of the organic matter formed in the surface ocean is remineralised in the subsurface and a small percentage (10-40 %) is exported to the deeper part of the ocean (Henson et al., 2012). At depth the opposite reactions occur as exported organic matter remineralises adding the CO_2 and DIC back to the deep seawater.

The carbonate pump (or counterpump) is associated with the formation of calcium carbonate, $CaCO_3$, in the surface waters from hard shelled calcifying organisms (e.g. foraminifera, coccolithophores). In the ocean surface, $CaCO_3$ formation is a source of CO_2 (Eq 1.6b) as the removal of CO_3^{2-} or HCO_3^- shifts the equilibrium towards CO_2 (Figure 1.4) as it effectively decreases DIC (CO_3^{2-} and HCO_3^- in Eq 1.3) and removes ALK from the ocean (Ca^{2+} or CO_3^{2-}/HCO_3^- terms in Eq 1.5 and 1.6), changing the ALK:DIC ratio by 2:1. In a similar fashion to the soft tissue pump, the carbonate pump exhibits the opposite reaction at depth where more corrosive waters from remineralised carbon dissolves $CaCO_3$ hence increasing ALK and DIC (in a 2:1 ratio).

It is worth noting that the relative strength of the carbonate counter pump is very dependent on the type of organism (calcifiers vs. non-calcifiers) living in seawater. The Southern Ocean for instance is dominated by non-calcifiers (e.g. diatoms) making this region more sensitive to variations in the soft-tissue pump (e,g Hain et al., 2014). On the other hand, low latitudes which have a higher abundance of calcifying organisms will be sensitive to any changes in both the soft tissue and carbonate pump. Regardless of the specifics, any change in the ratio of organic to inorganic carbon will impact the strength of these two pumps and cause atmospheric CO_2 to increase or decrease accordingly.

Another underexplored CO_2 pump is the microbial pump whereby microbes produce refractory dissolved organic carbon (DOC), that doesn't undergo remineralisation hence it contributes to a stored pool of carbon in the ocean (Jiao et al., 2010). This pump may play a role during reduced nutrient input to the ocean during eccentricity minima (Ma et al. 2017).

1.2.3 Causes of G-IG CO_2 variations: a control by the Southern Ocean.

CO_2 cycles are strongly correlated with climates cycles (recorded by a stack of benthic $\delta^{18}O$ that is sensitive to temperature and ice expansion, Figure 1.1 and 1.3). Despite many decades of study, the causes of the CO_2 cycles evident in the ice-core CO_2 records (Figure 1.2) remain uncertain. The size of the deep ocean carbon reservoir and the relevant rates of carbon exchange indicate that changes in ocean carbon storage are the most likely cause for these cycles, although the exact mechanism(s) are yet to be determined. Nonetheless, given their influence on surface water, and hence atmospheric CO_2, changes in the strength of the various CO_2 pumps (section 1.2.2) are thought to be important (e.g. Sigman and Boyle, 2010; Hain et al., 2010).

Several mechanisms have been proposed to explain the cyclic variations of CO_2 over the last 800 kyr, and there is a tendency to link the changes in the strengths of the various CO_2 pumps with ocean dynamics of the Southern Ocean due to its strong connection with the (carbon-rich) deep ocean and its significant role in ventilating deep waters. The first process to consider in this regard is that solubility pump. Glacial intervals were associated with a decrease in ocean temperature and so this constitutes a sink of CO_2 to the ocean corresponding to a ~ 30 ppm CO_2 decrease (Sigman and Boyle, 2000). This action of the solubility pump is however compensated by both the change in salinity under more extended ice sheet conditions, and the reduction in vegetation cover during glacial period that are both sources of CO_2 to the atmosphere (Sigman and Boyle, 2000).

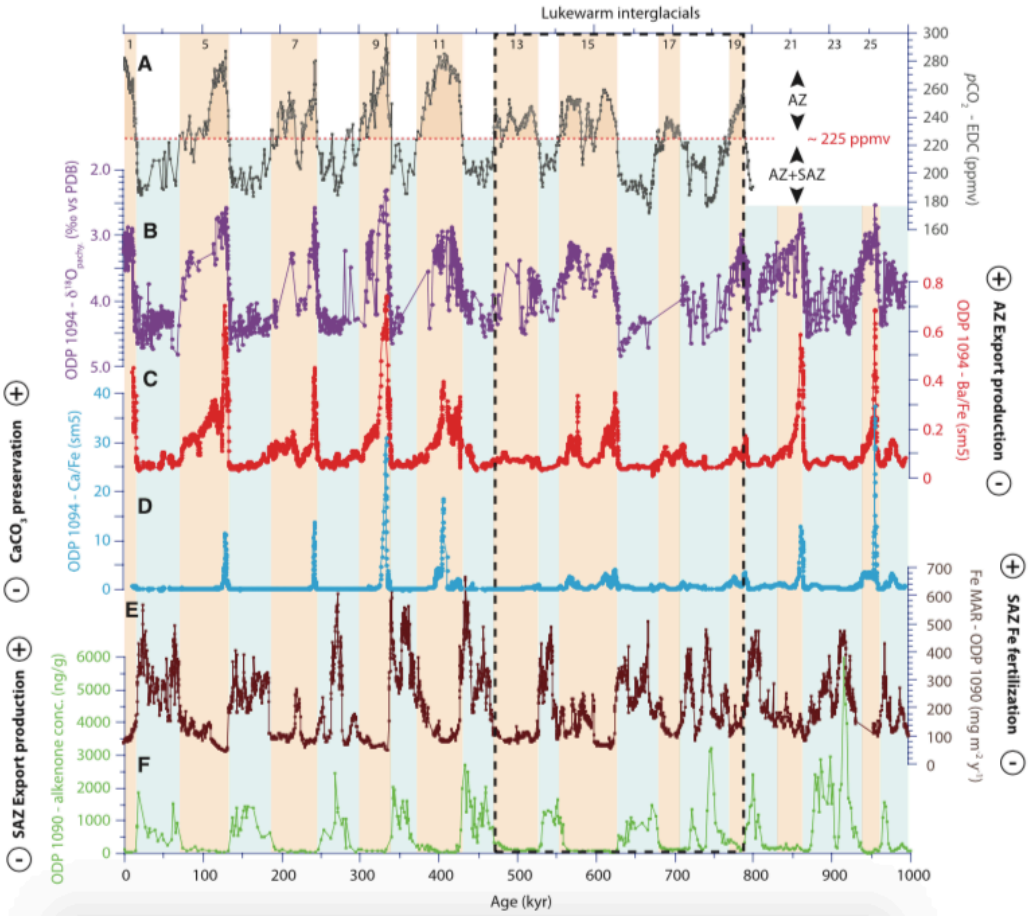

Figure 1.7 Variations of CO_2 from the ice cores (A) along with proxies of productivity in the Antarctic (AZ, panel B, C and D) and Subantarctic zone (SAZ, panel E and F) showing two modes of productivity in the Southern Ocean during the deglaciation. Figure adapted from Jaccard et al. (2013)

The modern Southern Ocean is a major source of CO_2 to the atmosphere (Figure 1.8) mostly due to the intensity of upwelling bringing deep remineralised carbon rich waters to the surface and to the inefficiency of the biological pump. Indeed, the Southern Ocean is a high nutrient low chlorophyll (HNLC) area, which means that most nutrients are not consumed (due to micro-nutrient limitation of iron, mainly) leaving a high quantity of so called "preformed nutrients" in seawater. Hence, any change in water masses or level of nutrients here will strongly influence the flux of CO_2 to the atmosphere.

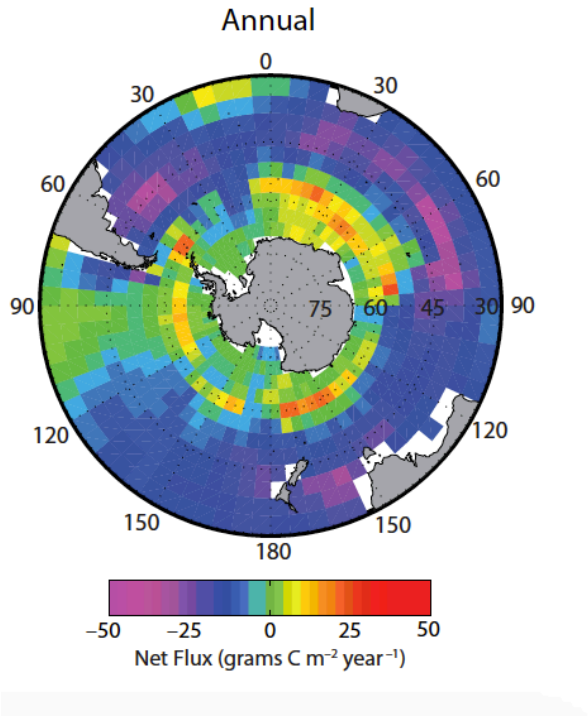

Figure 1.8 Annual flux in the Southern Ocean (Takahashi et al., 2012) showing the Antarctic Zone of the Southern Ocean is a source of CO_2 to the atmosphere.

The transition from interglacial to glacial state is characterised by increased sea-ice cover (Stephens and Keeling, 2000) and an increased stratification of the Southern Ocean, possibly due to a reduction or migration of westerlies (Toggweiler, 1999; Mortlock et al., 1991), both of which can equally drawdown CO_2 by reducing the degassing of CO_2 (e.g. Sigman and Boyle, 2010; Hain et al., 2010). This is consistent with the observation of reduced export in the Artic Zone (AZ) (Jaccard et al., 2013; Figure 1.7) during the first half of the glaciation. The second half of the glaciation, the transition to a fully glaciated state, is characterized by an increase in dust flux to Southern Ocean and an associated increase in the iron (Fe) content of deep-sea sediments in the sub Antarctic Zone (SAZ) of the Southern Ocean causing an associated increase in carbon export (Martinez-Garcia et al., 2014). This further draws down CO_2 due to a more efficient biological pump in the SubAntarctic zone. It has hence been suggested that the Southern Ocean acts in two modes with a productive (unproductive) AZ during interglacial (glacial) period and a productive (unproductive) SAZ during glacial (interglacial) (Jaccard et al., 2013, Figure 1.7). These mechanisms imply an increase in storage of carbon in the deep ocean. This is consistent with evidence of expansion of Antarctic bottom water (AABW, Figure 1.9) during glacial periods that can store an increased amount of carbon relatively to interglacials (Sigman et al., 2010). These carbon rich waters consequently became more corrosive (lower pH, e.g. Figure 1.4) impacting the preservation of deep-sea carbonate sediments, such that the carbonate dissolves and the lysocline (the depth zone below which carbonate sediments are dissolved) shoaled. This dissolution constitutes a source of alkalinity and DIC (Eq 1.6 and 1.5, Figure 1.5) and is known as carbonate compensation (Broecker and Peng, 1987). In detail, carbonate

compensation causes whole ocean ALK and DIC to increase with a 2:1 ratio further drawing down CO_2 from the atmosphere. This excess source of alkalinity (with added alkalinity input from riverine sources) eventually enables the system to reach steady state by restoring $CaCO_3$ burial (deepening of the lysocline).

Another mechanism that may contribute to these Southern Ocean centric mechanisms is the change in nutrients at low latitudes during the second half of the deglaciation as a consequence of the silica leakage hypothesis. Under Fe fertilisation in the SAZ, the consumption of nutrients by diatoms shifts the Si/N ratio of seawater from ~3:1 to less than 1:1 increasing the Si content in seawater (Matsumoto et al., 2002; Loubere et al., 2004; Matsumoto and Sarmiento, 2008). When these waters are advected to low latitudes by Antarctic intermediate waters (AAIW, Figure 1.9) or Subantarctic mode waters (SAMW), they supply the low latitudes with an excess of Si that favours silica organisms over calcifiers and reduce the carbonate pump (source of CO_2 by $CaCO_3$ precipitation). This mechanism which may be at play during the second half of the glaciation further reduces atmospheric CO_2 caused by the relative increase in whole ocean alkalinity.

Despite a growing appreciation of the likely mechanisms responsible for G-IG CO_2 change, the relative importance of the processes, particularly with regard to the role of whole ocean ALK and DIC change due to compensation vs. local changes in outgassing and soft tissue pump strength, remains uncertain.

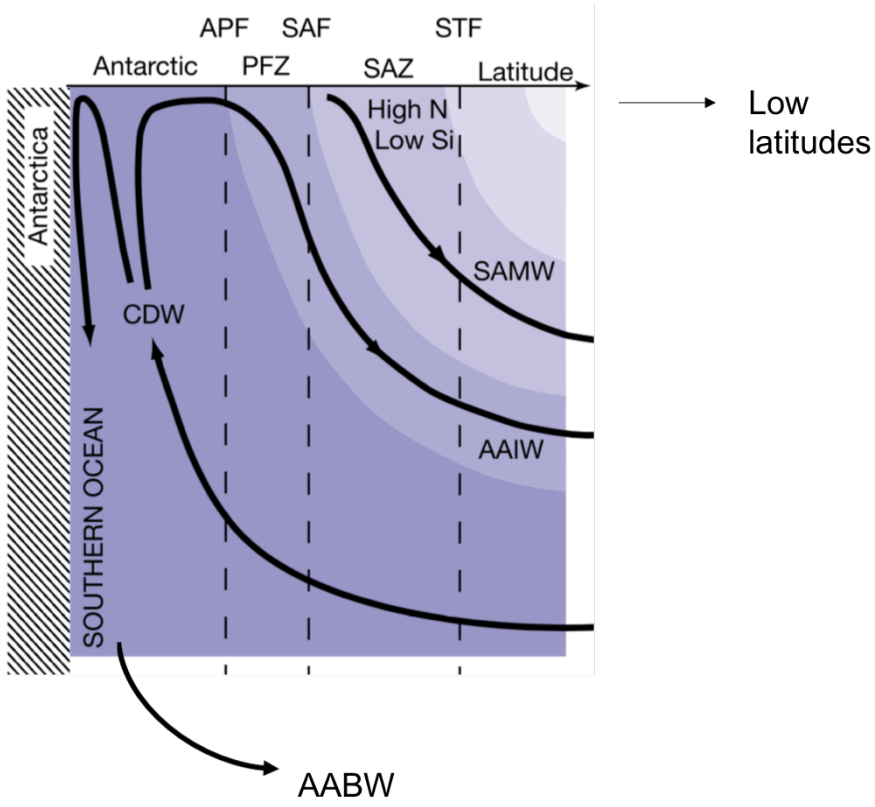

Figure 1.9 Schematic of main water masses between the Southern Ocean and the low latitudes highlighting its connection. PFZ Polar front zone, SAZ Subantarctic zone. CDW Circumpolar deep water, AABW Antarctic bottom water, AAIW Antarctic intermediate waters, SAMW Subantarctic mode waters. Modified from Sarmiento et al. (2003).

1.3 Proxies of CO_2

1.3.1 The boron isotope proxy.

1.3.1.1 Boron systematics

Boron isotopes has two stable isotopes ^{10}B and ^{11}B (present in nature at ~20 and 80 %, respectively) and is present in seawater in two forms, the trigonal boric acid $B(OH)_3$ and the tetragonal borate anion $B(OH)_4^-$ according to the following equilibrium:

$$B(OH)_3 + H_2O \leftrightarrow B(OH)_4^- + H^+ \quad \text{(Eq 1.7)}$$

The proportion of these two boron species varies as a function of seawater pH such as only $B(OH)_3$ is present at low pH and only $B(OH)_4^-$ is present at high pH (Figure 1.9a).

The boron isotopic composition of a material is expressed as $\delta^{11}B$, the deviation of the ratio of $^{11}B/^{10}B$ ratio relatively to the ratio of a standard (NIST 951), in parts per thousand, and defined as:

$$\delta^{11}B = \left(\frac{\frac{^{11}B}{^{10}B}sample}{\frac{^{11}B}{^{10}B}NIST951} - 1\right) * 1000 \text{ (Eq 1.8)}$$

The boron isotopic composition of seawater is 39.61 ‰ and due to the long residence of boron in the oceans (10-20 Ma; Lemarchand et al. 2002b) it has a uniform distribution (Foster et al., 2010). This isotopic composition results from a balance between the various sources (riverine input) and sinks (mid-ocean ridges, carbonate, clay and opal) of boron to the ocean (Lemarchand et al. 2002b).

There is a strong isotopic fractionation between the two aqueous species in seawater defined by α_B (or sometimes $\alpha_{3\text{-}4}$ or $^{11\text{-}10}K_B$):

$$\alpha_B = \frac{\frac{11}{10}\,R_{B(OH)3}}{\frac{11}{10}\,R_{B(OH)4^-}} \text{ (Eq 1.9)}$$

α_B has been experimentally determined by Klochko et al. (2006) and has a value of 1.0272. There is little evidence for a significant temperature effect on α_B (Foster and Rae, 2016). Hence, following previous studies (e.g. Henehan et al., 2014; Chalk et al., 2017), a temperature correction is often not applied to α_B.

Due to the uniformity of $\delta^{11}B_{sw}$, if the proportion of each boron species changes with pH (Figure 1.10a), their respective isotopic composition must also change to satisfy mass balance and the constant isotopic composition of seawater (Figure 1.10b). The $\delta^{11}B$ offset between the two boron species is caused by differences in their molecular structure (trigonal vs. tetragonal) where the $B(OH)_3$ preferentially incorporates ^{11}B due to higher bond strength in the trigonal structure leading to a relative concentration of ^{11}B on the trigonal site.

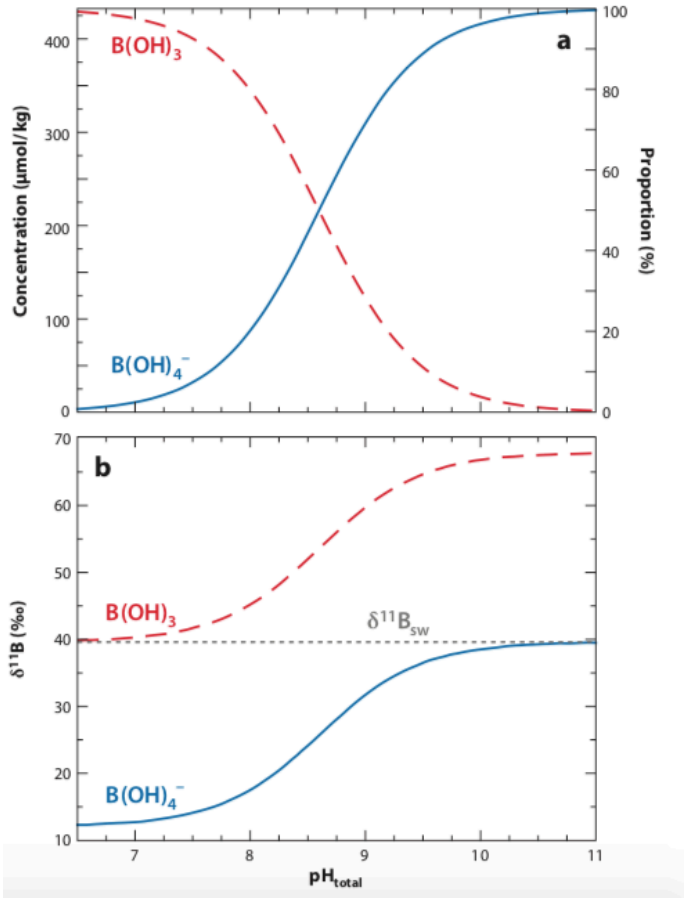

Figure 1.10 Relative proportion (a) and isotopic composition (b) of boron species as a function of pH (b). At low pH boron is entirely in the form of boric acid and at high pH, entirely in the form of borate ion. Adapted from Foster and Rae (2016).

Marine calcifying organisms are thought to incorporate boron via the following chemical reaction:

$$CaCO_3 + B(OH)_4^- \rightarrow Ca(HBO_3) + HCO_3^- + H_2O \text{ (Eq. 1.10)}$$

Although this equation implies sole incorporation of borate ion, there is evidence that trigonally coordinated boron (i.e. boric acid) is present in the calcium carbonate lattice of foraminifera that implied incorporation of $B(OH)_3$ (Kaczmarek et al., 2015). The lack of agreement between the boron isotopic composition of $CaCO_3$ and the $\delta^{11}B$ of boric acid, however, strongly implies a simple recoordination of $B(OH)_4^-$ into $B(OH)_3$ in the $CaCO_3$ lattice without fractionation (Noireaux et al., 2015). Consequently, since it is predominantly the borate ion that is incorporated in calcium carbonate (Hemming and Hanson, 1992), this gives the opportunity to reconstruct the variation in the $\delta^{11}B$ of borate in the past, and by extension pH, by measurements of $\delta^{11}B$ in ancient marine carbonates. Of particular importance in this regard are the planktonic foraminifera that inhabit the upper water column. Most foraminifera however do not directly record the $\delta^{11}B$ of seawater borate ion because of the influence of foraminifera calcification (a source of CO_2) and respiration (a sink of

CO_2) in their microenvironment (or diffusive boundary layer) and because many species live in symbiosis with dinoflagellates (photosynthetic algae) that live around the shell and whose combination of respiration and photosynthesis tends to increase the pH of the foraminifer's microenvironment (e.g. Vengosh et al., 1991; Hemming and Hanson, 1992; Rink et al., 1998; Wolf-Gladrow et al., 1999). Hence in order to reconstruct the $\delta^{11}B_{borate}$ (and pH) of bulk seawater it is essential to have a calibration between $\delta^{11}B$ of calcite (that reflects the microenvironment) and ambient seawater borate in order to account for these microenvironment effects (Sanyal et al., 1996; Henehan et al., 2013, 2016). Figure 1.11 illustrates the relation between $\delta^{11}B$ carbonate and borate for various foraminifera species (Henehan et al., 2016) showing a deviation from the 1:1 line caused by various degree of pH alterations by microenvironment.

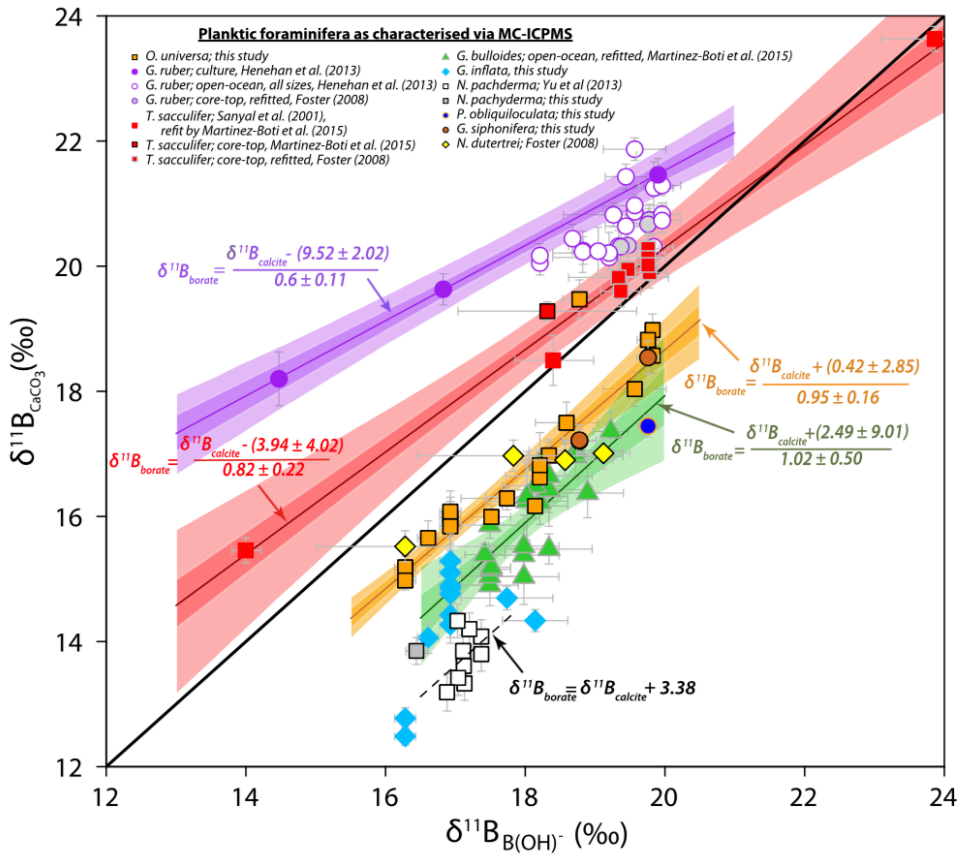

Figure 1.11 Existing calibration between $\delta^{11}B$ of borate and calcite for various planktonic foraminifera species reflecting the influence of microenvironment on pH. Whilst benthic foraminifera agree well with the 1:1 line (not shown), planktonic foraminifera exhibit a deviation from the theoretical line caused by the combination of symbionts' abundance, respiration and photosynthesis. Figure adapted from Henehan et al., (2016).

By considering mass balance and equilibrium constants of equations 7 and 9, pH can be expressed as :

$$pH = pK_B - \log(-\frac{\delta^{11}B_{sw} - \delta^{11}B_{borate}}{\delta^{11}B_{sw} - \alpha_B * \delta^{11}B_{borate}(\alpha_B - 1)}) \quad \text{(Eq 1.11)}$$

With pK_B derived from the equilibrium constant K_B of boron species in seawater (Eq 1.7) that is dependent of temperature and salinity. $\delta^{11}B_{sw}$ is the isotopic composition of seawater and α_B, the isotopic fractionation between between $B(OH)_3$ and $B(OH)_4^-$ (Eq 1.9).

1.3.1.2 Paleoreconstructions using boron isotopes, common assumptions and uncertainties

As detailed above (section 1.2.1) if two variables of the ocean carbonate system are known all other components can be calculated. Armed with a known $\delta^{11}B_{borate}$- $\delta^{11}B_{calcite}$ relationship and an expression of pH, aqueous CO_2 can be therefore be determined by knowing a second carbonate parameter.

For reconstructions of more recent geological intervals (i.e. the Quaternary), CO_2 estimates from the boron isotope system are often determined either assuming no change from modern values (e.g. using alkalinity, Henehan et al., 2013, Martinez-Boti et al., 2014, Chalk et al., 2017) or by using a simple modelling to account for alkalinity variation through time (Honisch et al., 2009). As long-term alkalinity changes are mostly controlled by slow weathering processes, it is acceptable to assume invariance from modern values (Hain et al. 2018). Another important point is that change in alkalinity impacts CO_2 by changing pH which we directly reconstruct with boron isotopes, hence there is only a weak effect of alkalinity on CO_2 when pH is known. This is illustrated in Figure 1.12 where ice core CO_2 is plotted (y-axis) against surface water pH derived from $\delta^{11}B$ (x-axis). The coloured lines show the expected relationship between these two variables, given a starting point at 8.16 and 280 ppm, when pH and CO_2 change are caused by DIC only (ALK constant; black), by ALK only (DIC constant; red) and by a ALK:DIC change with 1:1 ratio (green).

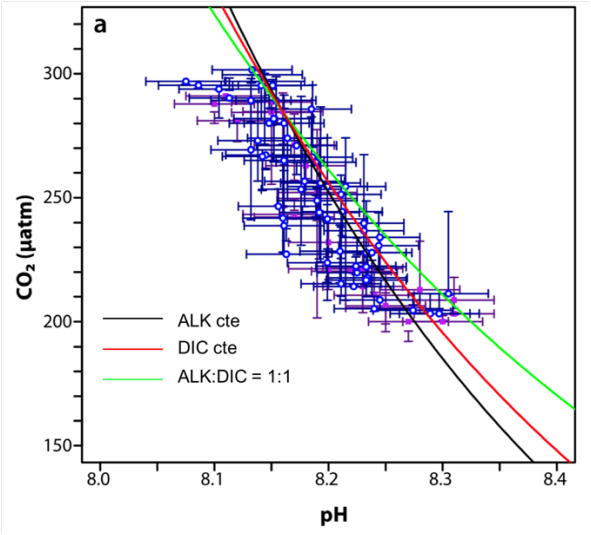

Figure 1.12 Cross-plot of interpolated ice core CO_2 as a function of boron-derived pH (blue and purple points from Chalk et al., (2017) late Pleistocene compilation) and theoretical lines when alkalinity is constant (black line), DIC constant (black line) and ALK:DIC evolving in a 1:1 ratio (green line). This shows that the data agrees well with the constant alkalinity line and that the constant alkalinity assumption is acceptable for at least late Pleistocene reconstructions.

For deeper time reconstructions, assumptions tend to be made relating to the saturation state of $CaCO_3$ (Ridgwell and Schmidt, 2010; Anagnostou et al., 2016). Recently, Sosdian et al. (2018) empirically estimated the dissolved inorganic carbon (DIC) and ALK evolution over the last 20 million years using boron isotopes in paired benthic and planktonic foraminifera and deep-sea carbonate ion reconstructions (Figure 1.13). This reconstruction showed only a minor long-term trend in DIC over the last 3 million years but nonetheless, in all cases, the second carbonate parameter is often a significant contributor to CO_2 uncertainty.

The expression of pH is dependent on T and S (in the pK_B term) and $\delta^{11}B_{sw}$. Temperature is commonly reconstructed in the paleo record using Mg/Ca of planktonic foraminifera (e.g. Annand et al., 2003) and modern salinity is commonly used and kept constant in paleo reconstructions due to the very weak effect of varying salinity on reconstructed CO_2 (1 PSU is equivalent to 1.5 ppm CO_2). The $\delta^{11}B_{sw}$ is also kept constant for recent reconstructions (i.e. Quaternary) and is an acceptable assumption on these timescales due to the long residence time of boron in seawater (10-20 Ma, Lemarchand et al. 2002b) and a maximum variation of $\delta^{11}B_{sw}$ of 0.1‰/My (Lemarchand et al 2002b). Deep time reconstructions however require estimates of $\delta^{11}B_{sw}$. These can be achieved by a variety of methods including models of riverine input, paired $\delta^{11}B$ measurements of benthic and planktonic foraminifera/pH gradients (Lemarchand et al., 2002b; Raitzsch and Hönisch, 2013; Anagnostou et al., 2016; Greenop et al., 2017). Figure 1.13 shows the evolution of reconstructed $\delta^{11}B_{sw}$ through time from different methods.

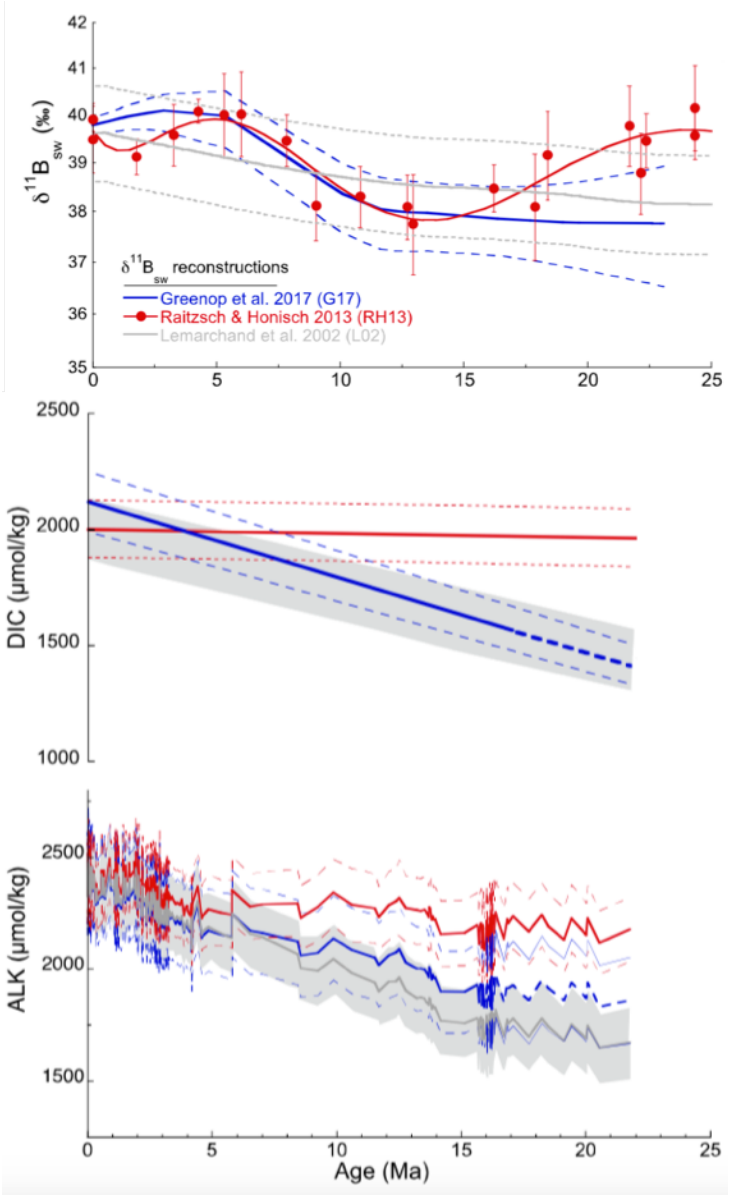

Figure 1.13 Reconstruction of $\delta^{11}B_{sw}$, grey (Lemarchand et al., 2002b), red (Raitzsch et al., 2013), blue (Greenop et al., 2017)) and alkalinity in the past based on surface pH and estimates of DIC (Sosdian et al., 2018) for different $\delta^{11}B_{sw}$. Modified from Sosdian et al (2018).

When using ALK as the second carbonate system parameter, the expression of aqueous CO_2 can then be written as a function of pH and ALK (Zeebe and Wolf-Gladrow, 2001) such as:

$$CO_2 = \frac{ALK - K_B * \frac{B_T}{K_B + [H^+]} - \frac{K_W}{[H^+]} + [H^+]}{\frac{K_1}{[H^+]} + \frac{2K_1K_2}{[H^+]^2}} \text{ (Eq 1.11).}$$

With B_T the total concentration of boron in seawater (0.432 mmol/kg; Lee et al., 2010), K_B, the equilibrium constant of boron species in seawater (Eq. 1.7), K_w the equilibrium constant of water, and $[H^+]$ the concentration of H^+.

An additional requirement to reconstruct atmospheric CO_2 accurately in the past is to choose a site that is in equilibrium with the atmosphere (green colours in Figure 1.6), hence reflecting global CO_2 that is well mixed with the atmosphere, avoiding upwelling areas that are major source of CO_2 to the atmosphere (e.g. Southern Ocean, East equatorial Pacific).

Atmospheric CO_2 is eventually reconstructed with Henry's law:

$$CO_{2(aq)} = K_0 * CO_{2(g)} \text{ (Eq 1.12)}$$

Where K_0 is dependent of temperature and salinity. pCO_2 is finally corrected for the minor disequilibrium at each site and this correction is kept constant throughout the record.

1.3.2 Other marine CO_2 proxies

A variety of other proxy systems are available to reconstruct atmospheric CO_2 in the past (e.g. Royer et al. 2001; Foster et al. 2017). Despite uncertainties remaining, the last decade has seen an improvement in the agreement between the various proxy systems (Beerling and Royer, 2011 NGS; Foster et al. 2017).

The available terrestrial proxies include the density of stomata in ancient leaves which is inversely proportional to the concentration of CO_2 in the atmosphere because plants increase the number of stomata (pores that serve as gas exchange between plant and air) under low CO_2 levels (e.g. Beerling and Woodward, 1996). This proxy requires a calibration between density of stomata and CO_2 that is species specific and is dependent on paleo altitude of the plant used, hence the use of this proxy requires careful assessments of paleo altitudes. Furthermore, records are rarely continuous due to the lack of continuous sedimentation in terrestrial sediments. Two other terrestrial proxies exist and serve as a threshold of CO_2 rather that absolute concentrations.

Two other terrestrial proxies exist such as the $\delta^{13}C$ in pedogenic carbonates (Cerling, 1991) and the presence/absence of Na carbonates ($NaHCO_3$, Nahcolite) that form above ~1125 ppm (Lowenstein and Demicco, 2006). These two either have no sensitivity (Nahcolite) or poor sensitivity ($\delta^{13}C$ of

pedogenic carbonates; Royer et al. 2001) at low CO_2 they are better suited for deep geological time scales where the earth was in a green-house high CO_2 world.

A frequently used marine-based proxy of CO_2 is the "alkenone proxy" (Pagani et al., 2011; Seki et al., 2010; Badger et al., 2013) that relies on the isotopic fractionation (ε_p) between $\delta^{13}C$ of seawater DIC and organic biomass, constrained by alkenones – molecules synthetized by some haptophytes algaes. This fractionation is dependent on the CO_2 concentration of seawater but is complicated by the influence of other parameters such as the species synthetizing alkenones, cell geometry (Popp et al., 1998), phosphate concentration (e.g. Pagani et al., 2011) and growth rate and other physiological processes such as carbon concentration mechanism (e.g. Laws et al., 1995; Bidigare et al., 1997; Bolton et al., 2012). The latter seems to be particularly active during periods where atmospheric CO_2 is relatively low, muting CO_2 variations during the end of the Cenozoic (e.g. Zhang et al., 2013; Beerling and Royer, 2011; Badger et al. 2019). Nevertheless, the main advantage of marine proxies over terrestrial proxies is their high resolution and better constraint on age.

Despite an improvement in terms of CO_2 proxy agreement on the large time scale (Foster et al. 2017), in detail and at shorter time scales (e.g. orbital) significant disagreements remain. These disagreements must indicate that some, or all, of the proxy estimates are inaccurate or the uncertainty associated with each estimate is underestimated. It is therefore key that a proxy undergoes extensive calibration and validation. One way to do this is to compare the proxy to the high-fidelity ice core CO_2 record. This has been done sparingly for the boron isotope proxy, and a central aim of this thesis to fully quantify the quality of the $\delta^{11}B$-CO_2 proxy by performing a thorough comparison with the ice core CO_2 record.

Figure 1.14 shows various CO_2 records from a number of different proxies showing some levels of disagreement highlighting above. The need to carefully test CO_2 proxies over a period where CO_2 is known with confidence is clearly needed as this is an effective way to address proxy confidence (Badger et al. 2019).

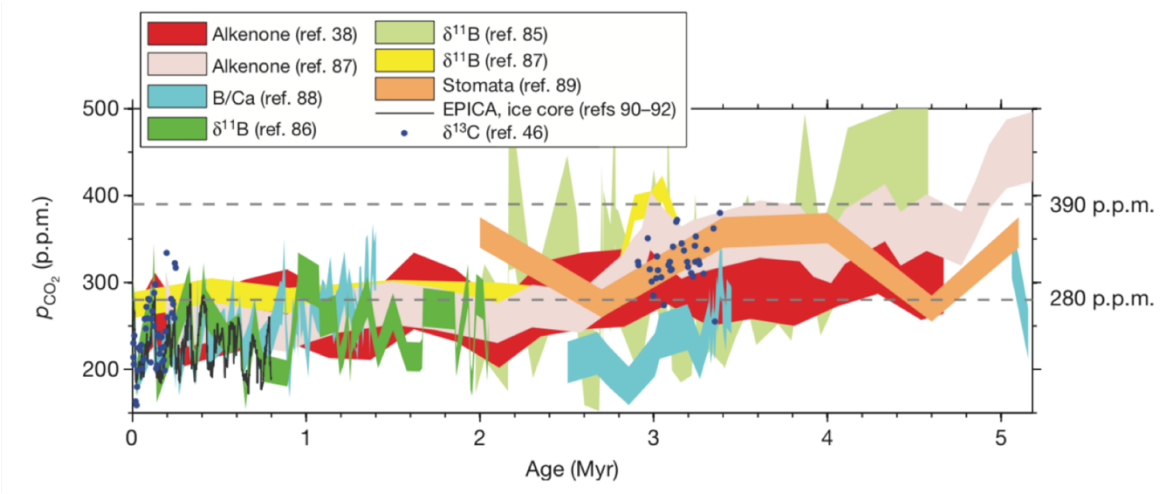

Figure 1.14 Compilation of various CO_2 record from different proxies over the past 5 Ma (figure adapted from Fedorov et al., 2013). Alkenones from Pagani et al. (2010) (red) and Seki et al. (2010) (pink); Ba/Ca from Tripati et al. (2009) (bleu); boron isotopes ($\delta^{11}B$) from Hönish et al., (2009) (dark green), Bartoli et al. (2001) (light green), and Seki et al. (2010) (yellow); stomata from Kürschner et al. (1996) (orange); ice core from Petit et al. (1999), Siegenthaler et al. (2005), Lüthi et al. (2008) (black)

1.4 Biological productivity proxies

Many methods have been used to reconstruct biological productivity in the past. Some proxies are based on sediment properties such as accumulation rates of $CaCO_3$, opal flux (e.g. Ragueneau et al., 2000), radiolaria flux (Lazarus et al., 2006, 2008), barite ($BaSO_4$) mass accumulation rate (MAR) and Bio-Ba (e.g. Bishop. 1998; Paytan and Griffith, 2007), total organic carbon or reactive phosphorus MAR (e.g. Schoepfer et al., 2014) whilst others rely on the assemblage of organisms such as benthic foraminifera accumulation rate (BFAR, e.g. Herguera and Berger, 1991; Diester-Haass et al. 2018, Diester-Haass and Faul, 2019). These proxies have a level of correlation with export productivity. Indeed, BFAR is sensitive to the organic matter produced in the surface and exported at depth since these foraminifera rely on the abundance of organic matter for food. The Ba based proxies are also sensitive to productivity due to the relationship between barite formation at the surface and degradation of organic matter. Reactive phosphorus MAR correlates with export productivity and organic carbon as they are related by the Redfield ratio (C:N:P = 106:16:1)

All these proxies however may be compromised by preservation, uncertainty in accumulation rates or sediment rates. Furthermore, the link between surface productivity and export productivity can be non-linear (Berger and Herguera, 1992), hence it is important to also have new proxies that constrain surface processes and importantly the magnitude of the soft tissue pump.

A number of geochemical proxies exist based on the isotopic and elemental composition of planktonic foraminiferal shells that are direct indicators of surface processes including nutrient

utilisation. These include $\delta^{13}C$ (an indicator of productivity by the preferential uptake of ^{12}C for photosynthesis, e.g. Gansen and Sarnthein, 1983; Mortlock et al., 1991), $\delta^{15}N$ in planktonic foraminifera a proxy of nitrate utilisation (e.g. Martinez-Garcia et al., 2014), or the Cd/Ca ratio of planktonic foraminifera that is a recorder of phosphate utilisation in seawater due to the extraction of Cd from seawater during photosynthesis (e.g. Boyle, 1988; Elderfield and Rickaby, 2000).

Barium-based proxies exist such as barite accumulation rate (BAR) (Paytan and Griffith, 2007), barium excess (Ba_{xs}, i.e. the barium not associated from the lithogenic phase and assumed to originate from barite in the water column), and barium normalised to the sedimentary phase (Ba/Ti, Ba/Al or Ba/Fe). These proxies however come with some uncertainty. Indeed, it has been shown that Ba_{xs} doesn't necessarily correlate with C export (Dymond and Collier, 1996, ADD REF) and uncertainty can arise from the sedimentary phase correction that can bias Ba from the biogenic phase, or with dissolution of barite under anoxic conditions when sulphate reduction operates (as sulphate concentration decrease below barite saturation). Such conditions can be monitored by indicators of pore water chemistry such as redox-sensitive trace metals (e.g. U, Fe, or Mn) (Paytan and Griffith, 2007).

Barium isotopes in seawater have recently been measured at several locations of the ocean and show an ability to track precipitation of barite and associated surface productivity through the preferential incorporation of the light isotope into barite (e.g. Horner et al., 2015; Bates et al., 2017; Hsieh and Henderson, 2018). Hence, measuring Ba isotopes in foraminifera could present an alternative to the limitations encountered with other Ba based proxies because (1) there are expected to be insensitive to redox conditions, and (2) should directly record the Ba isotopic composition of surface and subsurface seawater (after potential correction from species-specific fractionation) and associated change in biological productivity.

Exploring the potential of this novel proxy through measurement of the barium composition of foraminifera in the paleorecord is one of the aims of this thesis.

1.5 Thesis outline

This thesis comprises this introductory chapter, three chapters that include the generation of new data and new approaches in proxy development, and a conclusion chapter summarising the main findings. In detail:

Chapter 2 presents a new method to automate the separation of boron from a $CaCO_3$ matrix using the prepFAST-MC system by ESI (Elemental Scientific http://www.icpms.com/)The aim of this

study was to increase the throughput of samples for boron isotope analysis. Automated column chemistry is explored and evaluated, in particular, the effect of matrix loading, matrix wash, blank and speed of sample loading are detailed. A method suitable for the automated analysis of coral for $\delta^{11}B$ is then presented. The following questions are addressed:

Q1: Are the physico-chemical properties of ion exchange chromatography reproducible on an automated system?

Q2: to what extent automation increases the throughput of samples for boron isotopes analysis?

Chapter 3 presents two new high-resolution (1 sample every 3 to 6 kyr) record of boron isotopes in planktonic foraminifera over the last 600 kyr in order to fully evaluate the boron isotope proxy at several locations and test the assumptions underlying the proxy. The relationship between pH and CO_2 forcing is also investigated to validate a new formalism enabling the reconstruction of past CO_2 forcing by knowing pH only, removing the need of an assumption on a second carbonate parameter. This treatment also provides novel insights into the mechanisms responsible for the observed pH and CO_2 change.

Q3: Are boron isotopes a reliable proxy of CO_2 when tested at several location and time interval?

Q4: What can the new pH data reveal about the relationship between pH and CO_2 forcing over the late Pleistocene?

Chapter 4 explores the barium isotopic composition of ancient foraminifera over the last deglaciation in the upwelling east equatorial Pacific. The isotopic signals are investigated in mixed and monospecific species along with boron isotope data in order to evaluate the fidelity of barium isotopes as a tracer of productivity over time.

Q5: Do barium isotopes in foraminifera faithfully record the barium isotopic composition of seawater?

Q6: What are the ideal foraminifera species and ocean locations to reconstruct past changes in barium cycling?

Q7: Are barium isotopes in foraminifera a promising proxy for paleoproductivity reconstruction?

Chapter 5 summarises the themes and ideas presented and developed in chapter 2 to 4 and answers the questions addressed above. Guidelines are presented for future work in the field of boron-derived CO_2 and barium isotopes in foraminifera in the paleorecord. Preliminary boron-derived CO_2 data from the M2 glaciation during the Pliocene and other future work are briefly presented and discussed.

Chapter 2: Automation of boron chromatographic purification for $\delta^{11}B$ analysis of coral aragonite

Elwyn de la Vega[a], Gavin L. Foster[a], Miguel Angel Martínez-Botí[a], Eleni Anagnostou[a,b], M. Paul Field[c], M. Hwan Kim[c], Paul Watson[c], Paul A. Wilson[a]

[a]Ocean and Earth Science, National Oceanography Centre Southampton, University of Southampton, Southampton SO14 3ZH, UK
[b]GEOMAR Helmholtz Centre for Ocean Research Kiel, Wischhofstraße 1-3, 24148 Kiel, Germany
[c]Elemental Scientific, Inc., Omaha, NE, USA

Elwyn de la Vega wrote the manuscript and generated all boron isotope data
Gavin Foster, Miguel Martínez Botí, Eleni Anagnostou, and Paul Wilson provided discussion and gave feedback on the manuscript.
Paul Field, Paul Watson and Hwan Kim developed the prepFAST-MC system and provided technical assistance and discussion.
This chapter was formatted for publication.

Abstract

The boron isotopic composition of annually banded marine carbonates such as scleractinian corals is a powerful tool to reconstruct past changes in ocean pH over the last 100 years and more. To detect the small changes in past pH, the boron isotope ratio determination, expressed as $\delta^{11}B$, needs to be both precise and accurate (2sd<<1‰). Boron measurements on MC-ICPMS have shown to be sufficiently reproducible and accurate but this method requires boron to be carefully purified before analysis, which is time consuming, has relatively high sample requirements (~20 ng), and requires specialist training. We present here a new automated technique developed in collaboration with Elemental Scientific Inc. called the "prepFAST-MC" that enables the automatic extraction of B (up to 23 ng load) from a $CaCO_3$ matrix with a 25 µl column of resin Amberlite IRA743. An optimized method is established here with a specific matrix wash configuration and sample loading flow rate in order to efficiently remove matrix from sample carbonate and buffer without isotopic fractionation. Blank contribution was ~60 pg and hence can be considered negligible (<0.2% sample size). The efficiency of purification was demonstrated with the addition of up to 1.6 mg of dissolved low-B calcium carbonate to NIST SRM 951 with no impact on the accuracy of $\delta^{11}B$. The Japanese Geological Survey Porites reference material JCp-1, boric acid standard NIST SRM 951, and seawater all processed on the prepFAST-MC give a $\delta^{11}B$ within error of literature values ($\delta^{11}B_{JCp\text{-}1}$ = 24.31 ±0.20‰ (2sd, n=20); $\delta^{11}B_{NIST\ 951}$ = -0.02 ±0.15‰ (2sd, n=13) and $\delta^{11}B_{Seawater}$ = 39.50 ±0.06 ‰ (2sd, n=2)). In order to test the applicability of the approach to real samples, *Siderastrea siderea* coral purified with the prepFAST-MC are within uncertainty of the data processed with the manual ion exchange protocol, with an average offset between the two methods $\Delta\delta^{11}B$=0.01 ±0.28‰ (2sd, n=12). This demonstrates the capacity of the prepFAST-MC to generate accurate and reproducible $\delta^{11}B$ for a range of material.

2.1 Introduction

Measurements of atmospheric carbon dioxide (CO_2) over the last century have shown a significant increase with concentrations during the pre-industrial period (pre-mid 19th century) of around 280 ppm, reaching >400 ppm in 2015. This CO_2 rise has caused a decrease in surface seawater pH of ~0.1 unit on average due to the absorption of anthropogenic CO_2 into the ocean (Intergovernmental Panel for Climate change, IPCC WG1 AR5, chapter 3), and a strengthening of the greenhouse effect causing a rise in global mean surface temperature. The pH decrease and temperature rise have impacted the health of some marine calcifying organisms, including coral reefs that have experienced bleaching and decrease in skeletal extension or density (e.g. Bates et al., 2010; Castillo et al., 2011; Mollica et al., 2018). However, instrumental records of pH are scarce and only go back a few

decades. One way to reconstruct environmental parameters further in time is to use indirect measurement of pH using, for example, the boron isotope pH proxy in corals. This method has been used to capture existing records of surface pH change (e.g. Goodkin et al. 2015) and to extend the historical pH record (e.g. Liu et al. 2014; Fowell et al., 2018) but often at limited spatial and temporal resolution. To accurately and precisely evaluate environmental changes, pH and climate records are needed at high temporal resolution (e.g. a millennial resolution for geological time scales and sub annual for historic timescales). The principal reason for the scarcity in boron isotope data to date is the labour-intensive laboratory processes required during sample preparation for accurate boron analysis including material collection, clay and organic matter removal and, for some methodologies, time consuming boron purification by skilled users and facilities in a boron free clean laboratory.

Several mass spectrometer techniques are in common usage for measuring the isotopic composition of boron in marine carbonates: Negative and Positive Thermal Ionisation Mass Spectrometer NTIMS (Hemming and Hanson, 1992, 1994; Hönisch and Hemming, 2005; Foster et al., 2006) and PTIMS (Spivack and Edmond, 1986; Xiao et al., 1988; Lemarchand et al., 2002a), and more recently, Multi-collector Inductively Coupled Plasma Mass Spectrometer MC-ICPMS (e.g. Foster, 2008). The techniques require varying quantities of B (2-5 ng for NTIMS; 1 μg for PTIMS, 10-20 ng for MC-ICPMS), have different sample preparation protocols, and each yields different B isotope ratio precisions (from 0.1 to 0.7‰, roughly equivalent to 0-0.1 pH unit). The MC-ICPMS technique in general has arguably revolutionised the measurement of isotopic systems (e.g. Rehkämper et al., 2001). This approach offers many advantages when measuring dual isotope systems like boron because of the stability of the mass fractionation (although it is large: 16% per amu, Rehkamper et al., 2001) and efficient ionisation (boron: 60-90%). Previous studies have shown that MC-ICPMS allows the precise and accurate determination of $\delta^{11}B$ to, in some instances, better than 0.25‰ (at 95 % confidence) on as little as 10-20 ng of B (Foster et al., 2013).

The principal drawback of the MC-ICPMS methodology, however, is the need to purify the analyte prior to analysis to avoid interference and differential ionisation or instrumental mass fractionation between samples and the bracketing standard used to correct for it (e.g. Gregoire, 1987; Rehkamper et al. 2001). Thus, a requirement of accurate boron isotope analysis by MC-ICPMS is to remove the $CaCO_3$ matrix and isolate boron before analysis, while simultaneously avoiding isotopic fractionation (Foster, 2008). Here we present a new protocol that removes this significant bottleneck through the automation of boron purification using the prepFAST-MC (ESI, Omaha, NE, USA). This method has been used successfully for other isotopic systems measured in various materials, including Sr and Ca isotopes (Romaniello et al., 2015), Cu isotopes in biological samples (Enge et al., 2016) simultaneous separation of Sr, Pb and Nd isotopes from marine sediments (Retzmann et al., 2017), and U and Th isotopes in corals (Wefing et al., 2017).

Here for boron isotopes, we optimise blank contribution and matrix wash-out and test the method on a variety of standards and matrices including coral samples, seawater, and carbonate/boric acid reference materials or standards.

2.2 Experimental

2.2.1 Reagents and materials

Reagents used for sample cleaning, dissolution and boron purification (nitric acid HNO_3, hydrochloric acid HCl, 30% hydrogen peroxide H_2O_2, ammonium hydroxide NH_4OH, sodium acetate $NaCH_3CO_2$ and acetic acid CH_3COOH) were all reagent grade to minimise boron contamination. HNO_3 and HCl were further Teflon-distilled and these and other solutions were diluted to the required concentration with Milli-Q water (>18.2 MΩ/cm) dispensed with a Qguard B-pack. All laboratory procedures were carried out in an over-pressured box with HEPA-filtered boron-free air within a purpose made class-100 boron-free laboratory. All Teflon vials used for samples preparation were pre-washed in nitric acid (24 hours in 7M HNO_3 and 24 hours in 0.3M HNO_3), and plastic-ware was washed in 4M HCl for 24 hours.

2.2.2 Samples

In order to validate the accuracy of $\delta^{11}B$ on the prepFAST-MC, several reference materials and samples have been processed including a biogenic coral reference material (JCp-1, Okai et al., 2002, $\delta^{11}B = 24.3 \pm 0.18‰$ (2sd) see Table 2.1), seawater ($\delta^{11}B = 39.6 \pm 0.2‰$; Foster et al., 2010), matrix free boric acid NIST SRM 951 ($\delta^{11}B = 0 \pm 0.2‰$; Catanzaro et al., 1970), samples of corals *Siderastrea siderea* (hereafter *S. siderea*) from the forereef of the Mesoamerican barrier reef system (core FR-02, Belize, Castillo et al., 2011, Fowell et al., 2018). Sample size, B/Ca (when applicable), and long-term average $\delta^{11}B$ of these samples and reference materials are summarized in Table 2.2.

$\delta^{11}B$ JCp-1 (‰)	2sd (‰)	Reference	Boron separation
24.4	0.1	Dissard et al., 2012	Anion exchange chromatography
24.2	0.24	Liu et al., 2014	Micro sublimation
24.3	0.34	McCulloch et al., 2014	Cation and anion exchange chromatography
24.3	0.25	Henehan et al., 2013	Anion exchange chromatography

Table 2.1 Published $\delta^{11}B$ measurements of the carbonate reference material JCp-1 with boron separation methods. All measurements were conducted on MC-ICPMS

Standard or sample	**Type of matrix**	**Typical amount of buffer (µl)**	**Approximate amount of carbonate or standard used to yield ~20 ng of boron**	**Approximate B/Ca (µmol/mol)**	**$\delta^{11}B$ (‰) long-term average (or range for carbonate samples)**
JCp-1	Calcium carbonate (aragonite)	200	1 mg JCp-1 powder	500	24.25
Seawater	Ionic	10	5 µl	-	39.61
NIST 951	Boric acid only, no matrix	40	20 µl of 1 ppm	-	0
Siderastrea siderea	Calcium carbonate (aragonite)	200	1mg	460	23 to 26

Table 2.2 List of standards and samples processed on the prepFAST to assess accuracy of $\delta^{11}B$, with corresponding matrix, Na acetate –acetic acid buffer, mass of material used and long-term $\delta^{11}B$. Range of $\delta^{11}B$ observed in marine carbonates is 10 to 30 ‰.

The coral *S. siderea* were sampled at annual resolution and cleaned and dissolved using established protocols (Barker et al., 2003). Samples were oxidized to remove organic matter, weak acid leached to remove remaining cations and contaminants, and dissolved in ~ 0.15 M HNO_3. Samples were then split into two aliquots with one processed with the standard manual method (Foster, 2008, see section 2.2.3) and the other with the prepFAST-MC using the protocol established here with optimization tests on standards.

All prepFAST-MC data are compared with the respective long-term average at Southampton (for the reference materials) and the $\delta^{11}B$ of the same sample processed manually using the approach detailed in Foster (2008) and Foster et al. (2013) and briefly described below.

2.2.3 Boron separation

Boron purification for marine carbonates has traditionally been done manually via anion exchange chromatography (e.g. Foster, 2008; Foster et al. 2013, Rae et al. 2011, Henehan et al. 2013) or microsublimation (Misra et al. 2014; Wang et al. 2010, Pi et al. 2014, Raitzsch et al., 2018). The approach followed here involved the dissolution of the $CaCO_3$ sample in a small volume (usually ~ 300 µl) mixture of Milli-Q and 0.5 M HNO_3 and subsequent buffering (to pH≈5.5) with 2M sodium acetate – 0.5M acetic acid (with twice the volume of 0.5M HNO_3 used for dissolution).

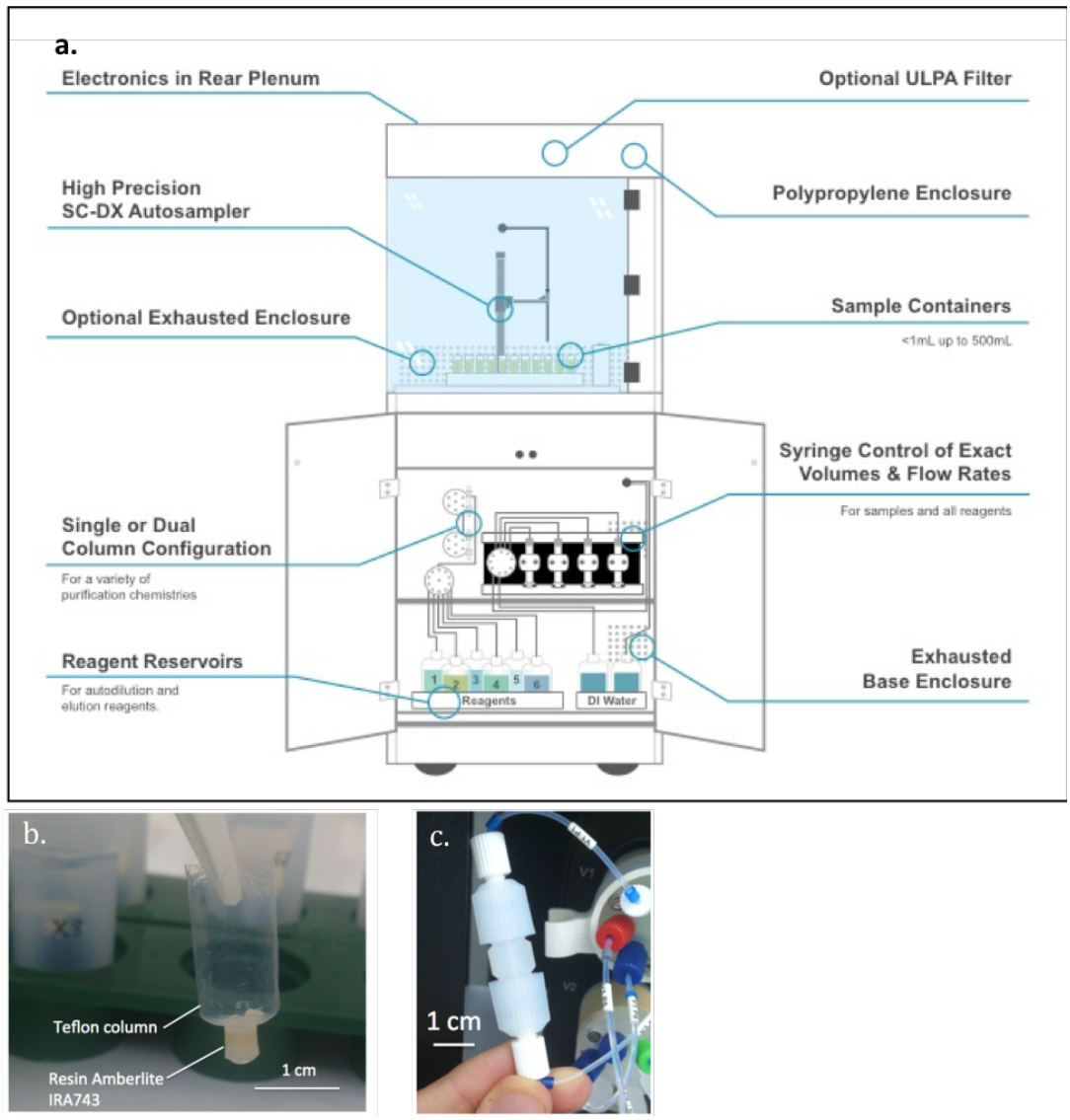

Figure 2.1 Illustration of the prepFAST-MC device automated system (ULPA filter and polypropylen enclosure was not used at Southampton) (a). Hand made Teflon micro-column used with the standard method (b) and prepFAST column (c) both filled with Amberlite resin IRA743.

Boron was then purified from the sample-buffer mixture by passing it through a 20 µl custom-made Teflon gravity-column (Figure. 2.1b) that contained boron specific anion exchange resin Amberlite IRA 743 (Kiss, 1988; Leeman et al., 1991; Lemarchand et al., 2002a) that has a strong affinity with boron at pH 5.5 (partition coefficient, $K_D \sim 10^4$, Lemarchand et al., 2002a). The maximum amount of boron loaded onto the column here was set at a maximum of 23 ng (based on long term data of manual gravity column) and sample load adjusted accordingly. The Amberlite was first hand-crushed and wet sieved to 63-120 µm to prevent fine grains escaping the column through the Teflon frit (10-30 µm pores) while ensuring a high surface area. At pH 5.5, boron is bound to the resin allowing the carbonate matrix and buffer to be removed with rinses of milli-Q water (Figure 2.2b).

It is important to minimize the amount of matrix remaining as this can be the cause isobaric interferences and instability of instrumental fractionation on MC-ICPMS (Foster, 2008; Guerrot et al., 2011). Once the matrix was removed, boron was eluted with five volumes of 0.5M HNO_3 of ~100 µl (~25 x resin volume; Figure 2.2c). The lower pH of the eluent causes the boron K_D to drop below 1 releasing the boron from the column. The protocol of this standard approach is described in Table 2.3a.

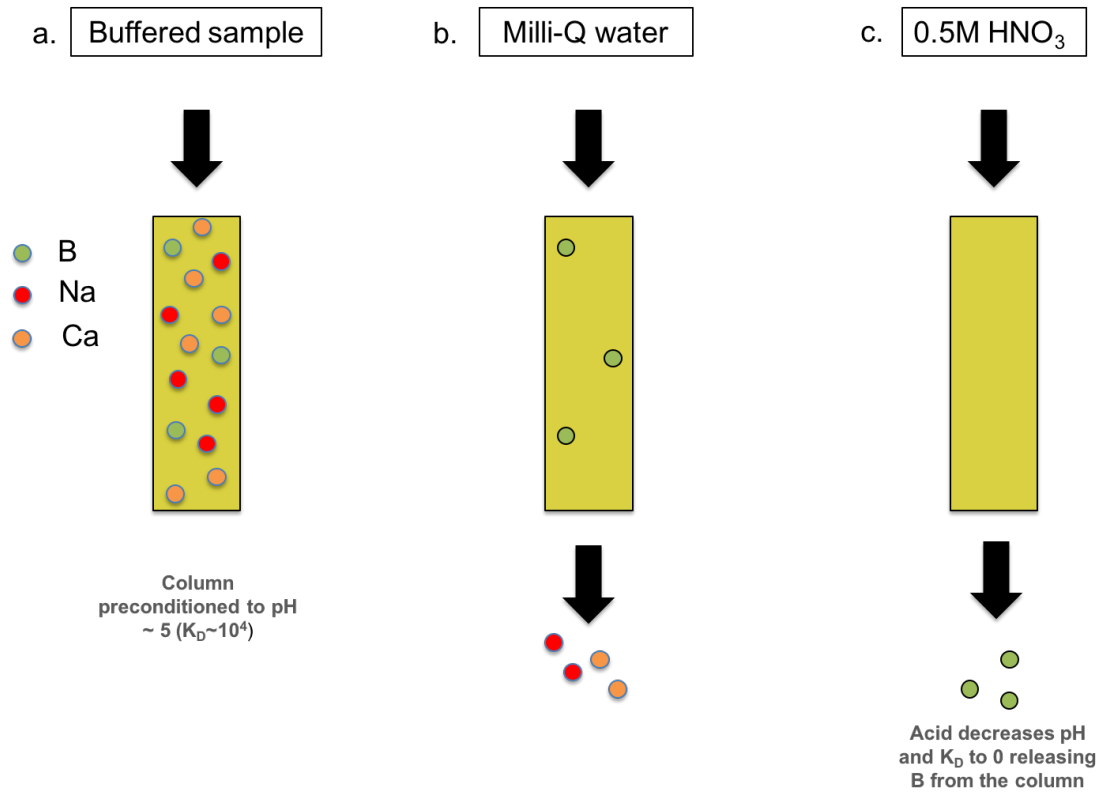

Figure 2.2 Illustration of ion exchange chromatography. Buffered sample is loaded onto a resin (yellow) (a) preconditioned with milli-Q (increasing the partition coefficient K_D between boron and resin to 10^4). Matrix is removed with milli-Q (b), and boron eluted with 0.5M nitric acid (c).

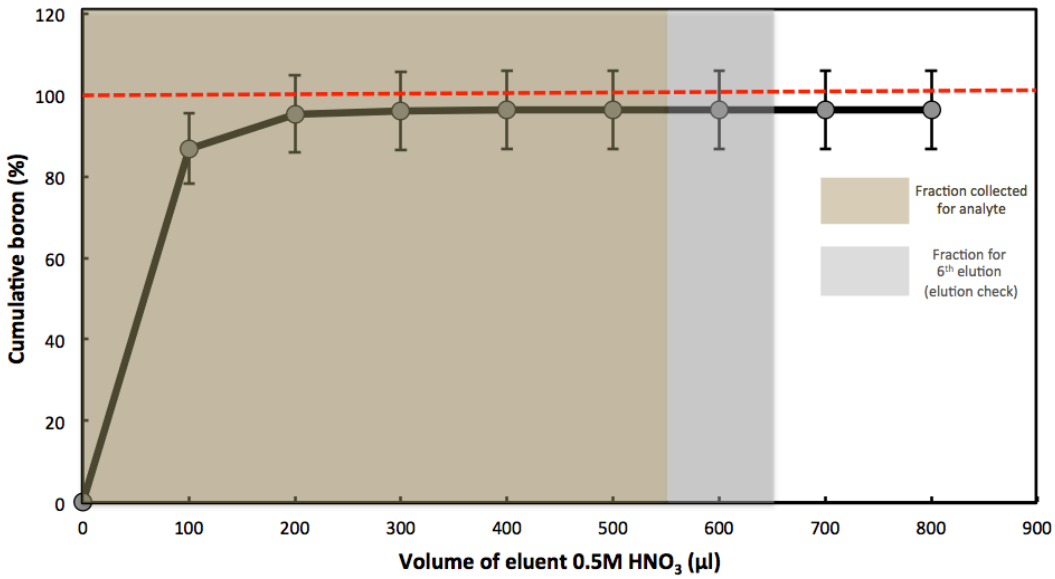

Figure 2.3 Elution curve for a 25 ng B size of standard NIST SRM 951. Boron concentration was measured by direct reading of ^{11}B intensity (in V) on MC-ICPMS, a 10% error was applied to the measurement to account for the uncertainty in manual reading. Red dotted line represents 100% yield target.

The principle of boron purification with the prepFAST-MC system (illustrated in Figure 2.1a) remains similar to the standard method described above but with several modifications to adapt to automation. Samples were first manually dissolved and buffered in the same way but in the prepFAST-MC samples were introduced with a probe that takes up the buffered sample and dispenses it through an online column CF-MC-B-25 (Figure 2.1c) made of 25 µl of hand-crushed Amberlite resin identical to the gravity columns in the manual method. The same resin was reused for each samples. The sample matrix was then rinsed with a succession of Milli-Q rinses and boron fraction was eluted with nitric acid. Five elutions of 100 µl 0.5M HNO_3 were sufficient to collect all boron from the prepFAST-MC column as shown on the cumulative elution curve in Figure 2.3. Complete collection of boron (100% yield) is necessary for measurements on MC-ICPMS (Lemarchand et al., 2002a) and was obtained after 300 µl with the prepFAST-MC. A further sixth elution (the 'elution check') was also collected and measured to monitor complete boron recovery (as is also done in the standard method).

As detailed in other prepFAST-MC methods (Romaniello et al., 2015; Enge et al., 2016; Retzmann et al., 2017; Wefing et al., 2017), volume and flow rate through the prepFAST-MC column were controlled through a set of syringe pumps. Contrary to gravity column, this enabled the user to precisely define the optimized flow rate of reagent going through the column at each stage. A rotary multivalve enables different reagents (sample, air, Milli-Q and acid) to be loaded and dispensed through the column. Each reagent was temporarily stored in the sample loop before being dispensed to the location of interest (column, probe or waste). All steps were controlled by software and parameterized by the user.

a.

Steps for manual gravity column	Reagents and volumes
Clean column	1 x fill the column with 0.5M HNO3 1 x 1ml 0.5M HNO3
Condition column (to pH~5)	2x 1ml Milli-Q
Load buffered sample	Buffered sample
Wash out matrix	4 x 200 µl Milli-Q around the rim of the column to wash the walls 4 x 200 µl Milli-Q
Elute boron	5 x 110 µl 0.5 M HNO3
Collect 6th elution (elution check)	1 x 110 µl 0.5 M HNO3
Clean column	1 x fill the column with 0.5M HNO3 1 x 1ml 0.5M HNO3
Wash acid and store column	2x 1ml Milli-Q

b.

Steps for prepFAST method	Volume (µl)	Reagent	Flow rate (µl/min)
Clean column	3 x 1000	0.5 M HNO3	2000
Condition column	2 x 1000	Milli-Q water	2000
Load sample	Sample volume	Buffered sample	100
Matrix wash out configuration 2	[1000 Forward 1000 Reverse] x 2 1000 Reverse x 4	Milli-Q water	10000
Elute boron	5 x 100	0.5 M HNO3	500
Elute tail	1 x 100	0.5 M HNO3	500

Table 2.3 Protocol of boron purification for the standard manual method (a), and optimised protocol for the prepFAST automated method (b).

2.2.4 Boron isotopes and elemental analysis

Boron isotope analyses were carried out on a Thermo Fisher Neptune MC- ICPMS with 10^{12} Ω amplifier resistors at the University of Southampton using bracketing standards of NIST SRM 951 following methods described elsewhere (Foster, 2008; Foster et al. 2013).

The external uncertainty is calculated based on long-term reproducibility of JCp-1 processed by gravity columns, typically <0.25‰ (2σ) and is expressed as:

$$2\sigma = 129600\ e^{-212 \times [^{11}B]} + 0.3385\ e^{-1.544 \times [^{11}B]}$$

Where 2σ is the uncertainty at 95 % confidence, and $[^{11}B]$ the blank corrected intensity in volts (V) of ^{11}B measured on MC-ICPMS.

Na intensity was measured on the Neptune prior to analysis on a six-fold diluted aliquot (20 µl) of the purified sample to assess the level of sodium-acetate buffer left in the sample, here used as an indicator of the efficiency of total matrix removal (i.e. Na and dissolved CaCO3 sample; Foster et al., 2013). Na concentrations are reported as parts per billion estimated from the Na peak height and a Na intensity of 400V per ppm.

Following previous studies, elemental analysis was also undertaken on a diluted aliquot of the dissolved carbonate samples (prior to boron purification) on a Thermo Fisher Element ICPMS and X-series ICPMS at the University of Southampton. This ensured that the carbonate cleaning was efficient (e.g. Rae et al., 2011) by monitoring levels of Al/Ca (indicator of clay), and Mn/Ca or Fe/Ca (indicators of metal crust).

2.2.5 prepFAST-MC method development

2.2.5.1 Matric wash-out and matrix effect

Two configurations of matrix wash-out were examined by varying the volume, flow-rate and direction of Milli-Q through the prepFAST column to determine the protocol with highest matrix washout efficiency (Table 2.4). Direction of flow was set in forward direction (forward direction as for sample loading and elution) for configuration 1 or alternated (forward and reverse) for configuration 2. Flow rate was also varied by washing out the matrix slowly (1000 µl/min, configuration 1) or rapidly (10 000 µl/min, configuration 2). We tested the influence of washout flow-rate on matrix removal on NIST 951 for configuration 1, and JCp-1 for configuration 2.

Matrix wash out configuration	Volume (µl)	Reagents	Flow rate (µl/min)	Na (ppb)
pF-Configuration 1	8 x 1000	Milli-Q water	1000	9±0.7 9 (n=2)
pF-Configuration 2	[1000 Forward + 1000 Reverse] x 2 1000 Reverse x 4	Milli-Q water	10 000	0.9±0.6 (n=20)
Gravity column	8 x 200	Milli-Q water	<250 µl/min	0.5±0.8 (n=50)

Table 2.4 Configurations of two types of matrix wash out on the prepFAST-MC (pF) tested on boron reference materials, standards and carbonate samples (for typically ~1-2 mg $CaCO_3$ and ~250 µl of buffer). Assessment of matrix removal efficiency by measurement of Na concentration in six-time diluted aliquot (20 µl) of purified sample. Na levels with the wash out on the prepFAST range between 9 ppb ± 0.7 (pF-Configuration 1) and 0.9 ppb ± 0.6 (pF-Configuration 2). The wash out with the standard gravity column method gives an average Na concentration of 0.5 ±0.8 ppb.

In the gravity column methodology described by Foster et al. (2013) the efficiency of the matrix wash-out is routinely assessed after boron purification, with measurements of Na intensity by MC-ICPMS as an indicator of the sample carbonate and buffer matrix (see section 2.2.4).

Here an aliquot taken of six JCp-1 samples before and after purification has been measured on ICPMS X-series to assess the levels of Na and Ca in the purified sample and to test how reliable Na is as an indicator of matrix removal.

To explore the effect of varying amount of carbonate matrix on boron separation, boron-free (B content was below blank levels) natural carbonates were added to NIST 951. These carbonates were dissolved stalagmite from diverse caves from five countries with a wide range of trace element concentration (e.g. Mg/Ca ranging from 1 to 60 mmol/mol). The carbonates were added to NIST 951 standard such that Ca ranged from 0 to 0.6 mg and processed with the prepFAST-MC. This range is equivalent to 0 to 1.6 mg of $CaCO_3$ and typically encountered for biogenic carbonates with B/Ca of ranging from 100 to 400 µmol/mol.

2.2.5.2 Flow rate of sample loading

The influence of the flow rate during sample loading was explored through altering the sample loading speed by varying the flow rate from 100, 200 and 500 µl/min. These tests were conducted with carbonate (JCp-1) and seawater samples as well as boric acid, to evaluate the influence of matrix type on the loading speed and measured $\delta^{11}B$.

2.2.5.3 Boron blank

In a similar way to the manual method, total procedural blanks (TPB) were processed with each batch of samples with the prepFAST-MC method and interspaced with samples of size 15-20 ng B to check if there is any carry over effect. TPBs are prepared with the same reagents used to prepare regular samples, i.e. Milli-Q, 0.5M HNO_3 and buffered with sodium acetate – acetic acid but without introducing any sample material. Measuring the boron content of the resulting eluent therefore allowed a quantification of the level of blank contamination related to the reagents used to prepare and process the sample: buffer, 0.5M HNO_3 (for column cleaning and elution), and Milli-Q (for column conditioning and matrix wash out) as well as the blank associated with the handling and sample exposure and sample carry over.

The configurations tested on the automated system pass a large volume of Milli-Q water (8 ml) through the column during the matrix wash-out stage in comparison to the manual method (1.6 ml) with the consequence of an expected elevation in TPB.

The eluent was collected in auto-sample vials with a small aspect ratio (~ 1cm^3 surface in contact with the air) and caped immediately to avoid fractionation due to evaporation and fall-in. At Southampton we observe ~0.02 ‰ lighter fractionation per hour, giving the possibility to leave the sample open up to 5 hours with acceptable fractionation. Fall-in contamination is estimated to be 8 pg per hour and negligible given sample size.

2.3 Results

2.3.1 Efficiency of matrix wash-out

The viability of Na as an indicator of matrix wash-out efficiency is confirmed by measurements of Na and Ca concentration prior to- and after purification (Figure 2.4). Post-purification concentrations of Na and Ca are, however, both low (0.08 and 0.34 ppm on average, respectively) suggesting efficient wash-out and the suitability of Na measured by MC-ICPMS as a proxy for Ca removal. Previous studies have found that these levels of Ca and Na contamination have no significant effect on the MC-ICPMS instrumental fractionation (Foster, 2008; Guerrot et al. 2011).

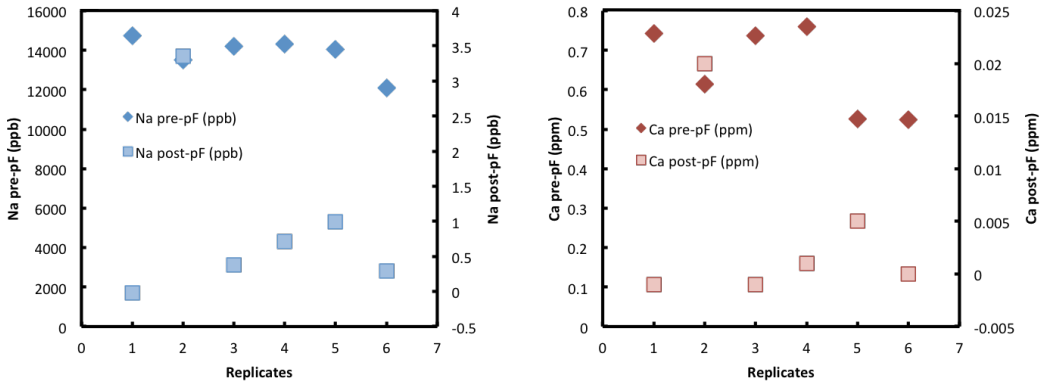

Figure 2.4 Concentration of Na and Ca on JCp-1 sample prior and after processing on the prepFAST (pF) to assess removal of Na from sodium acetate-acetic acid buffer and Ca from carbonate matrix.

The different configurations of matrix wash-out (Table 2.4) were tested on NIST 951 and JCp-1. The forward and low flow rate configuration-1 tested on NIST 951 boric acid show elevated levels of Na (9 ppb), significantly higher than the range found when using gravity columns (0.5 ppb). Wash configuration 2 shows a more efficient removal with a range of Na of 0.9 ppb, demonstrating the need for a fast flow rate when washing off the sample and buffer matrix and alternating flow for the most efficient removal (a matrix reduction of 1000 and 20 000 times for Ca and Na respectively). Overall, Na measured by the prepFAST-MC using configuration-2 is consistently twice that of the manually processed data. Although this indicates that the matrix is less effectively removed with the prepFAST-MC, it is important to note that matrix contamination levels of <1ppm are not associated with significant matrix effects for $\delta^{11}B$ by MC-ICPMS (Guerrot et al., 2011; Foster, 2008). Based on these results, configuration-2 was used for subsequent coral samples and standards.

To test potential matrix effects, NIST 951 was also processed with variable amounts of boron-free carbonate matrix (Figure 2.5). Results show no correlation between the matrix column-load (0 to 0.6 mg Ca loaded which is equivalent to a range of 0-1.5 mg of pure $CaCO_3$) and $\delta^{11}B$ ruling out any influence of Ca-matrix and sample B/Ca ratio (within the range 100-500 µmol/mol for a 20 ng B target) on the measured $\delta^{11}B$.

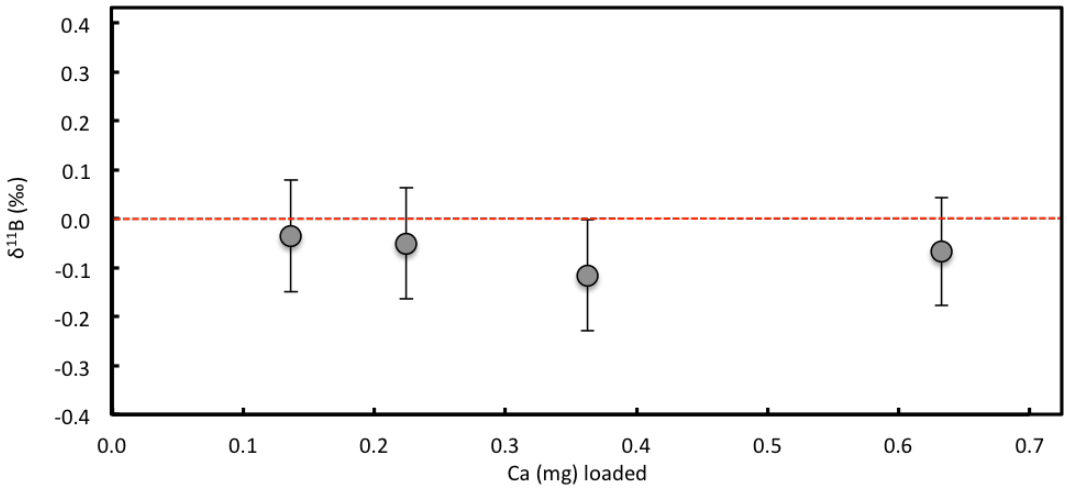

Figure 2.5 $\delta^{11}B$ NIST 951 standard loaded with various amount of boron free carbonate matrix from stalagmites showing no correlation between $\delta^{11}B$ and mass of matrix loaded. Red dotted line is the certified value of NIST 951 (0‰).

2.3.2 Influence of sample loading flow rate

The effect of sample loading flow rate on measured $\delta^{11}B$ was examined using boric acid NIST 951, JCp-1 and seawater (Figure 2.6, Table 2.5). NIST 951 which has no sample matrix (but is mixed with a Na acetate-acetic acid buffer) appears to be unaffected by the flow rate during sample loading whereas JCp-1 coral and seawater yield lower isotope ratios when loaded at faster flow rates (0.2 and 1‰ lighter for 250 and 500 µl/min, respectively). Thus, the accuracy of the method using standards with increasingly complex matrices is sensitive to loading speed flow. Given that the $\delta^{11}B$ for all samples at 100 and 250 µl/min agree within error and produce values in agreement with the long-term average, we infer that samples must be loaded with a flow rate no greater than 200 µl/ min. A flow rate of 100 µl/min was used for all samples.

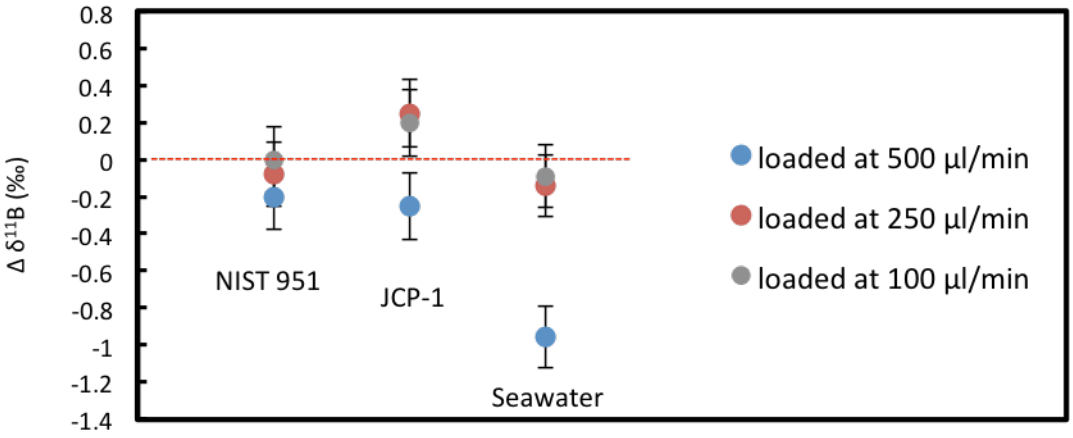

Figure 2.6 Effect of sample introduction flow rate on $\delta^{11}B$ ($\Delta\delta^{11}B = \delta^{11}B_{\text{sample prepFAST}} - \delta^{11}B_{\text{long term}}$), for standards and reference materials NIST 951, JCp-1 and seawater. Red dotted line represents an offset of 0‰ between the two methods.

Referenc e material	Matrix type	Long term $\delta^{11}B$ (‰)		**Sample load (µl/min)**		
				100	**200**	**500**
NIST 951	No matrix	0	$\delta^{11}B$ (‰)	0	-0.08	-0.2
JCp-1	Carbonate	24.25		24.45	24.5	24
Seawater	ionic	39.61		39.52	39.47	38.65

Table 2.5 Long-term average $\delta^{11}B$ of standards and reference materials processed at different flow rate.

2.3.3 Level of blank contamination

TPBs processed on the prepFAST-MC ranged between 7 and 60 pg of boron (4 replicates, Figure 2.7) for the standard matrix wash-out configuration 2 (Table 2.4). These values are similar to published values in the literature for the standard manual approach using gravity columns consistency (e.g. Foster, 2008; Rae et al., 2011) but tend to be slightly elevated compared to the standard manual approach currently in use at Southampton (0-40 ng; Henehan et al., 2013). Nevertheless, this level of blank represents less than 0.2% of the sample boron concentration (for a 20 ng sample) and therefore requires no correction on $\delta^{11}B$. The consistent and low TPB values (interspaced by 15-20 ng B samples) demonstrate little or no effect of carryover from one sample to another.

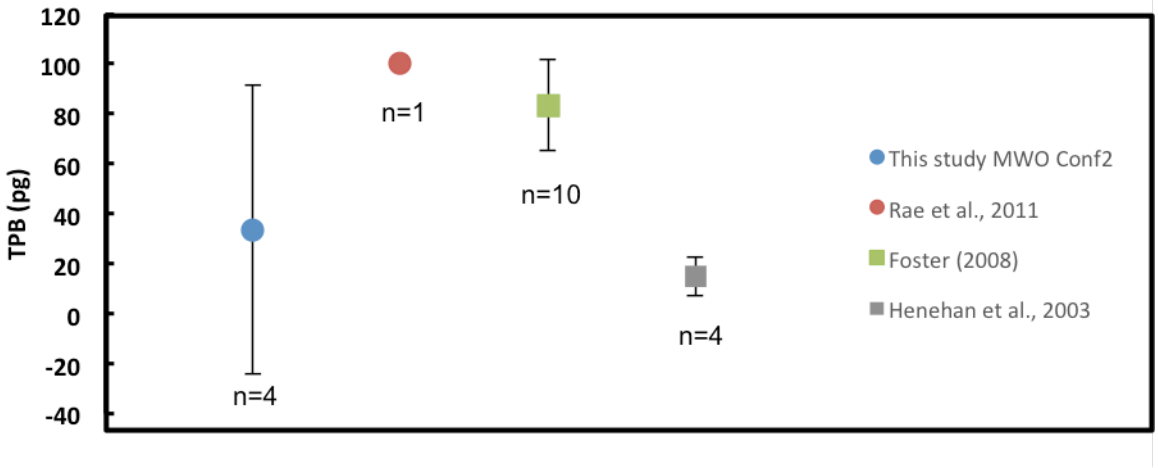

Figure 2.7 Total procedure blank (TPB) with number of replicates (n) processed with the prepFAST method (with matrix wash out (MWO) configuration 2, see table 2.4 for details) compared with published TPBs from standard manual column protocol.

2.3.4 Optimised method for marine carbonates

Based on our experiments, the optimal method (Table 2.3b) yielding the most efficient matrix wash-out and accurate isotope ratio was used to test long-term reproducibility by application to coral samples from Belize. Our optimised method utilises a sample load flow rate of 100 µl/min and the configuration 2 for the matrix wash-out stage. One sample is processed fully automatically in approximately 60 minutes and the column is stored in Milli-Q water at the end of a day of processing

2.3.5 Reproducibility and accuracy of the prepFAST-MC with the optimized method

2.3.5.1 Reproducibility and external precision

Using the optimized method, results for JCp-1 and NIST SRM 951 (for a 20 ng B sample size) show a good reproducibility (Figure 2.8a) with $\delta^{11}B_{JCp\text{-}1}$ = 24.31 ± 0.20‰ (2sd, n=20) and $\delta^{11}B_{951}$ = -0.02 ±0.15‰ (2sd, n=13). Seawater processed by the prepFAST yielded $\delta^{11}B_{seawater}$=39.50 ±0.06 ‰ (2sd, n=2), in agreement with the long-term $\delta^{11}B$ of 39.61 ±0.21 ‰ (2sd) (Foster, 2010).

Our data demonstrate that the prepFAST-MC method generates highly reproducible data for JCp-1, 951 and seawater similar to the manual gravity column method (long-term average at Southampton and previous studies, Table 2.2), with no significant mass fractionation induced by the fully automated B purification.

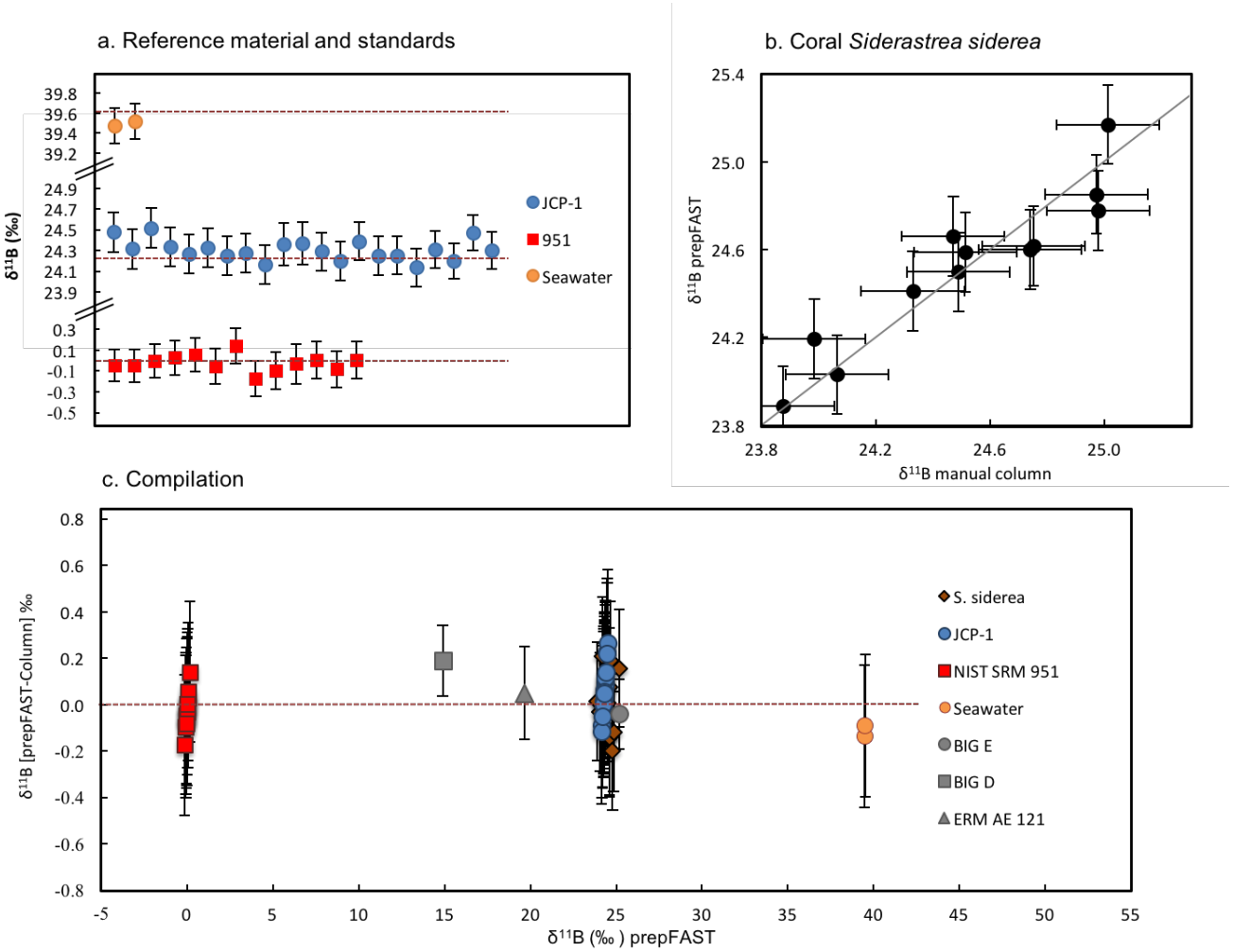

Figure 2.8 Compilation of standards, reference materials and coral samples processed on the prepFAST (a) $\delta^{11}B$ reproducibility of standards and reference materials NIST SRM 951, JCp-1 and seawater processed on the prepFAST. All points agree within error with their certified value or long term average (red dotted line, see text). (b) Cross plot of $\delta^{11}B$ prepFAST vs. manual columns for corals *S. siderea*. All data agree within error with the 1:1 line. (c) Compilation of various standards, reference materials and *S. siderea* samples processed on the prepFAST and compared with their long-term average or column $\delta^{11}B$ data. The [prepFAST-Column] offset is within error of the zero line (red dashed line).

2.3.5.2 Accuracy

To further test the prepFAST-MC method on real samples, purifications were performed with annual samples of the coral *S. siderea* and compared with replicates processed with gravity columns. A $\delta^{11}B$ cross-plot between the two methods for *S. siderea* (Figure 2.8b) has an average offset of 0.01‰ ± 0.25 (2sd). These results, along with a compilation of all standard and samples processed on the prepFAST-MC, compared with their certified value or long-term average on gravity column (Figure 2.8c), have an average offset of 0.02 ± 0.25‰ (2sd) given a sum of squares

propagation of the associated uncertainties. These results illustrate a high degree of accuracy for the prepFAST-MC purification method for the sample matrices examined here.

Na concentrations of diluted aliquots of each of these purified samples were also measured to attest the low level of Ca and Na contamination (from the sample and buffer, respectively). As with the tests performed with standards (Table 2.4), the prepFAST-MC method is associated with consistently higher Na (~0.9 vs. 0.5 ppb on gravity columns), however there is no significant relationship between Na and the offset in $\delta^{11}B$ from certified or long-term average values from gravity columns (r^2=0.04, p=0.20, Figure 2.9).

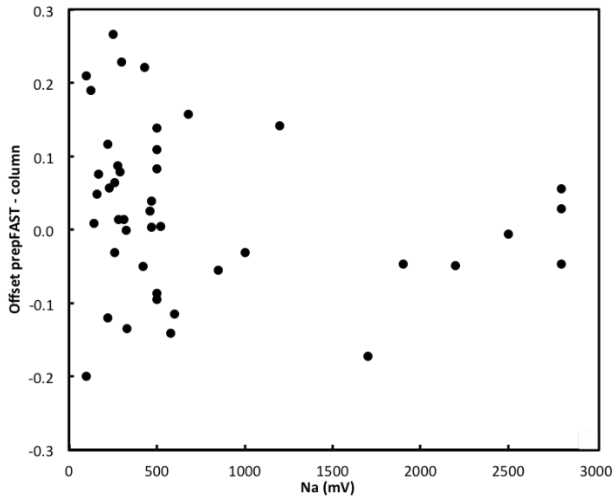

Figure 2.9 $\delta^{11}B$ offset between the prepFAST and manual standard method as a function of Na in purified samples (r^2=0.04. p=0.20) showing no correlation between the two.

Despite these encouraging results, samples with lower B/Ca than corals (<100 µmol/mol), such as foraminifera that involve a higher matrix column-load (up to 5 mg of $CaCO_3$ and 500 µl of Na acetate-acetic acid for a 20 ng B target), produce consistent positive offset relatively to the gravity column method by up to 0.5‰ (see Appendix A). The setup described here therefore requires additional fine-tuning before it can be applied to such low B/high Ca samples and this will be the subject of a future study.

2.3.6 Results for *Globigerinoides ruber* and *Globigerina bulloides* (summary of Appendix A).

Two species *Globigerinoides ruber* and *Globigerina bulloides* (herafter *G. ruber* and *G. bulloides*) were processed with the prepFAST and show a consistent positive offset relatively to the standard gravity column method. In order to achieve an acceptable boron content (target of 20 ng) for measurements on MC-ICPMS, more carbonate had to be loaded for these two species of

foraminifera relatively to *S. siderea*. Indeed the B/Ca content of *G. ruber* and *G. bulloides* is approximately 100 and 50 μmol/mol, respectively, whereas *S. siderea* has a B/Ca of ~ 400 μmol/mol.

The $\delta^{11}B$ offset on the prepFAST for *G. ruber* and *G. bulloides* is ~+0.2 and +0.4 permil on average respectively (Figure A1 and A2). The effect of matrix content on the boron purification is shown to be absent in the range tested here (0-1.5 mg of pure $CaCO_3$, Figure 2.5), which suggest the extra matrix added for *G. ruber* and *G. bulloides* is not responsible for the observe fractionation. Alternatively, more material loaded on the column is also associated with more organics loaded. Despite an oxidative step conducted for all samples prior to column load, some organics can remain within the carbonate lattice. The reason why excess organic produces a positive fractionation remains unclear and is beyond the scope of this study, but may involve degradation of the Amberlite resin, inefficient removal of organics with the prepFAST column, and/or interference with the binding sites of B onto the resin.

For these reasons, the boron isotope data on foraminifera presented in chapter 3, has been generated using the standard gravity column method.

2.4 Discussion

2.4.1 Effect of sample loading speed

The tests conducted with different sample load speed show that samples containing a carbonate or strong ionic matrix seem to be more sensitive to the flow rate than buffered boric acid (Figure 2.6). Since the observed fractionation is towards isotopically lighter values, it appears that the heavy isotope (^{11}B) is preferentially lost when the flow rates of the analyte over the resin bed is too fast. This fractionation occurs even though our sample yield did not reveal a significantly reduced boron content at the higher flow speeds (r^2=0.0006, p=0.96, Figure 2.10) within the precision of these yield measurements (±10 %).

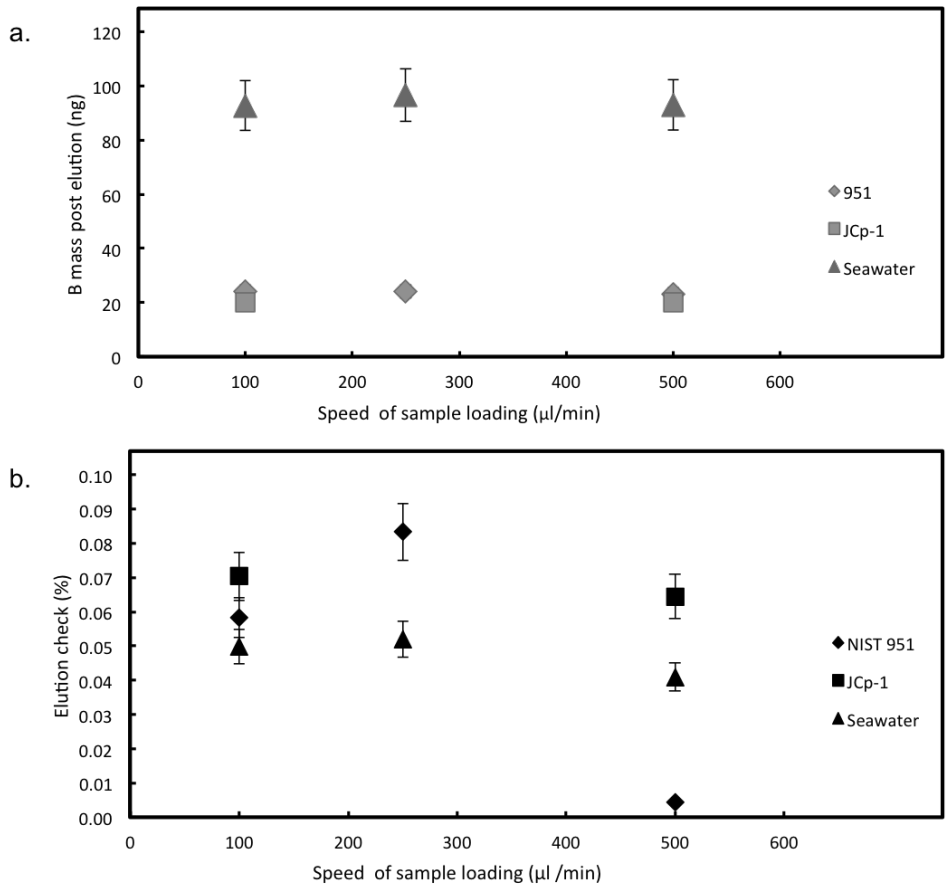

Figure 2.10 (a) Boron yield and (b) elution check as a function of speed of sample load.

Lemarchand et al. (2002a) observed that the very first fractions of the elution of boron from Amberlite 743 are enriched in the heavy boron isotope, and the later elutions are isotopically lighter. Thus, an incomplete removal of the boron from the column, for instance, missing the later stages of the elution curve, would result in an eluted sample being isotopically heavier, which is contrary to observations here, suggesting that the fractionations with high flow speed result from some other process. This is also consistent with a similar concentration of boron in the "elution-check" across the samples not correlating with loading speed (r^2= 0.24, p=0.21, Figure 2.10b) as would be expected under an incomplete elution scenario. Furthermore, the loss of boron during the matrix wash-outstep is also unlikely because of the high partition coefficient between the resin and B at the pH of that step (Milli-Q water pH~ 5, section 2.2.3). Instead we propose that the fractionation with high flow speed is associated with the inefficient exchange of boron onto the Amberlite 743 during loading at fast rates.

Seawater has a complex matrix composed of various anions and cations and shows the largest offset when loaded rapidly (500 µl/min). JCp-1 which has a simpler matrix (calcium carbonate and minor

trace metals) shows a smaller offset when loaded at 500 µl/min. A complex matrix, particularly one that contains other anions such as SO_4^{2-}, could reduce the surface of resin available for the boron to bind to during the sample load. As the Amberlite is an anion exchange resin, the species of aqueous boron that it binds to is the borate ion $B(OH)_4^-$. At the pH of our Na acetate-acetic acid buffer (~pH 5.5) boron is nearly entirely in the boric acid form, which is isotopically heavier than the small quantities of borate ion. Furthermore, during sample loading it is likely that kinetic effects would result in isotopically lighter borate ions (e.g. $^{10}B(OH)_4^-$ rather than $^{11}B(OH)_4$) bonding in priority to the resin. Also any kinetic effect associated to the conversion from $B(OH)_3$ to $B(OH)_4^-$ onto the resin could lead to $B(OH)_3$ to not convert quickly enough to $B(OH)_4^-$ and to escape the column during loading at fast rate. It is conceivable, therefore, that any boron not bound to the resin due to rapid flow rates and/or due to competing effect with matrix anions and kinetics effect, would be isotopically heavy (heavy $B(OH)_3$ and $^{11}B(OH)_4^-$), driving the remaining resin-bound boron isotopically light. Competition between borate and other anions may then be responsible for the effect being larger in an ionically complex media. Although we have demonstrated that for seawater and dissolved $CaCO_3$ flow rates of 100 µl/min are sufficiently slow to avoid any fractionation, when applying the prepFAST-MC method to other matrices will recommend further testing of the influence of flow rate during loading is carried.

2.4.2 Matrix wash-out and blank contamination

Although it does not influence the measured $\delta^{11}B$, there is a significant difference in efficiency of matrix wash-out between the standard method and the prepFAST-MC approach with on average ~0.5 ppb of Na for the standard method compared to 0.9 ppb (Table 2.4) for the prepFAST-MC method and raises interesting questions about the prepFAST-MC column physico-chemical dynamics.

Despite the use of a significantly greater volume of milli-Q to wash-out the matrix with the prepFAST-MC (8 ml) compared to the gravity column approach (1.6 ml), the Na concentration remains higher with the prepFAST-MC. This less efficient wash-out for the prepFAST-MC can likely be ascribed to: (i) the geometry of the column on the prepFAST-MC being long and narrow (~30x1 mm) compared to the wider standard gravity columns (~5x5 mm); and (ii) the greater wetted-volume of the prepFAST-MC (~0.1x70 cm of tubing). The matrix, which is not chemically bound to the resin, needs to be physically flushed out of the column and a rapid and hence turbulent Milli-Q flow rate used in configuration-2 appears to improve the removal of Na and matrix.

The TPBs processed with configuration 2 (Figure 2.7) show levels comparable to published values and on the high end of what is typically observed on gravity columns (0-40 pg). This result is attributed to the requirement to use a significantly greater volume of Milli-Q used to remove the matrix with the prepFAST-MC method. The blank associated with Milli-Q is estimated to be ~10

ppt, therefore the 6 ml of extra matrix washing in the prepFAST-MC method is easily accounted for by the elevated blank (an extra 60 pg). Even at this level of blank contamination however, given our sample sizes (10 to 20 ng B), no correction is required.

2.4.3 Matrix effect

Despite documenting a matrix effect during the sample loading stage (increasing fractionation toward lighter values when loading complex matrices - e.g. seawater – at high loading flow rate, Figure 2.6), the matrix addition tests conducted on NIST 951 with our effectively B-free $CaCO_3$ (Figure 2.5) showed no significant effect of increasing $CaCO_3$ matrix (0 to 0.6 mg Ca, equivalent to B/Ca of 100-400 μmol/mol for a 20 ng B target) on $\delta^{11}B$. Unlike seawater that contains other anions, dissolved $CaCO_3$ principally contains cations (Ca^{2+}) that are not expected to interact with the anion exchange resin. Hence, despite significant calcium loadings, at the low loading speed established in the optimised method (100 μl /min), all boron binds to the resin.

2.4.4 Resin lifetime

The analyses here were performed using two separate resin beds. Although no systematic study of resin lifetime was attempted, based on the accuracy found here, and the consistently low boron in the elution check, resin bed lifetime is judged to be a conservative ~ 200 samples (for a boron and $CaCO_3$ load of 20 ng and 1 mg on average respectively) and we recommend a replacement of the resin every 150 samples alongside regular checking of resin performance with carbonate reference materials or standards such as JCp-1 or NIST 951 and monitoring of the elution check. This level of performance is consistent with gravity columns.

2.5 Conclusion

Here we show that the prepFAST-MC system from ESI Scientific can fully automatically separate B from a variety of matrices without significant isotopic fractionation. We find the following major results: (i) $\delta^{11}B$ is accurate and reproducible for boric acid, seawater and coral $CaCO_3$ provided the sample is loaded slowly (100-200 μl/min) onto the column (Figure 2.6). (ii) For the majority of samples examined here, the matrix was washed off less efficiently using the prepFAST-MC method than the standard manual gravity column method (Table 2.4), however the excess of matrix monitored with Na did not impact the accuracy of $\delta^{11}B$ (Figure 2.8 and 2.9). (iii) The amount of $CaCO_3$ matrix loaded onto the column demonstrates no correlation with the accuracy of $\delta^{11}B$ (within the range 0-1.5 mg; Figure 2.5). (iv) The level of blank during boron purification was low (< 60 pg, Figure 2.7), within the range of published values for which no correction was needed.

Further work is needed to develop a prepFAST-MC method suitable for other carbonate material commonly used in paleoceanographic studies (in particular foraminifera). But importantly, the prepFAST-MC method requires little training and makes it possible to process one sample automatically every 60 minutes (up to 24 samples per day). The methodology described here will therefore speed up the sample throughput considerably for boron isotopes analysis in carbonates applied to different areas such as paleoclimatology, oceanography and environmental sciences.

Chapter 3: Orbital CO_2 reconstruction using boron isotopes during the late Pleistocene.

Elwyn de la Vega[a], Gavin L. Foster[a], Daniel Casey[a], Robin Gledhill[a], Chongguang Luo[ab], Thomas B. Chalk[a], Paul Wilson[a].

[a]Ocean and Earth Science, National Oceanography Centre Southampton, University of Southampton, Southampton SO14 3ZH, UK
[b]Institute of Geochemistry, Chinese Academy of Sciences, 99 Lincheng West Road Guiyang, Guizhou 550081,P.R. China

Elwyn de la Vega wrote the manuscript, identified and picked foraminifera, generated boron isotope and elemental data, and calculated CO_2.
Gavin Foster and Paul Wilson provided discussion and gave feedback on the manuscript
Chong-Huang Luo identified and picked some of the foraminifera
Daniel Casey and Robin Gledhill picked benthic foraminifera and generated the age model for ODP site 871 and 999
Tom Chalk supervised Daniel Casey and Robin Gledhill.

Abstract

Boron isotopes in planktonic foraminifera are a widely used proxy to determine ancient surface seawater pH and by extension atmospheric CO_2 concentration and CO_2-forcing on climate over geological time scales. Yet, to reconstruct absolute values for pH and CO_2, we require a $\delta^{11}B$-pH calibration and independent determinations of ocean temperature, salinity, a second carbonate parameter and the boron isotope composition of seawater. Although $\delta^{11}B$-derived records of atmospheric CO_2 have been shown to perform well against ice core- based CO_2 reconstructions these tests have been performed at only a few locations and with limited temporal resolution. Here we present two highly resolved CO_2 records for the late Pleistocene from ODP sites 999 and 871. Our $\delta^{11}B$-derived CO_2 record shows an excellent agreement with the ice core CO_2 record with an average offset of + 16 ppm ± 30 and a RMSE of 3 ppm, with minor short-lived overestimations of CO_2 (of up ~50 ppm) largely during periods of partial dissolution. We also validate a recently suggested novel approach for determining relative CO_2 change directly from pH fractional change without the need of a second carbonate parameter or detailed knowledge of $\delta^{11}B$ of seawater. This finding has great potential to help improve determinations of climate sensitivity for ancient intervals where these parameters are not well constrained.

3.1 Introduction

The boron isotope composition of ancient planktonic foraminifera is widely used to reconstruct past concentrations of atmospheric CO_2 to understand the drivers and responses of climate change over orbital and geological time scales. Several past intervals have been studied to validate the boron isotope proxy (Foster, 2008; Hönisch and Hemming, 2005; Henehan et al., 2013, Raitszch et al., 2018) over a period where CO_2 is determined in ice-core records, e.g. Bereiter et al., 2015). Studies also have investigated the interaction between CO_2, the ocean carbon cycle and climate beyond the ice cores, during the Mid-Pleistocene transition (Hönisch et al., 2009; Chalk et al., 2018), the Pliocene (Martinez-Boti et al., 2015), the Miocene (Foster et al., 2012; Greenop et al., 2014) and the Eocene (Anagnostou et al., 2016).

Application of the boron isotope proxy to deep-time reconstructions (beyond 3Ma) is complicated by the need for: (i) an empirical species-level calibration of $\delta^{11}B_{foraminifera}$ to $\delta^{11}B_{borate}$ in the pH expression (Henehan et al., 2013, 2016); (ii) $\delta^{11}B$ of seawater ($\delta^{11}B_{sw}$), temperature and salinity in the past to calculate pH from $\delta^{11}B$; and (iii) a second carbonate parameter (traditionally alkalinity or dissolved inorganic carbon DIC) to convert pH to CO_2. Recently, however, Hain et al. (2018) showed that, on short time scales relative to the residence time of carbon in the ocean (200 ky), change in

CO_2 forcing (ΔF_{CO2}) is mainly controlled by change in pH (ΔpH) rather than by change in alkalinity and/or DIC ($CaCO_3$ and C addition or removal controlled by change in carbonate and soft tissue pump) or by temperature-controlled CO_2 solubility.

One main priority for accurate reconstructions of past CO_2 levels is to allow determinations of climate sensitivity, defined as the temperature response to a radiative forcing, typically a doubling of CO_2 with associated slow and fast feedbacks (e.g. PALEOSENS, 2012; Rohling et al., 2018). Climate forcing is a perturbation of the planet's energy balance averaged over the planet (Hansen et al., 2008) and CO_2 forcing, ΔF_{CO2} expressed in $W.m^{-2}$, at a given time can be written as:

$$\Delta F_{CO2} \cong \alpha_{2xCO2} * \frac{\Delta \log_{10} CO_2}{\log_{10} 2} \quad (3.1)$$

where α_{2xCO2} is the sensitivity of the radiative balance per doubling of CO_2, and $\Delta\log_{10}CO_2$ is the difference in CO_2 between two time-intervals of interest (Hain et al., 2018).

By considering basic equilibrium reactions of carbon species, $\Delta\log_{10}CO_2$ can be derived and expressed as:

$$\Delta \log_{10} CO_2 \cong \Delta\log_{10} DIC + \Delta pK_0 + \Delta pK_1 - \Delta pH \quad (3.2)$$

Hain et al. (2008) showed that the terms $\Delta\log_{10}$DIC, ΔpK_0 and ΔpK_1 are negligible and that $\Delta\log CO_2$ can therefore simply be expressed as :

$$\Delta \log_{10} CO_2 \cong -\Delta pH \quad (3.3a)$$

$$\Delta F_{CO2} \cong -\frac{\log_{10} 2}{\alpha_{2xCO2}} \Delta pH \cong -12.3 \Delta pH \quad (3.3b)$$

Hain et al. (2018) also showed that the change in pH induced solely by a change in DIC, alkalinity, production/dissolution of $CaCO_3$, or temperature all result in a linear relationship between pH and CO_2 (Figure 3.1), close to the theoretical approximation of $\Delta\log_{10}CO_2 = -\Delta$pH, but each with a small difference in slope. Consequently, determining pH over short timescales (over periods where there are no substantial change in alkalinity or DIC) enables a straightforward calculation of $\Delta\log_{10}CO_2$ and ΔF_{CO2} with an uncertainty of -10% to account for the change being caused purely by $CaCO_3$ variations and +30% for pH change purely caused by DIC variations. This approach circumvents the need to determine a second carbonate system parameter. Knowledge of $\delta^{11}B_{sw}$ is still needed in the expression of pH but has been shown to be negligible when considering a change in pH rather than absolute pH (Hain et al., 2018). Furthermore, because the slope of a CO_2 to pH relationship is a function of the mechanism causing the pH change, derivation of the slope, in theory, therefore enables the mechanism (or combination of mechanisms) to be deciphered.

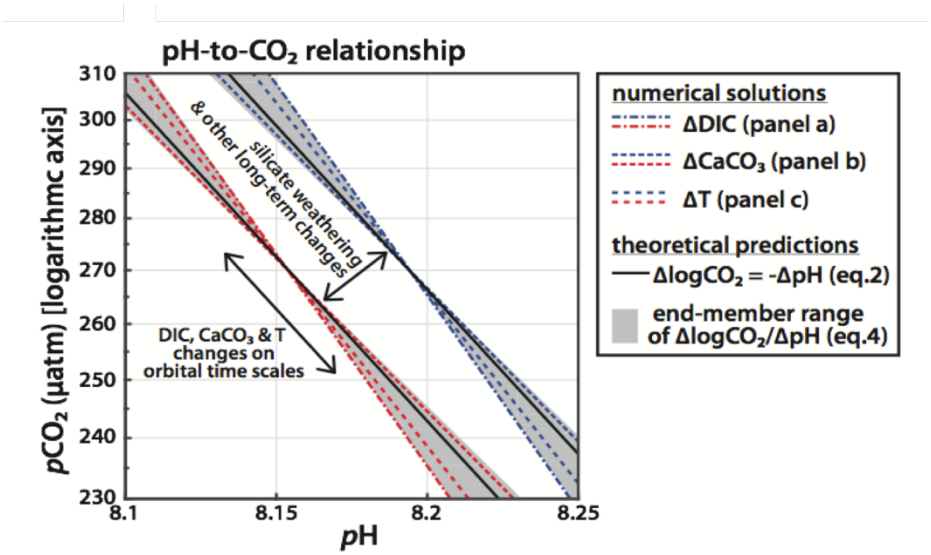

Figure 3.1 Relationship between pCO_2 and pH using the formalism of Hain et al (2018): $\Delta log_{10}CO_2$ as a function of pH only (black line), of DIC, $CaCO_3$ and T. Two scenarios of initial DIC are shown with 1800 µmol/kg (blue) and 2000 µmol/kg (red). Figure adapted from Hain et al. (2018).

Our aims here are twofold. First, we extend previous approaches (Sanyal et al., 1993, 1995; Hönisch and Hemming, 2005; Foster, 2008; Henehan et al. 2013; Chalk et al., 2017; Raitzch et al., 2018) to test the extent to which boron isotopes reconstruct CO_2 faithfully when traditional methods and assumptions are applied. In contrast to previous studies we use multiple sites and present $\delta^{11}B$ and CO_2 data at high temporal resolution (1 sample every ~3 to 6 kyr). This enables a thorough test of the assumptions typically made including (i) the central tenet of the boron isotope CO_2 proxy that surface ocean CO_2 remains in equilibrium with the atmosphere over time at any given site, (ii) an evaluation of the overall uncertainty of the proxy and (iii) an evaluation of the influence of variable foraminiferal preservation on the accuracy of the CO_2 reconstructed. Second, we extend the approach of Hain et al. (2018) to assess the ability of pH and atmospheric CO_2 to provide insights into the causes of CO_2 change over G-IG cycles by using the theoretical linear relationships between pH and ΔF_{CO2} (Figure 3.1; Hain et al., 2018).

3.2 Methods

3.2.1 Core location and oceanographic setting

To accurately reconstruct atmospheric CO_2 with the $\delta^{11}B$-CO_2 proxy, it is essential to measure $\delta^{11}B$ in foraminifera that inhabit waters in near-equilibrium with the atmosphere. Hence, we target regions of the ocean where the water column is stratified and oligotrophic. Here, we measure samples from ODP Site 999 (Figure 3.2, 12.75N, 78.73W, water depth 2827 m, sedimentation rate 3.7 cm/ky) in the Caribbean and ODP Site 871 in the Western Pacific (5.55N, 172.35E, water depth 1255m,

sedimentation rate ~1 cm/ky). The sediments studied at ODP Site 871 are shallowly buried and the site today features a deep thermocline and is located off the equator, hence they are unlikely to be influenced by significant dissolution and equatorial upwelling (Dyez and Ravelo, 2013, 2014). It has nevertheless a minor annual mean disequilibrium of +12 ppm (range ~0 to ~30 ppm, Takahashi et al., 2009). Site ODP 999 is also a minor source to the atmosphere with an annual +21 ppm (Olsen et al., 2004; Foster, 2008). These disequilibria are used to correct our CO_2 data from $\delta^{11}B$ and assumed constant throughout the whole record.

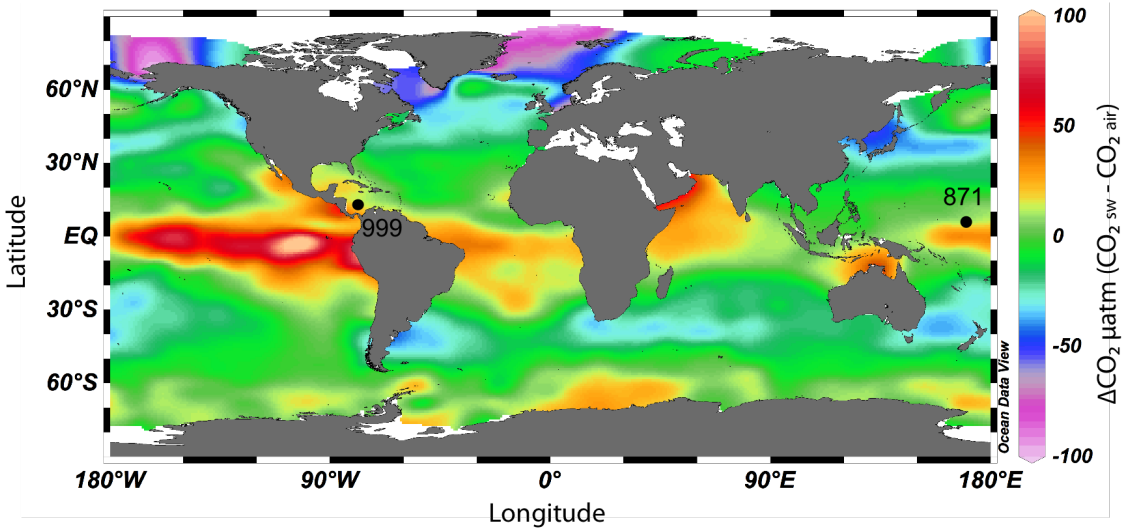

Figure 3.2 . Map of air-sea CO_2 disequilibrium (seawater – air) in ppm and location of ODP sites used in this study.

3.2.2 Samples

3.2.2.1 Sample selection and preparation

Samples of deep-sea sediment from our two study sites were taken at 6cm (3ky) and 10cm (6ky) resolution at ODP 871 and 999 respectively and washed over a 63 µm sieve to separate the fine fraction (0-63 µm) from the coarse fraction (>63 µm). Each part was dried, weighed and stored. For geochemical analysis we hand-picked individuals of *Globigerinoides ruber sensu stricto white* (here after *G. ruber ss*) from these samples. Our target sample size is between 5 and 20 ng of boron, typically requiring about 2 mg of foraminifera from the size fraction 300-355 µm (equivalent to 120-200 individual foraminifera with a B content of ~ 100 µmol/mol).

G. ruber was chosen here as it is readily identified, has sufficient abundance throughout our chosen time interval and a $\delta^{11}B_{borate}$-$\delta^{11}B_{calcite}$ calibration that accounts for vital effects has been made using culture, plankton tows and core-top samples (Henehan et al., 2013). It is also known to live in the

upper surface of the ocean with a relatively small depth range (Meilland et al., 2019) which prevents the influence of deeper more acidic waters on its measured $\delta^{11}B$. The morphotype *G. ruber sensu lato* (hereafter *G. ruber sl*) has slightly different morphology with an upper chamber less circular, flattened and usually asymmetric (Aurahs et al, 2001; Carter et al., 2017) and is thought to live in deeper water to *G. ruber ss* (Wang, 2000). The morphotype *G. ruber sl* was also hand separated and analysed at lower resolution at ODP 871 in order to monitor any change over time of the water column structure and in morphotype $\delta^{11}B$. For similar reasons, carbon and oxygen isotopes were also measured on *G. ruber ss* and *sl* for comparison on the whole record at ODP 871. For this, around 4 individuals were picked and crushed and 50 μg of the homogenised carbonate was separated. $\delta^{18}O$ and $\delta^{13}C$ analytical techniques follow that described below.

3.2.2.2 Age constraints

Samples were taken from 1.5 to 5 meters below sea level (mbsl) for ODP 871 and from 9 to 21 mbsl for ODP 999. Age was initially determined from sample depth using published age models (Dyez and Ravelo, 2013). These initial age constraints were then further refined with new measurements of $\delta^{18}O$ on the benthic species *Cibicoides wuellerstorfi* (50 μg of ~3 mixed, crushed and homogenised specimen) measured using on a Thermo KIEL IV Carbonate device at the University of Southampton. These new $\delta^{18}O$ data were then tuned to the benthic $\delta^{18}O$ LR04 stack (Lisiecki and Raymo, 2005) using Analyseries (Paillard et al., 1996). The benthic $\delta^{18}O$ records for each site and age model for ODP 871 are shown in Figure and table B1 (Appendix B).

3.2.2.3 Fragment counts

Foraminifera fragment counts were conducted on ODP site 871 to monitor variations in carbonate preservation. Samples were sub-sampled using a splitter (in order to maintain the homogeneity of grains) and poured onto a picking tray. Counts of whole intact grains and fragments of grains were conducted three time and averaged. The fragmentation index (FI) was calculated following the approach of Howard and Prell (1994) and Berger (1970) where percentage fragment is defined as:

$$FI = 100 * \frac{\text{number of fragments}}{number\ of\ fragments + number\ of\ whole\ tests} \quad (3.4)$$

Fragment counts for ODP 999 were measured in a similar fashion by Schmidt et al. (2006) and available up to 400 ky only.

3.2.2.4 Sample cleaning

The hand separated foraminifera for boron isotope analysis were crushed and cleaned in order to obtain a pristine carbonate signal using established methods (Barker et al., 2003) including a clay removal step to remove this phase characterised by light $\delta^{11}B$ (Schwarcz et al., 1969; Palmer et al., 1987) and an oxidative step using buffered peroxide to oxidise residual organic matter.

Cleaned samples were finally dissolved in 200 µl milli-Q water with incremental additions of 25 µl 0.5M HNO_3 up to a total of ~100 µl. If necessary the volume of acid was further increased until full dissolution. Samples were then centrifuged for 5 minutes to separate any remaining undissolved contaminants (e.g. silicate grains) and transferred to screw top 5 ml Teflon pots for subsequent boron separation. An aliquot equivalent to 7% of each sample was kept for elemental analysis and transferred in plastic vials in 130 µl 0.5M HNO_3.

3.2.2.5 Boron separation

The method for boron separation is extensively described in chapter 2, we therefore here only briefly describe the anion exchange column chemistry used to separate and purify boron for analysis by MC-ICPMS (Foster, 2008). Firstly, the dissolved samples are buffered to pH 5 with a mix of 2M sodium acetate and 0.5M acetic acid with a volume equal to twice the volume of acid used for dissolution. Columns were made of 20 µl of Amberlite resin (IRA 743, Kiss, 1988; Leeman et al. 1992) whose affinity with boron is high at pH≥5 (coefficient partition $K_D=10^5$) and low at pH=0 ($K_D < 1$) columns were pre-cleaned with 0.5M HNO_3 and conditioned to pH 5 with milli-Q before being loaded with the buffered samples. At this stage boron sticks to the column and matrix is removed with successive milli-Q rinses (8 x 200 µl). The purified boron is then eluted with 5 volumes of 0.5M HNO_3 (5 x 110 µl) and an extra elution of 110 µl is collected separately to monitor that all boron has been removed prior to that. Columns were then cleaned again with 0.5M HNO_3 (2ml) and milli-Q (2ml) and stored in milli-Q.

A total procedure blank (TPB) was conducted for each batch of samples. This monitored blank contribution from reagents used for boron separation (milli-Q buffer, acid). The TPBs ranged from 0-50 pg which represents a very small contribution relative to our sample size (0-0.25%). TPB correction was only conducted when TPB exceeded 50 pg. A long-term median of $\delta^{11}B_{TPB} = -7$ ‰ was used and the blank contribution is expressed as:

$$\delta^{11}B_{measured} = x * \delta^{11}B_{TPB} + (1-x)\,\delta^{11}B_{true} \quad (3.5)$$

with x the fraction of blank contribution and $\delta^{11}B_{true}$ the TPB corrected (true) value of the sample. Such a correction was only performed on 10% of the analysed samples.

3.2.3 Effect of dissolution (leaching experiment)

To investigate the effect of partial dissolution on measured $\delta^{11}B$, a leaching experiment was conducted on two species of planktic foraminifera: *G. ruber ss* and *Trilobitus sacculifer* (hereafter *T. sacculifer*). Around 180 *G. ruber ss* (size 300-355 μm) and 40 *T. sacculifer* (size 500-600 μm) per sample were picked. The picked separates were then split into 4 samples and treated like so: one control (no treatment), and the three other samples were placed in 0.0001 M HNO_3 (pH 4) for 2, 4 and 6 hours respectively. The foraminifera were then crushed, cleaned and boron separated following the same protocols described above.

3.2.4 Analytical techniques

The analytical techniques followed here for boron isotopes are similar to those described elsewhere (Foster, 2008; Foster et al., 2013; Henehan et al., 2016; see chapter 2 for more details). Elemental analysis was performed on a ~7% aliquot of each dissolved sample using a Thermo ELEMENT inductively coupled plasma mass spectrometer (ICPMS) at the University of Southampton. Elemental to calcium ratios were measured with ^{43}Ca and ^{48}Ca and measured against internal house standard. Elemental ratios measured include: Mg/Ca, B/Ca, Sr/Ca, Al/Ca, Mn/Ca. Based on the reproducibility of these standards, the uncertainty for most elements is ~ 5% at 95% confidence.

Boron isotope analysis were performed on a Thermo NEPTUNE multi collector inductively coupled plasma mass spectrometer (MC-ICPMS) with 10^{12} Ω amplifier resistors using a standard-sample bracketing routine with NIST 951 boric acid standard (following Foster et al. 2013).

3.2.5 Constrain on $\delta^{11}B$-derived pH and CO_2

3.2.5.1 From $\delta^{11}B$ to pH.

pH is related to the boron isotopic composition of dissolved borate ion by the following equation:

$$pH = pK_B - \log\left(-\frac{\delta^{11}B_{sw} - \delta^{11}B_{borate}}{\delta^{11}B_{sw} - \alpha_B * \delta^{11}B_{borate}(\alpha_B - 1)}\right) \quad (3.6)$$

where the isotopic fractionation factor α_B between $B(OH)_3$ and $B(OH)_4^-$, is 1.0272 as determined by Klochko et al. (2006) and the $\delta^{11}B$ of seawater set as 39.61 ‰ for both sites and kept constant throughout the record. As discussed in Chapter 1, the long residence time of boron (10-20 Ma) allows such assumptions for the last 500 ky period studied here.

The temperature values necessary to calculate pK_B in equation 3.6 were calculated at ODP 871 using the approach of Dyez and Ravelo (2013) that accounts for dissolution by applying a depth dependent correction on the Mg/Ca, so the unaltered surface Mg/Ca is calculated by:

$$\frac{Mg}{Ca}surf = \frac{\mathrm{Mg}}{\mathrm{Ca}}meas + 0.26 * z + 0.54 \quad (3.7)$$

with z the core depth in kilometre.
The sea surface temperature (SST) is then calculated using the Mg/Ca-T relationship of Anand et al. (2003).

$$\mathrm{SST} = \frac{\ln\left(\frac{\frac{\mathrm{Mg}}{\mathrm{Ca}}surf}{0.38(\pm 0.02)}\right)}{0.09(\pm 0.003)} \quad (3.8)$$

This correction applies a ~ +2 °C relatively to the uncorrected Mg/Ca record.
Salinity that also influences pK_B is kept constant for both sites (35 PSU) due to the very minor effect of salinity on calculated CO_2 (see section 3.2.6.2).
The SST at ODP core 999 was calculated using equation 3.7 and following Schmidt et al. (2006) by applying a +0.6 mmol/mol depth correction to Mg/Ca.

3.2.5.2 From pH to CO_2.

As mentioned above the calculation of CO_2 is dependent on the determination of a second parameter (also see Chapter 1). Here we use the modern value of alkalinity at each site (2279 and 2350 µmol/kg at ODP 871 and ODP 999, respectively) which was kept constant throughout the whole record. To account for any variations in alkalinity, a generous flat uncertainty of 100 µmol/kg is given (i.e. equal likelihood of values within the range of uncertainty). The CO_2 is then calculated as (Zeebe and Wolf-Gladrow, 2001):

$$\mathrm{CO_2} = \frac{\mathrm{TA} - \mathrm{K_B} * \frac{\mathrm{B_T}}{\mathrm{K_B} + [\mathrm{H^+}]} - \frac{\mathrm{K_W}}{[\mathrm{H^+}]} + [\mathrm{H^+}]}{\frac{\mathrm{K_1}}{[\mathrm{H^+}]} + \frac{2\mathrm{K_1K_2}}{[\mathrm{H^+}]^2}} \quad (3.9)$$

where TA is the total alkalinity, K_B the equilibrium constant of boron species in seawater, B_T the concentration of boron in seawater (432.6 µmol/kg), $[H^+]$ the concentration of H^+ determined from pH = - log $[H^+]$, K_W the dissociation constant of water (function of T, S and pressure), K_1 and K_2 the first and second dissociation constants of carbonic acid (function of T, S and pressure). The calculated CO_2 is then finally corrected for local disequilibrium (20 ppm and 12 ppm at ODP 999 and 871 respectively).

3.2.6 Uncertainty

3.2.6.1 Analytical uncertainty

The uncertainty on the measured $\delta^{11}B$ can be expressed in several ways. The internal uncertainty is the raw 2 standard error of 60 measurements of $^{11}B/^{10}B$ ratio made on each sample and is inversely proportional to signal size. The external uncertainty includes uncertainty associated with the instrumental error and that associated with the chemical separation of the sample. The latter was typically used because it takes into consideration more sources of uncertainty (analytical and chemical blank and random ionisation behaviour of the plasma) and is usually the highest, however the internal error was sometimes chosen if higher than the external. The external uncertainty is determined empirically by long-term repeat measurements of JCp-1 subject to the same chemical purification as our foraminiferal samples. As discussed by Rae et al. (2011) this uncertainty is dependent on the intensity of the ^{11}B signal and is expressed here by the following relationship:

$$2\sigma = 129600\ e^{-212 \times [^{11}B]} + 0.3385\ e^{-1.544 \times [^{11}B]} \quad (3.10)$$

where $[^{11}B]$ is the intensity of ^{11}B signal in volts.

3.2.6.2 pH and CO_2 uncertainty

To fully account for the uncertainty in all variables used in the calculation of pH and CO_2, a Monte Carlo simulation is done here. Such simulation samples a random value within the uncertainty of each variable and calculates the resulting CO_2. The shape of the distribution sampled is either normally distributed or uniform (see Table 3.1). The number of simulations was set to 10,000 and the mean of all realisations was used as the central value for CO_2 and an error envelope at 1 and 2σ was calculated based on the 68% and 95 % distribution of the realisations. Table 3.1 shows the effect of each variable uncertainty used in the calculation on the final CO_2. This treatment highlights the minor effect of salinity and SST on estimated pH and CO_2. TA is given a large uniform uncertainty of +/- 100 μmol/kg that contributes an uncertainty of +/-9 ppm in CO_2. This range in TA does encompass the likely range in this variable on glacial-interglacial (e.g. Cartapanis et al., 2018) and longer timescales (Hönisch et al. 2009). By assuming a uniform distribution for TA we avoid imposing a temporal evolution to this variable as how TA evolves through a glacial cycle is uncertain (Cartapanis et al. 2018) and is unlikely to be simply a function of salinity as assumed by some (e.g. Dyez et al. 2018). $\delta^{11}B_{sw}$ was kept at a constant modern value of 39.61 ‰ given the residence time of this variable (10-20 Ma; Lemarchand et al., 2002).

Variable	Uncertainty (2σ)	Type of uncertainty	Impact on CO_2 (ppm)
Temperature	0.75 °C	Normal	+4 ppm
Salinity	1.5	Normal	+2 ppm
$\delta^{11}B_{CaCO3}$	0.15-0.25‰ (external uncertainty from MC-ICPMS)	Normal	-14 ppm
Alkalinity	100 µmol/kg (total range)	Uniform (flat)	+ 9 ppm

Table 3.1 Value and type of uncertainty of each variable for calculating CO_2 using a Monte Carlo simulation and effect on CO_2 (the effect on CO_2 here is the response to a positive deviation of the variable)

3.2.6.3 Uncertainty on the CO_2 offset

To constrain the offset between $\delta^{11}B$-derived CO_2 and ice core CO_2, each sediment age is compared to the ice core CO_2 record by interpolation of the record of highest resolution, in this case the ice core compilation. The residual is defined by:

$$Residual_{CO2} = CO_{2\ \delta 11B\text{-}derived} - CO_{2\ ice}. \quad (3.11)$$

The uncertainty of this residual accounts for the uncertainty in the age of the interpolated ice core CO_2. For this, a 3 ky window is defined around the central age estimate interpolated ice core value and the minimum and maximum CO_2 values are determined within that interval. The upper and lower 2sd uncertainty (2σ) in the residual is then calculated by:

$$2\sigma = \sqrt{\sigma^2_{CO2.interpol} + \sigma^2_{CO2.\delta 11B-derived}} \quad (3.12)$$

3.2.7 The relationship between $\delta^{11}B$ -derived pH and ΔF_{CO2}

The linear relationships between ΔF_{CO2} and pH are determined with a York regression (York et al., 2004) that takes into account the uncertainty in both the independent and dependent variable (i.e x and y directions). To fully account for age uncertainty when estimating ΔF_{CO2} from the well-dated ice core record, a distribution of the ice core data was calculated within the 4σ uncertainty of the

$\delta^{11}B$ age and weighed by the respective likelihood based on the age difference between ice core and sediment core in a similar way to the above, to give confidence intervals on the York regression (Hain et al., 2018).

3.3 Results

3.3.1 Dissolution experiments

The leaching experiments on *T. sacculifer* and *G. ruber ss* show a different response for the two species (Figure 3.3). While *G. ruber ss* show no notable variations in measured $\delta^{11}B$ under different treatments, *T. sacculifer* shows no variations in $\delta^{11}B$ for the control and first two treatments (leached in 2 and 4 hours in 0.0001M HNO_3, pH 4) but shows a ~1‰ (relative to the control) shift towards lighter $\delta^{11}B$ after 6 hours at pH 4.

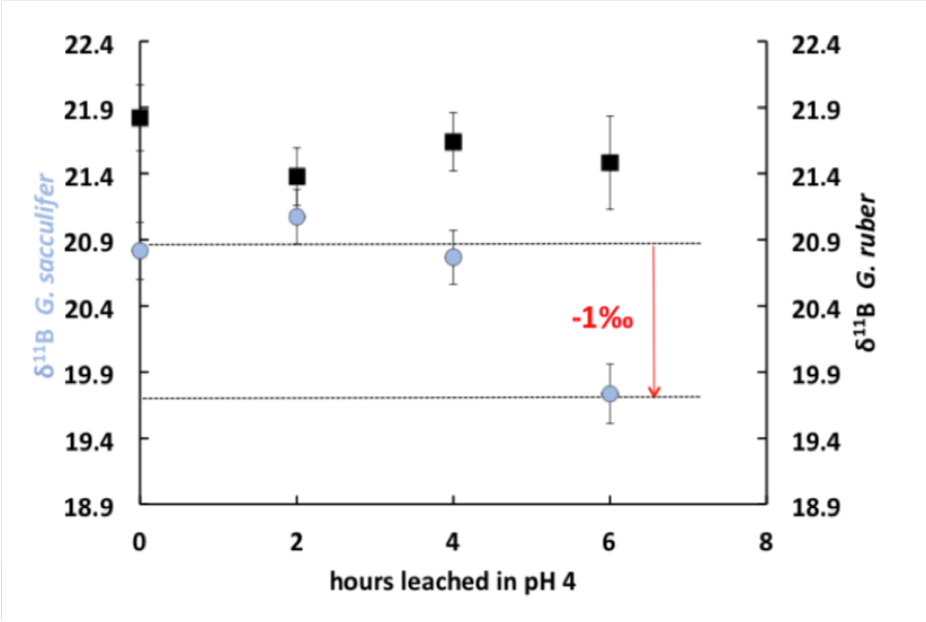

Figure 3.3 Dissolution tests conducted on *T. sacculifer* (size 500-600 µm) and *G. ruber ss* (size 300-355 µm). Whole foram tests were put in contact with 0.0001M HNO_3 (pH 4) for different durations. *T. sacculifer* shows a fractionation of $\delta^{11}B$ after 6 hours leached in pH 4 whilst *G. ruber ss* shows no response.

3.3.2 Temperature and fragment counts

The SST at ODP site 999 and 871 show a cyclicity that agrees with the well-known glacial interglacial cycles of the late Pleistocene (Figure 3.4). The SST determined on *G. ruber sl* (red dots Figure 3.4e), show systematically cooler temperatures than *G. ruber ss* (black line). The fragment

counts (Figure 3.4b,f) at ODP 871 range from 20 to 50 % and follow the well documented "Pacific style" dissolution cycles (Sexton and Barker, 2012) with well-preserved carbonate (low fragments) during glacials and less well-preserved carbonates (higher fragments) during interglacials. The percentage sand usually anticorrelates with fragments at both sites. Fragmentation counts reach maxima at ODP 999 of 20 % during interglacials and up to 50 % during MIS 11 which is concomitant with the mid-Brunhes dissolution interval (MBDI, Barker et al., 2006). The fragments at ODP 871 show no anomaly during the MBDI.

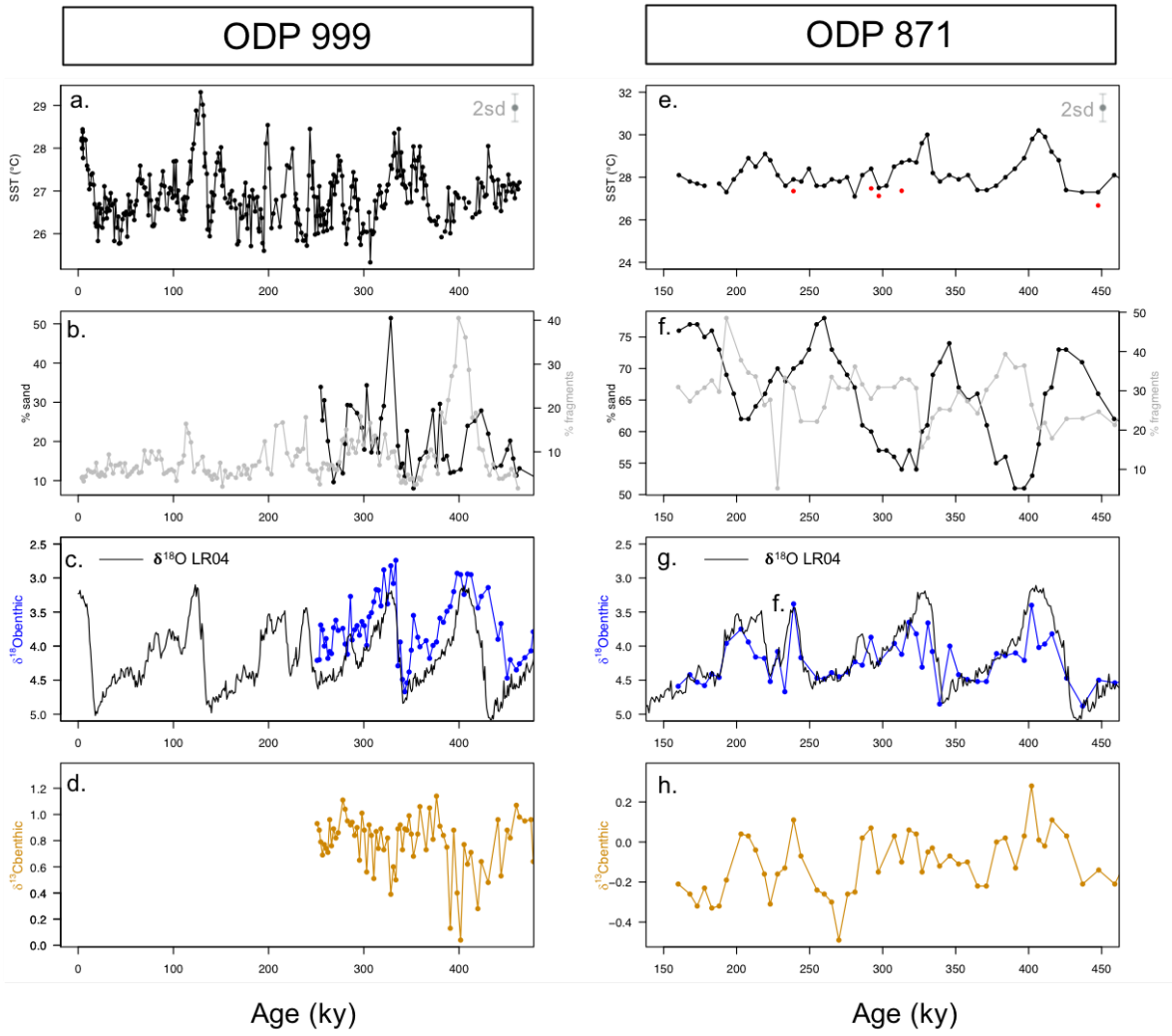

Figure 3.4 Mg/Ca derived temperature, coarse fraction (sand), fragmentation and benthic $\delta^{18}O$ and $\delta^{13}C$ at ODP site 999 and 871**a,e**. Temperature at ODP 999 (from *G. ruber ss*, black, Schmidt et al., 2006) and ODP 871 (*G. ruber ss*, black, *G.ruber sl*, red, 2sd indicated by the grey error bar). **b,f**. percentage fragments (light grey, data from Schmidt et al. (2006) for ODP 999) and sand (black line). **c,g**. Benthic *C. wuellestorfi* $\delta^{18}O$ (blue) and LR04 benthic $\delta^{18}O$ stack (black). A correction of +0.48‰ is applied to our $\delta^{18}O$ data in order to correct for species offset between *C. wuellestorfi* and *U. peregrina* when comparing to LR04. **d,h.** Benthic *C. wuellestorfi* $\delta^{13}C$ (orange). Note the age scale is different at site 999 and 871.

3.3.3 pH and CO_2 reconstruction

The $\delta^{11}B$, pH and $\delta^{11}B$-derived absolute CO_2 (Figure 3.5) from sites ODP 871 and ODP 999, show clear cyclicity related to glacial-interglacial cycles. Each CO_2 data point carries an uncertainty of around +/- 30 ppm and the mean of the interpolated ice core and the $\delta^{11}B$-derived CO_2 (combined two records) is 230 and 246 ppm, respectively and the mean offset for each core (based on a difference between $\delta^{11}B$-derived CO_2 and interpolated ice core CO_2) is +14 and +17 ppm for sites ODP 871 and ODP 999 showing that the boron-derived CO_2 is overall a minor overestimation of CO_2 yet agrees within uncertainty. The RMSE (root mean square error) of the offset for the combined record is 2.6 ppm.

The few measurements of $\delta^{11}B$ *G. ruber sl* at ODP 871 all agree within error with $\delta^{11}B$ *G. ruber ss* (Figure 3.5). The CO_2 derived from *G. ruber sl* (Figure 3.5f) is on average 15 ppm lower than ice core CO_2, though the much lower resolution (n=4) impedes close comparison.

Despite the overall close agreement between $\delta^{11}B$-derived CO_2 and ice core-derived CO_2, the $\delta^{11}B$-CO_2 record exhibits some local short-lived intervals with prominent offsets to the ice core record. This is further revealed by a calculation of the Residual CO_2 (see section 3.4.4.2). The principal mismatches occur at 100 ka, 220 ka and 380 ka at ODP 999, in all three cases, during the descent into glaciation (Figure 3.5c,f). The mismatches with the ice core at ODP Site 871 show a similar temporal pattern occurring at 220 ka, 290 ka and 380 ka. The anomaly at 290 ky is also documented by the low resolution $\delta^{11}B$ record from *G. ruber sl* morphotype.

At ODP Site 871, MIS 7 interglacial (250 ka) appears to be missing in the boron record (figure 3.5f). This may be due to a missed data point precisely located at the interglacial maxima where the short-lived maximum makes it less likely to be captured by lower resolution $\delta^{11}B$ data relatively to the ice cores.

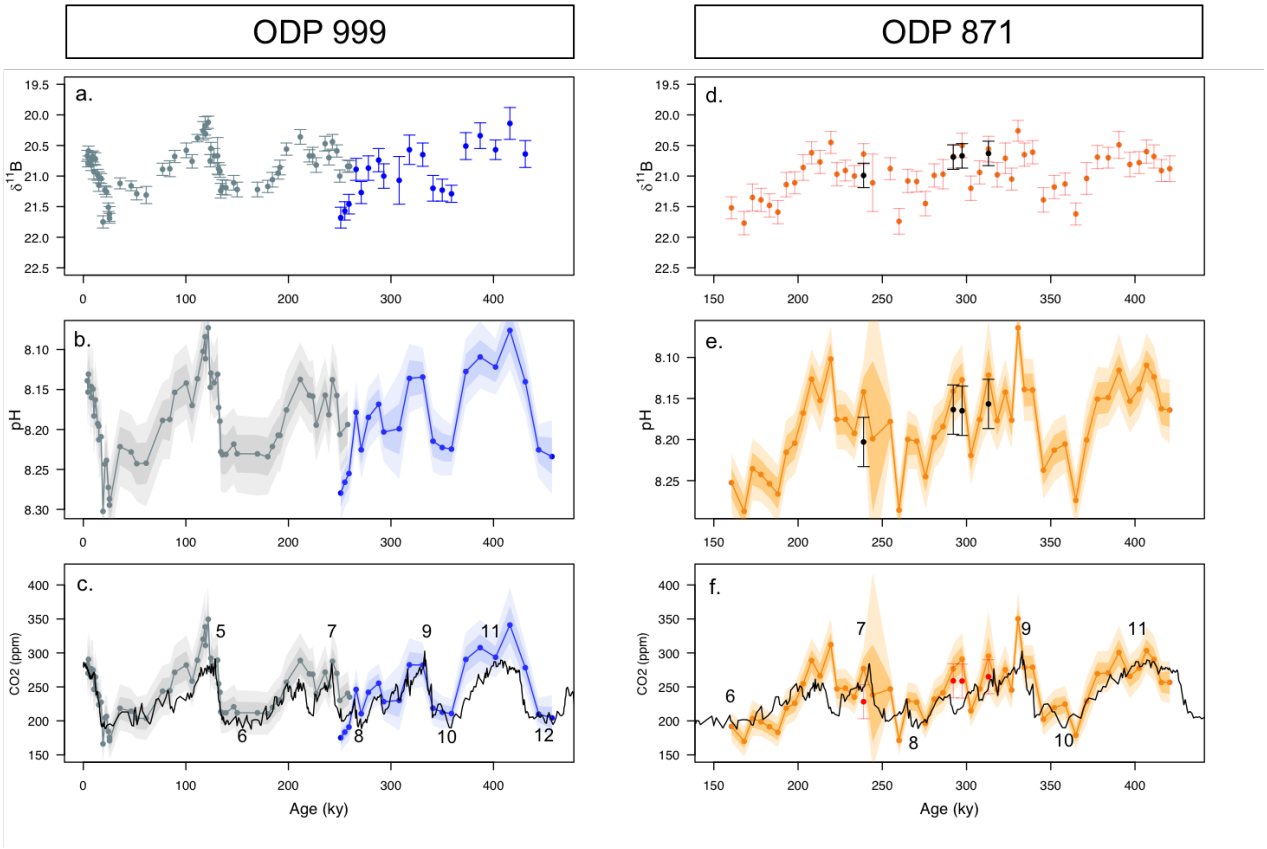

Figure 3.5 $\delta^{11}B$, pH and boron-derived CO_2 at site 999 and 871. $\delta^{11}B$ of *G. ruber ss* and *sl* (a,d) and boron-derived pH (b,e) and CO_2 (c,f) reconstruction from two core location. ODP 999 (grey published data, Foster, 2008; Henehan et al., 2013; Chalk et al., 2017), ODP 999 (blue, this study), ODP 871 (orange, this study, black and red points represent *G. ruber sl*). All data points are from *G. ruber ss* except black and red dots at ODP 871 measured on *G. ruber sl*. Numbers on the CO_2 records (c,f) represent marine isotope stages (MIS). Note the age scale is different at site 999 and 871.

3.3.4 Difference between morphotypes

As presented above, the $\delta^{11}B$ of *G. ruber ss* and *sl* agree within uncertainty albeit with the $\delta^{11}B$ of *G. ruber sl* being higher than *G. ruber ss* for all 4 data points available. The $\delta^{18}O$ and $\delta^{13}C$ of both morphotypes were compared for the whole records at ODP 871 (Figure 3.6) and a cross-plot shows a good agreement between *G. ruber ss* and *sl* (r^2=0.22 and 0.55 for $\delta^{18}O$ and $\delta^{13}C$ respectively, Figure 3.7). This is in contrast with other studies (Wang et al. 2000) that show a systematic offset to higher $\delta^{18}O$ in *G. ruber sl.*

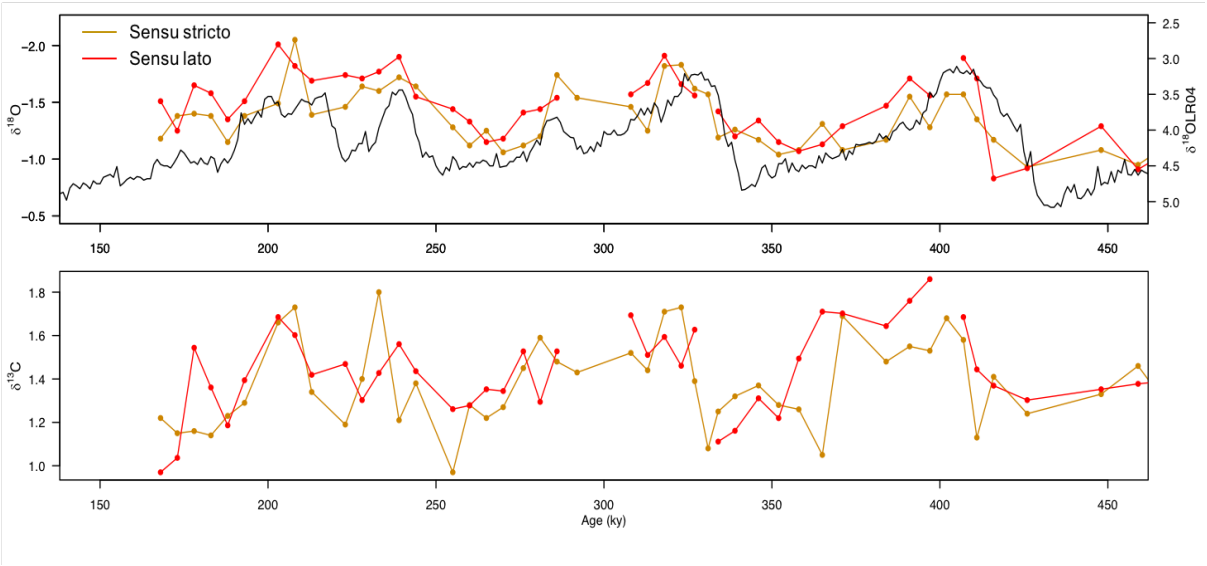

Figure 3.6 Time series of $\delta^{13}C$ and $\delta^{18}O$ of the two morphotypes of *G. ruber* (sensu stricto, orange; and sensu lato, red). The benthic $\delta^{18}O$ stack LR04 is plotted for reference (black).

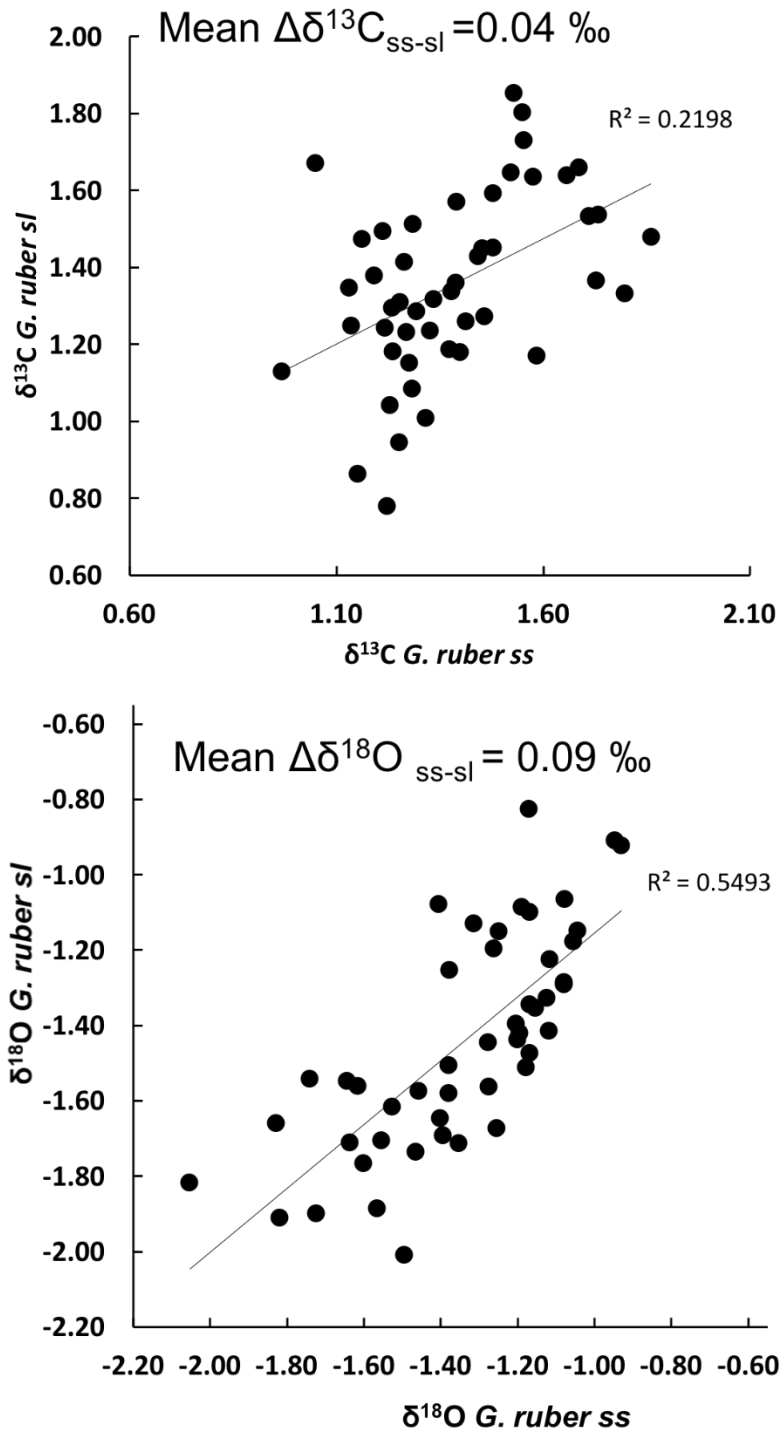

Figure 3.7 Cross plot of $\delta^{18}O$ and $\delta^{13}C$ of the two morphotypes of *G. ruber* (*sensu stricto* and *sensu lato)* showing some level of correlation between the two suggesting no major difference in habitat and recorded signal.

3.3.5 Relationship between $\delta^{11}B$ -pH and CO_2 forcing from the ice core

A cross plot of $\delta^{11}B$-derived pH (for ODP 999 and 871) and CO_2 forcing from the ice core is plotted for each core (Figure 3.8) along with the theoretical lines where ΔF_{CO2} is purely controlled by pH (black), $CaCO_3$ addition/removal (yellow), DIC addition/removal (blue) and temperature (red). The data is fitted with a York regression and, as discussed above, the uncertainty in ΔF_{CO2} accounts for error in interpolation caused when comparing $\delta^{11}B$-derived pH and ΔF_{CO2} from the well dated ice core (see methods).

The regressed slope is $\Delta F/\Delta pH$= - 12.4 W/m^2 +/- 0.3 and shows a remarkable agreement with what is expected from a relationship driven entirely by pH change (black line).

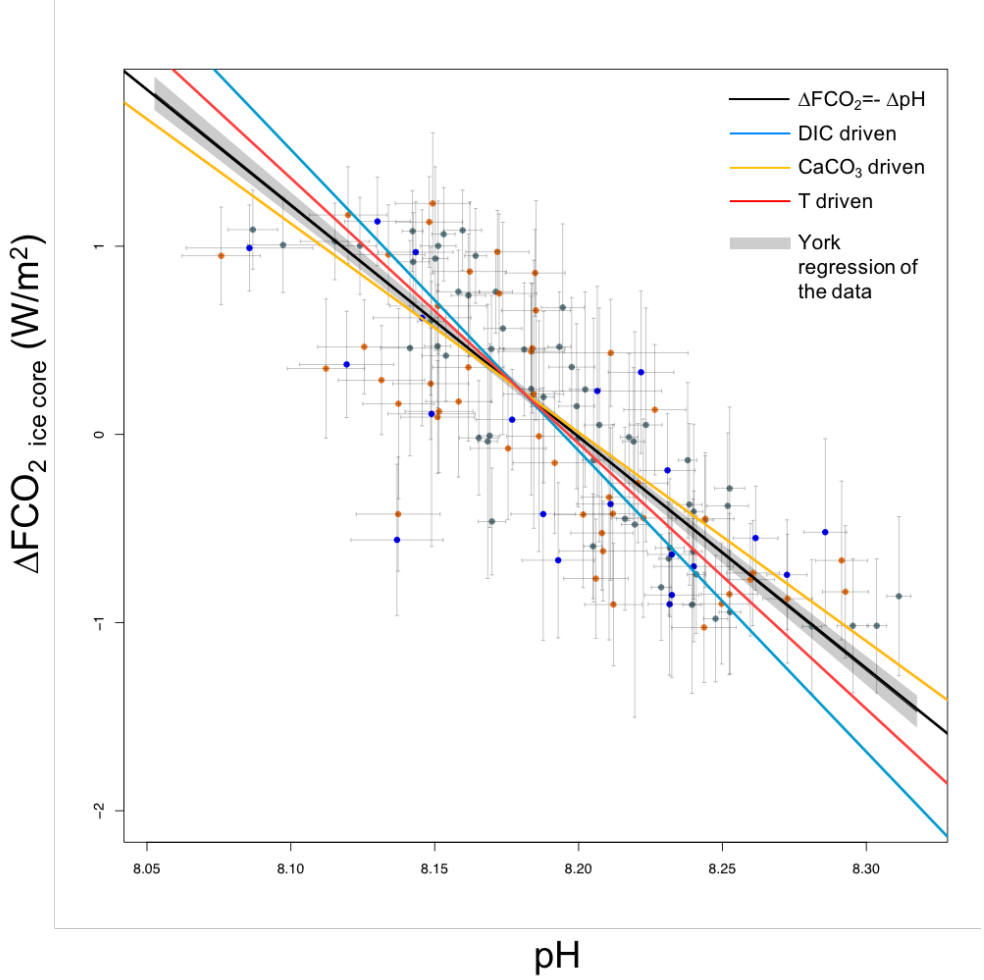

Figure 3.8 Ice core based ΔFCO_2 (CO_2 forcing) vs. $\delta^{11}B$-based pH for ODP 999 (grey dots published data, blue this study) and 871 (orange dots). The lines show the relationship between ΔFCO_2 and pH for the simplified formalism (see method) ΔFCO_2= - ΔpH (black line), and when driven by changes in DIC only (blue, $\Delta F/\Delta pH$= -16 W/m^2), $CaCO_3$ (yellow, $\Delta F/\Delta pH$= -11.1 W/m^2) and temperature T (red, $\Delta F/\Delta pH$= -14.1 W/m^2). The York regressed line (grey shade) falls on the theoretical only pH-driven line (black).

3.3.6 The particular case of MIS 13 (summary of Appendix C)

Boron-derived CO_2 data were generated until 600 ky and 550 ky at site 999 and 871 respectively, covering MIS 12, 13 and 14. This period is associated with a significant overestimation of CO_2 relatively to the ice core at both sites by 50 to 100 ppm (Figure C2), with MIS 13 and 14 impacted at site 999 and MIS 12, 13 and 14 at site 871. Surface temperatures reconstructed during this period are also colder (Figure C1), with levels comparable to subsequent glacials.

MIS 13 is associated worldwide with increased Asian, Indian and African summer monsoon (e.g. Yin and Guo, 2008; Guo et al., 2009, Barth et al. 2018) and a global positive anomaly in benthic and planktonic $\delta^{13}C$, known as $\delta^{13}C$-max II (Wang et al. 2004). Interpretation of this $\delta^{13}C$ maximum that is observed at longer timescale with a cyclicity of 400 to 500 ky, include change in the organic to inorganic ratio (Hoogaker et al., 2006), or a preferential expression of the microbial pump (Ma et al., 2017) that produces refractory dissolve organic carbon during periods of reduced nutrient input from continents at eccentricity minima (that correlate with $\delta^{13}C$ maxima during the early Pleistocene but becomes out of phase towards the late Pleistocene). Barth et al. (2018) propose an increased storage of vegetation after the relatively long and warm preceding glacial MIS 14, that constituted a pool of ^{12}C stored on land. All of these mechanisms however constitute a sink of CO_2 (stored vegetation) or are not in phase with $\delta^{13}C$ (minima in eccentricity happens later, during MIS 11), hence are not candidates to explain the overestimation of CO_2 around MIS 13.

Instead, we propose that a change in air-seaCO_2 disequilibrium could explain the observed high $\delta^{11}B$-derived CO_2. ODP 871 is located in the West Pacific and can be sensitive to change in equatorial dynamics and Walker circulation. In particular MIS 13 is associated with a maximum in East-West temperature gradient, indicating an increased upwelling in the East equatorial Pacific ("La Nina"-like conditions) (Yu et al 2016). This would spread CO_2-rich waters westward and slightly poleward on either side of the equator, making ODP site 871 a source of CO_2 during that period.

ODP site 999 may be sensitive to the same processes. The East equatorial Atlantic during the LGM has been shown to be a source of CO_2. This excess CO_2 was however dampened in central and Western Atlantic due to Fe fertilisation that increased biological productivity. The mid-state lukewarm interglacial MIS 13 was likely associated with increased trade winds and upwelling in the equatorial Atlantic but the absence of Fe fertilisation during interglacial (e.g. Barth et al, 2018) may have not dampened the CO_2-rich waters making the Western equatorial Pacific a source of CO_2.

An alternative explanation to the observed overestimation of CO_2 at ODP 999 and 871 is a change in nutrient inventory. Indeed, the Southern Ocean shows no productivity signal during MIS 13, as indicated by Ba/Fe in sediments (Figure 1.7. Jaccard et al., 2013). These SO waters would eventually feed low latitude with a low nutrient content. Under these conditions, foraminifera could migrate to deeper depth where nutrients are more abundant (potentially aided by competition with other

organisms, e.g. diatoms/radiolarian) and record more acidic waters, explaining the high $\delta^{11}B$-derived CO_2 levels observed during this period.

Both of these hypothetical scenarios (disequilibrium and foraminifera vertical migration) fit with the observed colder SST at both sites.

3.4 Discussion

3.4.1 Foraminifera preservation cyclicity

Both of the studied sites show a cyclicity in their percentage fragments and coarse fraction (> 63 μm), with better preservation of carbonates (low fragments and high coarse fraction, anticorrelated more visibly at ODP 871) during glacial periods (Figure 3.4b and f). This is well documented in previous studies and known as a "Pacific style" dissolution cyclicity (e.g. Sexton and Barker, 2012). It has been suggested that this pattern initiated after the mid Pleistocene transition (MPT) around 1 Ma, and that cycles in the Pacific prior to that had an "Atlantic style" dissolution cyclicity operating with better (worst) preservation occurring during interglacials (glacials). Several data sets, deep oxygen and carbon isotopes, CO_3^{2-} data, and silt point towards a strengthening of ventilated deep Pacific waters (lower circumpolar deep water LCDW) that lead to the better preservation during glacials in the Pacific after the MPT (Sexton and Barker, 2012).

The fact that fragments at ODP 999 (Schmidt et al., 2006) covary with the same phasing as ODP 871 rather than following the expected Atlantic pattern is attributable to different water masses that fill the Caribbean relative to the rest of the Atlantic basin. During glacials, the Atlantic is penetrated by nutrient- and carbon-rich corrosive southern sourced waters (Antarctic Bottom Water, AABW) with a reduced contribution from the less corrosive, nutrient-poor North Atlantic Deep Water (NADW) (Oppo and Lehman, 1993) making deep-sea sediments less well preserved during glacials. The reason for the opposite dissolution cycle pattern in the Caribbean is the shoaling of the northern sourced waters during glacials. This mid-depth penetration feeds the Caribbean through its deepest sill (1900 m, Johns et al., 2002), with less corrosive waters improving the preservation of carbonate during glacials in a similar pattern to a Pacific style dissolution cycle. During interglacials, the Northern sourced waters are mixed with corrosive southern sourced waters (Antarctic Intermediate Waters AAIW and upper circumpolar deep waters UCDW) leading to less well-preserved sediments in interglacials in the Caribbean.

The MIS 11 interglacial shows a good agreement between ice core and $\delta^{11}B$-derived which is perhaps unexpected as it is associated with fragments count maxima centred at 380ky (in particular at ODP 999). This is perhaps surprising because this interval falls during the mid-Brunhes dissolution interval (MBDI, or Mid-Brunhes event MBE, Barker et al., 2006). The MBDI is a dissolution event that has been observed world-wide in all ocean basins by various proxies (fragment counts,

percentage coarse fraction, carbonate content). Several causes have been proposed to explain this event: global long sea-level high stand, growth of coral reefs and increased coccolithophore production (Barker et al., 2006). The first two hypothesis invoke a scenario whereby enhanced production of carbonate occurs on continental shelves which would lead to less preservation in the deep ocean under steady state condition of Ca in seawater. Increased shelf $CaCO_3$ production should, however, produce more CO_2 (carbonate production being a source of CO_2), something that is not observed in the ice core record which shows similar levels to other fully developed interglacials. To reconcile this hypothesis with the observed CO_2 level, the increased coccolithophore production that has been observed worldwide (Barker et al, 2006; Rickabi et al., 2007) can be interpreted as a sink of CO_2 with the carbon export component from coccolithophore organic matter out balancing the CO_2 increase from their associated carbonate production. Coccolithophores being hard-shell organisms, they sink more efficiently than soft-tissue plankton (ballast effect) which induces a more efficient carbon export to the deep ocean, even counteracting the increased CO_2 induced by enhanced reef production (Barker et al., 2006).

The good agreement between ice core CO_2 and $\delta^{11}B$-derived at ODP 871 could fit in this framework, with increased dissolution at MIS 11 creating overestimated $\delta^{11}B$-derived CO_2, locally compensated by an increased coccolithophore production that would act a sink of CO_2 at the core site. These two combined phenomena could explain the apparent agreement between the two CO_2 records.

Our record from ODP 999 shows a greater CO_2 mismatch to the ice core record during MIS 11 (Figure 3.5) than that from ODP 871. The fragment counts stand out as an anomaly at ODP 999 compared to the rest of the record while at ODP 871 they are similar in range to other maxima. Hence, the MBDI appears better expressed at the Caribbean site and that could explain the poorer CO_2 reconstruction at ODP 999 during MIS 11. Furthermore, it is possible that local variations in coccolithophore production exist making the CO_2 compensation variable over the globe. No coccolithophore abundance data exist for ODP 999 and 871 but further work quantifying this abundance would help to test this idea.

3.4.2 Effect of dissolution on $\delta^{11}B$

Our dissolution experiment demonstrates a more resilient response of $\delta^{11}B$ in *G. ruber ss* than in *T. sacculifer* (Figure 3.3). Smaller individuals are typically more susceptible to dissolution (Berger et al., 1982, Hönisch et al., 2004) but we used larger *T. sacculifer* (400-500 μm) than *G. ruber* (300-355 μm). Furthermore, *G. ruber* is typically considered the species most susceptible to dissolution (Berger, 1970). The apparent resilience of *G. ruber* has however been observed before (e.g. Ni et al. 2007; Seki et al., 2010) and may relate to the different life habitat and shell structure of the two species (Caron et al., 1990), with *T. sacculifer* containing around 30 % of gametogenic calcite (Bé, 1980) which forms at the end of the life cycle of the foram in deeper lower pH cold waters.

It has been suggested that $\delta^{11}B$ is lower in gametogenic calcite than the primary test (Ni et al., 2007) reflecting the expulsion of symbionts (Bé et al., 1985) before gametogenesis (with no CO_2 uptake by photosynthesis). It has also been shown that this gametogenic calcite is more resistant to dissolution (Hemleben et al., 1989; Erez, 2003, Wycech et al., 2018). Hence, it is possible that partial dissolution acts preferentially on ontogenic calcite driving $\delta^{11}B$ in the residual test lower.

A caveat lies in the extent to which laboratory weak acid dissolution tests to imitate natural dissolution in seawater. Sadekov et al. (2010) pointed out that dissolution happening in seawater could be more selective to high-Mg calcite due to surface processes dependent on Mg^{2+} in seawater and Mg/Ca of surface calcite. However, our data are in line with open-ocean studies showing lower $\delta^{11}B$ for core-top samples from deeper burial sites with lower $CaCO_3$ saturation state (Hönisch and Hemming, 2004) and more resilience of *G. ruber* to dissolution than *T. sacculifer* (Seki et al., 2010). These tests, and the results of others (Seki et al. 2010) suggest that $\delta^{11}B$ in at least *G. ruber ss* is relatively robust to partial dissolution. Given what we know from *T. sacculifer*, it is reasonable to assume that, if dissolution were to proceed to a greater extent than is achieved in our leaching experiments or in the depth studies of Seki et al. (2010), the residual *G. ruber ss* would also be shifted towards lower $\delta^{11}B$.

3.4.3 Comparison between morphotypes of *G. ruber*

The Mg/Ca-derived temperature of *G. ruber sl* is consistently lower (~0.3 °C colder, Figure 3.4e) than *G. ruber ss* consistent with the preferred deeper habitat of *G. ruber sl* suggested by Wang et al. (2000). The $\delta^{18}O$ and $\delta^{13}C$ of *G. ruber ss* vs. *G. ruber sl* at ODP 871 however show a good agreement with no consistent offsets (Figure 3.6 and 3.7) that would point towards a different habitat for the two morphotypes. For instance, there is no evidence for a higher (i.e. colder) $\delta^{18}O$ of *G. ruber sl* nor consistently lighter $\delta^{13}C$ that we would expect at deeper depth, however the resolution of $\delta^{18}O$ and $\delta^{13}C$ of *G. ruber sl* is much higher than for the Mg/Ca temperature data and the water column profile of $\delta^{18}O$ and $\delta^{13}C$ is not only affected by salinity, temperature and change in biological productivity. This suggests overall that the environment of the two morphotypes is similar and that the habitat depth difference between them, at ODP 871 at least, is small.

Henehan et al. (2013) found that *G. ruber ss* and *sl* had similar $\delta^{11}B$ when found together. The $\delta^{11}B$-derived pH and CO_2 for *G. ruber sl* examined here are consistently higher and lower, respectively, than *G. ruber ss* by around 0.05 pH units and 15 ppm CO_2 (Figure 3.5). This is contrary to what we would expect if *G. ruber sl* lived in deeper more acidic waters as suggested by its lower Mg/Ca-temperature. We note however that the $\delta^{11}B$ of *G. ruber sl* has been used to calculate $\delta^{11}B_{borate}$ using the relationship described in Henehan et al. (2013) whose slope is very strongly dependent on the culture data based on mixed morphotypes *G. ruber ss* and *sl.* Because of this and the small scale of the $\delta^{11}B$ offsets observed between the morphotypes here and in Henehan et al. (2013), we caution

against any over interpretation at this stage. Nonetheless, the closeness of the morphotypes in terms of $\delta^{11}B$ and depth habitat throughout our record implies any inadvertent sampling of *G.ruber sl* in the *G.ruber ss* fraction would not significantly bias our reconstructions.

3.4.4 Causes of offset between $\delta^{11}B$-derived and ice core CO_2.

Although on the whole there is a good agreement between $\delta^{11}B$-derived CO_2 and ice core CO_2, there is some apparent structure in the $Residual_{CO2}$ (Figure 3.9). The potential causes of those differences are explored here.

3.4.4.1 Change in upwelling and CO_2 disequilibrium

Sites ODP 871 and 999 are both located today in stratified oligotrophic environments with a deep thermocline (base of the thermocline is at ~ 200 and 400 m at ODP 871 and 999, respectively) making it unlikely to have deeper more acidic water influence the surface carbonate system, as shown by the disequilibrium map exhibiting ΔpCO_2 close to zero for both locations (Figure 3.2). If periods of upwelling occurred in the past we would expect these periods to be characterised by low SST, high surface $\delta^{18}O$, and low surface $\delta^{13}C$ due to an increased influence of deep colder and more remineralised waters. The identified anomalies in $Residual_{CO2}$ at ODP 871 (at 210, 290 and 380 ky, Figure 3.5 and 3.9) show no particular anomaly in planktonic C and O isotopes (Figure 3.6) nor SST (Figure 3.5) which rules out influence of upwelling. Equally, no SST anomaly was identified at ODP 999. This suggests the CO_2 anomalies displayed in Figure 3.9 (grey bands) are not the result of enhanced local disequilibrium.

3.4.4.2 Partial dissolution

A visual inspection of the residual as a function of age along with fragment counts (Figure 3.9) shows that although most periods have $\delta^{11}B$-derived CO_2 and ice core CO_2 ice agreeing within propagated uncertainty (see methods), the areas with largest offset are associated with maxima in fragment counts. Although it should be noted that fragment counts are by no means able to describe all the variation in $CO_{2residual}$ observed. Indeed, a cross plot of the residual and percentage fragment (Figure 3.10) with a linear fit show a modest correlation for ODP 999 (r^2=0.20, p=0.00003) and no correlation for ODP 871 (r^2=0.008, p=0.55). We however note that this correlation doesn't account for the uncertainty with the interpolated ice core CO_2.

Nonetheless, it appears that increased fragmentation correlates to a certain extent with maximum offset between boron-derived and ice core CO_2 and are controlled by changes in water masses and

corrosiveness following a "Pacific style" dissolution cycle. This is in line with the dissolution tests on *T. sacculifer* that shows decreased $\delta^{11}B$ (higher CO_2) with dissolution (Figure 3.3).

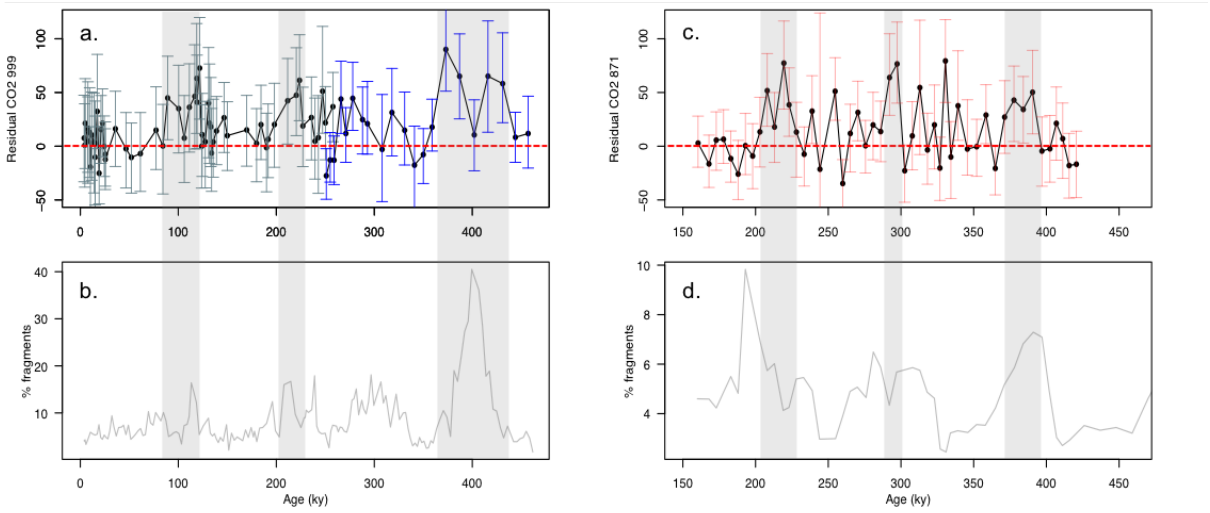

Figure 3.9 CO_2 residual (defined as residual = $CO_{2\text{-}\delta 11B\text{-}derived} - CO_{2\text{-}ice}$) for ODP 999 (a, grey published data see Figure 3.4 for references, blue this study) and 871 (c, red). See text for error bars calculations. b,d. Percentage fragments. Grey bars highlight periods where CO_2 residual and uncertainty are above 0.

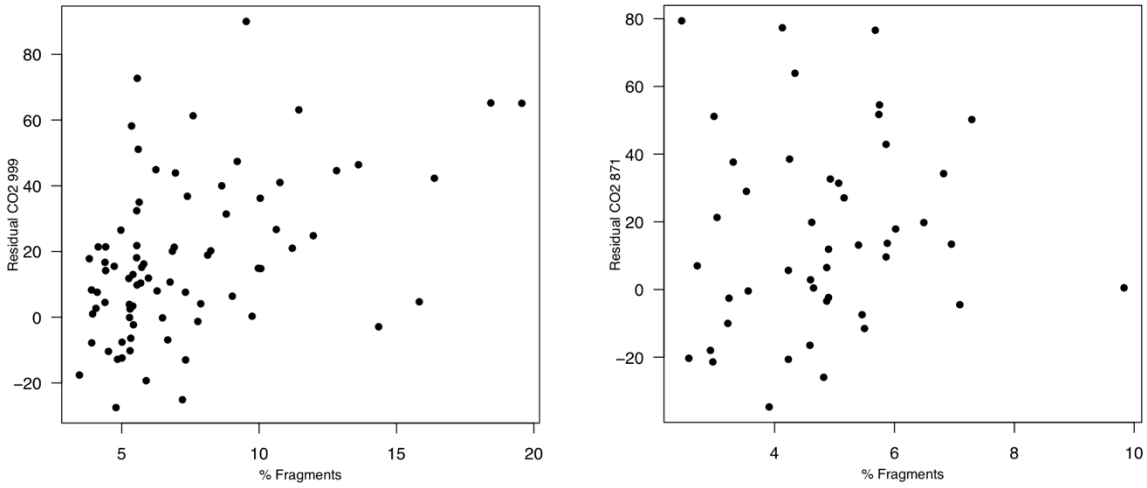

Figure 3.10 Cross plot of CO_2 residual and percentage fragments for ODP 999 (r^2=0.20, p=0.00003) and 871 (r^2=0.008, p=0.55).

3.4.4.3 Change in second carbonate parameter Alkalinity

Changes in ALK in the past are poorly constrained, although some constraints are starting to emerge (e.g. Cartapanis et al., 2018). However, since pH is directly determined by $\delta^{11}B$, it defines the ratio of alkalinity to DIC. Hence, any change in alkalinity is partly counteracted by a change in DIC. This

is demonstrated by the tight relation between pH and CO_2 highlighted by our data (Figure 3.8). To produce an effective alkalinity-driven change in CO_2 of 50 ppm, actually requires an alkalinity change of ~300 μmol/mol. This is greater than the uncertainty that is given to our alkalinity and far larger than any expected change, such a change is larger than all current estimates of change in alkalinity during the glacial cycles (Cartapanis et al., 2018, Hönisch et al., 2009). Furthermore, if partial dissolution is occurring over this interval there would be an increase in alkalinity, contrary to the direction of change required to align the $\delta^{11}B$ and ice core data. It is hence likely that direct partial dissolution of boron isotopes is the main cause for the overestimated CO_2 rather than change in alkalinity.

3.4.5 Relative CO_2 forcing and pH

Our new pH data added to the ΔF_{CO2}-pH relationship of Hain et al. (2018) shows a remarkable agreement with that formulated by Hain et al. (2018) grey data points, Figure 3.8. The regression between boron-derived pH and ice core CO_2 forcing falls between the lines controlled by $CaCO_3$ addition/removal, and by temperature. It should be noted that CO_2 in this case is provided by the ice core directly, and is not estimated from the $\delta^{11}B$-derived pH in any way. As these two proxies are therefore independent, the slope of their relationship can be used to interrogate the mechanisms of CO_2 change. As the data fall between the $CaCO_3$ (yellow line) and DIC (blue line) end-members it suggests that the CO_2 change observed on G-IG timescales was driven by a mix of the two mechanisms and is not down to a single cause. This is in line with studies that require a number of mechanisms to explain glacial interglacials CO_2 change (soft tissue pump, carbonate compensation pump and thermal pump, e.g. Brovkin et al., 2007, Kohfeld and Ridgwell, 2009; see thesis introduction for more details).

The good agreement of the pH and ice core CO_2 data with the theoretical lines has a number of consequences for the reconstruction of CO_2 during periods of earth's history where constrains on $\delta^{11}B_{sw}$ and a second carbonate parameter and temperature are uncertain. ΔpH still requires a determination of $\delta^{11}B_{sw}$ and temperature (in the pK_B term, eq 3.5), however as discussed in Hain et al. (2018), while absolute reconstruction of pH is significantly influenced by estimates of $\delta^{11}B_{sw}$ and T, a relative pH reconstruction is much less sensitive to these changes.

It is nevertheless important to stress that reconstructing ΔF_{CO2} from ΔpH can be applicable only on relatively short time scales up to 1Ma, as $\delta^{11}B_{sw}$ is kept constant within this interval. Hence, in order to reconstruct a relative pH change ΔpH, it should be done within an interval no longer than a few million years.

Secondly to reconstruct ΔF_{CO2} (and climate sensitivity), the formalism can be applied as long as in equation 3.2, ΔpH remains the overwhelming signal with respect to Δlog DIC. This is dependent on the resident time of DIC. The residence time of carbon in the ocean is 200 ky, and any addition/removal of carbon to the ocean from volcanic outgassing or silicate weathering is likely to be minor over the scale of ~ 1Ma. However, during some short events, such as the Palaeocene-Eocene Thermal Maximum, considerable carbon was added to the system in <200 kyr making the formulation described in equation 3.2 invalid. We also note that this formalism is valid as long as core sites remain in equilibrium with the atmosphere.

3.5 Conclusion

We test the $\delta^{11}B$-pH (CO_2) proxy by comparing high resolution (3 to 6 kyr) boron isotope-based pH and CO_2 at two locations with contemporaneous estimates of CO_2 from the ice core. Results suggest that the boron isotope proxy is largely robust and suited to reconstructing CO_2 to a precision of +/- 30 ppm, and an accuracy of +16 ppm, with little or no systematic bias (our RMSE = 3 ppm). Some evidence that partial dissolution may contribute to minor disagreement with the ice core CO_2 is observed. We therefore not only recommend future studies focus on generating high resolution datasets, but that a consideration of foraminiferal preservation is also made. We show here that the formalisation established by Hain et al. (2018), showing that relative CO_2 forcing in the past can be determined from pH change alone without a robust determination of $\delta^{11}B$ of seawater and without the need to determine a second carbonate parameter, is robust. This will not only be of great interest to determine CO_2 forcing in ancient geological times where $\delta^{11}B$ of seawater and a second carbonate parameter are poorly constrained, but the nature of the observed relationship confirms that multiple drivers are likely responsible for G-IG CO_2 change.

Chapter 4: Exploring barium isotopes in ancient foraminifera: a path to a new paleo-productivity proxy?

Elwyn de la Vega[a], Tristan Horner[b], Gavin Foster[a], Maureen Auro[b], Stephanie Bates[c] , Kate Hendry[c], Miguel Martínez-Botí[a], Paul Wilson[a].

[a]Ocean and Earth Science, National Oceanography Centre Southampton, University of Southampton, Southampton SO14 3ZH, UK
[b] Nirvana Labs, Woods Hole Oceanography Centre
266 Woods Hole Road,
Woods Hole, MA 02543, USA
[c]School of Earth Sciences, University of Bristol,
Wills Memorial Building,
Queen's Road, Bristol, BS3 1NH, United Kingdom

Elwyn de la Vega wrote the manuscript, identified and picked foraminifera, and performed chemical treatments on samples (foraminifera cleaning and Ba separation).
Tristan Horner measured barium isotopes, provided discussion and gave feedback on the manuscript.
Gavin Foster generated boron isotope data, provided discussion and gave feedback on the manuscript.
Paul Wilson gave feedback on the manuscript.
Maureen Auro performed barium separation on foraminifera.
Miguel Martínez-Botí generated boron isotope data.
Stephanie Bates and Kate Hendry provided discussion and laboratory assistance.

Abstract

Barium cycling in the modern ocean is well understood and is thought to be primarily controlled at the surface by barite precipitation that is closely linked to biological productivity. Barium isotopes offer the possibility to track such processes as barite discriminates in favour of the light isotope of barium. However, no direct records of ocean surface barium cycling exist in the paleorecord. The study of barium isotopes in ancient foraminifera gives the opportunity to track the barium isotopic signature of seawater in the past and hence may provide valuable insights into the temporal evolution of barium cycling and productivity. We present here barium isotopes (expressed as δ^{138}Ba) in ancient foraminifera from the East equatorial Pacific during the last deglaciation (0-20 ky) including mix species, the spinose surface dweller *O. universa*, and two non-spinose thermocline dwellers *N. dutertrei* and *G. menardii*. We also present new boron isotopes data (δ^{11}B) from *N. dutertrei* and *G. menardii* to constrain the pH environment the foraminifera inhabited. We find that each species has a distinctive δ^{138}Ba signature with a near constant interspecific offset over the last 20 kyr of 0.15‰, with *N. dutertrei* recording the heaviest δ^{138}Ba and *O. universa* the lightest. The δ^{11}B of *N. dutertrei* and *G. menardii* show a muted evolution over the deglaciation for the two species compared to published reconstructions of surface water pH. These signals along with the observation of high foraminifera Ba/Ca ratios could be attributed to specific marine snow habitats for non-spinose foraminifera whereas O. *universa* would be a direct recorder of seawater. *N. dutertrei* and *G. menardii* show a maximum in δ^{138}Ba at 14 ka that may be caused by a change in the chemistry of marine snow interstitial fluid under increased productivity, whereas *O. universa* is invariant throughout the deglacial potentially caused by compensating mechanisms between continental and upwelling input, and local biological productivity. In both cases, changes in biomineralization under varying temperature may also induce changes in foraminifera-environment fractionation but this currently remains unconstrained. The mixed foraminifera signal shows a clear effect of test size and a temporal evolution that is not correlated with independent reconstructions of paleo-productivity or what we see in our monospecific fractions. We interpret this as being a consequence of changes in the foraminiferal assemblage in the bulk fraction with size and with time, which implies that monospecific foraminifera that directly record seawater are best suited to reconstruct barium cycling in the paleorecord. We recommend however that future studies should focus on the nature of the intraspecific δ^{138}Ba signals.

4.1 Introduction

Dissolved Ba (barium) in seawater has a nutrient-type profile with depleted values at the surface increasing at depth, despite Ba not being utilized as a nutrient by organisms. The most likely cause of these profiles relates to barite formation, which precipitates during organic matter remineralisation (e.g. Dehairs et al., 1980, Bishop, 1988). Moreover, since barite precipitation appears to favour the incorporation of isotopically light Ba (e.g., von Allmen et al., 2010; Horner et al., 2017), the stable isotopic composition of Ba has recently emerged as a powerful tracer of the modern and ancient Ba cycling (e.g. Horner et al., 2015, 2017).

Barium isotopes (often expressed as the ratio of ^{138}Ba over ^{134}Ba relative to the NIST 3104a standard, hereafter $\delta^{138}Ba_{NIST}$) have been measured in seawater at several location profiles in the Atlantic (Horner et al., 2015; Bates et al., 2017), the North Pacific and Southern Ocean (Hsieh and Henderson, 2018) and typically show light isotopic ratios at the surface and heavy ratios at depth (Figure 4.1). This is consistent with the precipitation of barite in the shallow sub-surface that discriminates in favour of the light isotope (von Allmen et al., 2010) and remineralisation of barite in the deep. An anticorrelation between barium isotopes and barium concentration is thus typically seen in the water column (Figure 4.1). This gives the potential to Ba proxies to be an indicator of processes responsible for Ba cycling, which themselves are closely related to biological productivity.

Profiles of barium isotopes below 600 m (below the depth where barite forms) show variations that also track different water masses showcasing a conservative behaviour where water masses acquire their isotopic signature when last ventilated at the surface. Processes other than barite formation also have the potential to change seawater signature such as continental run-off (Hsieh and Henderson, 2018), benthic fluxes (Bates et al., 2017), and hydrothermal inputs (e.g. Feely et al., 1987, 1990).

Barite is known to form in association with decaying organic matter (e.g. Chow and Goldberg, 1960; Paytan and Griffith 2007), however, the mechanism by which barite precipitates remains uncertain. Evidence either points towards: (i) a biologically mediated precipitation, such as is done by some benthic organisms and bacteria (Bertram and Cowen, 1997, Gonzalez-Muñoz et al., 2012) through precipitation of barite via biofilm and extracellular polymeric substances, or (ii) abiotic precipitation in Ba and S in an enriched microenvironment, or an abiotic precipitation where the source of enriched Ba is attributed to decomposition of organic matter (Dehairs et al., 1980) by organisms such as phytoplankton (Bishop, 1988; Stecher and Kogut, 1999; Ganeshram et al., 2003).

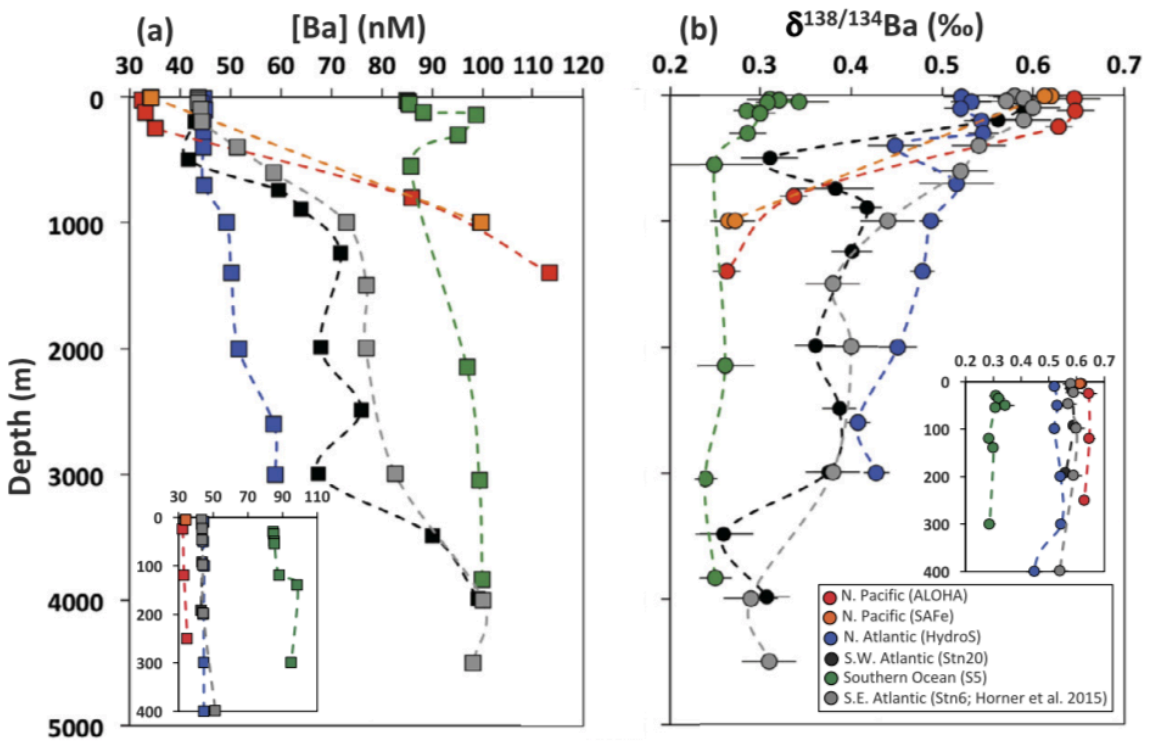

Figure 4.1 Compilation of δ^{138}Ba and Ba concentration of various seawater depth profiles around the global ocean (compilation by Hsieh and Henderson, 2018, including data from Horner et al., 2015). The upper 300 m have a constant δ^{138}Ba and Ba concentration for all regions.

Regardless of any uncertainties with respect to the exact mechanisms of marine barite formation, the link between biological production in the upper water column and barite production has led to the development of a number of robust Ba-based proxies for palaeo-productivity. For instance, Ba excess (Ba_{xs} ,e.g. Dehairs et al., 1991; Dymond et al., 1992), Ba normalised to a terrigenous element (Ba/Al and Ba/Ti) or barite have been used extensively in sediments as an indicator of barite precipitation in the water column thereby tracking biogenic production through time (e.g. Paytan and Griffith, 2007). Each of these Ba based proxies however comes with some caveats such as decoupling between Ba_{xs} and organic matter remineralisation or issues in barite preservation in the sediment column (Hernandez-Sanchez et al., 2011, also see thesis introduction for more details). Given the link between the isotopic composition of dissolved Ba and barite production in the upper water column (Figure 4.1), the barium isotope composition of foraminifera could therefore offer the potential to overcome these limitations and more directly trace barite production and palaeo-productivity as well acting as a tracer of deep-water masses and palaeo-ocean circulation. Indeed, in areas of the globe where anoxic conditions prevail, barite will not be preserved, whereas Ba isotopes in foraminifera should maintain its signal. Furthermore, given the strong influence of the Southern Ocean in regulating glacial–interglacial CO_2 cycles and its connection to low latitudes (Sarmiento et al., 2004), having access to tracers of productivity and ocean circulation at site ODP 1238 would be of great interest to evaluate more accurately the interconnection between high and low latitude and

the role of low latitude water masses (by their marine productivity, and level of nutrients) in influencing global atmospheric CO_2 on glacial-interglacial scales.

Planktonic foraminifera passively incorporate Ba^{2+} of surrounding fluid in their $CaCO_3$ shell where it substitutes for Ca^{2+} (Lea and Spero, 1992; Erez, 2003) making them a valuable archive to explore Ba cycling in seawater in the past. Ba/Ca in living calcifiers (planktic/benthic foraminifera and corals) has been used to estimate seawater Ba and trace ocean circulation, alkalinity or continental run-off (e.g. Honisch et al., 2011; Lea, 1993) due to the nutrient shape of Ba and abundance of Ba in continental run-off. Ba isotopes have been measured in marine sediments (e.g. Bridgestock et al., 2018; 2019) but the extent to which foraminifera faithfully capture ambient Ba isotope chemistry remains unconstrained.

Here, we explore the barium isotopes composition in different planktonic foraminifera species from a well-studied sediment core from the Eastern Equatorial Pacific. Specifically, our study investigates: (i) the effect of species-specific 'vital effects' on foraminiferal Ba isotope compositions, (ii) whether 'bulk' coarse sediment (i.e., > 63 μm) reliably reflects water column signatures, and (iii) how both (i) and (ii) vary across the last deglaciation (20 –10 ky). We augment these results with new boron isotope data for the same samples to constrain changes in ambient water column characteristics (such as pH) from those arising solely from vital effects. Lastly, we discuss the general utility of foram-bound Ba isotope compositions in the context of emerging 'bulk' and coral-bound records, and offer recommendations for future studies.

4.2 Methods

4.2.1 Oceanographic settings

ODP Site 1238 (1.87°S, 82.78°W; 2203m) is located beneath the upwelling region of the East Equatorial Pacific (EEP) known to be linked today to the high latitude Southern Ocean by Subantarctic mode waters (SAMW, Toggweiller et al., 1991). The Southern Ocean is currently a High Nutrient Low Chlorophyll regions (HNLC) and both this region and the EEP are significant sources of CO_2 to the atmosphere (Takahashi et al., 2009).

Surface water mass distributions are dominated by local wind patterns (Figure 4.2; Pennington et al., 2006). The South and North equatorial current (SEC and NEC) flow westwards and transport a significant mass of water to the West. The SEC is the location of open ocean upwelling created by the equatorial divergence: the combination of SE and NE trade winds forming Ekman transport away and either side of the equator. The heat accumulated in the WEP creates a deepening of the thermocline that shallows into the EEP with the input of cold Peru upwelling waters. The Equatorial undercurrent (EUC) is a subsurface current (~80m) that originates in the Western equatorial Pacific

(WEP, Kessler, 2006). It is driven by the accumulated heat in the WEP forming a pressure gradient and moves eastward along the equator and upwells in the EEP feeding waters located at ODP 1238 today. The EUC waters are currently fed mostly by a mix of Southern Ocean (70%) North Pacific (30%, Toggweiller et al., 1991) waters creating a direct connection between high and low latitudes.

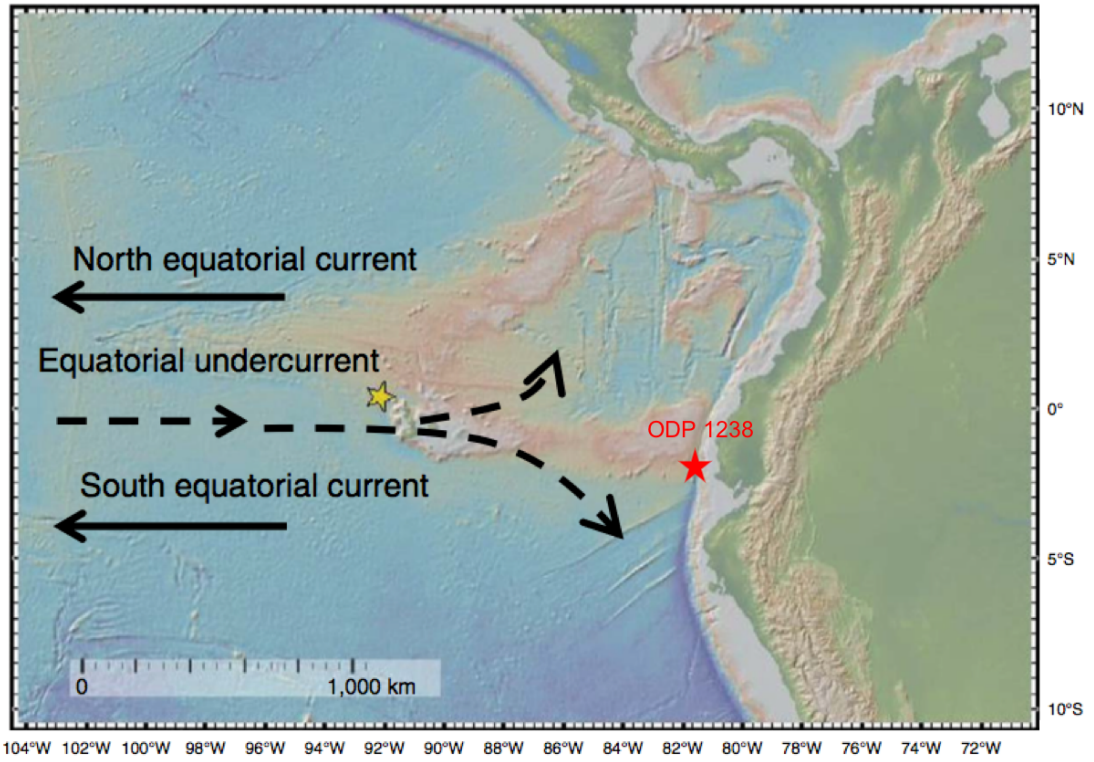

Figure 4.2 Illustration of water masses in the East Equatorial Pacific (EEP) with location of ODP 1238 (red star). Figure adapted from Umling and Thunnel (2017). ODP 1238 is mostly fed by the EUC (Equatorial undercurrent) a subsurface current that originates in the West Pacific.

During glacial periods, an increase in stratification, sea-ice cover and supply of dissolved iron to the Subantarctic region of the Southern Ocean reduced the leak of CO_2 to the atmosphere and increased the efficiency of the soft tissue pump through more complete nutrient consumption contributing to the fall in CO_2 observed during glacial periods (e.g. Hain et al., 2010; 2015; Sigman et al., 2010).

Boron isotope compositions of planktonic foraminifera have been used to reconstruct past pH and atmospheric CO_2 at site 1238 and show a degassing of CO_2 during the last deglaciation (Martínez-Botí et al., 2015) likely caused by the oceanic connection between the EEP and the Southern Ocean bringing CO_2-rich waters to the EEP. Other reconstructions of productivity and dust at site 1238 show that the central equatorial Pacific was less productive during the last glacial maximum, potentially caused by fewer nutrients available from the Subantarctic area due to higher consumption in the Southern Ocean (Costa et al., 2016).

4.2.2 Estimates of seawater barium isotopic composition

In order to examine possible influence of 'vital effects' on the δ^{138}Ba of the measured foraminifera, it is necessary to first constrain the isotopic composition of Ba in the ambient seawater. Existing seawater data show a range of between +0.2 ‰ and +0.6 ‰ for Ba-replete deep and Ba-poor surface waters, respectively (e.g., Horner et al., 2015; Bates et al., 2017; Hsieh and Henderson, 2018). Away from major upwelling areas, however, surface waters exhibit a narrower range in compositions, between +0.45 and +0.6 ‰ (e.g., Bates et al., 2017; Hsieh & Henderson, 2018) that is tightly anticorrelated with dissolved [Ba].

Thus, even in the absence of nearby seawater measurements of δ^{138}Ba, it appears possible to estimate δ^{138}Ba from [Ba] with a reasonable degree of accuracy (± 0.1 ‰). As such, we take advantage of nearby GEOTRACES data to estimate the water column Ba structure overlying ODP 1238 (Figure 4.3).

Based on interpolation along lines of neutral density from the nearest GEOTRACES profile that shows similar upwelling rates with ODP 1238 (Figure 4.4), we estimate the range in [Ba] to be between 30 and 140 nM (nmol/kg) above ODP 1238, and between 30 and 40 nM in the top 100 m of the water column. Accordingly, dissolved δ^{138}Ba in the top 200 m should be in the range of +0.55 to +0.65 ‰ based on a global compilation of δ^{138}Ba-Ba data (Figure 4.5), henceforth assumed to be ≈ +0.65 ‰.

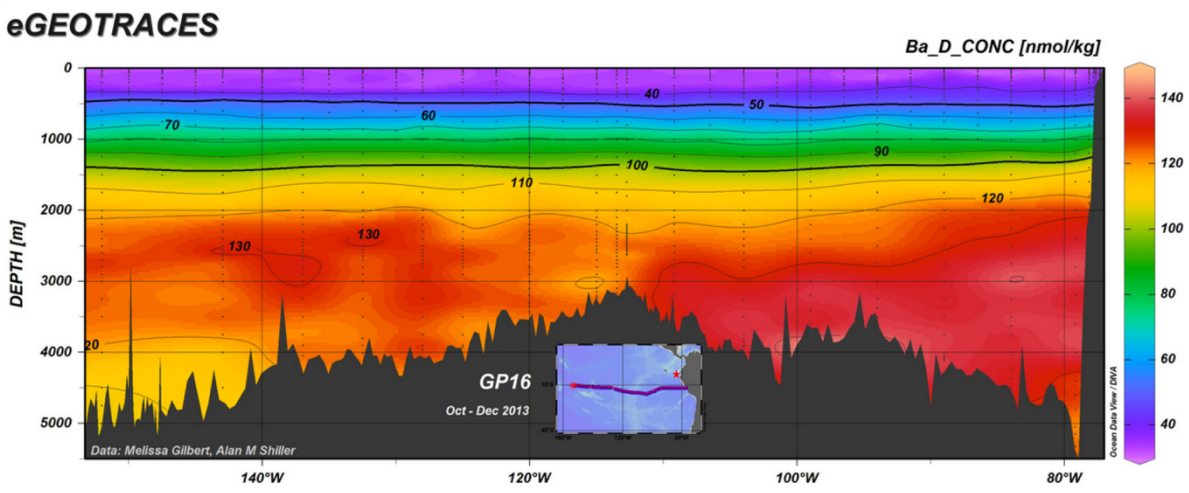

Figure 4.3 Seawater Ba concentration (unpub.) from GEOSECS profile located South of ODP 1238 (red star). Surface waters (0-200m) in the East part of the profile have Ba concentrations of ~ 30 nmol/kg.

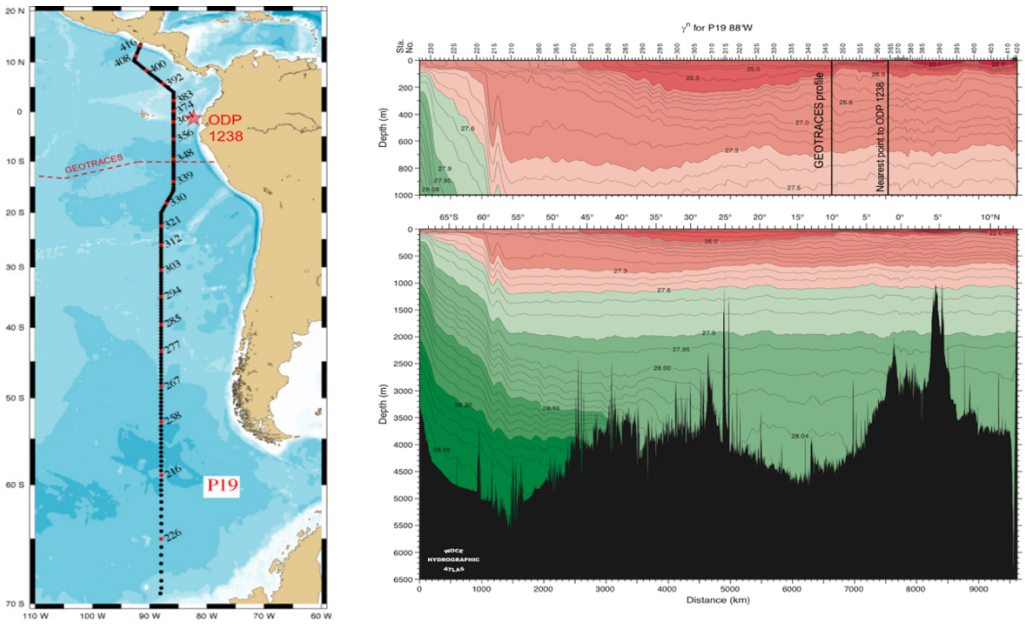

Figure 4.4 Depth profile of neutral density in the EEP (γ^n, right panel) along a North-South transect of the South-East Pacific (black line on left panel, data from World Ocean Circulation Experiment WOCE) showing intensity of upwelling on the γ^n profile point nearest to ODP 1238 (red star) and for the GEOTRACES profile (red dashed line on left panel).

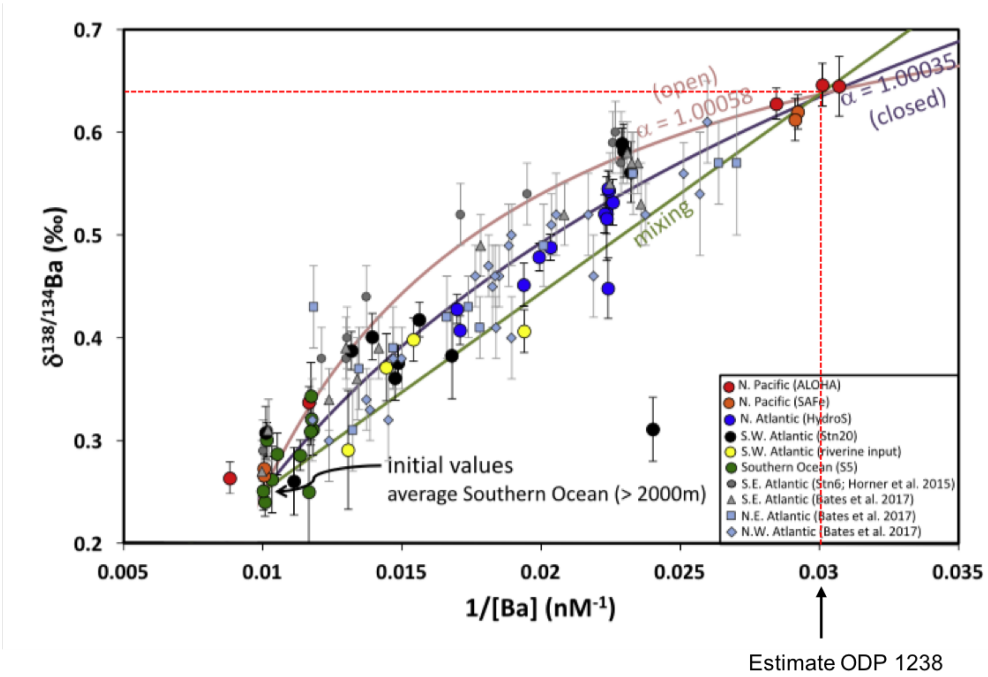

Figure 4.5 Compilation of existing seawater δ^{138}Ba and Ba concentration plotted as a cross-plot of δ^{138}Ba vs. 1/[Ba] showing an anticorrelation for all regions. This suggests a control of barite precipitation in the upper surface (by Hsieh and Henderson, 2017). 1/[Ba] is estimated at the EEP based on the nearby seawater Ba concentration of 30-40 nM (1/[Ba] ~ 0.03nM^{-1}) corresponding to δ^{138}Ba ~0.65‰. The three curves fit the data with a steady-state open model (pink), a Rayleigh fractionation closed model (purple) and a mixing model (green) between two low and high barium end-member.

4.2.3 Samples

4.2.3.1 For Ba isotopes

Mixed foraminifera and a selection of three species of foraminifera living at different depths in the upper water column were chosen for further study: the symbiont bearing spinose surface dweller *Orbulina universa* and the asymbiotic non-spinose thermocline dwellers *Neogloboquadrina dutertrei* and *Globorotalia menardii (*here after *O. universa, N. dutertrei and G. menardii)*. Each sample for Ba isotopes contains 20 mg for mixed foraminifera and 2 to 10 mg (200 to 360 specimens) for monospecific samples in order to obtain ≥10 ng of Ba after all foraminifera cleaning and Ba purification steps.

All monospecific samples were hand separated from the >355 μm size fraction and in order to examine the influence of size, mixed species were separated across multiple size fractions: 355-425, 425-500, and 500-600 μm.

All samples were cleaned to remove clay due to the potential Ba contamination from detrital sources (Van Zuilen et al., 2016). Then organic matter, metal-oxide coatings, and barite were removed using an oxidative, reductive (Barker et al., 2003) and DTPA (diethylenetriaminepentaacetic acid) mix (Putnis et al., 2008), respectively (S. Bates, pers. Com.). This cleaning was designed to minimize the influence of these phases on the final measured δ^{138}Ba and thus ensure that it was dominated by lattice-bound Ba. After dissolution in 1 ml of HCl, an aliquot (0.02%) of the dissolved sample was taken to measure element/Ca ratios and the rest kept for Ba isotopic analysis.

4.2.3.2 For B isotopes

In a similar way as for barium isotopes, boron isotopes were measured on the two foraminifera species *G. menardii* and *N. dutertrei.* For each species, around 2 mg of foraminifera from the 355-400 μm size fraction was hand separated (equivalent to 120-150 individuals) and cleaned following established methods (Barker et al., 2003) including clay removal, an oxidative treatment and a weak acid leach. A reductive step was also performed due to the presence of crust. Boron was separated from the carbonate matrix and measured on MC-ICP-MS following established methods (Foster, 2008; Foster et al., 2013, see chapter 1 for boron systematics and chapter 2 for details on methods). The data from *Tribolatus sacculifer* (hereafter *T. sacculifer*) is from Martínez-Botí et al. (2015) and is used for comparison and reflects the δ^{11}B signal from a mixed layer dwelling spinose symbiont-bearing foraminifera.

4.2.3.3 Age model

The age model of ODP site 1238 was determined by Martínez-Botí et al. (2015) by measurements of accelerator mass spectrometry (AMS) ^{14}C data on *N. dutertrei* and dates were calibrated with the Marine13 data set (Reimer et al., 2013). Unlike sites near Galapogos (Stott et al 2009), no age reversal was observed which suggest there was no or minimal influence of deep aged waters at the site.

4.2.3.4 Element and SST reconstructions.

Elemental ratio such as Ba/Ca and Sr/Ca and Mg/Ca in *T. sacculifer*, *G. menardii* and *N. dutertrei* were used for paleoenvironmental reconstruction and for ensuring samples were not contaminated by clays, trace metal crusts, or barite. Sea surface temperatures (SST) were reconstructed using Mg/Ca ratios of foraminifera. The conversion to SST was made using the calibration of Anand et al. (2003) for all three species. This calibration does not include *G. menardii*, however existing calibration of *G. menardii* (Regenberg et al., 2009) are in good agreement with Anand et al. (2003), hence the latter was used for consistency. SST was calculated as follow including a depth dependent correction dissolution on Mg/Ca (Dyez and Ravelo, 2013; see chapter 3 for details) :

$$SST = \frac{\ln\left(\frac{\frac{Mg}{Ca}surf}{0.38}\right)}{0.09}$$

Al/Ca ratios were used to verify the removal of clay contamination was efficient and Mn/Ca to check no Mn-oxides remained after the reductive clean. In both cases these ratios were low (<100 µmol/mol) and witness an efficient cleaning of the foraminifera. The ratios were cross plotted against Ba/Ca and showed no correlation showing that Al and Mn do not compromise Ba/Ca and Ba isotopes (See Appendix D).

4.2.3.5 pH reconstructions.

The $\delta^{11}B$ of each foraminifera species was converted into pH (see equation 10 chapter 1) whose expression is repeated here:

$$pH = pK_B - \log\left(-\frac{\delta^{11}B_{sw} - \delta^{11}B_{borate}}{\delta^{11}B_{sw} - \alpha_B * \delta^{11}B_{borate}(\alpha_B - 1)}\right)$$

pH is dependent on pK_B, the dissociation constant of boric acid in seawater (function of surface salinity and temperature), the boron isotopic composition of seawater ($\delta^{11}B_{sw}$) and the isotopic fractionation factor (α_B). Modern $\delta^{11}B$ of seawater was used (39.61, Foster et al., 2010) and kept constant and the fractionation factor α_B of Klochko et al. (2006) was used (1.0272). Temperature was reconstructed with Mg/Ca of foraminifera and modern salinity kept constant throughout the record. The $\delta^{11}B_{borate}$-$\delta^{11}B_{calcite}$ calibration of Martínez-Botí et al. (2015), recalculated from Sanyal et al. (2001), was used for *T. sacculifer* and the coretop data of Foster (2008) was used for *N. dutertrei.* No calibration to date exists for *G. menardii*, however data from Anagnostou et al. (2016) show that *G. menardii* have a $\delta^{11}B$ with minimal offset from borate, hence we assumed that $\delta^{11}B_{calcite}$ directly reflects $\delta^{11}B_{borate}$ for this species. Uncertainty in the pH calculated is determined as in chapter 3 with a Monte Carlo simulation.

4.2.4 Boron and Barium separation

Boron isotopes were separated following Foster (2008) and using the method described in chapter 2.

Barium was separated from its carbonate matrix by cation exchange chromatography in the NIRVANA laboratory facilities at WHOI. Since barium possesses more than four isotopes, double spike methods can be used for accurate and precise measurement on MC-ICP-MS. Unlike the bracketing standards technique used for boron (Chapter 2 and 3), the double-spike method does not require full recovery of barium off the column, though given the small sample sizes, quantitative recoveries are nonetheless desirable.

Dissolved samples were first weighed and double spiked with a solution of ^{135}Ba and ^{136}Ba aiming for a spike- to sample-derived barium (molar) ratio of between one and two. Spiked samples were then dried down overnight at 135 °C. 1ml of 6M HCl was added to each vial and left to reflux overnight at 135 °C to put the solution in HCl form and to fully equilibrate the spike. Samples were then dried down at 135°C, allowed to cool down and then dissolved in 250 µl 2.0M HCl and refluxed at 135°C for ion-exchange chromatography.

The separation of barium is conducted in several different stages, where the dissolved foraminifera is loaded on the columns and a specific volume of eluent is then passed, as illustrated in Figure 4.6. Home-made Teflon columns were stored in 6M HCl and rinsed with milli-Q. They were then individually filled with ~ 500 µl of AG 50W resin (e.g. Wolgemuth and Broecker, 1970) and carefully adjusted at the top of the stem. Each batch of resin (~ 1L) is calibrated once and volume of eluent required to elute each phase may vary from one batch of resin to another.

The column was then rinsed with 18.2 MΩ.cm grade water (Milli-Q water) and 6M HCl. The resin was then conditioned with 2M HCl and the sample (dissolved in 250 µl 2M HCl) was loaded onto

the column. The sample matrix was washed off with 2M HCl and barium was then eluted with 2M HNO_3. Each phase coming off the column is shown in Figure 4.6. Once the Ba phase was eluted, the resin was discarded. The whole procedure is repeated once with fresh new resin (two passes through the column in total) to improve the Ba to matrix ratio.

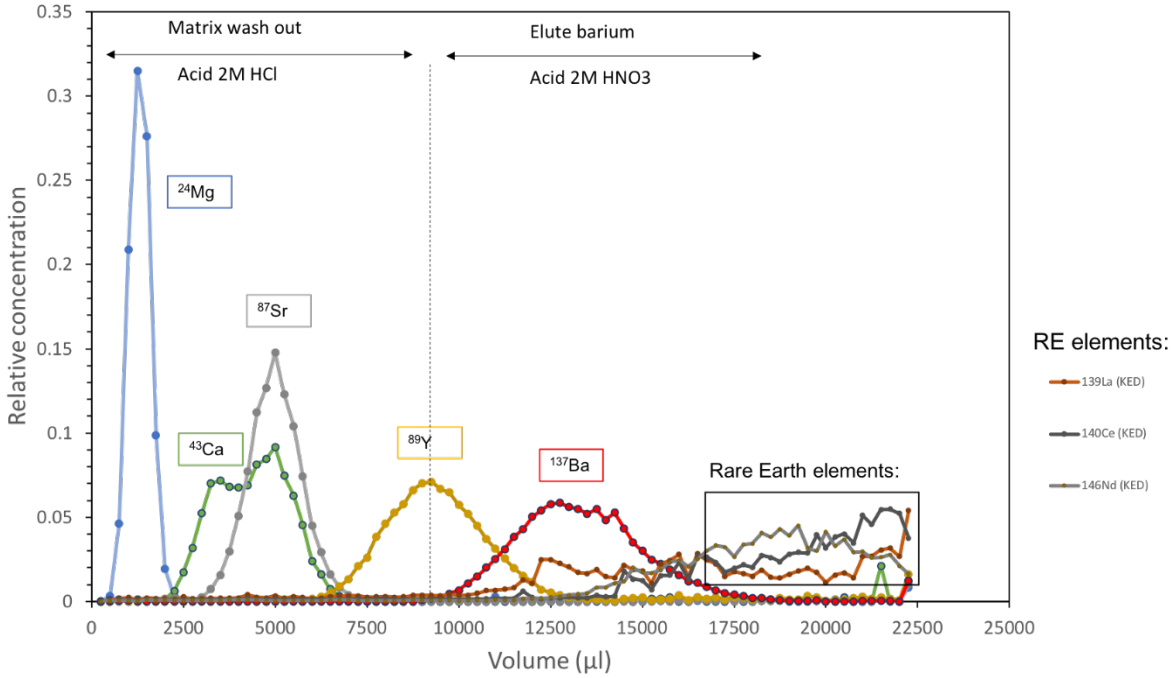

Figure 4.6 Elution curve for Ba and various element as a function of acid volume. Element from the matrix (Ca, Mg, Sr) are removed with 2M HCl acid and Ba is eluted with 2M HNO_3. Data from Tristan Horner (personal communication).

A total procedure blank (TPB) was also performed by passing through column chemistry an aliquot containing ≈ 1 ng of spike-derived Ba. The Ba content of this aliquot was determined via isotope dilution. The TPB for this study ranged from 19–64 pg Ba (n = 2), which is comparable to the long-term Ba blank of 31 ± 22 pg (± 1 SD; n = 27) (Horner et al., 2015). This constitutes 0.2 to 0.9 % of the sample size which doesn't require corrections.

4.2.5 Analytical technique

Elemental ratios and barium isotopes were measured on the Ba-isotope sample set on a Thermo Scientific iCAP ICPMS and on a Neptune MC-ICP-MS, respectively. Both instruments are situated at the WHOI Plasma Facility at Woods Hole Oceanographic Institution.

The isotopes ^{135}Ba, ^{136}Ba, ^{137}Ba, ^{138}Ba were measured and elements that interfere with Ba isotopes by isobaric overlap were measured to apply corrections: ^{131}Xe, ^{139}La, ^{140}Ce for correction of ^{136}Xe, ^{138}La and ^{138}Ce and ^{135}Ce (based on the expected abundance of each isotopes) that overlap with ^{136}Ba, ^{138}Ba and ^{135}Ba.

The barium isotope ratio was calculated using a three-dimensional interpretation of the double-spike equation (Siebert et al., 2001) with ^{138}Ba/^{135}Ba, ^{137}Ba/^{135}Ba and ^{136}Ba/^{135}Ba on the x, y and z axis, respectively. The ^{138}Ba/^{135}Ba ratio was then converted to ^{138}Ba/^{134}Ba assuming a mass dependent fractionation (Criss ,1999).

The barium isotopic ratio is expressed as the ratio of ^{138}Ba over ^{134}Ba of the sample relative to the Ba-isotope standard NIST 3104a:

$$\delta^{138}Ba = \left(\frac{\frac{^{138}Ba}{^{134}Ba}sample}{\frac{^{138}Ba}{^{134}Ba}NIST} - 1\right) * 1000$$

Boron isotopes were measured on a Thermo Neptune MC-ICPMS at the University of Southampton and University of Bristol following established methods (e.g. Foster, 2008). For these samples the associated elemental ratios were measured on an Element ICP-MS at the University of Southampton following Henehan et al. (2016).

4.3 Results

4.3.1 SST data

The temperature data derived from Mg/Ca show a distinct signature for all three species studied reflecting depth stratification of the species studies. *T. sacculifer* shows a warmer environment relative to *G. menardii* and *N. dutertrei* which confirms the preferred shallow habitat for *T. sacculifer* and deep, thermocline habitat of *G. menardii* and *N. dutertrei*. This is in line with previous studies in the EEP (e.g. Spero et al., 2003). All records for the three species show a warming until 10 ky followed by a slight cooling toward the Late Holocene. LGM temperatures are on average 1°C colder than Holocene temperature for all species.

4.3.2 Boron isotopes and pH

The boron isotopic composition of the three species examined, and the derived pH (Figure 4.7), show variations in absolute values and patterns over the deglaciation. *T. sacculifer* and *G. menardii* show

a decrease in pH of 0.25 units until 10 ky following the warming in temperature and increases by 0.1 unit at the beginning of the Holocene. Over the interval 0 to 17 ky, the range of pH is 0.25 and 0.1 for *T. sacculifer* and *G. menardii* respectively. The evolution of *N. dutertrei* drastically differs from the two other species as it shows a constant pH over the entire record with a range of ~0.05 unit.

4.3.3 Barium isotopes

Ba isotopes for mixed species (here after $\delta^{138}Ba_{mix}$ and monospecific foraminifera (here after $\delta^{138}Ba_{mono}$) show a distinct temporal evolution and suggests an influence of foraminifera size on the $\delta^{138}Ba$ of the mixed species (Figure 4.8). The mix at 355-425 µm size fraction shows a slight decrease in $\delta^{138}Ba$ over the deglaciation. The foraminifera from the 425-500 and 500-600µm size fraction only have two points in the time series and also show a moderate decrease in $\delta^{138}Ba$. The size effect between the 355-425µm and the two other size fractions is of 0.12 ‰ and constant throughout the record with higher $\delta^{138}Ba$ for the larger size fractions.

In contrast, the monospecific data show distinct signatures for each species, with the heaviest values observed in *N. dutertrei* (mean +0.30± 0.11‰, 2sd) followed by *G. menardii* (mean +0.14± 0.18‰, 2sd) and lightest value for *O. universa* (mean +0.01± 0.07‰, 2sd). The $\delta^{138}Ba$ for *G. menardii* and *N. dutertrei* show an apparent maximum at ~14 ky with lower (and within uncertainty) values during the LGM and Holocene. *O. universa* shows a near constant evolution with all points agreeing within error throughout the deglaciation.

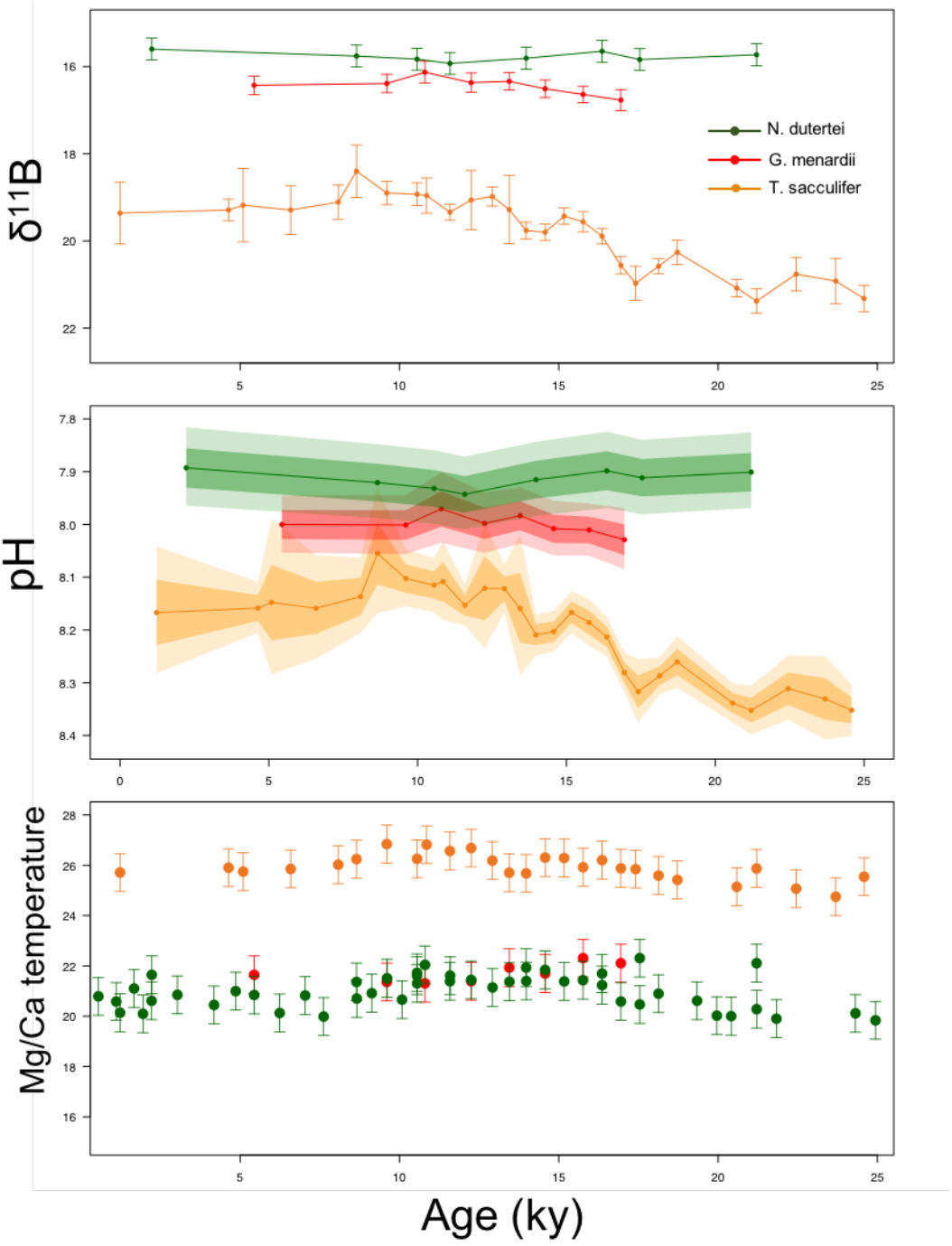

Figure 4.7 Evolution of $\delta^{11}B$, pH and SST in three planktonic foraminifera at ODP site 1238, surface *O. universa* (orange), and sub-surface *N. dutertrei* (green) and *G. menardii* (red) over the last deglacial in the East equatorial Pacific (EEP). *T. sacculifer* is from the size fraction 425-500µm, *N. dutertrei* from 355-500 µm, and *G.menardii* from 355-400µm.

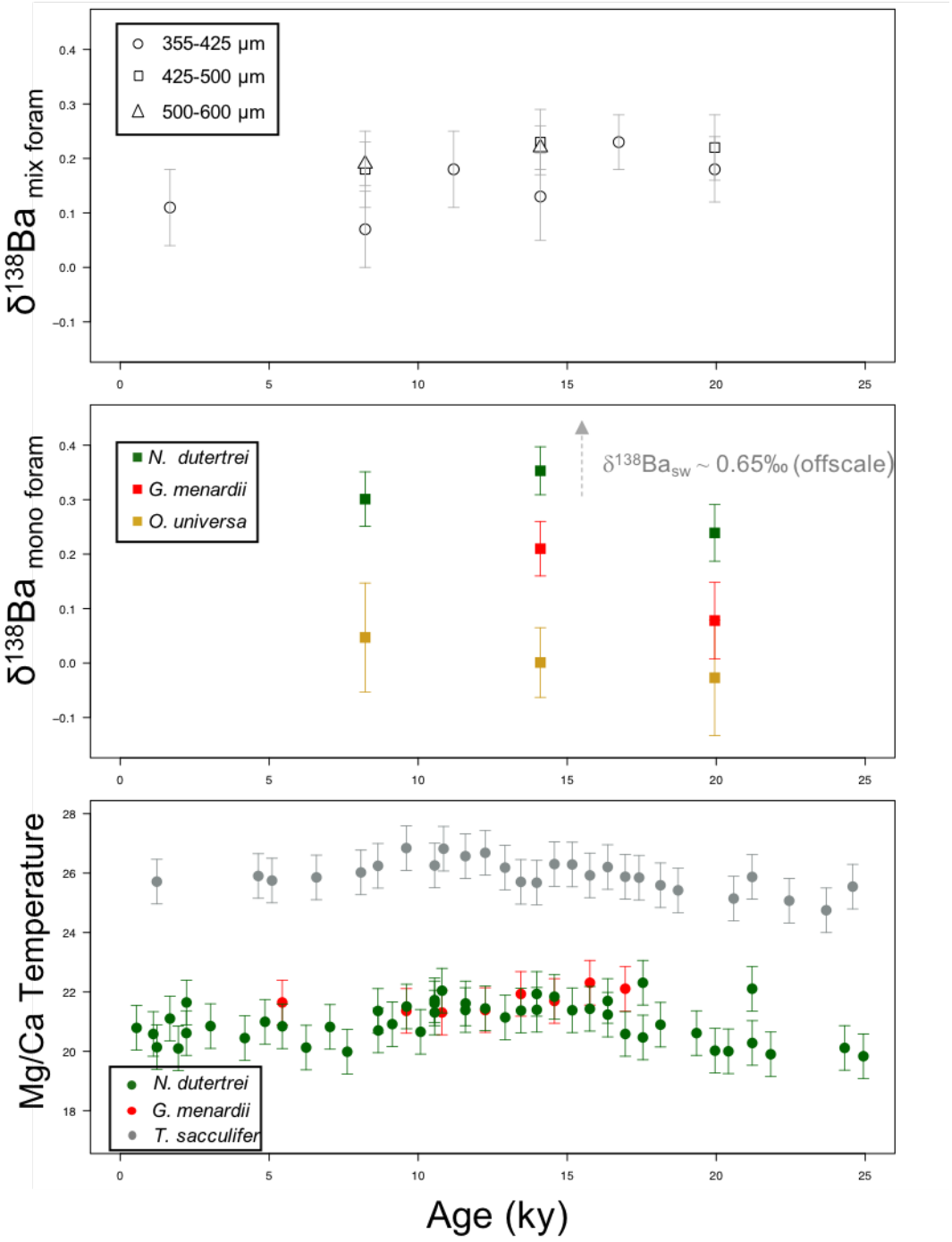

Figure 4.8 Evolution over the last deglacial in the EEP of foraminifera δ^{138}Ba for mixed foraminifera species at different size fractions (top) and evolution of δ^{138}Ba (middle, filled squares) and Mg/Ca-based SST (bottom, mmol/mol, dots) in three planktonic foraminifera, surface *O. universa* and *T. sacculifer,* and sub-surface *N. dutertrei* and *G. menardii*. δ^{138}Ba are measured on foraminifera from the size fraction > 355µm. Open circles in the SST data correspond to the same sample measured for δ^{138}Ba (with a cleaning including a reductive and barite removal step). Filled circles are from the size fraction 355-400µm for *G. menardii*, 425-500µm for *T. sacculifer* and 355-500µm for *N. dutertrei.*

4.3.4 Elemental ratio

Other elemental ratios of interest are plotted in Figure 4.9. Ba/Ca ratio of *N. dutertrei* show a range of 1 to 5 µmol/mol with maximum between 11 and 16 ky. *G. menardii*'s shorter record doesn't allow for the identification of a clear evolution but has similar range to *N. dutertrei* over the overlapping period 9 to 16 ka except for an outlier at 15 µmol/mol (~16 ky). Sr/Ca show higher values for *T. sacculifer* and a maximum at 11-14 ky. *N. dutertrei* shows a steady decrease over the deglacial. *G. menardii* exhibits the lowest Sr/Ca, and displays a constant ratio through the record.

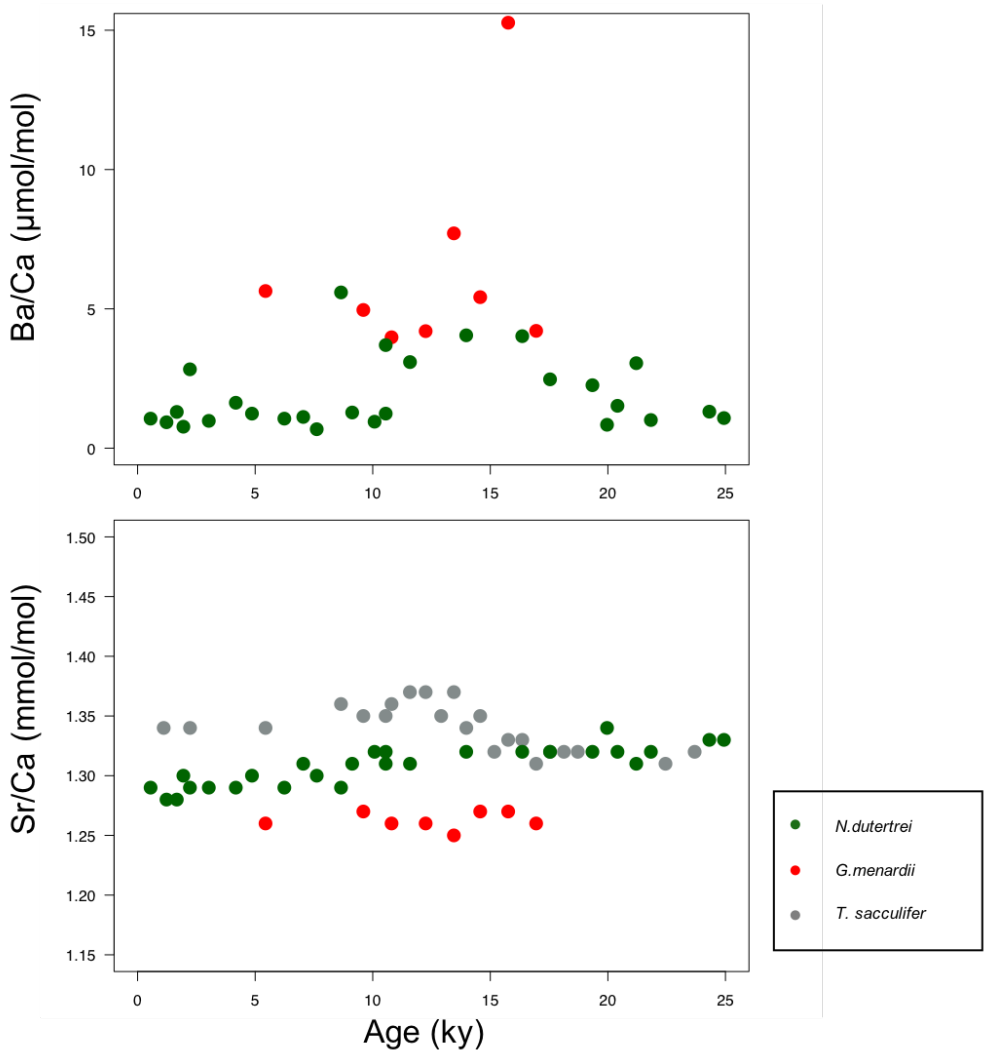

Figure 4.9 . Ba/Ca (µmol/mol) and Sr/Ca ratio (mmol/mol) for monospecific foraminifer *G. menardii , N. dutertrei and T. sacculifer* (Ba/Ca not available for *T. sacculifer*). (elemental data measured at NOC Southampton)

4.4 Discussion

4.4.1 Foraminifera Ba and δ^{138}Ba offset to seawater

4.4.1.1 δ^{138}Ba offset between foraminifera and seawater

The calculated δ^{138}Ba of the surface Ba in surface waters at site ODP 1238 are some of the lowest observed in the global ocean, indicative of high levels of Ba utilization. This is likely a consequence of the shallow and moderate upwelling rates and high biological productivity of the EEP .

Barium isotope composition of monospecific foraminifera ranges from −0.03‰ in *O. universa* to +0.35‰ in *N. dutertrei* (Figure 4.8); the range in $\delta^{138}Ba_{mix}$ is 0.07–0.22‰ for the 355-425 μm size fraction. All of these compositions are lighter than estimated ambient δ^{138}Ba by −0.3 to –0.6 ‰, with *O. universa* exhibiting the largest offset to seawater (Figure 4.10).

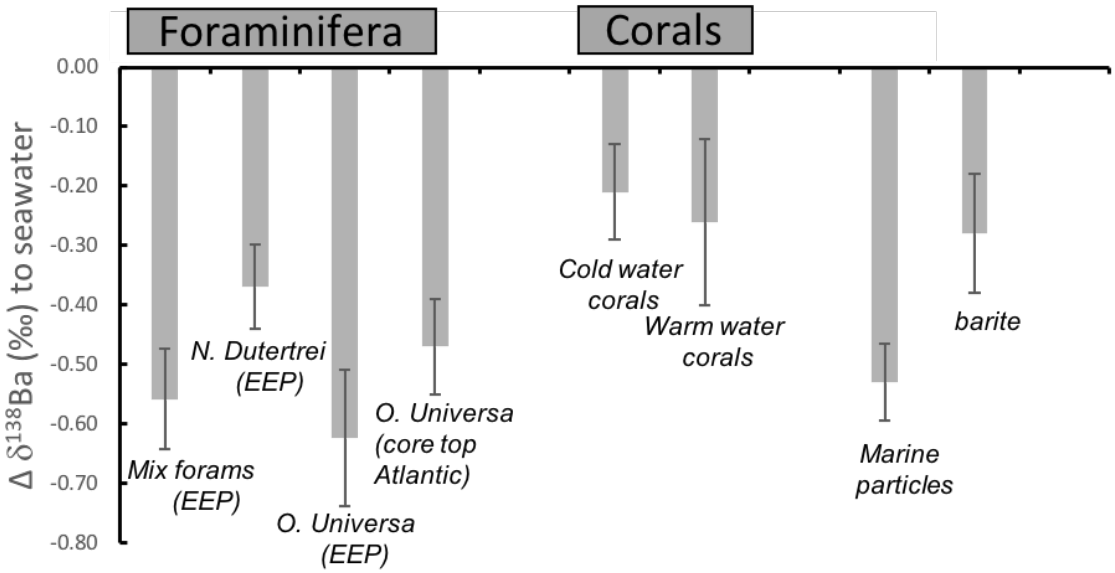

Figure 4.10 Maximum δ^{138}Ba offset to seawater observed for Holocene foraminifera from the EEP (this study), *O.universa* from Atlantic core top (S. Bates, personal communication), cold and warm water corals from various locations (Hemsing et al., 2018; Pretet et al., 2015), marine particles (Horner et al., 2017; Bridgestock et al., 2018) and barite (Horner et al., 2015). Seawater barium isotopic composition in the EEP is estimated at 0.65‰.

Comparing our youngest $\delta^{138}Ba_{mix}$ of 0.1‰ with the modern estimated value of ~ 0.67‰, shows a δ^{138}Ba offset between mixed foraminifera and seawater of ~0.55‰ and the Holocene monospecific data show an offset with seawater of 0.37 and 0.6‰ for *N. dutertrei* and *O.universa* respectively (since *G. menardii* is missing a Holocene δ^{138}Ba, we cannot compare this species with modern

estimates of seawater). The direction of fractionation in foraminifera, even though there is clearly variable absolute values between species, is in line with existing estimates of fractionation in corals with an overall offset between coral carbonate and seawater ranging between -0.21+/-0.08‰ (Hemsing et al., 2018) and -0.26+/-0.14‰ (Pretet et al., 2015). It is also consistent with the preferred light isotopic fractionation on incorporation into witherite of – 0.3 ‰ (barium carbonate $BaCO_3$; von Allmen et al., 2010). However, the clear distinct range of $\delta^{138}Ba$ observed between the foraminifera species measured here indicates that processes other than a strictly inorganic fractionation between seawater and calcite are operating (although such a fractionation may play a role). Alternative drivers of these values may include variations in habitat, i.e. the foraminifera inhabit different depths or perhaps within 'microhabitats', as well as additional vital effects driven by differences in biomineralization between different species. These possibilities are explored in section 4.4.2.

4.4.1.2 Ba/Ca offset between foraminifera and seawater.

Determination of the partition coefficient between calcite and seawater (defined as $D_{Ba} = Ba/Ca_{foram}/([Ba]/[Ca])_{seawater}$) for spinose foraminifera is well defined at around 0.15, based on culture data of *Globigerina bulloides*, *O. universa* and *G. sacculifer* (Lea and Spero, 1992; Honisch et al., 2011). Several results have been reported for non-spinose foraminifera with $D_{Ba} = 0.22$ (Lea and Boyle, 1991) or 0.11 for cultured *N. dutertrei* (Fehrenbacher et al., 2018), both of which are relatively similar to spinose foraminifera. Ba/Ca of our non-spinose foraminifera range 2 to 7 µmol/mol, and much higher values up to 20-30 µmol/mol have been reported in net tow specimens (Fehrenbacher et al., 2018; Bahr et al., 2013). Given expected ambient [Ba] of ≈ 35 nM, ambient dissolved Ba/Ca should be on the order of 3–4 µmol/mol, such that foraminifera exhibiting D_{Ba} between 0.1 and 0.2 should possess Ba/Ca ≈0.5 µmol/mol. In contrast, the lowest $(Ba/Ca)_{foram}$ we observe is ≈ 1 µmol/mol and some are as high as 7 µmol/mol. This implies there is some disconnect between what has been calculated in culture and what is observed in the field, perhaps suggesting wild foraminifera belonging to these species do not simply inhabit an ambient seawater environment (e.g. Fehrenbacher et al., 2018).

This is confirmed with a $\delta^{138}Ba$-Ba/Ca plot (Figure 4.11) aimed at imagining the water column based on depth of each species that show no anti-correlation like typically observed in modern seawater depth profiles under the control of barite precipitation (Figure 4.1). This suggests that the foraminifera (at least *N. dutertrei* and *G. menardii*) do not record a typical water column $\delta^{138}Ba$ - B/Ca signal.

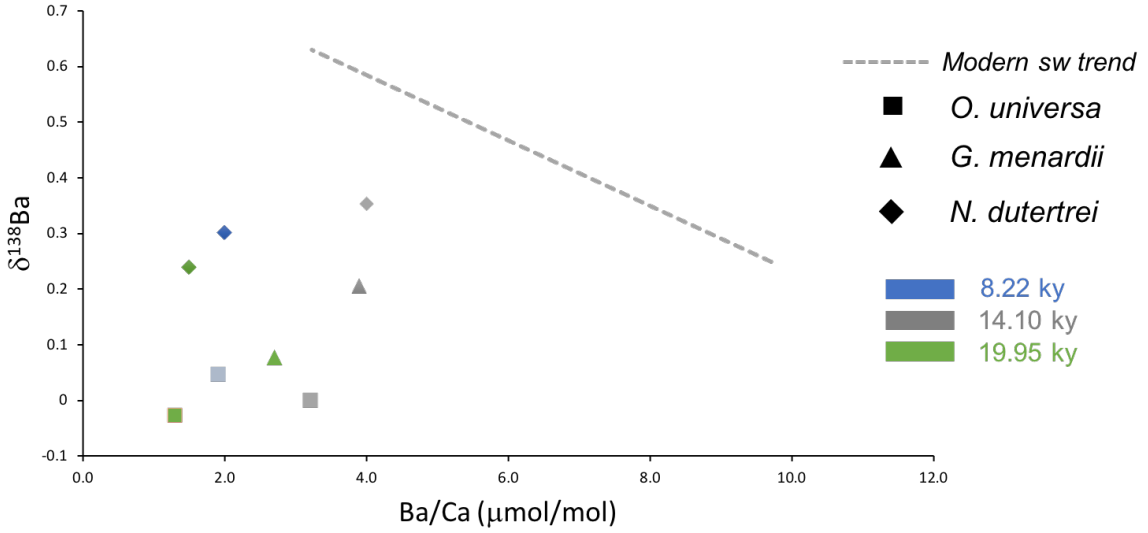

Figure 4.11 Cross plot of δ^{138}Ba and Ba/Ca for each foraminifera species (living at different water depth) at different age showing that for each age, there are no anticorrelation between δ^{138}Ba and Ba/Ca. Grey dotted line shows the expected trend that is observed in modern ocean seawater (Ba and δ^{138}Ba from Hsieh and Henderson, 2018 and Ba/Ca calculated assuming $[Ca]_{sw}$=10.3mmol/L)

4.4.2 Varying interspecific signal

The distinct range of δ^{138}Ba for each species (Figure 4.8) implies some heterogeneity in either the δ^{138}Ba of the environment in which the calcite was precipitated, or in the biomineralization of each foraminifera species causing variable isotopic fractionation. We explore both of these options in the next subsections (4.4.2.2 and 4.4.2.3).

4.4.2.1 Difference in depth habitat

As figure 4.11 shows habitat depth is unlikely to explain inter-species differences in δ^{138}Ba. Out of the three species studied, *O. universa* inhabits the shallowest part of the water column (usually 0-50 m, e.g. Dreuser et al., 1981), whereas *G. menardii* and *N. dutertrei* are thermocline dwellers (located at 100 m depth in the EEP), as supported by the SST reconstructions (Figure 4.8). Most seawater profiles show limited gradients in [Ba] and δ^{138}Ba over such shallow depth ranges; indeed, in well-mixed systems, the top several 100m may exhibit no Ba isotope gradients. Thus, it is unlikely that the Ba isotope gradient in the EEP is larger than ≈0.1 ‰ today, whereas the species studied exhibit inter-species differences of ≈0.3 ‰ (gradient requiring at least 1000 m of depth migration) far deeper than the habitat depth of any of the three species studied (0-100 m).

4.4.2.2 Difference in microenvironment and diet

The higher Ba/Ca observed in non-spinose foraminifera (Figure 4.9) species indicates differences in the mechanism by which Ba is incorporated into tests. Spinose foraminifera are indicative of a shallow depth habitat, since the spines are used to host photosynthetic symbionts. Likewise, non-spinose foraminifera don't need to reside in the euphotic zone, so they consequently do not require sunlight for their metabolic demands.

This observation of elevated Ba/Ca in certain species was recently noted by Fehrenbacher et al. (2018). Those authors observed that *G. menardii* and *N. dutertrei* (both non-spinose) record higher-than-expected Ba/Ca compared to spinose foraminifera species, postulating that Ba/Ca is set within a microenvironment of calcification, which is compositionally distinct from seawater. They present several arguments that this distinct microenvironment is associated with the foraminifera inhabiting particles of marine snow. An analogous argument can be made for the δ^{138}Ba of these foraminifera.

As discussed above barite is thought to precipitate in two pathways, biology mediated or by abiotic precipitation. In both cases this needs to happen in a microenvironment elevated in barium (Horner et al., 2017). These two possible pathways for barite precipitation presumably have different implications for the Ba chemistry of the marine snow fluid in which the foraminifera lived and an estimate of the barium isotopic composition of the ephemeral marine snow's fluid is desirable since it will influence the barium isotopic composition of the foraminifera calcite living in it.

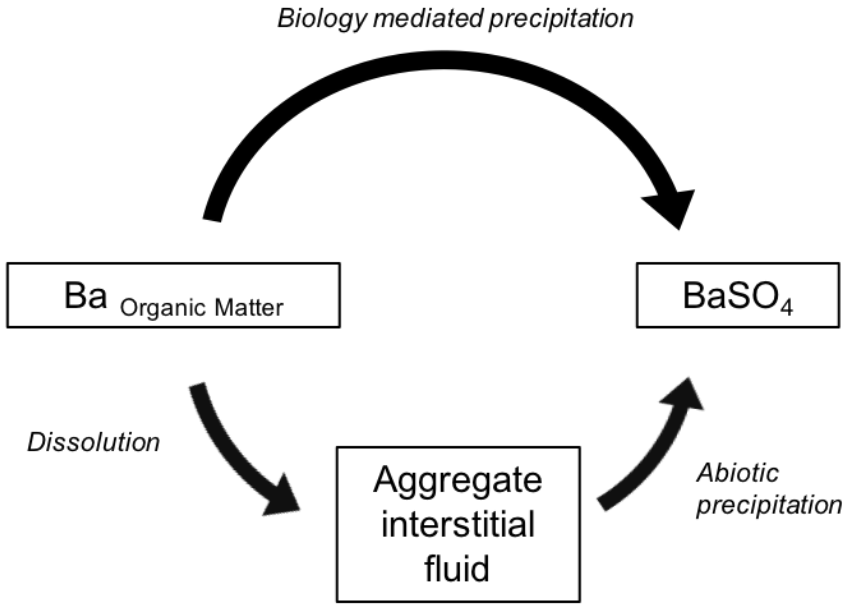

Figure 4.12 Schematic of sources of Ba for barite precipitation either directly biology mediated or abiotically precipitated from concentrated Ba in interstitial fluid of marine aggregates.

There are no reasons to think $\delta^{138}Ba_{foram}$ and $\delta^{138}Ba_{marine\text{-}particle}$ have similar values since the Ba isotopic composition of these two phases result from different processes (passive incorporation of Ba^{2+} for foraminifera vs. precipitation of barite and organic matter for particles). The $\delta^{138}Ba$ signature in interstitials fluid of marine particles ($\delta^{138}Ba_{Part\text{-}fluid}$) will be the result of the dissolution of organic matter and barite precipitation (Figure 4.12) and may have large variability due to the diversity in organisms that degrade in a particle and the completeness of any reaction. Several attempts of measuring $\delta^{138}Ba$ of marine particles and barite have been made and $\delta^{138}Ba_{particle}$ and $\delta^{138}Ba_{barite}$ have an offset from surface seawater of -0.53‰ (Horner et al., 2017) and between -0.2 to -0.4‰ (Von Almon et al., 2010; Horner et al., 2015, 2017), respectively. However, estimates of $\delta^{138}Ba_{particle}$ preclude the particle's interstitial fluid component as it is ephemeral and only measurable in situ.

Nonetheless, if the particle-seawater offset of ~ -0.5‰ holds true in the global ocean we estimate $\delta^{138}Ba_{particle}$ in the EEP to be ~0.15‰ (based on the estimated $\delta^{138}Ba_{surface}$ of 0.65‰, Figure 4.5).

The $\delta^{138}Ba$ offset between *G. menardii* and *N. dutertrei* however suggests that, if this process does play a role in non-spinose foraminifera $\delta^{134}Ba$, the recording of such a micro-environment by the foraminifera is not straightforward. Instead, species specific biomineralization and variations in food/diet may be important. These complications thus impede a direct reconstruction of marine particle's fluid.

Regardless, the two species of foraminifera *G. menardii* and *N. dutertrei* that Fehrenbacher et al. (2018) proposed inhabited marine snow are both heavier than *O. universa*. Since barite precipitation occurs in these marine particles, discriminating in favour or the light isotope, this would leave the interstitial fluid enriched in the heavy isotope. A marine snow habitat is therefore consistent with the observation that both of these species record a heavier $\delta^{138}Ba$ (Figure 4.8 and 4.10).

Another line of evidence that supports a microenvironment control is the invariance of pH in *N. dutertrei* (Figure 4.7). This suggests that there is a strong control of the carbonate system of the microenvironment as it has been observed that water column pH varied over the last deglacial (Martínez-Botí et al., 2015). The time interval examined of *G. menardii* is too small however to cover the whole deglaciation but shows a small yet gradual change over the interval 5-17 ky (of ~ 1‰; Figure 4.7). The gradual increase in pH this change equates to, even though largely within uncertainty, implies at least a partial control by the seawater carbonate system and is in line with the signal of bulk seawater recorder *T. sacculifer.* It thus appears that *N. dutertrei* and *G. menardii* exhibit slightly different behaviour, with *N. dutertrei* being a strict recorder of marine particle's fluid in a closed system, whereas *G. menardii* would have a hybrid behaviour with a recording of near constant pH from marine's particle fluid and partial recording seawater. This may be attributed to changes in habitat over the life-cycle of *G. menardii* compared to *N. dutertrei* living in marine particle throughout its whole cycle. This is consistent with Ba/Ca being constant for all chambers in *N. dutertrei* (Fehrenbacher et al., 2018). A complete $\delta^{11}B$/pH record of *G. menardii* and studies on its habitat may help to validate this hypothesis.

The difference in $\delta^{138}Ba$ between *G. menardii* and *N. dutertrei* may also be explained by their difference in ecology. It has been reported that both of these species may feed from Ba-rich acantharia (Hönisch et al., 2011; Bahr et al., 2013; Fehrenbacher et al., 2018). Dissolved celestite ($SrSO_4$) in the interstitial fluid of marine particles should enrich the fluid in both Sr and Ba. The Sr/Ca is also highest for *N. dutertrei* (Figure 4.9), which supports the idea of an (enriched) acantharia diet for this species, which conceivably could impart a specific $\delta^{138}Ba$ in order to drive an offset from *G. menardii*. However, a cross plot of Sr/Ca vs. Ba/Ca shows only a weak correlation for the non-spinose species (Figure 4.13). Furthermore, this is at odds with the preferred algal diet of *N. dutertrei* (Anderson et al., 1979; Hemleben et al., 1989) and partly omnivorous diet of *G. menardii* that also includes acantharia. Diatoms who also concentrate barium may have a specific $\delta^{138}Ba$ and influence marine's snow fluid if highly ingested by *N. dutertrei*. However, no clear evidence of diatom diet has been reported for *N. dutertrei* (Bird et al., 2018).

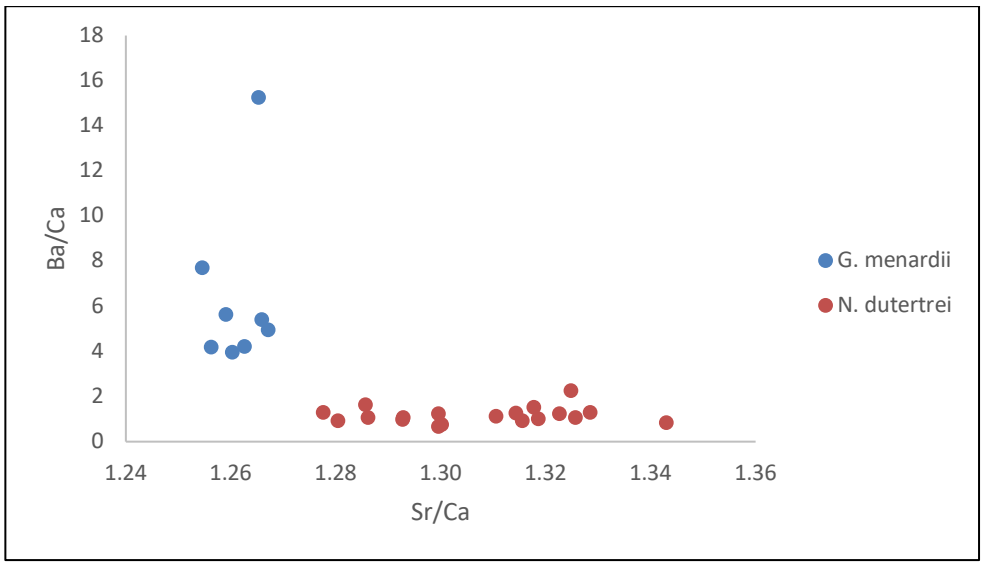

Figure 4.13 Cross plot of Ba/Ca (µmol/mol) against Sr/Ca (mmol/mol) showing weak correlation for all species (r^2=0.05, 0.017 for *G. menardii* and *N. dutertrei* respectively)

4.4.2.3 Difference in biomineralization

The discussion above highlights that δ^{138}Ba in non-spinose foraminifera that inhabit marine snow may be complicated by the variable δ^{138}Ba of that particular micro-habitat. Regardless of this, it can be assumed that *O. universa* inhabits the open ocean and hence its δ^{138}Ba reflects the δ^{138}Ba of seawater with some degree of isotopic fractionation related to the incorporation of Ba into foraminiferal calcite. Similarly to other calcifiers that exhibit a negative fractionation (-0.21‰ for corals, Hemsing et al., 2018), foraminifera are likely to show similar fractionation explaining the interspecific offsets between species.

The downcore variations in δ^{138}Ba are also potentially driven by change in biomineralization under changing temperature as it is the case for stable strontium isotopes, calcium and magnesium isotopes in coccolithophores (Stevenson et al., 2014; Gussone et al., 2006; Ra et al., 2010).

The specific fractionation caused by biomineralization needs to be addressed by culture studies of different species growing in similar seawater and/or varying temperatures. This will help to address the problems mentioned above and interpretation of foraminifer in the paleo record.

4.4.3 Paleoceanographic prospects for foram-bound $\delta^{138}Ba$

4.4.3.1 Mixed species signal and size effect

The signal from mixed foraminifera for the 355-425 μm fraction shows a constant decrease in $\delta^{138}Ba$ from 0.2 to ~ 0.07‰ throughout the deglaciation (Figure 4.8). There is no level of correlation with either $\delta^{138}Ba_{mono}$ or with a peak in productivity observed at 10-14ky (Martínez Botí et al., 2015, Figure 4.14). This lack of agreement with the monospecific foraminifera is likely due to changes in the dominant assemblage of foraminifera. No assemblage study has been made for our samples but a rough visual counting estimates *N. dutertrei*, *G. menardii* and *O. universa* at 70, 20 and 10% respectively for the modern. The ratio changes in favour of more *O. universa* towards the LGM. Although a precise assemblage study will be necessary to determine the relative contribution of each species to the mix.

The foraminifera size seems to influence $\delta^{138}Ba$ (Figure 4.8) with increasing $\delta^{138}Ba$ with size. Similarly to the temporal evolution of mixed foraminifera, change in assemblage can also occur with changing size, yet is not constrained.

Alternatively, change in chemistry of interstitial fluid may play a role in the observation of high $\delta^{138}Ba$ in larger specimens, because the assemblage is dominated by the non-spinose foraminifera (*N. dutertrei* and *G. menardii*) thought to live in marine snow. Alldredge (2000) observed that DOC is lower in larger aggregates caused by lower bacteria density, and a dilution effect by increased porosity and diffusion rate (Alldredge and Gotschalk, 1988). It is hence conceivable that the barium composition of these fluids undergoes similar dilution effect. This would induce a $\delta^{138}Ba$ of interstitial fluid closer to the $\delta^{138}Ba$ of seawater. As larger particles show heavier $\delta^{138}Ba$ and the $\delta^{138}Ba$ of seawater is larger than foraminifera (+0.65‰, Figure 4.5) it is consistent with a dilution of interstitial fluid with seawater.

On the other hand, the concentration of bacteria in marine aggregate has been observed to decrease with particle size (Alldredge, 2000). As barite formation is thought to be (at least in part) mediated by bacteria, lower density would lead to less barite formation than in smaller aggregates, hence decreasing (relatively) $\delta^{138}Ba$ of interstitial fluid.

Consequently, the observation of increasing $\delta^{138}Ba$ with foraminifera size, and changes in assemblage (in time and with size) suggest that the use of mixed foraminifera for paleo reconstruction is not suitable and that instead, monospecific foraminifera from a constrained size fraction are more adequate.

4.4.3.2 Change in local productivity.

The opal flux at ODP 1238 (Bradtmiller et al., 2006), a proxy for biological export, shows variations over the deglaciation with a peak in export between 10 and 14 ky (grey band in Figure 4.14) reflecting an increase in surface productivity. As discussed above, *O. universa* is the only species that is expected to record surface seawater, hence the invariance observed in $\delta^{138}Ba$ (Figure 4.8) is perhaps unexpected given these productivity changes and our understanding of the relationship between $\delta^{138}Ba$, Ba-export and productivity. The observed invariance of $\delta^{138}Ba$ is perhaps even more surprising given that the peak in opal flux is associated with an enhanced degassing of CO_2 (Martínez-Botí et al., 2015) due to an increase in upwelling of nutrients and CO_2.

In a regional study focused on the central equator, Costa et al. (2016) showed there was little to no variations in paleo-productivity between the LGM and Holocene based on opal flux, excess Barium, $^{231}Pa/^{230}Th$ and $\delta^{15}N$. This was interpreted as reflecting a lack of upwelled nutrients during the LGM due to their near complete consumption in the Southern Ocean (under increase Fe input) leaving advected waters from high to low latitudes depleted in nutrients. Despite observing an increase in dust and iron fertilization in the equatorial Pacific during the LGM, this was apparently insufficient to produce a substantial change in productivity (Costa et al., 2016). Unfortunately, these records only capture a Holocene and LGM snapshot, missing the deglaciation which impedes a comparison of our barium isotopes with nutrient consumption and other productivity proxies.

However, we can speculate that the resumption of upwelling at ~14 ky, both in the Southern Ocean and the EEP (Martínez-Botí et al., 2015), would bring preformed nutrients to the low latitudes and ODP 1238, increasing productivity as expected from the increased export during that period (Figure 4.14).

The apparent lack of a significant response of local $\delta^{138}Ba$ to these changes may be caused by: (i) issues with the fidelity of $\delta^{138}Ba$ in *O. universa* relating to morphotypes; (ii) other inputs to the EEP or (iii) it may be a consequence of larger scale processes (e.g. circulation) influencing waters upwelled in the EEP. These options are discussed in detail in the next sections.

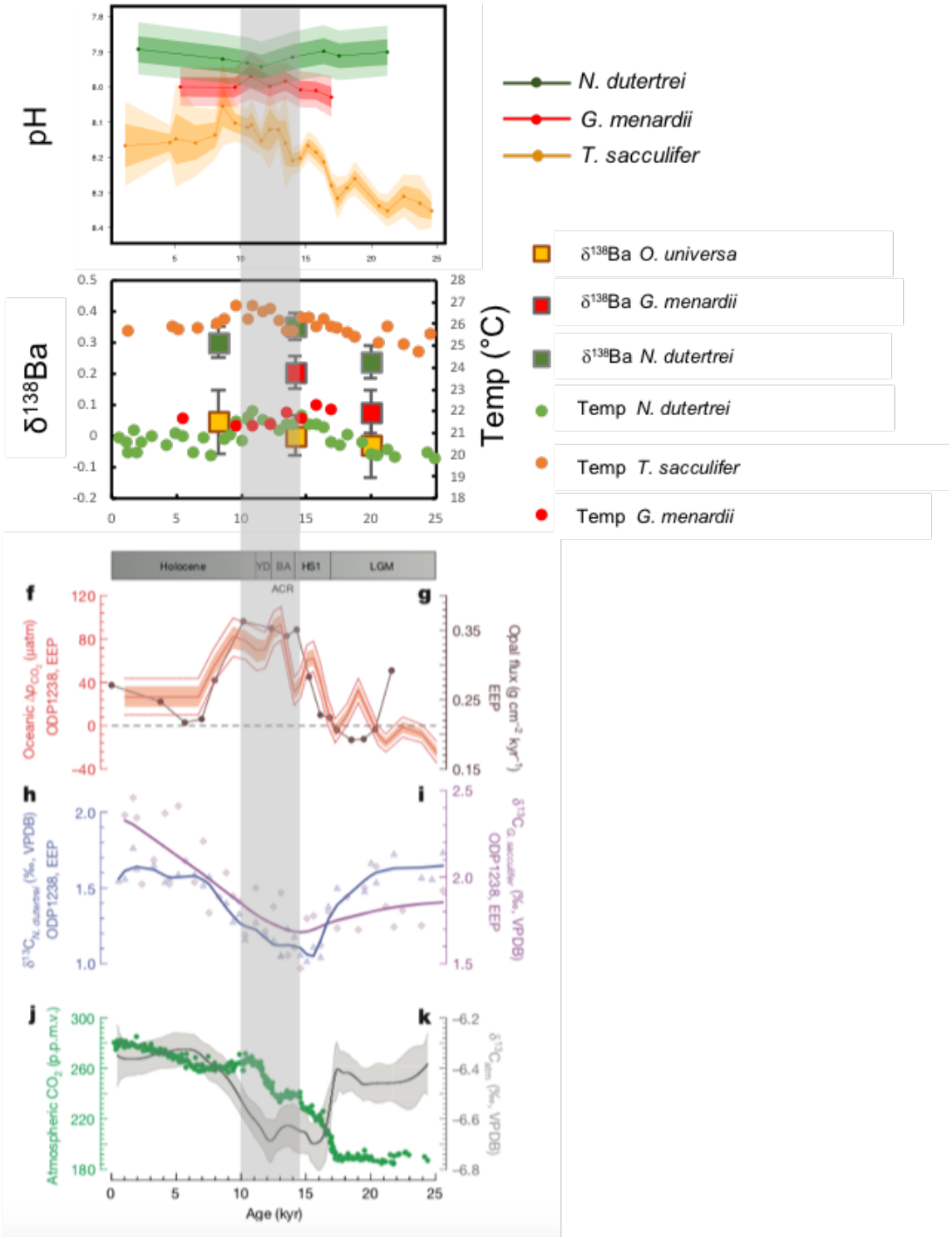

Figure 4.14 pH, $\delta^{138}Ba$ and Mg/Ca for monospecific foraminifera (this study, top two panels) and comparison with CO_2 disequilibrium at site 1238 from $\delta^{11}B$ in *T. sacculifer* (f, Martínez Botí et al, 2015), opal flux (g, Bradtmiller et al., 2006), $\delta^{13}C$ of *N. dutertrei* (h) and *T. sacculifer* (i), atmospheric CO_2 (j) and $\delta^{13}C$ of the atmosphere (k, Schmitt et al., 2012). Panels f to k by Martínez-Botí et al. (2015). Grey band highlights period of increased productivity as shown by opal flux.

4.4.3.3 Differences in morphotypes

O. universa has three morphotypes type I, II and III, which have been associated with different intensity of productivity with type I and II characterising oligotrophic areas and type III found in upwelling areas characterising eutrophic environments (de Vargas et al., 1999). However, these three types aren't easily recognisable without SEM imaging, and such a distinction was not carried out here. These morphotypes can also fit in the categories, 'thin' and 'thick' (Deuser et al., 1981; Marshall et al., 2015) based on the thickness or porosity of the last spherical chamber. It has been shown, based on $\delta^{13}C$ and $\delta^{18}O$ in specimens from the Cariaco basin (Venezuela) that the thick morphotype calcifies deeper in the water column under lower temperature, pH, oxygen and chlorophyll concentration (Marshall et al., 2015). The difference in depth calcification between the two morphotypes is however reduced during upwelling phases. Despite some known differences in depth habitat between morphotypes of *O. universa*, the upper water column of most seawater profiles shows a constant $\delta^{138}Ba$ down to 300 m (Figure 4.1, Horner et al., 2015; Bates et al., 2017; Hsieh and Henderson, 2018). It is therefore unlikely that morphotypes live deeper than this depth, hence we do not attribute the invariance of $\delta^{138}Ba_{O.universa}$ to morphotypes from different depth.

4.4.3.4 Change in water masses driving the $\delta^{138}Ba$ of surface water

The nutrient content and local biological productivity are only one component of the barium isotopic signature of surface seawater. Other inputs exist such as lateral advection and changes in water mass mixing, given different water masses have a $\delta^{138}Ba$ signature mostly acquired when these waters were last ventilated (Horner et al, 2015; Hsieh and Henderson, 2018). Other sources such as continental (e.g. Hsieh and Henderson, 2018), hydrothermal (Elderfield and Schultz, 1996) and deep sedimentary (e.g. Bates et al., 2017) input can also influence seawater $\delta^{138}Ba$.

In a stratified environment, the influence of various water masses is limited and $\delta^{138}Ba$ is mostly controlled by local productivity. However upwelling areas are highly impacted by the signature of underlying waters and, due to the connection between the Southern Ocean and the EEP, changes in the $\delta^{138}Ba$ signature of the Southern Ocean can potentially be seen in the EEP. Further studies recording a high latitude signal over the last deglacial will therefore be of great interest for the interpretation of $\delta^{138}Ba$ in foraminifera in the EEP and will allow an investigation of the connection between the regions as well as insights into the changing nature of Ba cycling between low and high latitudes.

The modern Southern Ocean exhibits the lowest surface to deep gradient in the water column (~ 0.1‰, Hsieh and Henderson, 2018, Figure 4.1), due to the influence of remineralised waters enriched

in the light Ba isotope upwelling at the surface and overprinting the surface biology driven signal (where barite formation enriches seawater in the heavy isotope). During the LGM, the Southern Ocean waters were more stratified with reduced upwelling and nutrients input (e.g. Sigman et al., 2010; Hain et al., 2010; Jaccard et al., 2013) making this area a smaller source of CO_2 to the atmosphere by the combination of reduced upwelling and more efficient biological pump in the Sub Antarctic Zone (SAZ) of the Southern Ocean caused by increased Fe fertilization (e.g. Martinez-Garcia et al., 2011). The waters from the SAZ are the source to the AAIW and SAMW (Toggweiller et al., 1991) that feed the low latitude thermocline, hence any change in the biogeochemistry of the SAZ may influence the EEP (Figure 4.15).

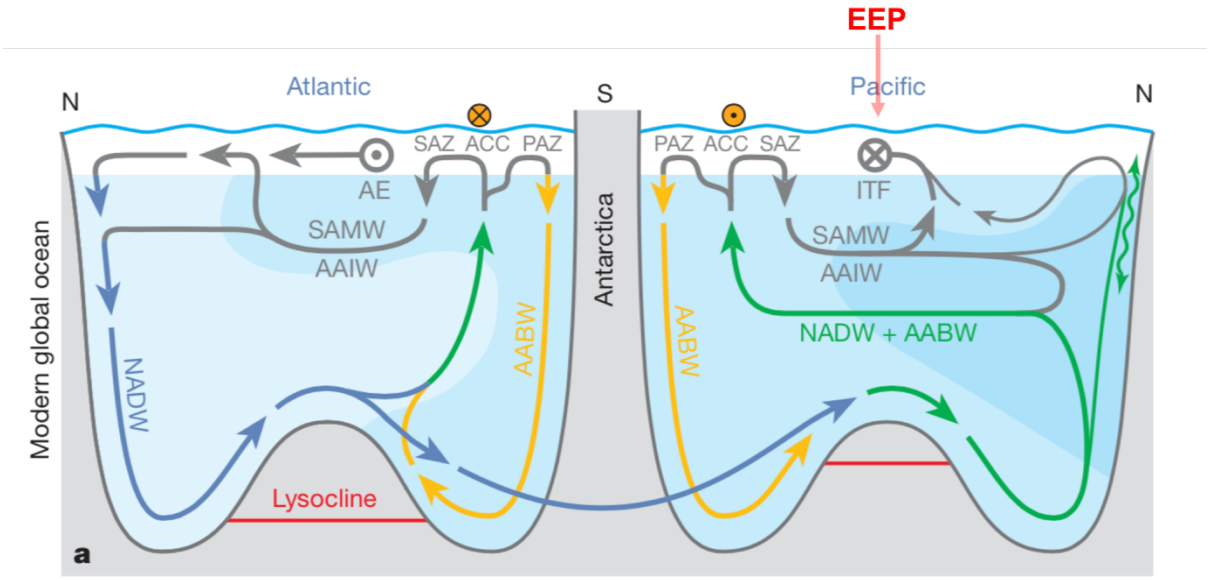

Figure 4.15 Illustration of water masses in the modern indicating the connexion between high and low latitudes through SAMW and AAIW. Figure by Sigman and Boyle (2010). SAMW sub-Antarctic mode waters; AAIW Antarctic intermediate waters, AABW, Antarctic bottom water, NADW North Atlantic deep water. PAZ polar Arctic zone, ACC Antarctic circumpolar current, SAZ sub Antarctic zone. AE Agulhas eddies, ITF Indonesian through-flow.

The geochemical signature of these waters in the low latitudes will therefore be influenced by both local productivity and by any changes in the underlying waters that upwell. These upwelled waters are the result of: (1) the Antarctic bottom waters (AABW) loop that has various inputs along the path between the Arctic Zone (AZ) and the deep ocean where it spreads Northward during the LGM and (2) the NADW loop that is much shallower and becomes the glacial North Atlantic intermediate water (GNAIW).

Hsieh and Henderson (2018) and Bates et al. (2017) have characterised the modern δ^{138}Ba of NADW and AABW below 2000 m at 0.45 and 0.24‰, respectively, based on a mixing model between two end members. During the LGM, the unproductive AZ would have little influence on barite precipitation at the surface and would deliver AABW with a lighter δ^{138}Ba. We note that sedimentary

input along the AABW path extended northwards during LGM, would increase δ^{138}Ba (Bates et al., 2017 and reference therein) but extra data are needed to quantify this input during the LGM. Furthermore, the extra sedimentary input may be compensated by the shoaling of the NADW since the GNAIW was more nutrient depleted than NADW (Lynch-Stieglitz et al., 2017) and would therefore carry a heavier δ^{138}Ba. The productive SAZ under iron fertilisation during the LGM would also increase the δ^{138}Ba of mode waters.

Qualitatively, we can therefore speculate that the resumption of upwelling during the deglacial would have brought up deep remineralised waters with a light δ^{138}Ba eventually feeding the low latitudes, but this remains to be tested (with high latitude data). Within this framework, we would expect *O. universa* to record a decrease in δ^{138}Ba around 14 ky, rather than record the invariant ratio we observe. This lack of observed change could therefore, conceivably at least, be the consequence of two competing effects – a decrease in the δ^{138}Ba from more vigorous upwelling, and, an increase in δ^{138}Ba from higher productivity (as observed in other proxies and as suggested by the δ^{11}B-CO_2 data; Martínez-Botí et al., 2015). Modelling studies with estimations on different barium sources at the EEP and effect from change in productivity on $\delta^{138}Ba_{sw}$ would help to test this idea.

4.4.3.5 Change in interstitial fluid of marine aggregates.

As discussed above, it is possible that the chemistry of interstitial fluid of marine aggregate is expected to directly influence the δ^{138}Ba of the two non-spinose foraminifera (*G. menardii* and *N. dutertrei*). This interstitial fluid chemistry is also known to change with the size of marine particles (e.g. decrease in DOC with aggregate size, Alldredge, 2000). The high δ^{138}Ba of the two species at 14 ky occur during a period of enhanced export and productivity (Figure 4.14) which could have an effect on the size of marine aggregates. The constant pH in *N. dutertrei* (and to a lesser extent *G. menardii*, Figure 4.7), suggests that the pH of the interstitial fluid remains constant throughout the deglaciation which may be at odds with a varying $\delta^{138}Ba_{fluid}$ as we'd expect barite formation and remineralisation in the particle to be correlated. It is beyond the scope of this study however to determine the variation of δ^{138}Ba and pH of interstitial fluid with particle size, temperature or pH but all these variables may have an effect on the δ^{138}Ba of these non-spinose foraminifera and this need to be tested for accurate determination of the environment recorded aggregate-living foraminifera.

4.4.3.6 Influence of continental input.

The barium isotopic signature of continental run-off is lighter than seawater with $\delta^{138}Ba_{\text{ silicate rocks}}$ = 0.10 ±0.05‰ (Van Zuilen et al., 2016), hence any continental input would also serve to decrease the δ^{138}Ba of seawater. ODP 1238 is ~ 200 km away from the coast of Ecuador. Data from Hsieh and Henderson (2018) show no influence of continental input (that brings lighter δ^{138}Ba) at their site nearest to the coast. ODP 1238 is however located under the area where the ITCZ moves which can provide significant rain fall and increased continental run-off. The modern ITCZ is located north of ODP 1238 (~ 10°N) implying no enhanced run-off from the continent in the modern. The position of the ITCZ over deglaciation has been linked to ice cover (Chiang and Bitz, 2005) and weakening of Asian monsoon (Barnett et al. 1988), shifting the ITCZ south. This was also the case during the Younger Dryas (12 ky) and Heinrich Stadial 1 (15-18 ky) and this could have impacted the EEP (Denton et al., 2010). The resolution of our record may be too limited to infer an influence of continental sources. However, if continental input were increased during the deglacial, this could have had a similarly compensating effect on the $\delta^{138}Ba_{O.universa}$, potentially augmenting any changes due to changes in upwelled δ^{138}Ba. A higher resolution of barium isotopes in spinose foraminifera (expected to directly record seawater) is needed to further test this hypothesis. The two non-spinose foraminifera under the control of marine aggregate's chemistry would be relatively unimpacted by this continental signal.

4.4.3.7 A conceptual model of barium incorporation

On one hand, the *O. universa* data shows no variations in δ^{138}Ba, despite varying pH of surface waters; on the other hand, the two non-spinose species *N. dutertrei* and *G. menardii* show modest varying δ^{138}Ba but near constant pH. The first case implies an invariant Ba isotope composition of water masses potentially as the result of compensation between upwelling waters, local productivity and to a lesser extent, continental input. The reported change in pH is plausible with these scenarios. The second case implies an invariant pH as the result of microenvironment marine particle. The cause of the varying δ^{138}Ba may thus be a response to changing productivity and chemistry of interstitial fluid (under varying degree of barite precipitation).

Regardless of the source of barium, the interspecific offset between foraminifera species is perhaps best explained by differences in biomineralization processes. Consequently, the downcore variations could alternatively also be controlled by changes in biomineralization with varying temperature changing the δ^{138}Ba fractionation on incorporation. This later hypothesis is particularly suitable for future testing with cultures studies.

Figure 4.16 shows a conceptual model of different sources and processes involved in the barium signature recorded by foraminifera.

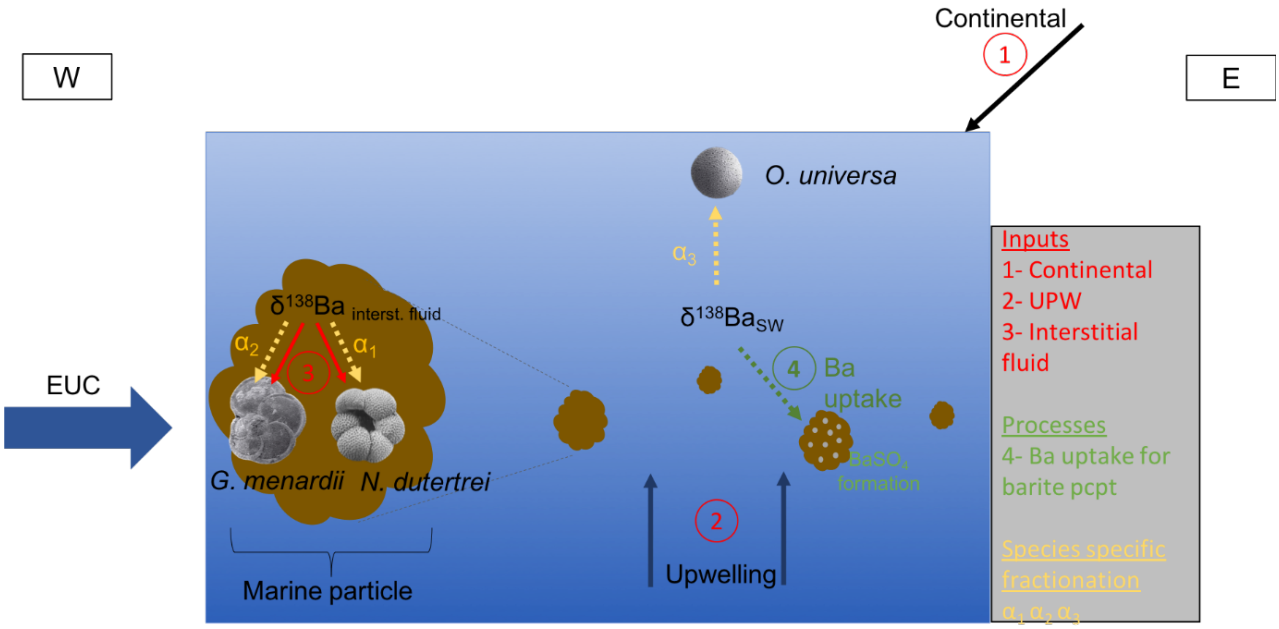

Figure 4.16 Conceptual model of barium recording by foraminifera in the surface ocean. Non-spinose foraminifera (G. menardii and N. dutertrei) record the barium isotopic composition of interstitial fluid (3) (at least in part controlled by barite precipitation) of marine particles with each species having a specific fractionation (α_1 and α_2) controlled by biomineralization. Spinose foraminifera *O. universa* directly records the barium isotopic composition of seawater with its own isotopic fractionation (α_3). The seawater signal may be the result of various input/mechanism including signal form continental input (1), the underlying upwelling waters (2), and biological productivity and associated barite precipitation (4).

4.5 Conclusion

We measure here, for the first time, the barium isotopic ratio (δ^{138}Ba) of foraminifera over the last deglaciation in the East Equatorial Pacific. The results for two non-spinose foraminifera (*G. menardii* and *N. dutertrei*) are distinct from the measurement in a spinose foraminifera (*O. universa*). The δ^{138}Ba of *O. universa* that is expected to directly record the signal from bulk seawaters is invariant over the deglaciation and may be a result of compensating mechanisms between local productivity and input from continents and change in upwelling whose signature is potentially dictated, in part, by high latitude processes. The non-spinose foraminifera *G. menardii* and *N. dutertrei* have δ^{138}Ba that evolve in tandem with a near constant offset. The high Ba/Ca of these two species, reported here and in the literature, suggests an influence by barium rich microenvironment such as marine particles. This is supported by the heavier δ^{138}Ba observed in these species relative to *O. universa* where increased barite formation would enrich the microenvironment in the heavy isotope and by the constant and more acidic pH that suggests a control by microenvironment with degrading organic matter. The δ^{138}Ba variation of these two species shows a maximum at 14 ky concomitant with a peak in biological export, that may be related to a change in the Ba chemistry of the interstitial fluid of marine particles under enhanced biological productivity or by change in biomineralization. The measurements on mixed foraminifera species show a size effect with higher δ^{138}Ba for bigger species and the time series show no clear relationship with paleo-productivity, likely caused by changes in assemblage in size fractions and with time. We hence suggest the use of monospecific foraminifera and species that are direct recorders of bulk seawater for the reconstruction of barium cycling in the past. However, additional work is needed to constrain the nature of "vital effects" arising from biomineralisation and habitats.

Chapter 5: Conclusions

5.1 Key conclusions

This thesis has looked into advancing the utility, application and knowledge of two proxies used in the field of palaeoceanography by: (1) validating and testing the boron isotope pH-CO_2 proxy over the ice core period at two locations and at high resolution;(2) improving the ease at which boron isotope data can be generated from carbonate (corals), an important step in removing an analytical bottle neck and improve the throughput of boron isotopes data for pH and CO_2 reconstructions in the past; (3) measuring the barium isotopic composition of planktonic foraminifera for the first time in three species with the aim to explore if this system serves as a viable proxy for reconstructing palaeoproductivity. In light of these findings, the key questions presented in the thesis introduction (chapter 1) are reassessed here.

5.1.1 Chapter 2 Automation of boron purification

Q1: Are the physico-chemical properties of ion exchange chromatography reproducible on an automated system?

The automated boron purification using the prepFAST-MC has been shown to be able to accurately reproduce the boron isotopic composition of boric acid standards, seawater and corals with no carryover and high reproducibility. The blank with the automated method was shown to be consistently higher than with the manual column but remained within an acceptable range without the need to apply a correction. The matrix wash-out was found to be less efficient than gravity column caused by the different column shape and style of flow (laminar prepFAST column vs. gravity column that allows resin in suspension). These features were also not found to compromise the accuracy of $\delta^{11}B$ generated. An important aspect of the automated method was the speed of loading of the sample onto the column that was shown to produce negative isotopic fractionation at speeds above 200 µl/min. This not only indicates that load speed must be set at a <200 µl/min, but also highlights that manual gravity columns may also fractionate if the volume of buffered sample loaded is too high, due to the increase in flow speed this would induce given of the larger hydraulic head (and has been observed, Foster Lab pers. com). Using a pure carbonate matrix to dope NIST 951 it was shown that the amount of carbonate matrix loaded did not influence accuracy (up to 0.65 mg Ca, 1.5 mg pure $CaCO_3$). However, preliminary foraminifera data have shown to produce a significant positive $\delta^{11}B$ offset in the range 0.2 to 0.5 ‰ with the offset being proportional to the amount of carbonate matrix loaded. We speculate that this effect of matrix is associated to organic matter within

the carbonate lattice, that despite an oxidative step being conducted on all samples processed, remains post cleaning. This organic material quickly sticks to the columns and degrades the resin.

Q2: to what extent automation increases the throughput of samples for boron isotopes analysis?

The prepFAST-MC system enables an automation of the boron separation method by ion exchange chromatography at the rate of 1 sample/ hour. In a working day, this is equivalent to 1 to 2 batches (~8-12 samples) of samples processed with manual gravity columns. This enables a day of manual of processing to be saved. In practice however, it has been found that a batch of samples (~8) can be purified using the prepFAST while the Neptune MC-ICPMS is warming up, and run for isotopic composition that same day. This greatly speeds up throughput and productivity.

5.1.2 Chapter 3: CO_2 reconstruction using boron isotopes during the late Pleistocene

Q3: Are boron isotopes a reliable proxy of CO_2 when tested at several location and time interval?

The two new $\delta^{11}B$-derived CO_2 records generated at ODP 999 and 871 on the planktonic foraminifera *G. ruber sensu stricto* from ~200 to 400 ka are in good agreement with the ice core record (EPICA dome C) with an average offset of +16 ± 30 ppm We find that episodes of increased corrosiveness recorded by fragments counts are possibly associated with minor short-lived overestimations of boron-derived CO_2 (+50 ppm) likely caused by the fractionation of boron isotopes towards light values under partial dissolution. Despite these intervals of brief offset, on the whole the $\delta^{11}B$ -CO_2 proxy reproduces the ice core CO_2 well (RMSE 3 ppm).

Despite this good agreement for 200 to 400 ka, it was also found that MIS 12 to 14 (450 to 600 ka) were associated, at both core locations, with a significant overestimation of CO_2 relatively to the ice cores (see appendix B). Whilst the reasons of these offsets remain inconclusive and are the subject of ongoing study, several reasons can be invoked including: (1) a change in air-sea disequilibrium at both location due to enhanced monsoon activity during this period, changing walker circulation dynamics in the Pacific (ODP site 871) and maybe associated with reduced iron fertilisation and increased CO_2 degassing in the equatorial Atlantic (ODP site 999) during luke warm interglacials*;* (2), a reduction in nutrient inventory in the high latitude and by extension, the low latitudes through the supply of intermediate waters, and parallel input of nutrients from increased continental run-off (under increased monsoon) could have favoured the

blooming of silica-rich organisms over calcifiers leading to depth migration of foraminifera and their $\delta^{11}B$ recording more acidic deep waters.

Q4: What can the new pH data reveal about the relationship between pH and CO_2 forcing over the late Pleistocene?

The data from 200 to 400 ka, along with published boron-derived pH/CO_2 estimates show that the relation between pH and ice core CO_2 is in very good agreement with the formalism that variation in CO_2 forcing is expressed by variation in pH alone such as $\Delta F_{CO2} = -12.3\Delta pH$ (Hain et al., 2018). This supports the use this formalism to reconstruct relative CO_2 forcing in the past without the need to estimate a second carbonate parameter or robustly estimate $\delta^{11}B$ of seawater, parameters often poorly constrained in deep geological times. Moreover, the relationship between boron-derived pH and ice core CO_2 forcing highlights that there are likely a number of mechanisms involved in glacial-interglacial cycles including carbonate compensation, DIC and temperature change. This formalism is valid as long as local ΔpH is determined in areas of the ocean in near equilibrium with the atmosphere. Any areas of source or sink of CO_2 won't reflect atmospheric CO_2.

5.1.3 Chapter 4: Barium isotopes in foraminifera as a paleoproductivity proxy.

Q5: Do barium isotopes in foraminifera faithfully record the barium isotopic composition of seawater?

The three species of foraminifera studied here (*O. universa*, *G. menardii* and *N. dutertrei*) show a distinct $\delta^{138}Ba$ signature with variable offsets from seawater that imply either: (1) differences in environment recorded; or (2) differences in biomineralization and barium fractionation specific to each species. Option (1) is supported by the high Ba/Ca of the non-spinose foraminifera (higher than predicted by published, culture-based, partition coefficients and the Ba/Ca of seawater) in line with recent published studies (Fehrenbacher et al., 2018)as well as by a (near)constant pH recorded for these two species suggesting a specific microenvironment habitat enriched in barium such as marine particles/aggregates (also referred as marine snow). *O. universa* as a spinose foraminifera is expected to directly record seawater.

The down core evolution of each species is constant for *O. universa* and variable for *G. menardii* with a maximum recorded at 14 ka. Independent proxy records of biological export (opal flux) also show an increase in productivity centred around 14 ka. Under a pure environment/microenvironment scenario (Option 1), the invariant $\delta^{138}Ba$ of open water recorder *O. universa* may be explained by

compensation mechanisms between local productivity, change in upwelling intensity and to a lesser extent continental input. The varying δ^{138}Ba of the two non-spinose foraminifera may, in this case, be explained by changes in the chemistry of marine particle fluid under increased productivity.
Whilst changes in isotopic fractionation on incorporation (Option 2) through time, and, between species is a possibility, it remains untested but cannot yet be ruled out without future culture studies. It can however have a temperature effect on δ^{138}Ba, like has been proposed for δ^{44}Ca (Stevenson et al., 2014), and could explain (at least in part), the interspecific δ^{138}Ba offset and evolution through time given changing temperatures.

Q6: What are the ideal foraminifera species and ocean locations to reconstruct past changes in barium cycling?

In order to deconvolve the biological productivity signal (associated with barite formation) from δ^{138}Ba in planktonic foraminifera, it is necessary to avoid foraminifera that may live in specific microenvironment (i.e. within marine snow). In our case, the use of *G. menardii* and *N. dutertrei* are possibly not suitable for the recording of open water signal. Yet, these may be of interest if the down core signal records the chemistry of marine particle's interstitial fluid that could shed light on mechanisms of barite formation, or the role of the degradation of organic matter in marine particles. However, an assessment of the influence of biomineralization and species-specific fractionation under changing environments (e.g. ambient δ^{138}Ba and temperature) needs to be determined before to confirm or refute this approach.
Secondly, a location in a stratified environment is preferable to remove the variablity associated with upwelling waters that may have a different barium isotopic composition than surface waters and integrate large scale processes independent of local biological productivity. Thirdly, the size fraction of foraminifera needs to be constrained as there is a visible change in δ^{138}Ba for different size fractions and the mixing of foraminifera morphotypes should be avoided without the knowledge of specific fractionation for species and morphotypes.
Lastly, and as evident in Figure 4.8, the species specific δ^{138}Ba means the use of mixed species foraminifera is not suitable to record seawater δ^{138}Ba in the presence of changes in foraminifera assemblage.

Q7: Are barium isotopes in foraminifera a promising proxy for paleoproductivity reconstruction?

Even though the δ^{138}Ba data presented do not clearly demonstrate it, there remains a potential of barium isotopes to be a useful proxy in the field of palaeoceanography. However, the complications we highlight need to be resolved first. In particular, the determination of the magnitude and cause of species-specific δ^{138}Ba fractionation is urgently needed to enable the variations in the paleorecord

to be deconvolved and to examine if a paleoproductivity signal is preserved. Several other spinose foraminifera have the potential to overcome the issues discussed above and may be more direct recorders of seawater $\delta^{138}Ba$. These include the species *T. sacculifer* and *G. ruber* whose morphotypes are clearly distinguishable and are wildly used in palaeoceanography.

5.2 Future work

The work presented in this thesis has shed light on a number of processes and mechanisms previously unknown or understudied. Yet, these phenomena remain incompletely understood and I discuss here several avenues to continue the investigation of these outstanding issues. These include: (1) the method development of boron purification for foraminifera; (2) the recording of CO_2 from foraminifera $\delta^{11}B$ during luke warm interglacial; (3) the recording of barium isotopes in foraminifera from different species; and (4) the application of boron-derived CO_2 to periods beyond the ice core.

5.2.1 Automation of boron purification for foraminifera

The foraminifera data presented in Appendix A records a positive isotopic fractionation when processed with the prepFAST-MC relative to gravity columns (Figure A1 and A2). This is interpreted to reflect the influence of the extra load of organics when more carbonate is dissolved (as is the case for low B/Ca foraminifera such as *G. bulloides*). A direction to take is to first test, that extra organic matter compromises column chemistry by measuring a foraminifera sample that is organic free. One way to do that is by UV treatment on a cleaned and dissolved foraminifera sample as UV has been shown to degrade organic matter (Wang et al., 2006). If that method proves successful, it can be an added step in the cleaning protocol for organic rich samples. An alternative is to define a threshold of carbonate loaded above which we start observing fractionation and load columns with minimal carbonate insuring the B content is sufficient for measurement on MC-ICPMS.

5.2.2 Boron- derived CO_2 during lukewarm interglacial

The number of boron-derived CO_2 records covering the luke warm interglacials (500 to 800 ka) is currently minimal, with only a handful of data during MIS 15 and 17 in Hönisch et al. (2009) and no published data at MIS 13. In order to decipher between the dynamics of luke warm interglacials and/or monsoon-related perturbations in air-sea CO_2 disequilibrium, a focus on generating boron-derived CO_2 during these intervals will help to further test the boron isotope proxy against the ice-

core CO_2 record. Furthermore, this will also help investigate the potential link between reduced nutrients in high latitudes during luke-warms and foraminifera migration in the low latitudes.

5.2.3 Barium isotopes in foraminifera

An obvious direction for future investigation that comes out of this study (chapter 4) is the need to qualify the species-specific fractionation in $\delta^{138}Ba$. This can be done by performing culture studies of foraminifera in varying $\delta^{138}Ba$ composition of seawater and akin to strontium (Stevenson et al., 2014) calcium (Gussone et al., 2006) and magnesium (Ra et al., 2010) isotopes in calcifiers, by evaluating the effect of temperature (and other variables) on fractionation. An emphasis on spinose foraminifera is preferable given the potential of the non-spinose species to inhabit marine snow (Fehrenbacher et al., 2018). Secondly, an alternative avenue would be to fully explore the potential of the barium isotope proxy in foraminifera as a paleoproductivity proxy. For this data are needed from open water planktonic foraminifera in stratified environments to avoid the input of upwelling barium isotopic signal.

5.2.4 The Pliocene warm period

The boron isotopic composition of foraminifera is one of the most promising pH and hence CO_2 proxies, therefore its use in periods beyond the ice core record period (0-800 ky) is of great interest and use in understanding the evolution of CO_2 on long-term and/or orbital time scales. Of particular interest is the Pliocene, a period of warm temperatures and atmospheric CO_2 with current estimates ranging 290-450 ppm (Martínez-Botí et al., 2015) making this period a potential analogue to predicted near-future CO_2 estimates. Of particular importance is the PRISM (Pliocene Research Interpretation and Synoptic Mapping) interval (~3.3-3.05Ma) subsequent to the M2 glaciation occurs as a warming within a warm-world (Haywood et al., 2016).

As a preliminary study, I have recently generated boron isotope data from *G. ruber ss* over that period 3.35-3.15 Ma (MG1 to KM3) at a 3ky resolution (Figure 5.1). These data show atmospheric CO_2 averaging around 369 ppm during KM5c (the PlioMIP window) and exhibiting coherent orbital cycles of around 100 ppm. Furthermore, although the M2 glaciation is characterised by a significant decrease in $\delta^{18}O$ (-0.6‰), the CO_2 is apparently significantly delayed (CO_2-$\delta^{18}O$ lag ~ 30 ky) relatively to the decrease in $\delta^{18}O$. This either implies chronological issues or some unexpected drivers of CO_2 variation. Unfortunately, the $\delta^{11}B$ data during the M2 interval exhibit poor reproducibility and requires repeating to confirm or refute the existence of this lead-lag relationship. These data however nicely illustrate the potential of the $\delta^{11}B$-CO_2 proxy to generate orbital scale records of CO_2 way beyond the reach of the Antarctic ice cores.

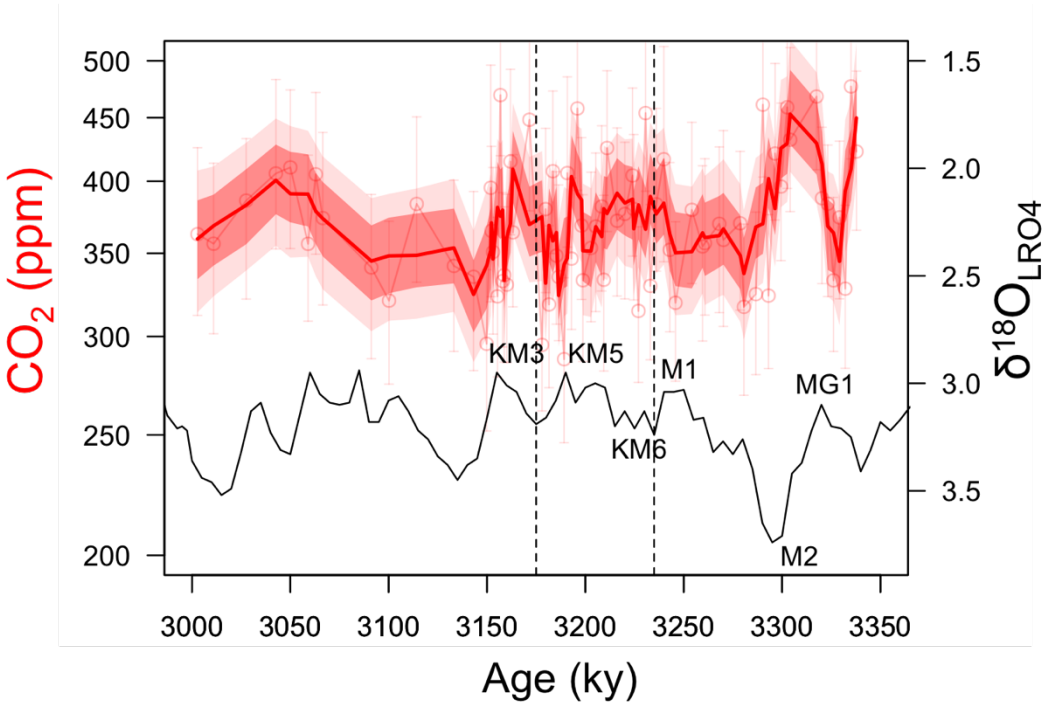

Figure 5.1 Boron-derived CO_2 over the MG1 to KM3 (red) and LR04 $\delta^{18}O$ stack (black, Lisiecki and Raymo, 2004). CO_2 is calculated from $\delta^{11}B$ data on *G. ruber ss* white at ODP site 999. A constant modern alkalinity was used a second carbonate parameter. The CO_2 shows a lag of 30 ky relatively to $\delta^{18}O$ during the MG1 to M1 interval.

Appendix A **Automated boron purification for foraminifera**

Two species of foraminifera *Glogerinoides ruber* and *Globigerina bulloides* have been processed on the prepFAST and by gravity column. The data shows a systematic $\delta^{11}B$ offset with the prepFAST automated method by +0.24± 0.28 ‰ 2sd, for *G. ruber* (Figure A1) and 0.53 ± 0.25 ‰, 2sd for *G. bulloides* (Figure A2). Due to the different B/Ca ratio of each species, different amount of carbonate was picked and loaded onto the column to reach a target of ~ 20 ng of boron, with 2 and 4 mg of picked foraminifera loaded for *G. ruber* ang *G. bulloides* respectively. This illustrated by an anticorrelation between $\delta^{11}B$ offset between the two methods and B/Ca (Figure A3).

This amount of foraminifera loaded can be estimated at 1.5 and 3.8 mg of pure calcite when accounting for material loss during cleaning (~30 %), which is within the range of matrix addition tested (Figure 2.5, Chap 2) for *G. ruber* but above for *G. bulloides*. Hence the offset observed are unlikely to be attributable to excess matrix. Instead the excess amount of organics loaded may contribute to the observed fractionation. Indeed, despite an oxidative step conducted on all samples, some organics can remain within the carbonate lattice and not be in contact with the oxidative mixture. The presence of organics seems to interact with the binding boron sites on the resin and induce a positive fractionation. This hypothesis remains to be tested by removing organic on organic rich sample (e.g. UV treatment, Wang et al., 2006).

The reason why the gravity columns don't seem to be impacted by excess organics may be due, in a similar fashion to the matrix wash out on the prepFAST, to the geometry of the column. With the inline laminar and compact resin on the prepFAST, the evacuation of organics may be less efficient. This is consistent with the less efficient matrix removal observed on the prepFAST (Table 2.4).

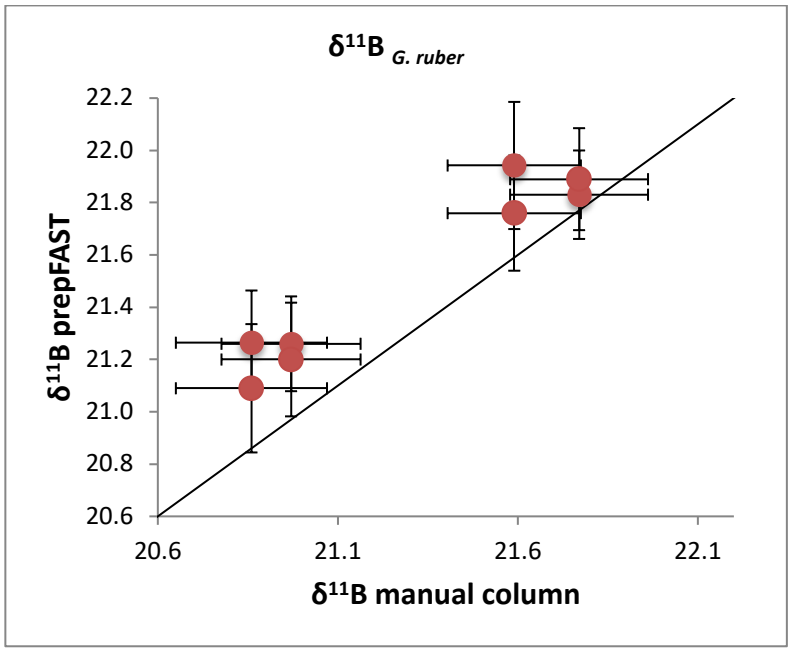

Figure A1. Cross plot of $\delta^{11}B$ processed with the prepFAST and gravity column for the foraminifera species G. ruber sensu stricto white (B/Ca ~ 100 µmol/mol), showing an offset of +0.24± 0.28 ‰, on average for data generated with the prepFAST method.

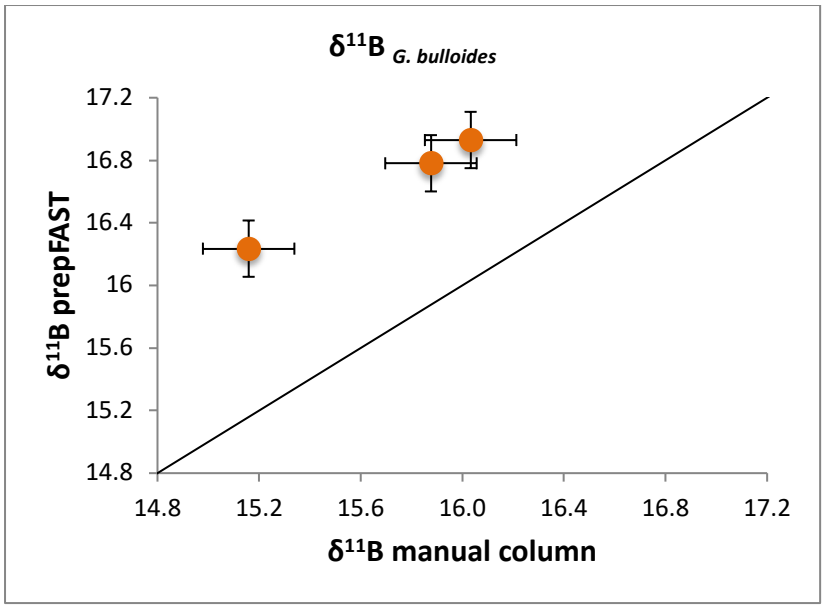

Figure A2. Cross plot of $\delta^{11}B$ processed with the prepFAST and gravity column for the foraminifera species G. bulloides (B/Ca ~ 50 µmol/mol), showing an offset of +0.53 ± 0.25 ‰, on average for data generated with the prepFAST method.

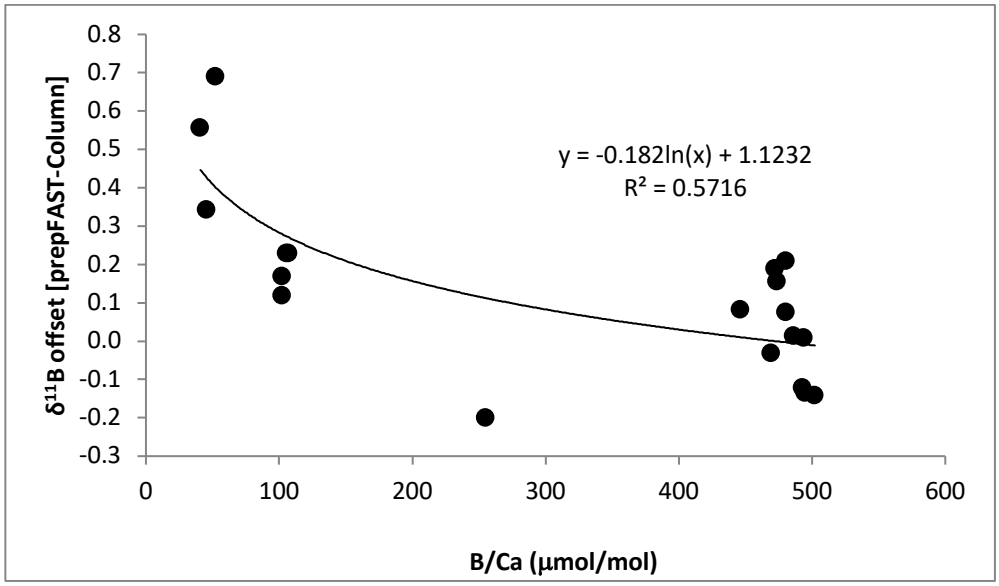

Figure A3. $\delta^{11}B$ offset (prepFAST-gravity column) as a function of B/Ca showing increased offset with smaller B/Ca (equivalent to more $CaCO_3$ loaded to maintain sufficient boron for analysis).

Appendix B **Supplementary information for chapter 3**

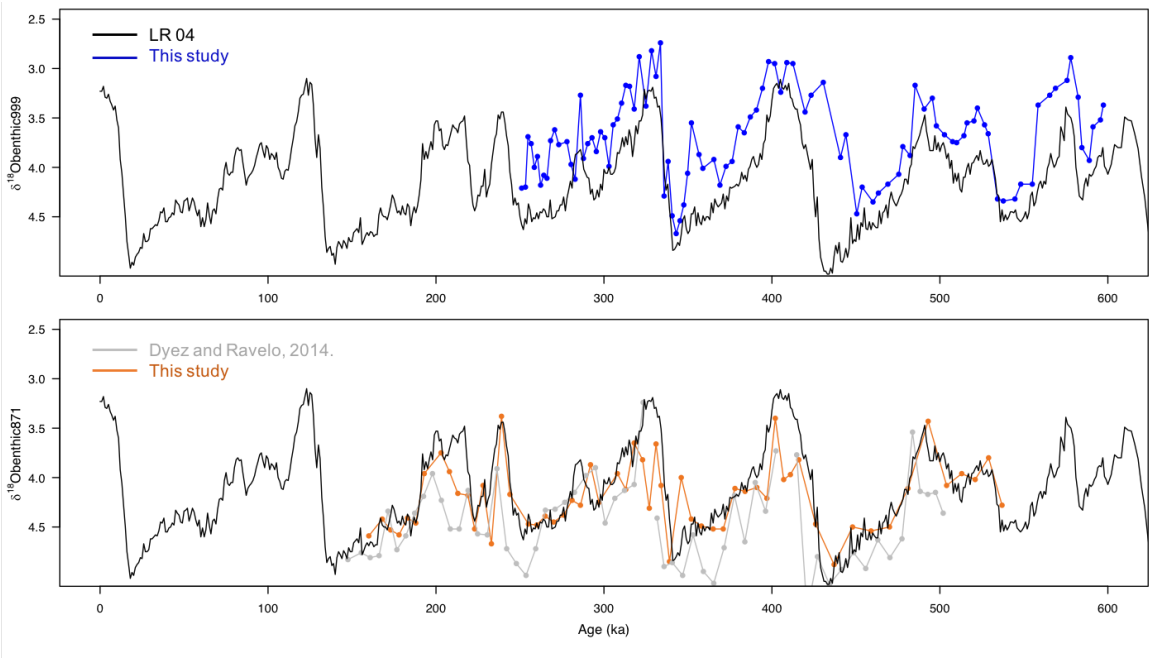

Figure B1. Age model for ODP 999 (top, blue line) and ODP 871 (bottom) based on measurement of $\delta^{18}O$ on *Cibicidoided wuellerstorfi* orbitally tuned to the LR04 benthic stack (Lisiecki and Raymo, 2004) using Analyseries software. A correction of +0.48‰ was applied to our data for comparison with LR04 that is normalised to *Uveregina pergerina*.

ID	Leg	Site	H	Cor	T	Sc	Top(cm)	Bot(cm)	Depth(mbsf)	$\delta^{18}O$ (DR)	**Age (DR)**	$\delta^{18}O$ **(this study)**	**Age (this study)**
EV1	144	871	B	1	H	2	3	5	1.53	4.35	147.56	4.11	**160**
EV2	144	871	B	1	H	2	9	11	1.59	4.28	155.51	3.94	**168**
EV3	144	871	B	1	H	2	15	17	1.65	4.33	160.81	4.05	**173**
EV4	144	871	B	1	H	2	21	23	1.71	4.31	166.11	4.10	**178**
EV5	144	871	B	1	H	2	27	29	1.77	3.86	171.41	3.93	**183**
EV6	144	871	B	1	H	2	33	35	1.83	4.25	176.71	3.98	**188**
EV7	144	871	B	1	H	2	39	41	1.89	4.11	182	3.48	**193**
EV8	144	871	B	1	H	2	45	47	1.95	3.88	187.3	NA	**198**
EV9	144	871	B	1	H	2	51	53	2.01	3.71	192.6	3.27	**203**
EV10	144	871	B	1	H	2	57	59	2.07	3.48	197.9	3.46	**208**

EV11	144	871	B	1	H	2	63	65	2.13	3.75	203.2	3.68	**213**
EV12	144	871	B	1	H	2	69	71	2.19	4.04	208.5	3.70	**219**
EV13	144	871	B	1	H	2	75	77	2.25	4.04	213.8	4.04	**223**
EV14	144	871	B	1	H	2	81	83	2.31	3.65	219.1	3.60	**228**
EV15	144	871	B	1	H	2	87	89	2.37	4.09	224.78	4.19	**233**
EV16	144	871	B	1	H	2	93	95	2.43	4.1	230.55	2.90	**239**
EV17	144	871	B	1	H	2	99	101	2.49	3.43	236.31	3.69	**244**
EV18	144	871	B	1	H	2	105	107	2.55	4.24	242.08	NA	**250**
EV19	144	871	B	1	H	2	111	113	2.61	4.39	247.84	3.99	**255**
EV20	144	871	B	1	H	2	117	119	2.67	4.51	253.61	4.00	**260**
EV21	144	871	B	1	H	2	123	125	2.73	4.24	259.37	3.91	**265**
EV22	144	871	B	1	H	2	129	131	2.79	3.85	265.14	3.97	**270**
EV23	144	871	B	1	H	2	135	137	2.85	3.84	270.91	3.90	**276**
EV24	144	871	B	1	H	2	141	143	2.91	3.77	276.67	3.75	**281**
EV25	144	871	B	1	H	2	146	148	2.96	3.67	282.44	3.80	**286**
EV26	144	871	B	1	H	3	4	6	3.04	3.5	289.16	3.39	**292**
EV27	144	871	B	1	H	3	10	12	3.1	3.42	294.93	3.77	**297**
EV28	144	871	B	1	H	3	16	18	3.16	3.98	300.69	NA	**303**
EV29	144	871	B	1	H	3	22	24	3.22	3.73	306.46	3.48	**308**
EV30	144	871	B	1	H	3	28	30	3.28	3.65	312.23	3.64	**313**
EV31	144	871	B	1	H	3	34	36	3.34	3.59	317.99	3.17	**318**
EV32	144	871	B	1	H	3	40	42	3.4	2.76	323.29	3.34	**323**
EV33	144	871	B	1	H	3	46	48	3.46		327.46	3.83	**327**
EV34	144	871	B	1	H	3	52	54	3.52	3.93	331.62	3.18	**331**
EV35	144	871	B	1	H	3	58	60	3.58	4.42	335.79	3.60	**334**
EV36	144	871	B	1	H	3	64	66	3.64	4.38	340.67	4.37	**339**
EV37	144	871	B	1	H	3	70	72	3.7	4.51	346.84	3.52	**346**
EV38	144	871	B	1	H	3	76	78	3.76	4.1	353.01	3.94	**352**
EV39	144	871	B	1	H	3	82	84	3.82	4.47	359.19	4.01	**358**
EV40	144	871	B	1	H	3	88	90	3.88	4.59	365.36	4.04	**365**
EV41	144	871	B	1	H	3	94	96	3.94	4.23	371.53	4.04	**371**
EV42	144	871	B	1	H	3	100	102	4	3.7	377.71	3.63	**378**
EV43	144	871	B	1	H	3	106	108	4.06	4.17	383.88	3.66	**384**
EV44	144	871	B	1	H	3	112	114	4.12	3.57	390.05	3.62	**391**
EV45	144	871	B	1	H	3	118	120	4.18	3.86	396.23	3.73	**397**
EV46	144	871	B	1	H	3	124	126	4.24	3.25	402.4	2.92	**402**
EV47	144	871	B	1	H	3	130	132	4.3		408.57	3.54	**407**

EV48	144	871	B	1	H	3	136	138	4.36	3.29	414.75	3.49	**411**
EV49	144	871	B	1	H	3	142	144	4.42	4.89	420.92	3.34	**416**
EV50	144	871	B	1	H	3	148	150	4.48	4.32	427.09	NA	**421**
EV51	144	871	B	1	H	4	4	6	4.54	4.6	434.24	3.99	**426**
EV52	144	871	B	1	H	4	10	12	4.6	4.45	441.44	4.40	**437**
EV53	144	871	B	1	H	4	16	18	4.66	4.28	448.64	4.02	**448**
EV54	144	871	B	1	H	4	22	24	4.72	4.44	455.84	4.06	**459**
EV55	144	871	B	1	H	4	28	30	4.78	4.15	463.04	4.02	**470**
EV56	144	871	B	1	H	4	34	36	4.84	4.33	470.24	3.63	**481**
EV57	144	871	B	1	H	4	40	42	4.9	4.14	477.45	2.95	**493**
EV58	144	871	B	1	H	4	46	48	4.96	3.06	483.7	3.60	**504**
EV59	144	871	B	1	H	4	52	54	5.02	3.66	488.26	3.48	**513**
EV60	144	871	B	1	H	4	58	60	5.14	3.69	492.82	3.54	**521**
EV61	144	871	B	1	H	4	64	66	5.2	3.67	497.38	3.32	**529**
EV62	144	871	B	1	H	4	70	72	ND	3.88	501.95	3.80	**537**

Table B1. Age model determined from $\delta^{18}O$ tuning to LR04 stack. DR stands for Dyez and Ravelo (2013)

Appendix C **The particular case of MIS 13**

Extending the records discussed in the previous sections to cover MIS13 (i.e. from 470-550ky) has revealed a dramatic increase in the scale of the discrepancy between ice core CO_2 and that determined by $\delta^{11}B$. What follows is a presentation of these results and a discussion of their potential causes. A full understanding of these data however is beyond the scope of this study and is the subject of ongoing work at Southampton. Data from *G. ruber ss*, *sl* and *T. sacculifer* are presented and cover MIS 12, 13 and 14.

C.1 Results

C.1.1 $\delta^{11}B$-derived CO_2 from *G. ruber* during MIS 13

The Mg/Ca-derived temperatures in *G. ruber ss* during MIS 13 show colder temperatures for both site 999 and 871 compared with subsequent fully-developed interglacials and the temperatures at site 871 show levels similar to subsequent glacials. The temperature recorded by *G. ruber sl* at site 871 show colder temperature than *G. ruber ss* by 1 to 2°C (Figure C1-a and e). The percentage fragment and sand fraction during MIS 13 show similar value than other interglacials at site 871. The sand fraction at site 999 shows a maximum at MIS 13 (40 %) similar to MIS 9. (Figure C1-b and f). The benthic $\delta^{13}C$ are shown in Figure C1-d and h and show a maximum in $\delta^{13}C$ during MIS 13 (+0.3‰ relatively to other interglacials).

The CO_2 estimates at ODP Site 871 and Site 999 based on $\delta^{11}B_{G.ruber\ ss}$ during the lukewarm interglacial MIS 13 show an overestimation of CO_2 at both sites (Figure C2) up to ~420 ppm at ODP 871 (+170 ppm overestimation) and 350 ppm at ODP 999 (+100 ppm overestimation). These offsets are repeatable which gives confidence in the reality of the signal and makes an unknown laboratory bias unlikely. The estimates of CO_2 from $\delta^{11}B_{G.ruber\ sl}$ at ODP 871 show a better agreement with ice core CO_2, although these are of lower resolution and are a less complete dataset.

Figure C3 shows boron-derived CO_2 calculated at site 999 compared with preliminary data of benthic B/Ca measured in *C. wuellestorfi*. B/Ca shows lower value by 50 µmol/mol during MIS 13.

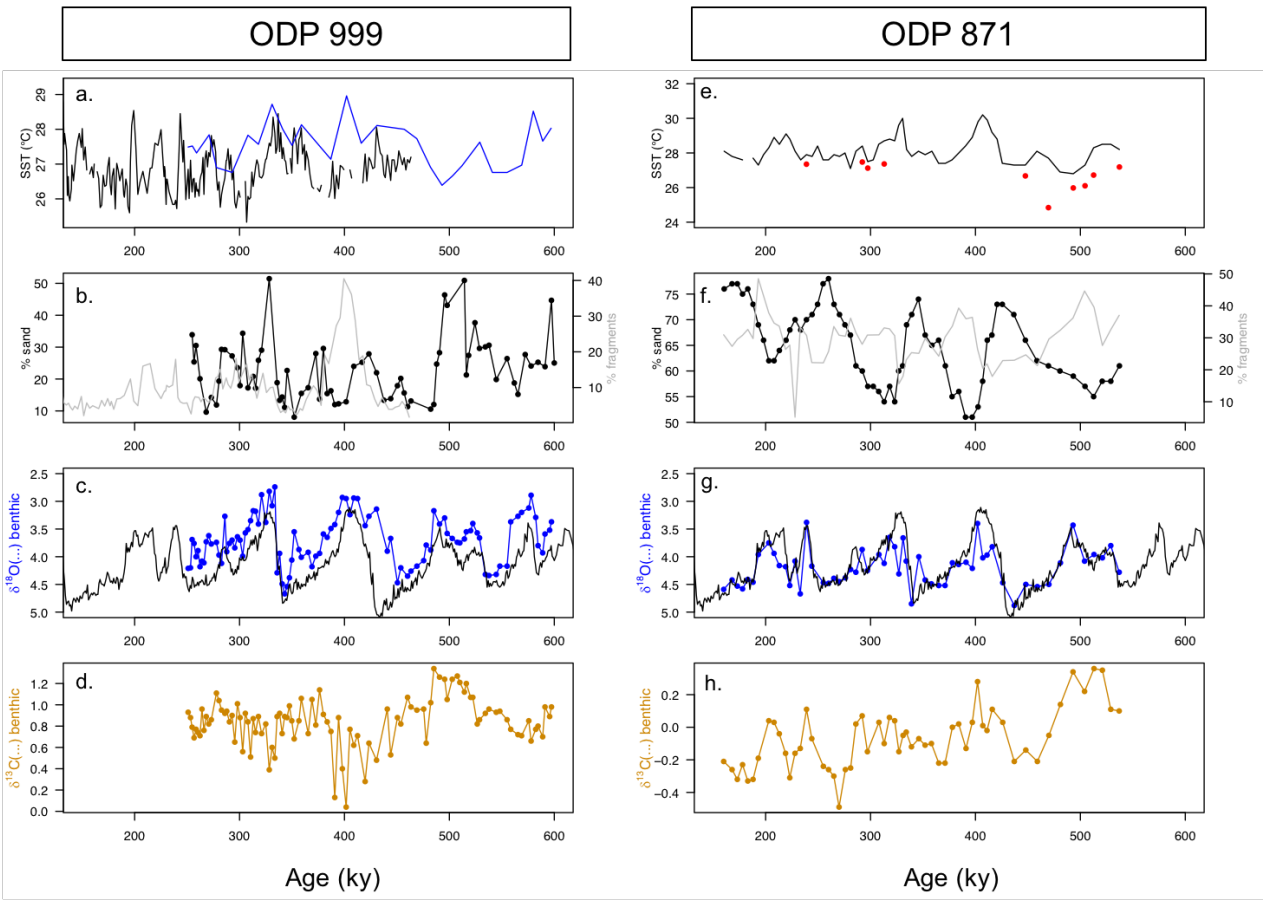

Fig C1 .Mg/Ca derived temperature, coarse fraction (sand), fragmentation and benthic $\delta^{18}O$ and $\delta^{13}C$. **a,e**. Temperature at ODP 999 (from *G. ruber ss*, black, Schmidt et al., 2006; blue this study) and ODP 871 (*G. ruber ss*, black, *G.ruber sl*, red). **b,f**. percentage fragments (light grey, data from Schmidt et al. (2006) for ODP 999) and sand (black line). **c,g**. Benthic *C. wuellestorfi* $\delta^{18}O$ (blue) and LR04 benthic $\delta^{18}O$ stack (black). A correction of +0.48‰ is applied to our $\delta^{18}O$ data in order to correct for species offset between *C. wuellestorfi* and *U. peregrina* when comparing to LR04. **d,f.** Benthic *C. wuellestorfi* $\delta^{13}C$ (orange).

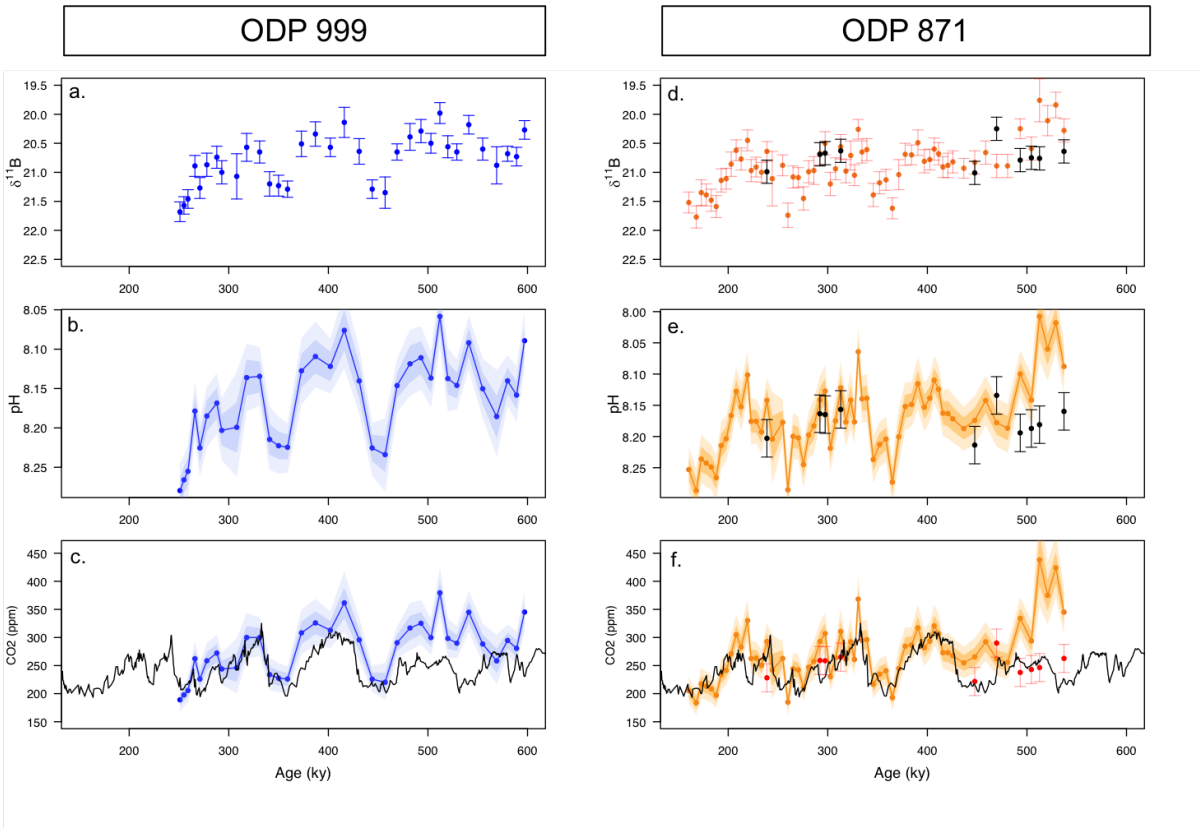

Fig C2. $\delta^{11}B$, pH and $\delta^{11}B$ -derived CO_2 for ODP 999 and 871. **a,d.** $\delta^{11}B$ measured on *G. ruber ss* (blue, ODP 999, and orange, ODP 871) and *G. ruber sl* (black, ODP 871). **b,e**. Calculated pH. Colour scheme identical to panels a and d. **c,f**. $\delta^{11}B$-derived CO_2 reconstructions at ODP 999 (left panels, blue) and ODP 871 (right panels, orange *G. ruber ss* and red *G. ruber sl*) compared with ice core CO_2 (EPICA record, black). Periods of significant CO_2 anomaly covers MIS 13 and MIS 14 (470-550 ky).

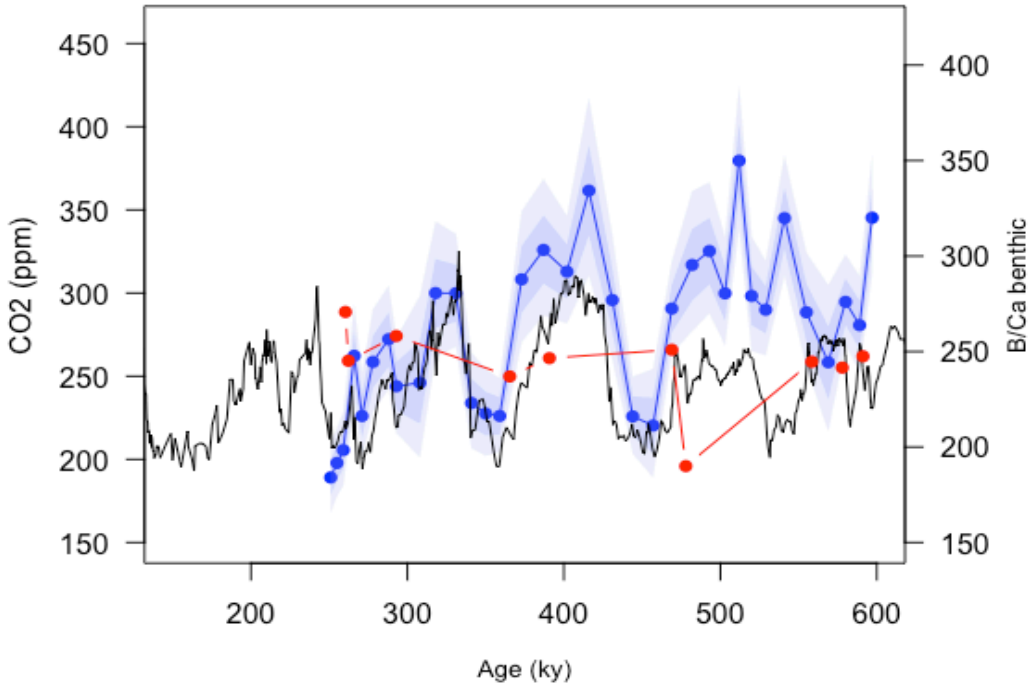

Figure C3. Boron-derived CO_2 at site 999 (blue) and ice core CO_2 (black) compared with benthic B/Ca (µmol/mol) measured on *C. wuellestorfi* (red).

C.1.2 δ^{11}B-derived CO_2 from *T. sacculifer* during MIS 13

The boron derived-CO_2 for the species *T. sacculifer* at ODP site 871 (size fraction 500-600 µm) have been calculated using the δ^{11}B borate-calcite calibration of Martinez-Boti et al. (2015). All other inputs for CO_2 calculation are identical to the methods used for *G. ruber* at ODP 871 (chapter 3 section 3.2.5). The calculated CO_2 show a similar offset to the ice core record than *G. ruber ss* with an overestimation of +50 ppm during MIS 13/14 and +100 ppm during MIS 12 (Figure C4).

Other intervals show poor CO_2 reconstructions with significant overestimation of CO_2 during MIS 8 (+100-150 ppm at 260-300 ky) whereas *G. ruber* show a good agreement (Figure C2).

The Mg/Ca derived temperatures show that *T. sacculifer* record a similar range than *G. ruber ss* with a systematic warmer signal (~+1°C) during MIS 13 and 14.

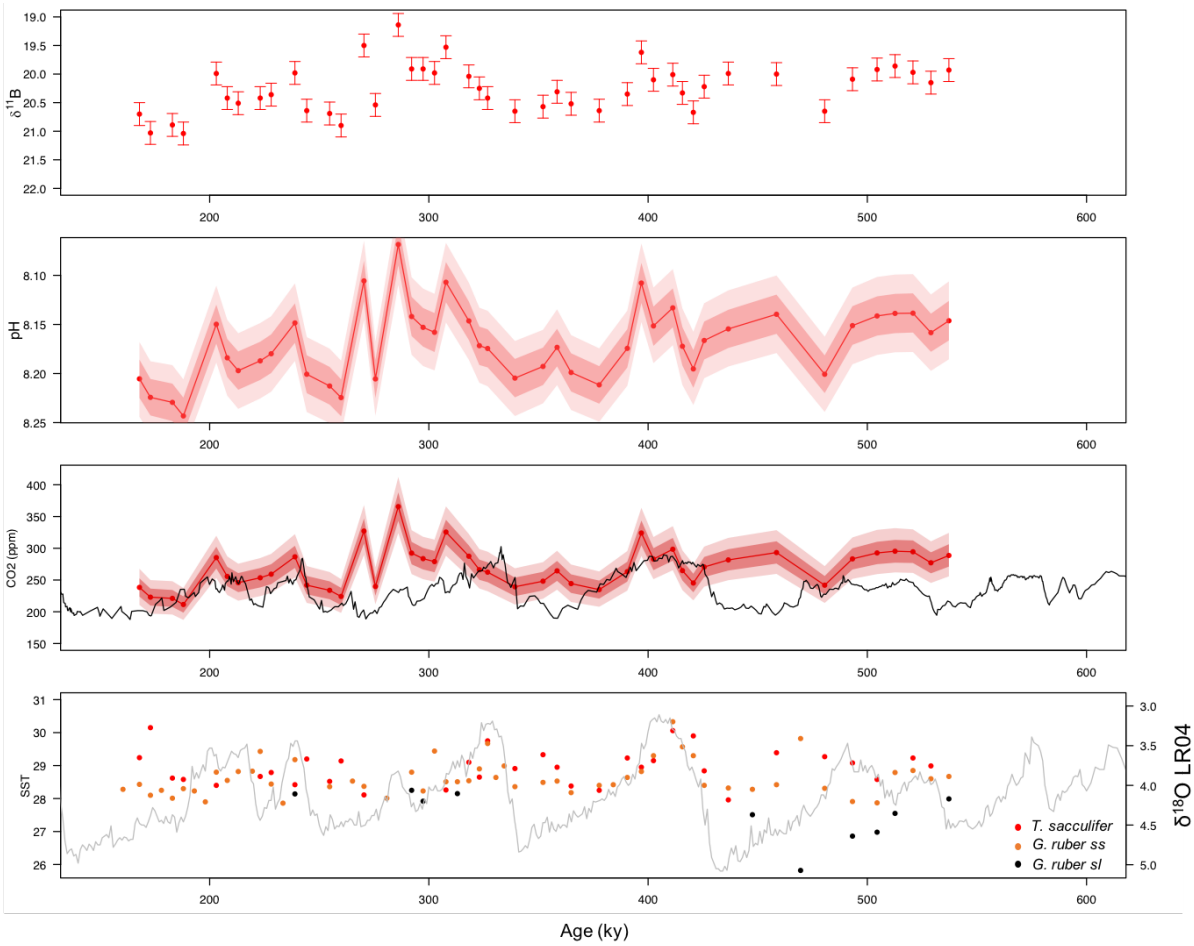

Figure C4. Boron isotopic composition, pH and boron derived CO_2 from the species *T. sacculifer*. Mg/Ca-derived temperatures are plotted for *T. sacculifer*, *G. ruber ss* and *G. ruber sl.*

C.1.3 Anomalies in $\delta^{13}C$, $\delta^{18}O$ *and SST at MIS13.*

As mentioned above, the benthic $\delta^{13}C$ record (Figure C1) shows a clear cyclicity with a range of 0.2 to 1‰ and -0.4 to 0.1‰ post MIS13 at ODP 999 and 871 respectively, and reaches a maximum at MIS 13 with 1.3‰ at ODP 999 and 0.4‰ at ODP 871. This $\delta^{13}C$ maxima is also present in most other benthic record throughout the global ocean (e.g. Wang et al., 2004; Lisiecki, 2014 and references therein) and is sometimes referred as $\delta^{13}C$max-II (Wang et al., 2004).

Planktonic $\delta^{18}O$ and $\delta^{13}C$ at ODP 871 show a visible cyclicity following glacial cycles, however MIS 13 is apparently associated with a missed cycle with levels of $\delta^{18}O$ as high as subsequent glacial (Figure C5-b, blue shade). This evolution is similar for both morphotypes of *G. ruber.* This missed cyclicity is not as visible in the $\delta^{13}C$ record and this shows a maximum similar to other interglacials. However, it may not reflect a surface signal and is likely to be overprinted by the $\delta^{13}C$ maximum observed globally.

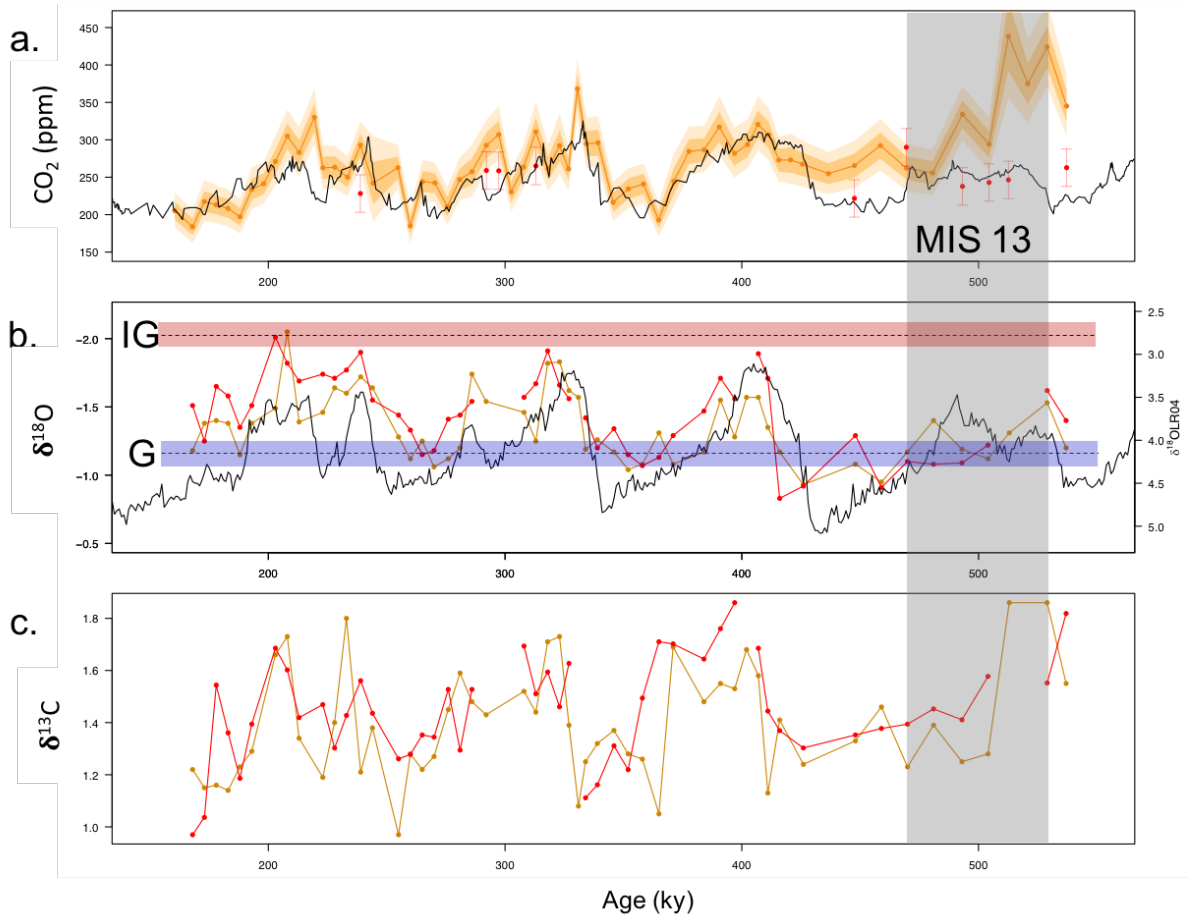

Figure C5. Comparison of CO_2 at ODP 871 (δ^{11}B-derived CO_2 in orange ; EPICA ice-core CO_2 in black) with C and O isotopes of *G. ruber ss* (orange) and *sl* (red). The benthic δ^{18}O stack LR04 is plotted for reference in panel b (black line).

C.2 Discussion

C.2.1 Global anomaly in ocean δ^{13}C

The maximum in δ^{13}C centred at 500 ky (hereafter δ^{13}Cmax-II following Wang et al. 2004) is global and has remained an enigma for decades. The cyclicity of δ^{13}C has followed long-eccentricity 400-500 ky cycles during most of the Pleistocene (with δ^{13}C maxima occurring during eccentricity minima), but this phasing appears disturbed during the late Pleistocene. Indeed, the last eccentricity minima occurred at 0 and 400 kyr and was unaccompanied by a δ^{13}C maximum.

δ^{13}Cmax-II is also concomitant with other anomalies around the global such as (1) low levels of productivity in the Antarctic Zone of the Southern Ocean as shown by the almost complete absence of Ba/Fe signal, (Jaccard et al., 2013), (2) high rainfall/run-off is recorded in several locations of the globe such as showed by high intensity of Asian summer monsoon in China (Yin and Guo, 2008;

Guo et al., 2009), high terrigenous input in the Indian ocean (Bassinot et al., 1994b) and the Amazon basin (Harris et al., 1997) and Asia (Prokopenko et al., 2002), and sapropel layers in the Mediterranean (Rossignol-Strick et al., 1998).

Several hypotheses have been invoked to explain the variations in $\delta^{13}C$. Modelling studies suggest a change in burial fluxes of organic and inorganic carbon (Hoogakker et al., 2006). An alternative hypothesis of "dissolved organic carbon" has been proposed by Ma et al. (2017), involving the microbial carbon pump (MCP) producing refractory dissolved organic carbon (RDOC). In this hypothesis, minima eccentricity is associated with weak chemical weathering, produces a nutrient depleted state in the oceans. Under these conditions a background slow carbon cycle is predominant and the carbon pump is dominated by the MCP (in opposition to a heterotroph biological pump under nutrient rich conditions). Since the MCP produces more RDOC with a light $\delta^{13}C$, the DIC pool becomes enriched in ^{13}C and $\delta^{13}C$ increased. Whilst this hypothesis may be convincing when $\delta^{13}C$ and long-eccentricity are in phase (early Pleistocene), the dephasing that happened during the late Pleistocene including MIS 13 is at odds with this mechanism. Furthermore, the enhanced monsoon and continental run-off increases the nutrient inventory in the ocean which is opposite to this expressed MCP scenario.

Barth et al. (2018) suggested that the maxima in $\delta^{13}C$ could be caused by the enhanced growth of vegetation on land. This would have been caused by the unusually warm previous glacial (MIS 14). Indeed MIS 14 was associated with reduced ice-sheet (Elderfield et al., 2012; Shakun et al., 2015) which would have favoured the growth of vegetation on land that is further developed thanks to increased humidity during MIS 13. The stored pool of ^{12}C needed for terrestrial plants would have increased the $\delta^{13}C$ of oceanic basins. If the $\delta^{13}C$max-II anomaly and this scenario were directly linked to our overestimation in CO_2 at ODP 871 and ODP 999, we would expect a mechanism that increases atmospheric CO_2. However, if the hypothesis of stored vegetation on land during MIS 13 is true, this acts as a sink of carbon. We therefore conclude the $\delta^{13}C$ anomaly is not directly linked to our boron-derived CO_2 anomaly, rather it is simply coincident with it.

C.2.2 Upwelling and anomaly in Monsoon activity at MIS13.

As mentioned above, MIS 13 (as well as MIS 14) is also linked to high intensity of Asian summer monsoon in China (Yin and Guo, 2008; Barth et al., 2018). Since ODP 871 is located relatively close to an area of air-sea CO_2 disequilibrium (Figure 3.2), it is plausible that variations in disequilibrium at the core site could be linked to change in monsoon intensity. The $\delta^{18}O$ of both *G. ruber ss* and *sl* show that MIS 13, unlike subsequent interglacials is not associated with a minimum (Figure C5-b). This is consistent with the decrease in temperature observed from Mg/Ca in both *G. ruber ss* and *sl* that suggests either the upwelling of deep colder waters or the migration of foraminifera into a deeper

environment. In both cases we'd expect lighter $\delta^{13}C$ but the $\delta^{13}C$ of *G. ruber* doesn't show a clear decrease (Figure C5-c), although this is likely due to overprinting of global $\delta^{13}C$max-II.

In contrast to *G. ruber ss*, the $\delta^{11}B$-derived CO_2 of *G. ruber sl* is in good agreement with the ice core CO_2 (Figure C2-f). Taken at face value this would imply a water column structure with less acidic waters at depth (as suggested by the lower SST from *G. ruber sl*) or a very different response of this morphotypes to change in ambient water conditions.

Nevertheless, an increase in upwelling at both sites, or species migration are plausible scenarios to explain the observed anomalies in temperature, $\delta^{18}O$ and $\delta^{11}B$.

A link between monsoon intensity and walker circulation has been shown by some studies (Wu et al., 2003) and it has been demonstrated that El Niño like conditions are associated to small East-West temperature gradients in the Pacific and weak East Asian summer monsoon (EASM) (Yu et al. 2016). On the contrary La Niña-like conditions are linked to high East-West temperature gradients and increased EASM. Zonal SST reconstructions have been made across the Pacific (De Garidel-Thoron et al., 2005; McClymont and Rosell-Melé, 2005; Dyez and Ravelo, 2014) and show that the West equatorial Pacific is indeed associated with increased zonal SST when compared to the East Pacific during MIS 13 (De Garidel-Thoron et al., 2005). The monsoon record of Yu et al. (2016) (Figure C6) based on clay mineral evidence show the strong anomaly in precipitation centred at 500 ky that is broadly synchronous with strong SST gradient that witness La Niña-like conditions.

Based on these observations it is plausible to attribute the overestimation of $\delta^{11}B$-derived CO_2 at ODP 871 to local disequilibrium caused by changes in the dynamic of Walker circulation in the Pacific. Based on the CO_2 disequilibrium map (Figure 3.2) a disequilibrium is likely not to exceed 50 to 100 ppm (dependent on the intensity upwelling). Hence, since some of our data points exceed these values, other mechanism may be at play to explain the full overestimation of CO_2 at site 871.

ODP site 999 may also be impacted by change in disequilibrium during MIS 13. The SST at site 999 indeed shows cold temperatures for an interglacial period (similar than subsequent glaciers, Figure C1-a). It has been shown that the equatorial Atlantic had a strong CO_2 gradient during the last glacial maximum caused by enhanced upwelling in the East Atlantic (Foster and Sexton, 2014). The CO_2-nutrient-rich waters when advected westward did not constitute a source of CO_2 due to the enhanced biological productivity (caused in part by Fe fertilisation) that pumped down CO_2. The mid-state luke-warm interglacial during MIS 13 was presumably associated with more upwelling than during fully developped interglacials due to stronger east trade winds. Furthermore, there are no Fe fertilisation during MIS 13 (e.g. Barth et al., 2018) which would not be associated to enhanced biological productivity. The combination of upwelling in the East Atlantic and CO_2 rich waters (not consumed) would make the equatorial Atlantic a bigger source of CO_2 than it is in glacial periods and potentially would cause a disequilibrium at site 999 explaining the observed CO_2 anomaly. A record of biological productivity in the East and West equatorial Atlantic during that period would help to validate that hypothesis.

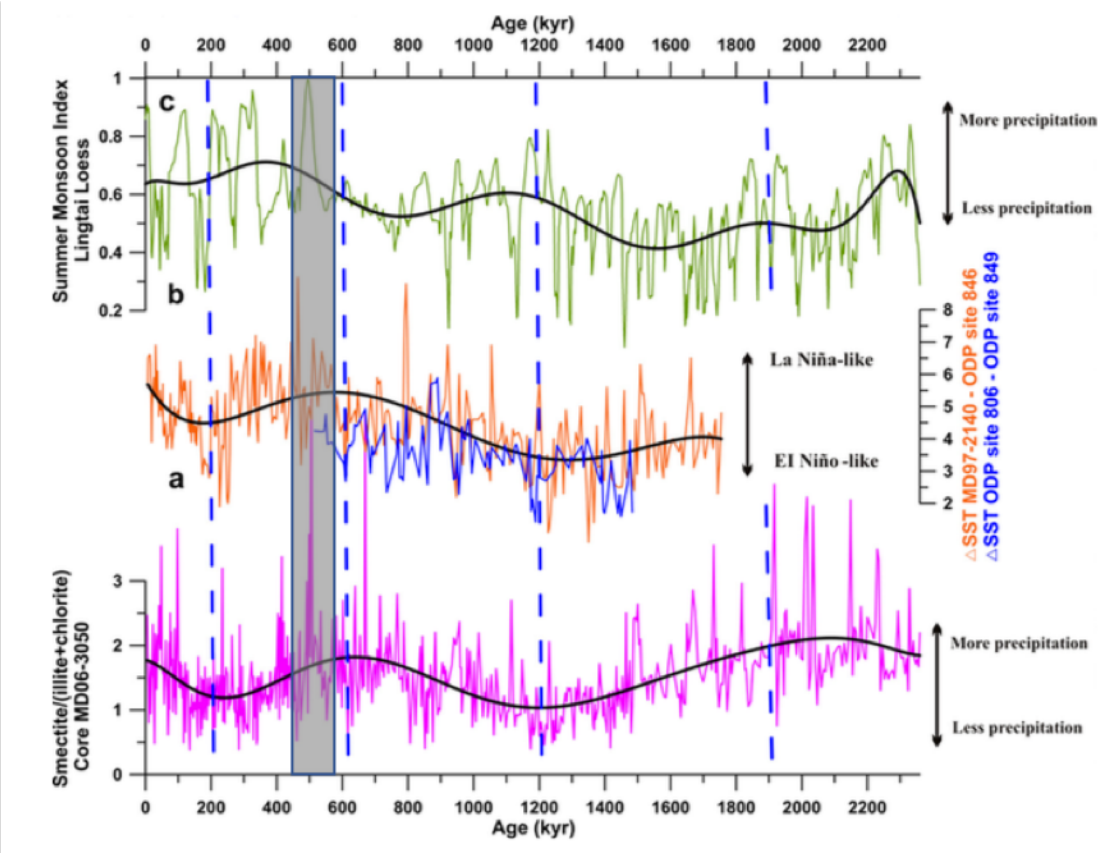

Figure C6. Summer monsoon indicators in East Asia (Yu et al., 2016). Clay minerals ratio (a), compared with equatorial East-West temperature gradient (b) and summer monsoon index from the Loess plateau (c). Grey shade highlights period of increased precipitation and zonal temperature gradients witnessing La-Niña like conditions around MIS 13.

C.2.3 Change in nutrient inventory

Another hypothesis that could explain the $\delta^{11}B$-derived CO_2 anomaly is a change in nutrient inventory that would influence the depth habitat of foraminifera. MIS 13 is the only luke-warm interglacial measured in our record. Luke-warm intervals occur prior to the MBE and differences in global ocean circulation, nutrients and productivity have been reported.

The position in westerlies is located further north during luke-warm interglacials (Kemp et al., 2010) with increased sea-ice in the Southern Ocean (Wolff et al., 2006) and more Antarctic Bottom Water (AABW) formation caused by insolation feedback (Yin, 2013). The Southern Ocean is also associated with a decrease in productivity as recorded by lower levels of Ba/Fe in the polar Antarctic zone relatively to subsequent fully-developed interglacials (Jaccard et al., 2013) and an absence of

productivity during MIS 13. This absence of productivity and associated level of nutrients at the surface presumably caused by extended sea-ice, could have changed the nutrients inventory in the low latitudes when advected from high latitudes via intermediate waters. This scenario combined to more continental run-off under enhanced monsoon could have favoured silica organisms over calcifiers. This is consistent with a record or radiolaria in a nearby core in the West Pacific (ODP 806, Diester-Hass et al., 2018), showing a modest, yet distinctive increase at MIS 13. Under these nutrient conditions, calcifiers like foraminifera could have migrated deeper in the water column in more nutrient rich waters recording more acidic waters and explaining the apparent high CO_2. SST at both ODP site 999 and 871 are colder (with levels comparable to subsequent glacial) and fit with this hypothesis.

The increased monsoon scenario and associated upwelling at ODP 871 (scenario 1) and Southern Ocean nutrient decrease and associated vertical foraminifera migration (scenario 2) are candidates to explain the CO_2 offset during MIS 13. We however note that the previous glacial MIS 14 (540 ky) is also affected by significant $\delta^{11}B$ -derived CO_2 overestimation. MIS 14 is a particular glacial as it is unusually warm and long-lived. It is also associated to single deposits of large monospecific giant diatoms *Ethmodiscus rex* (herafter *E.rex*) in the South Atlantic (e.g. Schmieder et al., 2000). Whilst today, the limitation in silicic acid prevents a significant formation of silica organisms, these particular deposits require a mechanism that supplies silica. Rackebrandt et al. (2011) suggested that these deposits are associated to the particular position of the Agulhas system that would favour silica rich waters from the Indian Ocean to "leak" into the Atlantic. Indeed, the maximum in silica leakage is controlled by the position of the subtropical front and usually occurs at the second half of the glacial terminations but is short lived. The weak and warm MIS 14 interglacials would have put the subtropical front in a position similar to the glacial termination and supplied silicic acid for a long period allowing significant deposits of *E.rex* to form in the Atlantic. The consequence of such silica leakage is similar to scenario 2 where foraminifera at low latitudes would compete with silica organisms and migrate deep in the water column.

C.2.4 Increased corrosiveness

There are suggestions that the Southern Ocean turnover was lower prior to the MBE (Jaccard et al., 2013; Howe and Piotrowski, 2017). Recent reconstructions of water masses during luke-warm interglacials using Nd isotopes (Howe and Piotrowski, 2017) suggest that NADW was stronger yet there are evidence AABW spread further North (but remaining South of the equator) relatively to post-MBE conditions (Yin, 2013; Barth et al., 2018) holding more stored carbon (explaining the lower CO_2 levels during luke-warms). There are also suggestions that AAIW (that unlike AABW impact ODP site 999), was more vigorous during luke-warm interglacials (Howe and Piotrowski, 2017). Whether the Caribbean was impacted by Northern or Southern sources waters during luke-warms remains unclear and requires direct evidence from this area. Benthic B/Ca from ODP 999 (Figure C3) shows an excursion of low B/Ca during MIS 13 which suggests more corrosive southern

water source. This would have altered the $\delta^{11}B$ with partial dissolution producing lighter values and high CO_2 at ODP 999. A higher resolution is however needed to confirm this trend only shown so far by a single data point.

In a similar fashion, ODP 871 could have been impacted by more corrosive AABW and drive lighter $\delta^{11}B$. The water masses in the Pacific sector are less well documented during luke-warm interglacials. However, proxies of preservation and corrosiveness such as shell normalised weight (Qin et al. 2018) and B/Ca (Kerr et al., 2017) show no anomaly during MIS 13. Moreover, our fragment counts record (Figure C1) show no particular high values which doesn't support partial dissolution as being the main cause of CO_2 offset during MIS 13.

C.2.5 CO_2 reconstruction from *T. sacculifer*

Boron-derived CO_2 from *T. sacculifer* at ODP 871 during MIS 12, 13 and 14 also show a disagreement from the ice core, yet with a smaller offset than *G. ruber ss* (+ 50 ppm vs. + 50-100 ppm for *G. ruber ss,* Figure C2 and C4). The Mg/Ca temperatures show a distinct pattern during MIS 13 with warmer temperatures for *T. sacculifer* and colder for G. ruber sl. This is at odd with the $\delta^{11}B$ reported for each of this species that shows increasing acidic environment from *G. ruber sl* to *T. sacculifer* and *G. ruber ss* (Figure C2 and C4).

We note that *T. sacculifer* also exhibits poor CO_2 reconstruction during MIS 8 which is broadly synchronous with a peak in percentage fragments. A higher susceptibility to dissolution for this species is consistent with the leaching experiments conducted on *G. ruber* ss and *T. sacculifer* (Figure 3.3, Chapter 3). However, the other intervals of maxima in fragmentation are not all associated with a CO_2 offset making the $\delta^{11}B$ signal of *T. sacculifer* unclear for interpretation. A full resolution of the record and repeats of $\delta^{11}B$ measurement when off with the ice cores are needed to have a full assessment of boron-derived CO_2 in *T. sacculifer*.

C.3 Conclusion

We show that the dynamics of luke-warm interglacials of MIS 13 and 14 disturb the low latitude $\delta^{11}B$ signal by mostly likely changing the extent of CO_2 disequilibrium. We therefore caution against over interpretation of $\delta^{11}B$ record over these periods and highlight the need to choose core locations that are unlikely to be impacted by change in CO_2 disequilibrium. Further boron isotope studies targeting luke-warm interglacials will help to decipher whether the anomaly we observe is caused by luke-warm interglacial dynamics (change in water masses and nutrients inventory) or are particular to MIS 13 and 14 (associated to strong monsoon). Going forward, we recommend studies follow a multi-site approach but chose sites that are widely distributed and do not share similar oceanographic conditions. Furthermore, we recommend that a wide range of ancillary data is collected (e.g.

$\delta^{18}O/\delta^{13}C$, Mg/Ca) to help interpret and identify any intervals where cold, CO_2-rich water influences an otherwise oligotrophic location.

Appendix D **Supplementary data for Chapter 4**

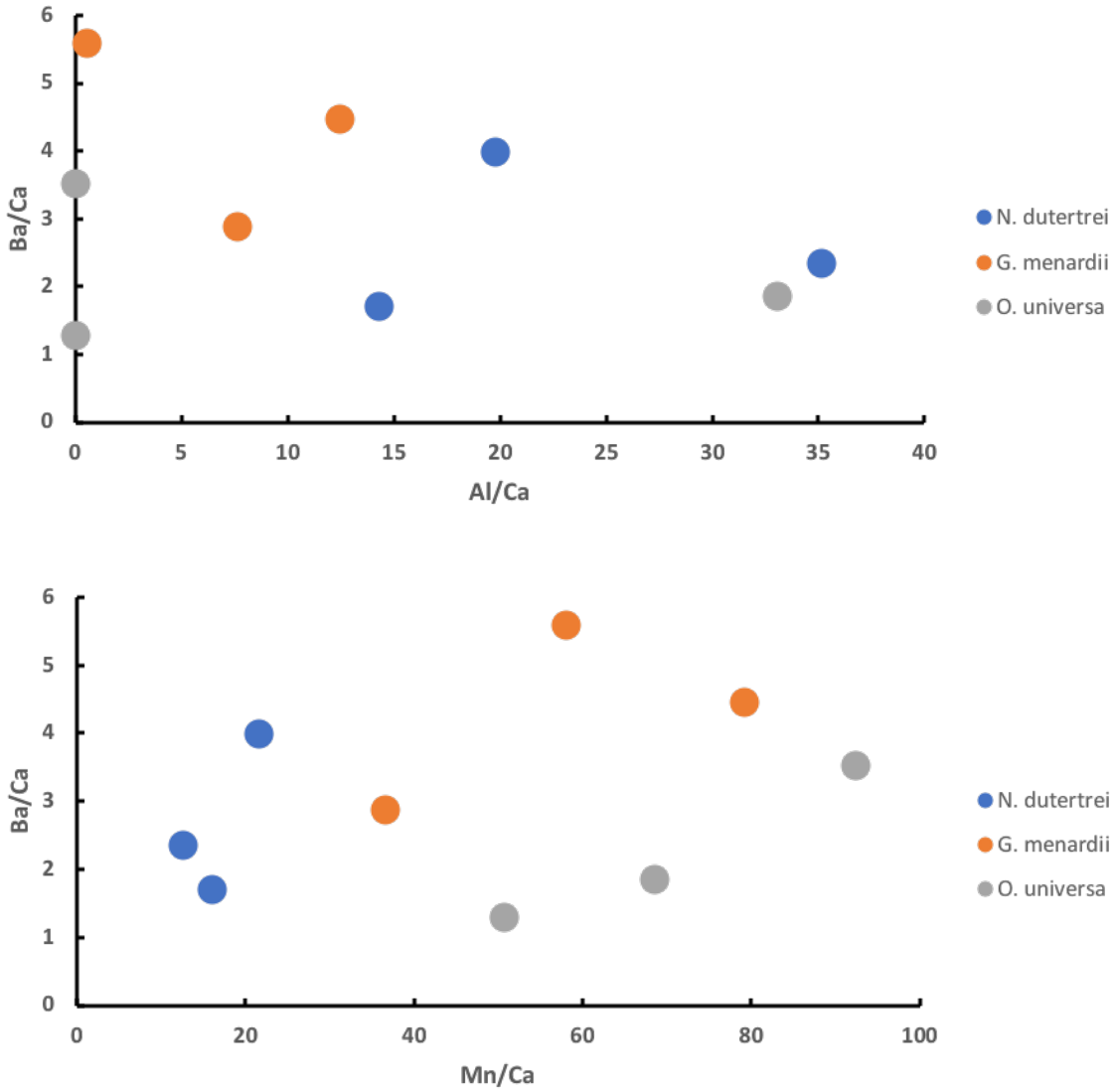

Figure D1. Cross plot of Ba/Ca against Al/Ca and Mn/Ca showing no correlation hence no contamination by clay or metal oxides.

List of References

Alldredge, A.L., 2000. Interstitial dissolved organic carbon (DOC) concentrations within sinking marine aggregates and their potential contribution to carbon flux. Limnology and Oceanography 45, 1245-1253.

Alldredge, A.L., Gotschalk, C., 1988. In situ settling behavior of marine snow1. Limnology and Oceanography 33, 339-351.

Anagnostou, E., John, E.H., Edgar, K.M., Foster, G.L., Ridgwell, A., Inglis, G.N., Pancost, R.D., Lunt, D.J., Pearson, P.N., 2016. Changing atmospheric CO 2 concentration was the primary driver of early Cenozoic climate. Nature 533, 380.

Anand, P., Elderfield, H., Conte, M.H., 2003. Calibration of Mg/Ca thermometry in planktonic foraminifera from a sediment trap time series. Paleoceanography 18.

Anderson, O.R., Spindler, M., Bé, A.W.H., Hemleben, C., 1979. Trophic activity of planktonic foraminifera. Journal of the Marine Biological Association of the United Kingdom 59, 791-799.

Aurahs, R., Treis, Y., Darling, K., Kucera, M., 2011. A revised taxonomic and phylogenetic concept for the planktonic foraminifer species Globigerinoides ruber based on molecular and morphometric evidence. Marine Micropaleontology 79, 1-14.

Badger, M., Chalk, T., Foster, G., Bown, P., Gibbs, S., Sexton, P., Schmidt, D., Palike, H., Mackensen, A., Pancost, R., 2019. Insensitivity of alkenone carbon isotopes to atmospheric CO2 at low to moderate CO2 levels. Climate of the Past.

Badger, M.P., Schmidt, D.N., Mackensen, A., Pancost, R.D., 2013. High-resolution alkenone palaeobarometry indicates relatively stable p CO2 during the Pliocene (3.3–2.8 Ma). Philosophical Transactions of the Royal Society A: Mathematical, Physical and Engineering Sciences 371, 20130094.

Bahr, A., Schönfeld, J., Hoffmann, J., Voigt, S., Aurahs, R., Kucera, M., Flögel, S., Jentzen, A., Gerdes, A., 2013. Comparison of Ba/Ca and δ18OWATER as freshwater proxies: A multi-species core-top study on planktonic foraminifera from the vicinity of the Orinoco River mouth. Earth and Planetary Science Letters 383, 45-57.

Barker, S., Archer, D., Booth, L., Elderfield, H., Henderiks, J., Rickaby, R.E.M., 2006. Globally increased pelagic carbonate production during the Mid-Brunhes dissolution interval and the CO2 paradox of MIS 11. Quaternary Science Reviews 25, 3278-3293.

Barker, S., Greaves, M., Elderfield, H., 2003. A study of cleaning procedures used for foraminiferal Mg/Ca paleothermometry. Geochemistry, Geophysics, Geosystems 4.

BARNETT, T.P., DÜMENIL, L., SCHLESE, U., ROECKNER, E., 1988. The Effect of Eurasian Snow Cover on Global Climate. Science 239, 504-507.

Barth, A.M., Clark, P.U., Bill, N.S., He, F., Pisias, N.G., 2018. Climate evolution across the Mid-Brunhes Transition. Climate of the Past 14, 2071-2087.

Bartoli, G., Hönisch, B., Zeebe, R.E., 2011. Atmospheric CO2 decline during the Pliocene intensification of Northern Hemisphere glaciations. Paleoceanography 26.

Bassinot, F.C., Beaufort, L., Vincent, E., Labeyrie, L.D., Rostek, F., Müller, P.J., Quidelleur, X., Lancelot, Y., 1994. Coarse fraction fluctuations in pelagic carbonate sediments from the tropical Indian Ocean: A 1500-kyr record of carbonate dissolution. Paleoceanography and Paleoclimatology 9, 579-600.

Bates, N.R., Amat, A., Andersson, A.J., 2010. Feedbacks and responses of coral calcification on the Bermuda reef system to seasonal changes in biological processes and ocean acidification. Biogeosciences 7, 2509-2530.

Bates, S.L., Hendry, K.R., Pryer, H.V., Kinsley, C.W., Pyle, K.M., Woodward, E.M.S., Horner, T.J., 2017. Barium isotopes reveal role of ocean circulation on barium cycling in the Atlantic. Geochimica et Cosmochimica Acta 204, 286-299.

Bé, A., 1980. Gametogenic calcification in a spinose planktonic foraminifer, Globigerinoides sacculifer (Brady). Marine Micropaleontology 5, 283-310.

Be´, A.W.H., Bishop, J.K.B., Sverdlove, M.S., Gardner, W.D., 1985. Standing stock, vertical distribution and flux of planktonic foraminifera in the Panama Basin. Marine Micropaleontology 9, 307-333.

Beerling, D., Woodward, F., 1996. Palaeo-ecophysiological perspectives on plant responses to global change. Trends in Ecology & Evolution 11, 20-23.

Beerling, D.J., Royer, D.L., 2011. Convergent cenozoic CO 2 history. Nature Geoscience 4, 418.

Bereiter, B., Eggleston, S., Schmitt, J., Nehrbass-Ahles, C., Stocker, T.F., Fischer, H., Kipfstuhl, S., Chappellaz, J., 2015. Revision of the EPICA Dome C CO2 record from 800 to 600 kyr before present. Geophysical Research Letters 42, 542-549.

Berger, W., Herguera, J., 1992. Reading the sedimentary record of the ocean's productivity, Primary productivity and biogeochemical cycles in the sea. Springer, pp. 455-486.

Berger, W.H., 1970. Planktonic Foraminifera: Selective solution and the lysocline. Marine Geology 8, 111-138.

Bertram, M.A., Cowen, J.P., 1997. Morphological and compositional evidence for biotic precipitation of marine barite. Journal of Marine Research 55, 577-593.

Bidigare, R.R., Fluegge, A., Freeman, K.H., Hanson, K.L., Hayes, J.M., Hollander, D., Jasper, J.P., King, L.L., Laws, E.A., Milder, J., 1997. Consistent fractionation of 13C in nature and in the laboratory: Growth-rate effects in some haptophyte algae. Global Biogeochemical Cycles 11, 279-292.

Bird, C., Darling, K.F., Russell, A.D., Fehrenbacher, J.S., Davis, C.V., Free, A., Ngwenya, B.T., 2018. 16S rRNA gene metabarcoding and TEM reveals different ecological strategies within the genus Neogloboquadrina (planktonic foraminifer). PLOS ONE 13, e0191653.

Bishop, J.K., 1988. The barite-opal-organic carbon association in oceanic particulate matter. Nature 332, 341.

Bolton, C.T., Stoll, H.M., Mendez-Vicente, A., 2012. Vital effects in coccolith calcite: Cenozoic climate-pCO2 drove the diversity of carbon acquisition strategies in coccolithophores? Paleoceanography 27.

Boyle, E.A., 1988. Cadmium: Chemical tracer of deepwater paleoceanography. Paleoceanography and Paleoclimatology 3, 471-489.

Bradtmiller, L.I., Anderson, R.F., Fleisher, M.Q., Burckle, L.H., 2006. Diatom productivity in the equatorial Pacific Ocean from the last glacial period to the present: A test of the silicic acid leakage hypothesis. Paleoceanography 21.

Bridgestock, L., Hsieh, Y.-T., Porcelli, D., Henderson, G.M., 2019. Increased export production during recovery from the Paleocene–Eocene thermal maximum constrained by sedimentary Ba isotopes. Earth and Planetary Science Letters 510, 53-63.

Bridgestock, L., Hsieh, Y.-T., Porcelli, D., Homoky, W.B., Bryan, A., Henderson, G.M., 2018. Controls on the barium isotope compositions of marine sediments. Earth and Planetary Science Letters 481, 101-110.

Broecker, W.S., Peng, T.H., 1987. The role of CaCO3 compensation in the glacial to interglacial atmospheric CO2 change. Global Biogeochemical Cycles 1, 15-29.

Brovkin, V., Ganopolski, A., Archer, D., Rahmstorf, S., 2007. Lowering of glacial atmospheric CO2 in response to changes in oceanic circulation and marine biogeochemistry. Paleoceanography 22.

Caron, D.A., Roger Anderson, O., Lindsey, J.L., Faber, W.W., Lin Lim, E.E., 1990. Effects of gametogenesis on test structure and dissolution of some spinose planktonic foraminifera and implications for test preservation. Marine Micropaleontology 16, 93-116.

Cartapanis, O., Galbraith, E.D., Bianchi, D., Jaccard, S.L., 2018. Carbon burial in deep-sea sediment and implications for oceanic inventories of carbon and alkalinity over the last glacial cycle. Clim. Past 14, 1819-1850.

Carter, A., Clemens, S., Kubota, Y., Holbourn, A., Martin, A., 2017. Differing oxygen isotopic signals of two Globigerinoides ruber (white) morphotypes in the East China Sea: Implications for paleoenvironmental reconstructions. Marine Micropaleontology 131, 1-9.

Castillo, K.D., Ries, J.B., Weiss, J.M., 2011. Declining coral skeletal extension for forereef colonies of Siderastrea siderea on the Mesoamerican Barrier Reef System, Southern Belize. PloS one 6, e14615.

Catanzaro, E.J., 1970. Boric acid: isotopic and assay standard reference materials. National Bureau of Standards, Institute for Materials Research.

Cerling, T.E., 1992. Use of carbon isotopes in paleosols as an indicator of the P (CO2) of the paleoatmosphere. Global Biogeochemical Cycles 6, 307-314.

Chalk, T.B., Hain, M.P., Foster, G.L., Rohling, E.J., Sexton, P.F., Badger, M.P., Cherry, S.G., Hasenfratz, A.P., Haug, G.H., Jaccard, S.L., 2017. Causes of ice age intensification across the Mid-Pleistocene Transition. Proceedings of the National Academy of Sciences 114, 13114-13119.

Chiang, J.C.H., Bitz, C.M., 2005. Influence of high latitude ice cover on the marine Intertropical Convergence Zone. Climate Dynamics 25, 477-496.

Chow, T.J., Goldberg, E.D., 1960. On the marine geochemistry of barium. Geochimica et Cosmochimica Acta 20, 192-198.

Costa, K.M., McManus, J.F., Anderson, R.F., Ren, H., Sigman, D.M., Winckler, G., Fleisher, M.Q., Marcantonio, F., Ravelo, A.C., 2016. No iron fertilization in the equatorial Pacific Ocean during the last ice age. Nature 529, 519.

Criss, P.D.E.P.S.R.E., Criss, R.E., 1999. Principles of Stable Isotope Distribution. Oxford University Press, USA.

de Garidel-Thoron, T., Rosenthal, Y., Bassinot, F., Beaufort, L., 2005. Stable sea surface temperatures in the western Pacific warm pool over the past 1.75 million years. Nature 433, 294-298.

de Vargas, C., Norris, R., Zaninetti, L., Gibb, S.W., Pawlowski, J., 1999. Molecular evidence of cryptic speciation in planktonic foraminifers and their relation to oceanic provinces. Proceedings of the National Academy of Sciences 96, 2864-2868.

Dehairs, F., Chesselet, R., Jedwab, J., 1980. Discrete suspended particles of barite and the barium cycle in the open ocean. Earth and Planetary Science Letters 49, 528-550.

Dehairs, F., Stroobants, N., Goeyens, L., 1991. Suspended barite as a tracer of biological activity in the Southern Ocean. Marine Chemistry 35, 399-410.

Denton, G.H., Anderson, R.F., Toggweiler, J.R., Edwards, R.L., Schaefer, J.M., Putnam, A.E., 2010. The Last Glacial Termination. Science 328, 1652-1656.

Deuser, W.G., Ross, E.H., Hemleben, C., Spindler, M., 1981. Seasonal changes in species composition, numbers, mass, size, and isotopic composition of planktonic foraminifera settling into the deep sargasso sea. Palaeogeography, Palaeoclimatology, Palaeoecology 33, 103-127.

Diester-Haass, L., Billups, K., Lear, C., 2018. Productivity changes across the mid-Pleistocene climate transition. Earth-science reviews 179, 372-391.

Diester-Haass, L., Faul, K., 2019. Paleoproductivity reconstructions for the Paleogene Southern Ocean: a direct comparison of geochemical and micropaleontological proxies. Paleoceanography and Paleoclimatology 34, 79-97.

Dissard, D., Douville, E., Reynaud, S., Juillet-Leclerc, A., Montagna, P., Louvat, P., McCulloch, M., 2012. Light and temperature effects on $\delta^{11}B$ and B/Ca ratios of the zooxanthellate coral Acropora sp.: results from culturing experiments. Biogeosciences 9, 4589.

Dyez, K.A., Hönisch, B., Schmidt, G.A., 2018. Early Pleistocene Obliquity-Scale pCO2 Variability at ~1.5 Million Years Ago. Paleoceanography and Paleoclimatology 33, 1270-1291.

Dyez, K.A., Ravelo, A.C., 2013. Late Pleistocene tropical Pacific temperature sensitivity to radiative greenhouse gas forcing. Geology 41, 23-26.

Dyez, K.A., Ravelo, A.C., 2014. Dynamical changes in the tropical Pacific warm pool and zonal SST gradient during the Pleistocene. Geophysical Research Letters 41, 7626-7633.

Dymond, J., Suess, E., Lyle, M., 1992. Barium in Deep-Sea Sediment: A Geochemical Proxy for Paleoproductivity. Paleoceanography 7, 163-181.

Elderfield, H., Ferretti, P., Greaves, M., Crowhurst, S., McCave, I., Hodell, D., Piotrowski, A., 2012. Evolution of ocean temperature and ice volume through the Mid-Pleistocene climate transition. Science 337, 704-709.

Elderfield, H., Rickaby, R., 2000. Oceanic Cd/P ratio and nutrient utilization in the glacial Southern Ocean. Nature 405, 305.

Elderfield and, H.E., Schultz, A., 1996. Mid-Ocean Ridge Hydrothermal Fluxes and the Chemical Composition of the Ocean. Annual Review of Earth and Planetary Sciences 24, 191-224

Enge, T.G., Field, M.P., Jolley, D.F., Ecroyd, H., Kim, M.H., Dosseto, A., 2016. An automated chromatography procedure optimized for analysis of stable Cu isotopes from biological materials. Journal of Analytical Atomic Spectrometry 31, 2023-2030.

Erez, J., 2003. The Source of Ions for Biomineralization in Foraminifera and Their Implications for Paleoceanographic Proxies. Reviews in Mineralogy and Geochemistry 54, 115-149.

Feely, R. A., Lewison, M., Massoth, G. J., Robert-Baldo, G., Lavelle, J. W., Byrne, R. H., ... & Curl, H. C. (1987). Composition and dissolution of black smoker particulates from active vents on the Juan de Fuca Ridge. *Journal of Geophysical Research: Solid Earth*, *92*(B11), 11347-11363.

Feely, R. A., Geiselman, T. L., Baker, E. T., Massoth, G. J., & Hammond, S. R. (1990). Distribution and composition of hydrothermal plume particles from the ASHES Vent Field at Axial Volcano, Juan de Fuca Ridge. *Journal of Geophysical Research: Solid Earth*, *95*(B8), 12855-12873

Fedorov, A., Brierley, C., Lawrence, K.T., Liu, Z., Dekens, P., Ravelo, A., 2013. Patterns and mechanisms of early Pliocene warmth. Nature 496, 43.

Fehrenbacher, J.S., Russell, A.D., Davis, C.V., Spero, H.J., Chu, E., Hönisch, B., 2018. Ba/Ca ratios in the non-spinose planktic foraminifer Neogloboquadrina dutertrei: Evidence for an organic aggregate microhabitat. Geochimica et Cosmochimica Acta 236, 361-372.

Foster, G., Sexton, P., 2014. Enhanced carbon dioxide outgassing from the eastern equatorial Atlantic during the last glacial. Geology 42, 1003-1006.

Foster, G.L., 2008. Seawater pH, pCO2 and [CO_2^{3-}] variations in the Caribbean Sea over the last 130 kyr: A boron isotope and B/Ca study of planktic foraminifera. Earth and Planetary Science Letters 271, 254-266.

Foster, G.L., Hönisch, B., Paris, G., Dwyer, G.S., Rae, J.W.B., Elliott, T., Gaillardet, J., Hemming, N.G., Louvat, P., Vengosh, A., 2013. Interlaboratory comparison of boron isotope analyses of boric acid, seawater and marine CaCO3 by MC-ICPMS and NTIMS. Chemical Geology 358, 1-14.

Foster, G.L., Lear, C.H., Rae, J.W., 2012. The evolution of pCO2, ice volume and climate during the middle Miocene. Earth and Planetary Science Letters 341, 243-254.

Foster, G.L., Ni, Y., Haley, B., Elliott, T., 2006. Accurate and precise isotopic measurement of sub-nanogram sized samples of foraminiferal hosted boron by total evaporation NTIMS. Chemical Geology 230, 161-174.

Foster, G.L., Pogge von Strandmann, P.A.E., Rae, J.W.B., 2010. Boron and magnesium isotopic composition of seawater. Geochemistry, Geophysics, Geosystems 11, Q08015.

Foster, G.L., Rae, J.W., 2016. Reconstructing ocean pH with boron isotopes in foraminifera. Annual Review of Earth and Planetary Sciences 44, 207-237.

Foster, G.L., Royer, D.L., Lunt, D.J., 2017. Future climate forcing potentially without precedent in the last 420 million years. Nature Communications 8, 14845.

Fowell, S., Foster, G., Ries, J., Castillo, K., De La Vega, E., Tyrrell, T., Donald, H., Chalk, T., 2018. Historical trends in pH and carbonate biogeochemistry on the Belize Mesoamerican Barrier Reef System. Geophysical Research Letters 45, 3228-3237.

Ganeshram, R.S., François, R., Commeau, J., Brown-Leger, S.L., 2003. An experimental investigation of barite formation in seawater. Geochimica et Cosmochimica Acta 67, 2599-2605.

Goodkin, N.F., Wang, B.S., You, C.F., Hughen, K.A., Grumet-Prouty, N., Bates, N.R., Doney, S.C., 2015. Ocean circulation and biogeochemistry moderate interannual and decadal surface water pH changes in the Sargasso Sea. Geophysical Research Letters 42, 4931-4939.

Greenop, R., Foster, G.L., Wilson, P.A., Lear, C.H., 2014. Middle Miocene climate instability associated with high-amplitude CO2 variability. Paleoceanography and Paleoclimatology 29, 845-853.

Greenop, R., Hain, M., Sosdian, S.M., Oliver, K., Goodwin, P., Chalk, T., Lear, C.H., Wilson, P., Foster, G., 2017. A record of Neogene seawater δ11B reconstructed from paired δ11B analyses on benthic and planktic foraminifera. Climate of the Past 13, 149-170.

Gregoire, D.C., 1987. The effect of easily ionizable concomitant elements on non-spectroscopic interferences in inductively coupled plasma-mass spectrometry. Spectrochimica Acta Part B: Atomic Spectroscopy 42, 895-907.

Guerrot, C., Millot, R., Robert, M., Négrel, P., 2011. Accurate and High-Precision Determination of Boron Isotopic Ratios at Low Concentration by MC-ICP-MS (Neptune). Geostandards and Geoanalytical Research 35, 275-284.

Gussone, N., Eisenhauer, A., Heuser, A., Dietzel, M., Bock, B., Böhm, F., Spero, H.J., Lea, D.W., Bijma, J., Nägler, T.F., 2003. Model for kinetic effects on calcium isotope fractionation (δ44Ca) in inorganic aragonite and cultured planktonic foraminifera. Geochimica et Cosmochimica Acta 67, 1375-1382.

Hain, M., Foster, G., Chalk, T., 2018. Robust constraints on past CO2 climate forcing from the boron isotope proxy. Paleoceanography and Paleoclimatology 33, 1099-1115.

Hain, M., Sigman, D., Haug, G., 2014. 8.18–The biological Pump in the Past. Reference Module in Earth Systems and Environmental Sciences, Treatise on Geochemistry (Second Edition), The Oceans and Marine Geochemistry 8, 485-517.

Hain, M.P., Sigman, D.M., Haug, G.H., 2010. Carbon dioxide effects of Antarctic stratification, North Atlantic Intermediate Water formation, and subantarctic nutrient drawdown during the last ice age: Diagnosis and synthesis in a geochemical box model. Global Biogeochemical Cycles 24.

Hansen, J., Sato, M., Kharecha, P., Beerling, D., Berner, R., Masson-Delmotte, V., Pagani, M., Raymo, M., Royer, D.L., Zachos, J.C., 2008. Target atmospheric CO2: Where should humanity aim? arXiv preprint arXiv:0804.1126.

Harris, S.E., Mix, A.C., King, T., 1999. Biogenic and terrigenous sedimetations at Ceara rise, western tropical Altantic, supports Pliocene - Pleistocene deep - water linkage between hemispheres. College Station, Tex. : Ocean Drilling Program, Texas A & M University.

Haywood, A.M., Dowsett, H.J., Dolan, A.M., 2016. Integrating geological archives and climate models for the mid-Pliocene warm period. Nature Communications 7, 10646.

Hemleben, C., Spindler, M., Anderson, O., 1989. Modern Planktonic Foraminifera• Springer. New York.

Hemming, N.G., Hanson, G.N., 1992. Boron isotopic composition and concentration in modern marine carbonates. Geochimica et Cosmochimica Acta 56, 537-543.

Hemming, N.G., Hanson, G.N., 1994. A procedure for the isotopic analysis of boron by negative thermal ionization mass spectrometry. Chemical Geology 114, 147-156.

Hemsing, F., Hsieh, Y.-T., Bridgestock, L., Spooner, P.T., Robinson, L.F., Frank, N., Henderson, G.M., 2018. Barium isotopes in cold-water corals. Earth and Planetary Science Letters 491, 183-192.

Henehan, M.J., Foster, G.L., Bostock, H.C., Greenop, R., Marshall, B.J., Wilson, P.A., 2016. A new boron isotope-pH calibration for Orbulina universa, with implications for understanding and accounting for ‘vital effects’. Earth and Planetary Science Letters 454, 282-292.

Henehan, M.J., Rae, J.W., Foster, G.L., Erez, J., Prentice, K.C., Kucera, M., Bostock, H.C., Martínez-Botí, M.A., Milton, J.A., Wilson, P.A., 2013. Calibration of the boron isotope proxy in the planktonic foraminifera Globigerinoides ruber for use in palaeo-CO2 reconstruction. Earth and Planetary Science Letters 364, 111-122.

Herguera, J.C., Berger, W., 1991. Paleoproductivity from benthic foraminifera abundance: Glacial to postglacial change in the west-equatorial Pacific. Geology 19, 1173-1176.

Hernandez-Sanchez, M.T., Mills, R.A., Planquette, H., Pancost, R.D., Hepburn, L., Salter, I., FitzGeorge-Balfour, T., 2011. Quantifying export production in the Southern Ocean: Implications for the Baxs proxy. Paleoceanography 26.

Hönisch, B., Allen, K.A., Russell, A.D., Eggins, S.M., Bijma, J., Spero, H.J., Lea, D.W., Yu, J., 2011. Planktic foraminifers as recorders of seawater Ba/Ca. Marine Micropaleontology 79, 52-57.

Hönisch, B., Hemming, N.G., 2004. Ground-truthing the boron isotope-paleo-pH proxy in planktonic foraminifera shells: Partial dissolution and shell size effects. Paleoceanography 19, PA4010.

Hönisch, B., Hemming, N.G., 2005. Surface ocean pH response to variations in pCO2 through two full glacial cycles. Earth and Planetary Science Letters 236, 305-314.

Hönisch, B., Hemming, N.G., Archer, D., Siddall, M., McManus, J.F., 2009. Atmospheric Carbon Dioxide Concentration Across the Mid-Pleistocene Transition. Science 324, 1551-1554.

Hoogakker, B.A.A., Rohling, E.J., Palmer, M.R., Tyrrell, T., Rothwell, R.G., 2006. Underlying causes for long-term global ocean delta C-13 fluctuations over the last 1.20 Myr. Earth and Planetary Science Letters, 15-29.

Horner, T.J., Kinsley, C.W., Nielsen, S.G., 2015. Barium-isotopic fractionation in seawater mediated by barite cycling and oceanic circulation. Earth and Planetary Science Letters 430, 511-522.

Horner, T.J., Pryer, H.V., Nielsen, S.G., Crockford, P.W., Gauglitz, J.M., Wing, B.A., Ricketts, R.D., 2017. Pelagic barite precipitation at micromolar ambient sulfate. Nature Communications 8, 1342.

Howard, W.R., Prell, W.L., 1994. Late Quaternary CaCO3 production and preservation in the Southern Ocean: Implications for oceanic and atmospheric carbon cycling. Paleoceanography 9, 453-482.

Howe, J.N., Piotrowski, A.M., 2017. Atlantic deep water provenance decoupled from atmospheric CO 2 concentration during the lukewarm interglacials. Nature communications 8, 2003.

Hsieh, Y.-T., Henderson, G.M., 2017. Barium stable isotopes in the global ocean: tracer of Ba inputs and utilization. Earth and Planetary Science Letters 473, 269-278.

Jaccard, S., Hayes, C.T., Martínez-García, A., Hodell, D., Anderson, R.F., Sigman, D., Haug, G., 2013. Two modes of change in Southern Ocean productivity over the past million years. Science 339, 1419-1423.

Jiao, N., Herndl, G.J., Hansell, D.A., Benner, R., Kattner, G., Wilhelm, S.W., Kirchman, D.L., Weinbauer, M.G., Luo, T., Chen, F., 2010. Microbial production of recalcitrant dissolved organic matter: long-term carbon storage in the global ocean. Nature Reviews Microbiology 8, 593.

Jiao, N., Robinson, C., Azam, F., Thomas, H., Baltar, F., Dang, H., Hardman-Mountford, N., Johnson, M., Kirchman, D., Koch, B., 2014. Mechanisms of microbial carbon sequestration in the ocean–future research directions. Biogeosciences 11, 5285-5306.

Johns, W. E., Townsend, T. L., Fratantoni, D. M., & Wilson, W. D. (2002). On the Atlantic inflow to the Caribbean Sea. *Deep Sea Research Part I: Oceanographic Research Papers*, *49*(2), 211-243.

Kaczmarek, K., Langer, G., Nehrke, G., Horn, I., Misra, S., Janse, M., Bijma, J., 2015. Boron incorporation in the foraminifer Amphistegina lessonii under a decoupled carbonate chemistry. Biogeosciences 12, 1753-1763.

Kemp, A., Grigorov, I., Pearce, R.B., Garabato, A.N., 2010. Migration of the Antarctic Polar Front through the mid-Pleistocene transition: evidence and climatic implications. Quaternary Science Reviews 29, 1993-2009.

Kerr, J., Rickaby, R., Yu, J., Elderfield, H., Sadekov, A.Y., 2017. The effect of ocean alkalinity and carbon transfer on deep-sea carbonate ion concentration during the past five glacial cycles. Earth and Planetary Science Letters 471, 42-53.

Kessler, W.S., 2006. The circulation of the eastern tropical Pacific: A review. Progress in Oceanography 69, 181-217.

Kiss, E., 1988. Ion-exchange separation and spectrophotometric determination of boron in geological materials. Analytica Chimica Acta 211, 243-256.

Klochko, K., Kaufman, A.J., Yao, W., Byrne, R.H., Tossell, J.A., 2006. Experimental measurement of boron isotope fractionation in seawater. Earth and Planetary Science Letters 248, 276-285.

Kohfeld, K.E., Ridgwell, A., 2009. Glacial-interglacial variability in atmospheric CO2. Surface ocean-lower atmosphere processes 187, 251-286.

Kürschner, W.M., van der Burgh, J., Visscher, H., Dilcher, D.L., 1996. Oak leaves as biosensors of late Neogene and early Pleistocene paleoatmospheric CO2 concentrations. Marine Micropaleontology 27, 299-312.

Laws, E.A., Popp, B.N., Bidigare, R.R., Kennicutt, M.C., Macko, S.A., 1995. Dependence of phytoplankton carbon isotopic composition on growth rate and [CO2] aq: Theoretical considerations and experimental results. Geochimica et cosmochimica acta 59, 1131-1138.

Lazarus, D., Bittniok, B., Diester-Haass, L., Billups, K., Ogawa, Y., Takahashi, K., Meyers, P., 2008. Radiolarian and sedimentologic paleoproductivity proxies in late Pleistocene sediments of the Benguela Upwelling System, ODP Site 1084. Marine Micropaleontology 68, 223-235.

Lazarus, D., Bittniok, B., Diester-Haass, L., Meyers, P., Billups, K., 2006. Comparison of radiolarian and sedimentologic paleoproductivity proxies in the latest Miocene–Recent Benguela Upwelling System. Marine Micropaleontology 60, 269-294.

Lea, D.W., 1993. Constraints on the alkalinity and circulation of glacial circumpolar deep water from benthic foraminiferal barium. Global Biogeochemical Cycles 7, 695-710.

Lea, D.W., Boyle, E.A., 1991. Barium in planktonic foraminifera. Geochimica et Cosmochimica Acta 55, 3321-3331.

Lea, D.W., Spero, H.J., 1992. Experimental determination of barium uptake in shells of the planktonic foraminifera Orbulina universa at 22°C. Geochimica et Cosmochimica Acta 56, 2673-2680.

Leeman, W.P., Vocke Jr, R.D., Beary, E.S., Paulsen, P.J., 1991. Precise boron isotopic analysis of aqueous samples: Ion exchange extraction and mass spectrometry. Geochimica et Cosmochimica Acta 55, 3901-3907.

Lemarchand, D., Gaillardet, J., Göpel, C., Manhès, G., 2002a. An optimized procedure for boron separation and mass spectrometry analysis for river samples. Chemical Geology 182, 323-334.

Lemarchand, D., Gaillardet, J., Lewin, É., Allègre, C.J., 2002b. Boron isotope systematics in large rivers: implications for the marine boron budget and paleo-pH reconstruction over the Cenozoic. Chemical Geology 190, 123-140.

Lisiecki, L.E., 2014. Atlantic overturning responses to obliquity and precession over the last 3 Myr. Paleoceanography 29, 71-86.

Lisiecki, L.E., Raymo, M.E., 2005. A Pliocene-Pleistocene stack of 57 globally distributed benthic δ18O records. Paleoceanography 20.

Liu, Y., Peng, Z., Zhou, R., Song, S., Liu, W., You, C.-F., Lin, Y.-P., Yu, K., Wu, C.-C., Wei, G., 2014. Acceleration of modern acidification in the South China Sea driven by anthropogenic CO2. Scientific reports 4, 5148.

Loubere, P., Mekik, F., Francois, R., Pichat, S., 2004. Export fluxes of calcite in the eastern equatorial Pacific from the Last Glacial Maximum to present. Paleoceanography 19.

Lowenstein, T.K., Demicco, R.V., 2006. Elevated Eocene atmospheric CO2 and its subsequent decline. Science 313, 1928-1928.

Lunt, D.J., Haywood, A.M., Schmidt, G.A., Salzmann, U., Valdes, P.J., Dowsett, H.J., 2010. Earth system sensitivity inferred from Pliocene modelling and data. Nature Geoscience 3, 60.

Luthi, D., Le Floch, M., Bereiter, B., Blunier, T., Barnola, J.-M., Siegenthaler, U., Raynaud, D., Jouzel, J., Fischer, H., Kawamura, K., Stocker, T.F., 2008. High-resolution carbon dioxide concentration record 650,000-800,000 years before present. Nature 453, 379-382.

Lynch-Stieglitz, J., Adkins, J.F., Curry, W.B., Dokken, T., Hall, I.R., Herguera, J.C., Hirschi, J.J.-M., Ivanova, E.V., Kissel, C., Marchal, O., Marchitto, T.M., McCave, I.N., McManus, J.F., Mulitza, S., Ninnemann, U., Peeters, F., Yu, E.-F., Zahn, R., 2007. Atlantic Meridional Overturning Circulation During the Last Glacial Maximum. Science 316, 66-69.

Ma, W., Wang, P., Tian, J., 2017. Modeling 400–500-kyr Pleistocene carbon isotope cyclicity through variations in the dissolved organic carbon pool. Global and planetary change 152, 187-198.

Marshall, B.J., Thunell, R.C., Spero, H.J., Henehan, M.J., Lorenzoni, L., Astor, Y., 2015. Morphometric and stable isotopic differentiation of Orbulina universa morphotypes from the Cariaco Basin, Venezuela. Marine Micropaleontology 120, 46-64.

Martínez-Botí, M.A., Foster, G.L., Chalk, T.B., Rohling, E.J., Sexton, P.F., Lunt, D.J., Pancost, R.D., Badger, M.P.S., Schmidt, D.N., 2015a. Plio-Pleistocene climate sensitivity evaluated using high-resolution CO2 records. Nature 518, 49-54.

Martínez-Botí, M.A., Marino, G., Foster, G.L., Ziveri, P., Henehan, M.J., Rae, J.W.B., Mortyn, P.G., Vance, D., 2015b. Boron isotope evidence for oceanic carbon dioxide leakage during the last deglaciation. Nature 518, 219-222.

Martínez-García, A., Sigman, D.M., Ren, H., Anderson, R.F., Straub, M., Hodell, D.A., Jaccard, S.L., Eglinton, T.I., Haug, G.H., 2014. Iron fertilization of the Subantarctic Ocean during the last ice age. Science 343, 1347-1350.

Matsumoto, K., Sarmiento, J.L., 2008. A corollary to the silicic acid leakage hypothesis. Paleoceanography and Paleoclimatology 23.

Matsumoto, K., Sarmiento, J.L., Brzezinski, M.A., 2002. Silicic acid leakage from the Southern Ocean: A possible explanation for glacial atmospheric pCO2. Global Biogeochemical Cycles 16, 5-1-5-23.

McClymont, E.L., Rosell-Melé, A., 2005. Links between the onset of modern Walker circulation and the mid-Pleistocene climate transition. Geology 33, 389-392.

McCulloch, M.T., Holcomb, M., Rankenburg, K., Trotter, J.A., 2014. Rapid, high-precision measurements of boron isotopic compositions in marine carbonates. Rapid Communications in Mass Spectrometry 28, 2704-2712.

Meilland, J., Siccha, M., Weinkauf, M.F., Jonkers, L., Morard, R., Baranowski, U., Baumeister, A., Bertlich, J., Brummer, G.-J., Debray, P., 2019. Highly replicated sampling reveals no diurnal vertical migration but stable species-specific vertical habitats in planktonic foraminifera. Journal of Plankton Research. 00(00): 1–15. doi:10.1093/plankt/fbz002

Misra, S., Owen, R., Kerr, J., Greaves, M., Elderfield, H., 2014. Determination of δ11B by HR-ICP-MS from mass limited samples: Application to natural carbonates and water samples. Geochimica et Cosmochimica Acta 140, 531-552.

Mollica, N.R., Guo, W., Cohen, A.L., Huang, K.-F., Foster, G.L., Donald, H.K., Solow, A.R., 2018. Ocean acidification affects coral growth by reducing skeletal density. Proceedings of the National Academy of Sciences 115, 1754-1759.

Morcillo, F., Gonzalez-Muñoz, M.T., Martinez-Ruiz, F., Martin-Ramos, J.D., Paytan, A., 2012. Precipitation of barite by marine bacteria: A possible mechanism for marine barite formation. Geology 40, 675-678.

Mortlock, R., Charles, C., Froelich, P., Zibello, M., Saltzman, J., Hays, J., Burckle, L., 1991. Evidence for lower productivity in the Antarctic Ocean during the last glaciation. Nature 351, 220.

Ni, Y., Foster, G.L., Bailey, T., Elliott, T., Schmidt, D.N., Pearson, P., Haley, B., Coath, C., 2007. A core top assessment of proxies for the ocean carbonate system in surface-dwelling foraminifers. Paleoceanography 22, PA3212.

Noireaux, J., Mavromatis, V., Gaillardet, J., Schott, J., Montouillout, V., Louvat, P., Rollion-Bard, C., Neuville, D., 2015. Crystallographic control on the boron isotope paleo-pH proxy. Earth and planetary science letters 430, 398-407.

Okai, T., Suzuki, A., Kawahata, H., Terashima, S., Imai, N., 2002. Preparation of a New Geological Survey of Japan Geochemical Reference Material: Coral JCp-1. Geostandards and Geoanalytical Research 26, 95-99.

Olsen, A., Triñanes, J.A., Wanninkhof, R., 2004. Sea–air flux of CO2 in the Caribbean Sea estimated using in situ and remote sensing data. Remote Sensing of Environment 89, 309-325.

Oppo, D.W., Lehman, S.J., 1993. Mid-Depth Circulation of the Subpolar North Atlantic During the Last Glacial Maximum. Science 259, 1148-1152.

Pagani, M., Huber, M., Liu, Z., Bohaty, S.M., Henderiks, J., Sijp, W., Krishnan, S., DeConto, R.M., 2011. The role of carbon dioxide during the onset of Antarctic glaciation. science 334, 1261-1264.

Pagani, M., Liu, Z., LaRiviere, J., Ravelo, A.C., 2010. High Earth-system climate sensitivity determined from Pliocene carbon dioxide concentrations. Nature Geoscience 3, 27.

Paillard, D., Labeyrie, L., Yiou, P., 1996. AnalySeries 1.0: a Macintosh software for the analysis of geophysical time-series. Eos 77, 379.

Palmer, M.R., Spivack, A.J., Edmond, J.M., 1987. Temperature and pH controls over isotopic fractionation during adsorption of boron on marine clay. Geochimica et Cosmochimica Acta 51, 2319-2323.

Paytan, A., Griffith, E.M., 2007. Marine barite: Recorder of variations in ocean export productivity. Deep Sea Research Part II: Topical Studies in Oceanography 54, 687-705.

Pearson, P.N., Palmer, M.R., 2000. Atmospheric carbon dioxide concentrations over the past 60 million years. Nature 406, 695-699.

Pennington, J.T., Mahoney, K.L., Kuwahara, V.S., Kolber, D.D., Calienes, R., Chavez, F.P., 2006. Primary production in the eastern tropical Pacific: A review. Progress in Oceanography 69, 285-317.

Petit, J.R., Jouzel, J., Raynaud, D., Barkov, N.I., Barnola, J.M., Basile, I., Bender, M., Chappellaz, J., Davis, M., Delaygue, G., Delmotte, M., Kotlyakov, V.M., Legrand, M., Lipenkov, V.Y., Lorius, C., Pepin, L., Ritz, C., Saltzman, E., Stievenard, M., 1999. Climate and atmospheric history of the past 420,000 years from the Vostok ice core, Antarctica. Nature 399, 429-436.

Pi, J.-l., You, C.-F., Chung, C.-H., 2014. Micro-sublimation separation of boron in rock samples for isotopic measurement by MC-ICPMS. Journal of Analytical Atomic Spectrometry 29, 861-867.

Popp, B.N., Kenig, F., Wakeham, S.G., Laws, E.A., Bidigare, R.R., 1998. Does growth rate affect ketone unsaturation and intracellular carbon isotopic variability in Emiliania huxleyi? Paleoceanography 13, 35-41.

Pretet, C., van Zuilen, K., Nägler, T.F., Reynaud, S., Böttcher, M.E., Samankassou, E., 2015. Constraints on barium isotope fractionation during aragonite precipitation by corals. The Depositional Record 1, 118-129.

Prokopenko, A.A., Williams, D.F., Kuzmin, M.I., Karabanov, E.B., Khursevich, G.K., Peck, J.A., 2002. Muted climate variations in continental Siberia during the mid-Pleistocene epoch. Nature 418, 65.

Putnis, C.V., Kowacz, M., Putnis, A., 2008. The mechanism and kinetics of DTPA-promoted dissolution of barite. Applied Geochemistry 23, 2778-2788.

Qin, B., Li, T., Xiong, Z., Algeo, T., Jia, Q., 2018. Deep-Water Carbonate Ion Concentrations in the Western Tropical Pacific Since the Mid-Pleistocene: A Major Perturbation During the Mid-Brunhes. Journal of Geophysical Research: Oceans 123, 6876-6892.

Ra, K., Kitagawa, H., Shiraiwa, Y., 2010. Mg isotopes and Mg/Ca values of coccoliths from cultured specimens of the species Emiliania huxleyi and Gephyrocapsa oceanica. Marine Micropaleontology 77, 119-124.

Rackebrandt, N., Kuhnert, H., Groeneveld, J., Bickert, T., 2011. Persisting maximum Agulhas leakage during MIS 14 indicated by massive Ethmodiscus oozes in the subtropical South Atlantic. Paleoceanography and Paleoclimatology 26.

Rae, J.W.B., Foster, G.L., Schmidt, D.N., Elliott, T., 2011. Boron isotopes and B/Ca in benthic foraminifera: Proxies for the deep ocean carbonate system. Earth and Planetary Science Letters 302, 403-413.

Ragueneau, O., Tréguer, P., Leynaert, A., Anderson, R., Brzezinski, M., DeMaster, D., Dugdale, R., Dymond, J., Fischer, G., Francois, R., 2000. A review of the Si cycle in the modern ocean: recent progress and missing gaps in the application of biogenic opal as a paleoproductivity proxy. Global and Planetary Change 26, 317-365.

Raitzsch, M., Bijma, J., Benthien, A., Richter, K.-U., Steinhoefel, G., Kučera, M., 2018. Boron isotope-based seasonal paleo-pH reconstruction for the Southeast Atlantic–A multispecies approach using habitat preference of planktonic foraminifera. Earth and Planetary Science Letters 487, 138-150.

Raitzsch, M., Hönisch, B., 2013. Cenozoic boron isotope variations in benthic foraminifers. Geology 41, 591-594.

Regenberg, M., Steph, S., Nürnberg, D., Tiedemann, R., Garbe-Schönberg, D., 2009. Calibrating Mg/Ca ratios of multiple planktonic foraminiferal species with δ18O-calcification temperatures: Paleothermometry for the upper water column. Earth and Planetary Science Letters 278, 324-336.

Rehkämper, M., Schönbächler, M., Stirling, C.H., 2001. Multiple Collector ICP-MS: Introduction to Instrumentation, Measurement Techniques and Analytical Capabilities. Geostandards Newsletter 25, 23-40.

Reimer, P.J., Bard, E., Bayliss, A., Beck, J.W., Blackwell, P.G., Ramsey, C.B., Buck, C.E., Cheng, H., Edwards, R.L., Friedrich, M., Grootes, P.M., Guilderson, T.P., Haflidason, H., Hajdas, I., Hatté, C., Heaton, T.J., Hoffmann, D.L., Hogg, A.G., Hughen, K.A., Kaiser, K.F., Kromer, B., Manning, S.W., Niu, M., Reimer, R.W., Richards, D.A., Scott, E.M., Southon, J.R., Staff, R.A., Turney, C.S.M., van der Plicht, J., 2013. IntCal13 and Marine13 Radiocarbon Age Calibration Curves 0–50,000 Years cal BP. Radiocarbon 55, 1869-1887.

Retzmann, A., Zimmermann, T., Pröfrock, D., Prohaska, T., Irrgeher, J., 2017. A fully automated simultaneous single-stage separation of Sr, Pb, and Nd using DGA Resin for the isotopic analysis of marine sediments. Analytical and bioanalytical chemistry 409, 5463-5480.

Rickaby, R.E.M., Bard, E., Sonzogni, C., Rostek, F., Beaufort, L., Barker, S., Rees, G., Schrag, D.P., 2007. Coccolith chemistry reveals secular variations in the global ocean carbon cycle? Earth and Planetary Science Letters 253, 83-95.

Ridgwell, A., Schmidt, D.N., 2010. Past constraints on the vulnerability of marine calcifiers to massive carbon dioxide release. Nature Geoscience 3, 196.

Rink, S., Kühl, M., Bijma, J., Spero, H., 1998. Microsensor studies of photosynthesis and respiration in the symbiotic foraminifer Orbulina universa. Marine Biology 131, 583-595.

Rohling, E.J., Marino, G., Foster, G.L., Goodwin, P.A., Von der Heydt, A.S., Köhler, P., 2018. Comparing climate sensitivity, past and present. Annual Review of Marine Science 10, 261-288.

Rohling, E.J., Sluijs, A., Dijkstra, H.A., Köhler, P., van de Wal, R.S., von der Heydt, A.S., Beerling, D.J., Berger, A., Bijl, P.K., Crucifix, M., 2012. Making sense of palaeoclimate sensitivity. Nature 491, 683.

Romaniello, S.J., Field, M.P., Smith, H.B., Gordon, G.W., Kim, M.H., Anbar, A.D., 2015. Fully automated chromatographic purification of Sr and Ca for isotopic analysis. Journal of Analytical Atomic Spectrometry 30, 1906-1912.

Rossignol-Strick, M., Paterne, M., Bassinot, F., Emeis, K.-C., De Lange, G., 1998. An unusual mid-Pleistocene monsoon period over Africa and Asia. Nature 392, 269.

Royer, D.L., Berner, R.A., Beerling, D.J., 2001. Phanerozoic atmospheric CO2 change: evaluating geochemical and paleobiological approaches. Earth-Science Reviews 54, 349-392.

Sadekov, A.Y., Eggins, S.M., Klinkhammer, G.P., Rosenthal, Y., 2010. Effects of seafloor and laboratory dissolution on the Mg/Ca composition of Globigerinoides sacculifer and Orbulina universa tests — A laser ablation ICPMS microanalysis perspective. Earth and Planetary Science Letters 292, 312-324.

Sanyal, A., Bijma, J., Spero, H., Lea, D.W., 2001. Empirical relationship between pH and the boron isotopic composition of Globigerinoides sacculifer: Implications for the boron isotope paleo-pH proxy. Paleoceanography 16, 515-519.

Sanyal, A., Hemming, N., Hanson, G.N., Broecker, W.S., 1995. Evidence for a higher pH in the glacial ocean from boron isotopes in foraminifera. Nature 373, 234.

Sanyal, A., Hemming, N.G., Broecker, W.S., Lea, D.W., Spero, H.J., Hanson, G.N., 1996. Oceanic pH control on the boron isotopic composition of foraminifera: Evidence from culture experiments. Paleoceanography 11, 513-517.

Sarmiento, J.á., Gruber, N., Brzezinski, M., Dunne, J., 2004. High-latitude controls of thermocline nutrients and low latitude biological productivity. Nature 427, 56.

Schmidt, M.W., Vautravers, M.J., Spero, H.J., 2006. Western Caribbean sea surface temperatures during the late Quaternary. Geochemistry, Geophysics, Geosystems 7.

Schmieder, F., von Dobeneck, T., Bleil, U., 2000. The Mid-Pleistocene climate transition as documented in the deep South Atlantic Ocean: initiation, interim state and terminal event. Earth and Planetary Science Letters 179, 539-549.

Schmitt, J., Schneider, R., Elsig, J., Leuenberger, D., Lourantou, A., Chappellaz, J., Köhler, P., Joos, F., Stocker, T.F., Leuenberger, M., Fischer, H., 2012. Carbon Isotope Constraints on the Deglacial CO2 Rise from Ice Cores. Science 336, 711-714.

Schoepfer, S.D., Shen, J., Wei, H., Tyson, R.V., Ingall, E., Algeo, T.J., 2015. Total organic carbon, organic phosphorus, and biogenic barium fluxes as proxies for paleomarine productivity. Earth-Science Reviews 149, 23-52.

Schwarcz, H.P., Agyei, E.K., McMullen, C.C., 1969. Boron isotopic fractionation during clay adsorption from sea-water. Earth and Planetary Science Letters 6, 1-5.

Seki, O., Foster, G.L., Schmidt, D.N., Mackensen, A., Kawamura, K., Pancost, R.D., 2010. Alkenone and boron-based Pliocene pCO2 records. Earth and Planetary Science Letters 292, 201-211.

Sexton, P.F., Barker, S., 2012. Onset of ‘Pacific-style’deep-sea sedimentary carbonate cycles at the mid-Pleistocene transition. Earth and Planetary Science Letters 321, 81-94.

Shakun, J.D., Lea, D.W., Lisiecki, L.E., Raymo, M.E., 2015. An 800-kyr record of global surface ocean δ18O and implications for ice volume-temperature coupling. Earth and Planetary Science Letters 426, 58-68.

Siebert, C., Nägler, T.F., Kramers, J.D., 2001. Determination of molybdenum isotope fractionation by double-spike multicollector inductively coupled plasma mass spectrometry. Geochemistry, Geophysics, Geosystems 2.

Siegenthaler, U., Stocker, T.F., Monnin, E., Lüthi, D., Schwander, J., Stauffer, B., Raynaud, D., Barnola, J.-M., Fischer, H., Masson-Delmotte, V., 2005. Stable carbon cycle–climate relationship during the late Pleistocene. Science 310, 1313-1317.

Sigman, D.M., Boyle, E.A., 2000. Glacial/interglacial variations in atmospheric carbon dioxide. Nature 407, 859.

Sigman, D.M., Hain, M.P., Haug, G.H., 2010. The polar ocean and glacial cycles in atmospheric CO2 concentration. Nature 466, 47-55.

Sosdian, S., Greenop, R., Hain, M., Foster, G., Pearson, P., Lear, C., 2018. Constraining the evolution of Neogene ocean carbonate chemistry using the boron isotope pH proxy. Earth and Planetary Science Letters 498, 362-376.

Spero, H.J., Mielke, K.M., Kalve, E.M., Lea, D.W., Pak, D.K., 2003. Multispecies approach to reconstructing eastern equatorial Pacific thermocline hydrography during the past 360 kyr. Paleoceanography 18.

Spivack, A.J., Edmond, J.M., 1987. Boron isotope exchange between seawater and the oceanic crust. Geochimica et Cosmochimica Acta 51, 1033-1043.

Stecher, H.A., Kogut, M.B., 1999. Rapid barium removal in the Delaware estuary. Geochimica et Cosmochimica Acta 63, 1003-1012.

Stephens, B.B., Keeling, R.F., 2000. The influence of Antarctic sea ice on glacial–interglacial CO 2 variations. Nature 404, 171.

Stevenson, E.I., Hermoso, M., Rickaby, R.E.M., Tyler, J.J., Minoletti, F., Parkinson, I.J., Mokadem, F., Burton, K.W., 2014. Controls on stable strontium isotope fractionation in coccolithophores with implications for the marine Sr cycle. Geochimica et Cosmochimica Acta 128, 225-235.

Stocker, T., 2014. Climate change 2013: the physical science basis: Working Group I contribution to the Fifth assessment report of the Intergovernmental Panel on Climate Change. Cambridge University Press.

Stott, L., Southon, J., Timmermann, A., Koutavas, A., 2009. Radiocarbon age anomaly at intermediate water depth in the Pacific Ocean during the last deglaciation. Paleoceanography 24.

Takahashi, T., Sutherland, S.C., Wanninkhof, R., Sweeney, C., Feely, R.A., Chipman, D.W., Hales, B., Friederich, G., Chavez, F., Sabine, C., 2009. Climatological mean and decadal change in surface ocean pCO2, and net sea–air CO2 flux over the global oceans. Deep Sea Research Part II: Topical Studies in Oceanography 56, 554-577.

Takahashi, T., Sweeney, C., Hales, B., Chipman, D.W., Newberger, T., Goddard, J.G., Iannuzzi, R.A., Sutherland, S.C., 2012. The changing carbon cycle in the Southern Ocean. Oceanography 25, 26-37.

Toggweiler, J., 1999. Variation of atmospheric CO2 by ventilation of the ocean's deepest water. Paleoceanography 14, 571-588.

Toggweiler, J.R., Dixon, K., Broecker, W.S., 1991. The Peru upwelling and the ventilation of the south Pacific thermocline. Journal of Geophysical Research: Oceans 96, 20467-20497.

Tripati, A.K., Roberts, C.D., Eagle, R.A., 2009. Coupling of CO2 and ice sheet stability over major climate transitions of the last 20 million years. science 326, 1394-1397.

van Zuilen, K., Nägler, T.F., Bullen, T.D., 2016. Barium Isotopic Compositions of Geological Reference Materials. Geostandards and Geoanalytical Research 40, 543-558.

Vengosh, A., Kolodny, Y., Starinsky, A., Chivas, A.R., McCulloch, M.T., 1991. Coprecipitation and isotopic fractionation of boron in modern biogenic carbonates. Geochimica et Cosmochimica Acta 55, 2901-2910.

Von Allmen, K., Böttcher, M.E., Samankassou, E., Nägler, T.F., 2010. Barium isotope fractionation in the global barium cycle: First evidence from barium minerals and precipitation experiments. Chemical Geology 277, 70-77.

Wang, B.-S., You, C.-F., Huang, K.-F., Wu, S.-F., Aggarwal, S.K., Chung, C.-H., Lin, P.-Y., 2010. Direct separation of boron from Na-and Ca-rich matrices by sublimation for stable isotope measurement by MC-ICP-MS. Talanta 82, 1378-1384.

Wang, G.S., Liao, C.H., Chen, H.W., Yang, H.C., 2006. Characteristics of Natural Organic Matter Degradation in Water by UV/H2O2 Treatment. Environmental Technology 27, 277-287.

Wang, L., 2000. Isotopic signals in two morphotypes of Globigerinoides ruber (white) from the South China Sea: implications for monsoon climate change during the last glacial cycle. Palaeogeography, Palaeoclimatology, Palaeoecology 161, 381-394.

Wang, P., Tian, J., Cheng, X., Liu, C., Xu, J., 2004. Major Pleistocene stages in a carbon perspective: The South China Sea record and its global comparison. Paleoceanography 19.

Wefing, A.-M., Arps, J., Blaser, P., Wienberg, C., Hebbeln, D., Frank, N., 2017. High precision U-series dating of scleractinian cold-water corals using an automated chromatographic U and Th extraction. Chemical Geology 475, 140-148.

Wolf-Gladrow, D.A., Bijma, J., Zeebe, R.E., 1999. Model simulation of the carbonate chemistry in the microenvironment of symbiont bearing foraminifera. Marine Chemistry 64, 181-198.

Wolff, E.W., Fischer, H., Fundel, F., Ruth, U., Twarloh, B., Littot, G.C., Mulvaney, R., Röthlisberger, R., De Angelis, M., Boutron, C.F., 2006. Southern Ocean sea-ice extent, productivity and iron flux over the past eight glacial cycles. Nature 440, 491.

Wolgemuth, K., Broecker, W.S., 1970. Barium in sea water. Earth and Planetary Science Letters 8, 372-378.

Wu, R., Hu, Z.-Z., Kirtman, B.P., 2003. Evolution of ENSO-Related Rainfall Anomalies in East Asia. Journal of Climate 16, 3742-3758.

Wycech, J.B., Kelly, D.C., Kitajima, K., Kozdon, R., Orland, I.J., Valley, J.W., 2018. Combined Effects of Gametogenic Calcification and Dissolution on δ18O Measurements of the Planktic Foraminifer Trilobatus sacculifer. Geochemistry, Geophysics, Geosystems 19, 4487-4501.

Xiao, Y.K., Beary, E.S., Fassett, J.D., 1988. An improved method for the high-precision isotopic measurement of boron by thermal ionization mass spectrometry. International Journal of Mass Spectrometry and Ion Processes 85, 203-213.

Yin, Q., 2013. Insolation-induced mid-Brunhes transition in Southern Ocean ventilation and deep-ocean temperature. Nature 494, 222.

Yin, Q., Guo, Z., 2008. Strong summer monsoon during the cool MIS-13. Climate of the Past 4, 29-34.

York, D., Evensen, N.M., Martínez, M.L., Delgado, J.D.B., 2004. Unified equations for the slope, intercept, and standard errors of the best straight line. American Journal of Physics 72, 367-375.

Yu, Z., Wan, S., Colin, C., Yan, H., Bonneau, L., Liu, Z., Song, L., Sun, H., Xu, Z., Jiang, X., Li, A., Li, T., 2016. Co-evolution of monsoonal precipitation in East Asia and the tropical Pacific ENSO system since 2.36 Ma: New insights from high-resolution clay mineral records in the West Philippine Sea. Earth and Planetary Science Letters 446, 45-55.

Zeebe, R.E., Wolf-Gladrow, D., 2001. CO2 in Seawater: Equilibrium, Kinetics, Isotopes: Equilibrium, Kinetics, Isotopes. Elsevier.

Zhang, Y.G., Pagani, M., Liu, Z., Bohaty, S.M., DeConto, R., 2013. A 40-million-year history of atmospheric CO2. Philosophical Transactions of the Royal Society A: Mathematical, Physical and Engineering Sciences 371, 20130096.